Experimental and Theoretical Investigations of Nanosecond Fibre Laser Micromachining

Eleri Williams

Cardiff School of Engineering,
Cardiff University.

Thesis submitted for the degree of Doctor of Philosophy to
Cardiff University.

2014

Declaration

This work has not previously been accepted in substance for any degree and is not concurrently submitted in candidature for any degree.

Signed ……………………………………….. (candidate)   Date ……………………….

This thesis is being submitted in partial fulfillment of the requirements for the degree of PhD.

Signed ……………………………………….. (candidate)   Date ……………………….

This thesis is the result of my own independent work/investigation, except where otherwise stated. Other sources are acknowledged by explicit references.

Signed ……………………………………….. (candidate)   Date ……………………….

I hereby give consent for my thesis, if accepted, to be available for photocopying and for inter-library loan, and for the title and summary to be made available to outside organisations.

Signed ……………………………………….. (candidate)   Date ……………………….

Abstract

Pulsed ytterbium-doped fibre lasers based on a master oscillator power amplifier (MOPA) architecture possess attractive characteristics over their Q-switched diode-pumped solid-state counterparts. These include a relatively low cost of ownership and a flexible operating window with respect to the pulse duration, shape and repetition rate. For micro machining applications, given this inherent large processing window available with respect to the pulse characteristics, the effect of process parameters on particular machining outcomes needs to be investigated.

The literature review conducted identified four important gaps in the knowledge surrounding the nanosecond fibre laser machining of materials. These gaps included the optimisation of the nanosecond fibre laser machining during milling operations, with the aim of obtaining both high surface quality and material removal rates, as well as the need for complimentary theoretical and experimental studies on the basic nanosecond laser material interaction for a wide range of engineering materials. In addition, the characterisation of the nanosecond laser machining of bulk metallic glasses, and the investigation of processing conditions leading to crystallisation of their amorphous structure, were identified as knowledge gaps that need to be addressed.

The first knowledge gap was the focus of Chapter 3. The particular parameters under investigation in this study were the pulse duration and repetition frequency, the pulse overlap, the scanning strategy and the distance between linear machined tracks when processing aluminium. The results showed that, for each of the pulse durations studied, the specific frequency at which both the highest energy and average power are delivered leads to the maximum material removal rate (MRR) achievable, and to high values of surface roughness. It was also observed that the lowest surface roughness obtained corresponds to a specific

frequency range which is common for all pulse durations. Following this, a design of experiments was conducted for a given pulse duration with the aim of identifying an optimum combination of parameters with respect to the attained surface roughness while operating at the frequency resulting in the highest MRR. This optimisation study resulted in a 60% decrease in the achieved surface roughness and also showed that the distance between machined tracks had the highest influence on the surface finish among the parameters considered.

In the following chapter, a theoretical model was developed to predict the topographical evolution of the single pulse craters as a result of the time-dependent temperature rise in the processed materials when the laser beam is incident on its surface. In addition to this theoretical study, in an to attempt to understand the laser material interaction on a more fundamental level, single pulse experiments were conducted at varying laser fluence values and pulse durations leading to the formation of single craters on the surface of a number of materials namely, titanium, silicon and silicon carbide. In particular, different pulse lengths were investigated at decreasing values of fluence until no visible effect on the material surface could be observed. Based on this investigation, the fluence corresponding to the ablation threshold for each material at different pulse durations could be found whilst identifying the relationship between the laser processing parameters and the dimensions of the single craters. Scanning Electron Microscopy (SEM) micrographs of the craters were also used to observe phenomena such as melt ejection as a result of varying the process parameters. The experimental results were compared with the theoretical predictions and a good agreement between both set of data was found with respect to the achieved depths and diameters of the craters.

The additional knowledge gaps were the focus of Chapter 5. In particular, the characterisation of nanosecond laser machining of a zirconium-based bulk metallic glass (BMG) was conducted using the approach employed in Chapter 4. Similar conclusions were reached with regard to the single pulse material removal behaviour when varying the fluence and pulse duration. In addition, milling of the material with different parametric combinations was implemented to investigate the crystallisation behaviour of the BMG. To complement these experimental tests, the theoretical model reported in Chapter 4 was further developed to predict the heating and cooling rates of the milling process. From this study, it was found that varying the process parameters of the machining of BMG results in a variation in the critical cooling rate (from the melt temperature to the glass transition temperature) which may result in crystallisation of the material.

Acknowledgements

My deepest gratitude goes to both of my supervisors, Prof. Stefan Dimov, for his guidance through my first year as an independent researcher and Dr. Emmanuel Brousseau for his unquestionable support through the inevitable ups and downs of this research and for always keeping me focused and giving me sound advice in all aspects of my studentship.

Extra special thanks goes to Dr. Christian Griffiths and Dr. Andrew Rees for allowing me this opportunity, for their friendship, always being on my side, and for their invaluable industrial and academic insights. Their belief in me never wavered.

I would also like to thank Dr. Petko Petkov and Dr. Todor Dobrev for their guidance in the lab and for allowing me to call upon their expertise whenever I needed. My gratitude also extends to the Chemistry department and Cardiff University, in particular, Dr Colan Hughes and Victoria Keast for their help with the XRD analysis and for brainstorming ideas with me.

I will also take this opportunity to thank my industrial sponsors at SPI Lasers, Southampton, not only for their financial support but also for allowing me to gain an industrial perspective on my work, and specifically Dr. Paul Harrison for lending me his expertise to allow me to fix issues I may have had and to be able to come to meaningful conclusions.

Finally, this research would not have been possible without the never-ending support of my family. I hope to make them proud, especially my daughter who has been my welcome distraction and ray of sunshine throughout.

Nomenclature

k = thermal conductivity (W.m^{-1} K^{-1})

T = temperature (K)

C_p = heat capacity (J.kg^{-1} K^{-1})

w_0 = spot size (µm)

F = laser fluence (J.cm^{-2})

F_{th} = threshold fluence (J.cm^{-2})

v_s = scanning speed of the laser beam on the surface of the material (m.s^{-1})

f = frequency of the laser pulse (Hz)

ρ = density (kg.m^{-3})

α = optical absorption coefficient (m^{-1})

$I0$ = peak output beam power (W)

E = laser beam energy (J)

τ = laser pulse width at full width half maximum (s)

L_h = latent heat of fusion (J.kg^{-1})

D = diffusivity (m^2.s^{-1})

l_t = thermal penetration depth (m)

T_m = melting temperature (K)

z = distance into the material as measured in the direction perpendicular to the surface (m)

Table of contents

List of figures

Figure 3.3 Image showing the optical set up of the optical beam delivery system. The beam from the source laser is reflected from moveable mirrors, through a 100 mm F-Theta lens, ontp the surface of the workpiece (Courtesy of Lasertec).

Figure 3.4 Sample images and their corresponding line profiles for the overall image and separated into its waviness (low-frequency) and roughness (high-frequency) components (Brebbia and Klemm, 2013).

Figure 3.5 MRR evolution with the pulse repetition frequency for a pulse duration of 140 ns. The vertical dashed line indicates the PRF0 for this waveform which is 51 kHz.

Figure 3.6 Evolution of the MRR with the frequency for three waveforms with different pulse durations. The vertical dashed lines represent the PRF0 for each waveform 55 kHz, 60 kHz and 63 kHz for waveforms 17, 18 and 19 respectively.

Figure 3.7 Variation of the material removal rate (MRR) at repetition rate, PRF0 for different waveforms at 35% of the maximal power. The table displays the pulse durations and their accompanying PRF0 value.

Figure 3.8 Evolution of the surface roughness (Ra) with the pulse repetition frequency for a pulse duration of 140 ns. The vertical dashed line indicates the PRF0 value for this waveform which is 51 kHz.

Figure 3.9 Percentage of pulse overlap as a function of the pulse repetition frequency for a scanning speed of 600 mm.s^{-1} *and a spot diameter of 32 µm.*

Figure 3.10 SEM images of the bottom of pockets machined at (a) 15 kHz and (b) 30 kHz Scale bar: 10 µm.

Figure 4.3 Variation of temperature with time for a complete single pulse heating and cooling cycle using a pulse width of 140 ns and at 43.7 J.cm^{-2} for (a) silicon carbide, (b) silicon and (c) titanium.

Figure 4.4 Temperature variation with time for varying fluence values and for a constant pulse duration of 140 ns for (a) silicon carbide, (b) silicon and (c) titanium. The horizontal lines are the melt temperature for each material and the vaporisation temperature for titanium and silicon. The dotted curve represents the intensity evolution for the highest fluence in GW.m^{-3}.

Figure 4.5 Predicted depth (a) and diameter (b) of craters machined at 140 ns pulse duration with varying fluence.

Figure 4.6 Temperature variation with time at 14 J.cm^{-2} at the centre of the substrate for a variety of peak powers for (a) silicon carbide (b) silicon and (c) titanium. The peak power varies with pulse duration according to; 140 ns – 785 W, 85 ns – 1294 W, 55 ns – 2000 W and 25 ns – 4000 W.

Figure 4.7 Variation of the temperature on the top surface of titanium for a fluence of 14 J.cm^{-2}, and for pulse durations of 140 ns and 25 ns. The higher temperature reached for the shorter pulse duration is a direct consequence of the higher values of peak power resultant at the shorter pulse duration.

Figure 4.8 a) Depth and (b) diameter variation with fluence for three materials investigated at 140 ns.

Figure 4.9 Semi-log graph used to determine the threshold for material removal at a pulse duration of 140 ns.

Figure 4.10i SEM images of three single pulse craters machined in silicon at 140 ns and at: (a) 19.4 J.cm^{-2} (b) 29.1 J.cm^{-2} and (c) 43.67 J.cm^{-2}. Scale bar: 10 µm.

Figure 5.6 Craters machined in Vitreloy 1 at the same energy but different peak powers: (a) 1.4 kW at 140 ns and (b) 3.6 kW at 55 ns. Scale bars: 10 µm.

Figure 5.7 Peak power variation with pulse duration at 0.1 mJ, and the corresponding SEM images of craters machined in Vitreloy 1 with (a) 25 ns, (b) 55 ns, (c) 85 ns, (d) 100 ns and (e) 140 ns pulse length. Scale bars: 10 µm.

Figure 5.8 Theoretical temperature distribution with time for a heating and cooling cycle for a single pulse of 140 ns and with a fluence of 43.7 J.cm^{-2}*. The time taken for the material to cool down to 350 K is 67 µs.*

Figure 5.9 Theoretical temperature distribution with time for a variety of fluence values at 140 ns pulse duration. The horizontal line shows the melt temperature of the material at 937 K.
The dotted curve represents the intensity distribution with time for the highest fluence of 43.7 J.cm^{-2}*.*

Figure 5.10 Effect of varying the peak power at the same fluence on the temperature variation with time for four different pulse durations; 140 ns, 85 ns, 55 ns and 25 ns and for a fluence of 14 J.cm^{-2}*. The peak power value is also given for each curve.*

Figure 5.11 Predicted (a) depth and (b) diameter for craters machined in Vitreloy 1 with pulse durations of 140 ns, 85 ns, 55 ns and 25 ns at varying fluence values.

Figure 5.12 (a) SEM image of a crater machined at 15 ns with 7.6 J.cm^{-2} *with (b) close up of the feature of interest. The arrows on image (b) measures 2.5 µm. Scale bars: (a) 10 µm (b) 2 µm.*

Figure 5.13 The theoretical temperature distribution on the surface of the crater shown above. The vertical solid line represents the edge of the crater which has a diameter of about 30 µm and the outside region of the material that is heated to the glass transition temperature, and the horizontal dotted line indicates the glass transition temperature of Vitreloy 1 which is stated to be 623 K (Waniuk et al, 2007).

Figure 5.30 Temperature distribution for multiple pulses in the centre of the top of sample 6 over 500 µs.

Figure 5.31 The temperature distribution with time for multiple pulses for sample 1 over 1600 µs.

Figure 5.32 Theoretical heating and cooling curves for each sample in the centre of the top surface of Vitreloy 1.

Figure 5.33 Comparison of effective cooling curves for the final pulse that causes phase change in the centre of the top surface of the substrate, between the melt temperature and the glass transition temperature for all samples processed.

Figure 5.34 Cooling curve of the final pulse that induces phase change from solid to liquid for each sample machined between the melt temperature and the glass transition temperature. The dotted lines represent the melt temperature (937 K) and the glass transition temperature (623 K). The dotted curve represents a hypothetical version of the critical cooling curve for this material.

List of tables

Introduction

1.1 Motivation

Laser machining is gradually becoming a commonly used tool in industry due to its advantages as a versatile, cost efficient, non-contact process. Specifically, the fibre laser industry is growing significantly, with this sector contributing to an increasing number of industrial applications year after year (Belfotre, 2014). The recent advances in Ytterbium fibre lasers based on a master oscillator power amplifier (MOPA) architecture have led to laser systems with high energy, high brightness pulses with a short duration whilst also being efficient, comparatively low in cost and exhibiting a flexible operating window with respect to the pulse duration, shape and repetition rate. These systems have demonstrated the ability to process a wide range of materials, with applications ranging from engraving, cutting, drilling, scribing, thin film patterning and polishing. Even though these lasers have demonstrated these capabilities, further research is still necessary for them to be able to successfully challenge traditional Nd:YAG or CO2 laser systems used in industry. In this context, an important motivation behind the research contained within this thesis is to contribute to the optimisation of the process during nanosecond laser machining, using a 20 W Yb fibre laser, for a variety of different materials, including engineering metals, semiconductors and amorphous alloys. Through the comparison of the effectiveness of different pathways to optimisation, it may be possible to make the identification of optimal parameters for specific outcomes more efficient, cutting down on pre-experimentation time and resources. Optimisation is not the only motivation however. In particular, through experimental and theoretical investigations, it is expected that a deeper understanding be gained of the underlying phenomena driving the removal of material and how changing the material and system parameters affect them. An understanding of these phenomena could allow the classification of system parameters that result in various processing regimes. In turn, this knowledge can be utilised for applications that require specific machining outcomes such as micro milling where a high level of surface finish is required whilst also operating at comparatively large removal rates, or polishing which relies on the laser not removing material. The workpiece materials considered in this thesis are those commonly employed in industry so that the findings can be used in actual industrial processes. In addition, particular attention is paid to the processing of a Zr-based bulk metallic glass (BMG) substrate given the attractive mechanical and chemical characteristics of such alloys, which is inherent to their amorphous nature and their promising potential in a range of applications such as consumer goods and scientific instruments. In this case, specific attention is given to the microstructural changes of the material at varying heating and cooling cycles, both experimentally and theoretically, to assess and predict its crystallisation behaviour at the ultra-high temperature gradients induced when using a nanosecond laser.

1.2 Research objectives and aims

This work attempts to address optimisation issues encountered when using a commercially available fibre laser with a wavelength of 1064 nm to machine a variety of different classes of materials including metals, amorphous metals and semiconductors. Particular interest is focused on the ability to control the pulse duration of the laser over a wide range of values from 15 ns to 220 ns. This freedom of choice for the pulse selection, results in a large parametric range available on one system. This work also addresses the need to understand the underlying physical mechanisms that occur when processing materials with laser radiation, specifically the material removal thresholds and the topographical changes when varying the laser parameters. In addition, special attention is paid, both experimentally and theoretically, to the crystallisation processes occurring when machining a zirconium-based bulk metallic glass.

Research aims

1. To investigate the machining of aluminium with a 1064 nm fibre laser with the aim of identifying a processing window for the optimisation of both a high material removal rate and a low surface roughness when conducting laser milling operations.
2. To investigate the underlying physical phenomena occurring during the laser material interaction process for three different materials which include metals and semiconductors, through the use of experimental and theoretical techniques.
3. To study the laser material interaction occurring when machining a zirconium-based bulk metallic glass at ultra-high heating and cooling rates, using single and multiple pulses with a particular focus on the topographical changes induced and the possible crystallisation process generated.

1.3 Thesis synopsis

Chapter 2

In Chapter 2, a literature review is conducted to identify knowledge gaps relevant to the context of the thesis. This chapter begins with an introduction to laser machining, in particular the ablation processes with nanosecond fibre lasers, and their positive and negative attributes. Process optimisation studies are then reviewed including single pulse investigations and those that use the design of experiment method. This review shows that studies in this area are dominated by Nd:YAG laser systems and thus investigations using MOPA-based Yb fibre lasers are more scarce. The chapter then moves on to present literature where the laser-material interaction is specifically studied including the effect of various parameters on the process. The conclusions of this part of the chapter include that the identification of various fluence regimes is useful due to different industrial applications needing different mechanisms to be involved. The laser machining of bulk metallic glasses is then reviewed and the main conclusion reached is that the laser processing of metallic glasses with nanosecond laser pulses is, as yet, under researched. The final part of Chapter 2 includes a comprehensive report about the modelling of the laser ablation process. The physical processes involved in the laser material interaction are discussed first before moving on to the basics of the theoretical modelling approaches. The section discusses analytical and numerical modelling as well as the molecular dynamics approach. It concludes that, although the modelling of the laser material interaction process has been well researched, the modelling itself is still a useful tool for the identification of various machining regimes as well as an offline optimisation tool to reduce waste of resources.

Chapter 3

Chapter 3 addresses the optimisation of the nanosecond fibre laser machining of aluminium through the characterisation of the material removal rate and the surface roughness. The chapter begins with a first set of experiments that were carried out over a large range of pulse durations and frequencies. The second set of experiments reported used the design of experiments approach to achieve further optimisation based on the results of the first set of experimental results.

Chapter 4

Laser milling, which is the focus of Chapter 3, involves the overlapping of single craters to form grooves that then overlap themselves with subsequent lines of single pulses to achieve the desired cavity. The laser material interaction process in this case can be complex due to heat accumulation affects associated with multiple, moving pulses. In order to avoid these effects, Chapter 4 focuses on the basic laser material interaction for single pulses. The first half of the chapter introduces the theoretical approach followed to develop a model which is then implemented in the FlexPDE software. This model is used to predict the temperature variation and the material removal over a wide range of system parameters and for three materials; namely pure titanium, silicon and silicon carbide. An experimental study is then presented where the effects of fluence, pulse duration and peak power on the geometry and morphology of the single pulses is discussed. Finally the results of the theoretical and experimental studies are compared for each material.

Chapter 5

A similar method of analysis as that reported in Chapter 4 is conducted first for the laser material interaction of a zirconium based bulk metallic glass known as Vitreloy 1. The chapter then proceeds with a study of the crystallisation of Vitreloy 1 with different parametric combinations. An x-ray diffraction (XRD) analysis of each sample machined with different combinations is presented as well as the theoretical modelling of the process with multiple moving pulses in an attempt to determine the reasons for the retainment of the amorphous structure or crystallisation when the material is irradiated with various parametric combinations.

Chapter 6

The final chapter of this thesis reiterates the knowledge gaps identified in the literature review conducted in Chapter 2. It then goes on to discuss the contributions and conclusions from each chapter as well as the future work that has been identified as a result of the thesis as a whole.

Literature Review

2.1 Laser Machining

2.1.1 Introduction

Laser machining is a commonly used material removal process, suitable for a range of industrial applications. Unlike traditional machining and grinding processes, which rely on the mechanical interaction between the workpiece and a harder tool or abrasive particles to remove the softer workpiece material, laser machining relies on energy-assisted processing for material removal. By applying laser machining, it is possible to generate complex three-dimensional (3D) precision surfaces (Bruening et al, 2011, Zimmer et al, 2000 and Heyl et al, 2001). In addition, the process is versatile and can be used for drilling, cutting, milling and engraving applications (Wang et al, 2009 and Lee et al, 2008).

The energy assisted mechanism for material removal on which laser machining relies can take place through melting, vaporisation or ejection. The particular applied mechanism depends on the laser source and the material being machined (Pham et al, 2002). For pulsed lasers specifically, the laser beam interacts with the substrate material in a series of pulses. Each pulse contains a specific amount of energy, which is a function of the average power and pulse duration. Pulse durations are classified into four main categories: namely microsecond (μs), nanosecond (ns), picoseconds (ps) and femtoseconds (fs). Each pulse category displays process/material response characteristics that are unique to the pulse duration. However, all laser sources must initially create a phase transition in the substrate material from a solid to a ‘volatile phase’ (Von der Linde and Sokolowski-Tinten, 2000). The process of phase transition varies depending on the applied pulse durations (Amer et al, 2005).

2.1.2 Ablation with nanosecond pulses

Particular laser sources are more appropriate to certain types of machining regimes (Knowles et al, 2007). Ablation depends on the characteristics of the laser beam being delivered and on the properties of the material that is being ablated, as the pulse energy will only be absorbed at certain wavelengths and ablation will only occur above a specific fluence threshold. For nanosecond pulses, the energy delivered by the laser pulse to the substrate is absorbed by electrons and then it is propagated through to the electron subsystem of the material and transferred to the lattice. Due to the length of the pulse, there is enough time for the energy absorbed by the electrons to be transferred to the lattice and for both the electrons and the lattice to achieve thermal equilibrium. In addition, given that there is sufficient time, with nanosecond pulses, for the absorbed energy to melt the material, a thermal wave propagates into the workpiece leading to the occurrence of undesirable effects. These will materialise in the form of a heat-affected zone (HAZ), recast layer, micro cracks, shock wave surface damage and debris from ejected material (Petkov et al, 2008). However, machining with shorter pulses decreases the amount of time that the heat can transfer and thus results in a reduction of thermal damage (Yasa and Kruth, 2010). This can be visualed in Figure 2.1 where the effects of a short pulse laser are compared to those caused by ultrashort lasers (Petkov et al, 2008).

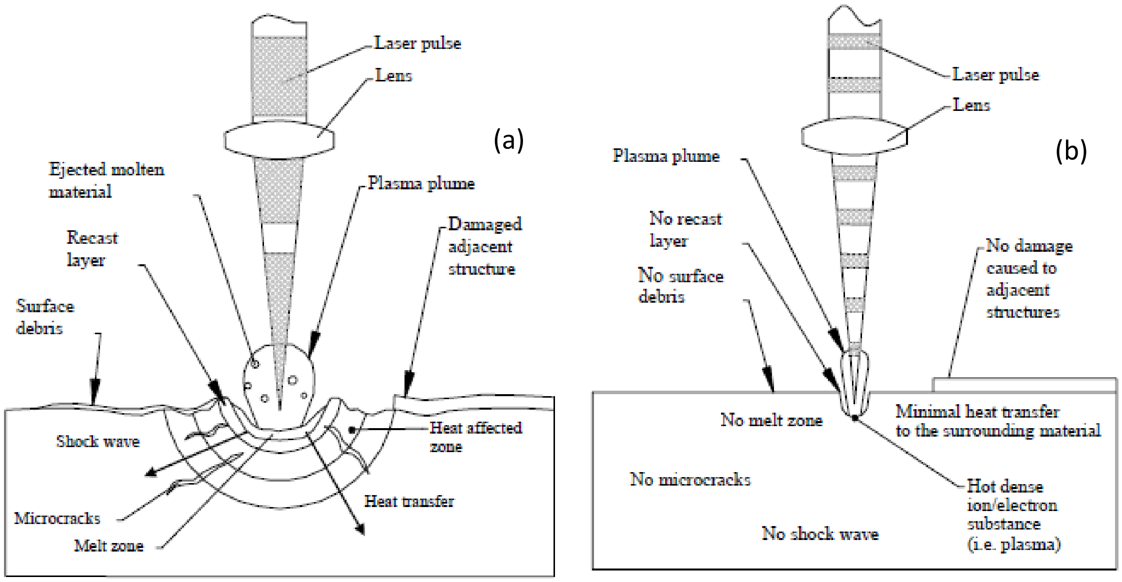

Figure 2.1 Thermal effects resultant from (a) short-pulse laser compared to (b) ultrashort laser on the incident material. The ultrashort pulses result in negligible thermal damage due to the limitation of the time that the laser irradiates the surface of the material (Petkov et al, 2008).

2.1.3 Introduction to fibre lasers

The light that emits from a laser has been created through the process of ‘stimulated emission’. Initially a source of light, often at a wavelength different to that of the emitted laser beam, is used to ‘pump’ electrons within a material (referred to as the gain medium) to a higher orbit than their stable state. The excited electrons will then drop to a meta-stable state where they will remain until stimulated to drop to another energy level and emit a photon. Once this happens to one electron it will cause a cascade as the resulting emitted photons excite other electrons in their meta-stable states to drop down and emit other photons. A diagram of this process can be seen in Figure 2.2 *(http://www.orc.soton.ac.uk/61.html. Accessed: 24.03.2015)*. In this Figure, the pump photon excites an electron to a higher energy level where it will eventually relax to a meta-stable energy level. An incoming photon will then stimulate the electron to return to its’ ground energy level and a secondary photon will be released. These photons are restrained within the laser material using reflective mirrors so that they stimulate enough electrons. The laser material restricted at each end is called a laser cavity and this is where the laser beam of a specific frequency is created through the process of stimulated emission. The mirror at one end will allow a small percentage of photons through and this creates the laser beam.

Traditional solid state lasers have a gain medium that is usually crystal or glass. This gain medium is pumped by a flash lamp or a separate diode laser system. The control of the beam within the gain medium occurs with mirrors and diffraction gratings. For fibre lasers, a fibre is doped with elements, such as Erbium or Ytterbium, and is then pumped with a suitable source such as a diode laser. If using a diode laser, the beam is too low-quality to focus into the smaller fibre core so the core is usually surrounded by a cladding and an outer sheath which reflects the diode laser through the inner fibre core, exciting electrons as it passes through. A schematic diagram of a fibre laser can be seen in Figure 2.3 *(Maini, 2013)*.

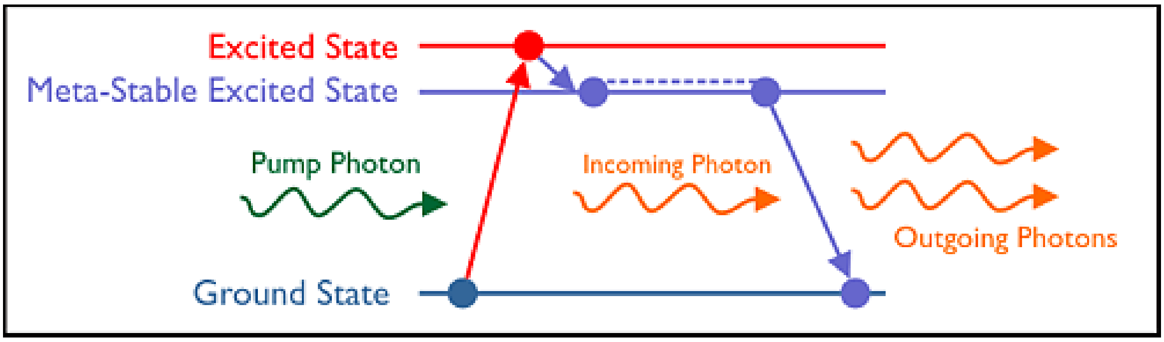

Figure 2.2 A diagram showing the process of exciting electrons to excited states with a pump photon. Relaxation of the electron to a meta-stable state will follow, until an incoming photon stimulates the electron to return to its original ground energy level producing the emission of secondary photons. (http://www.orc.soton.ac.uk/61.html. Accessed: 24.03.2015)

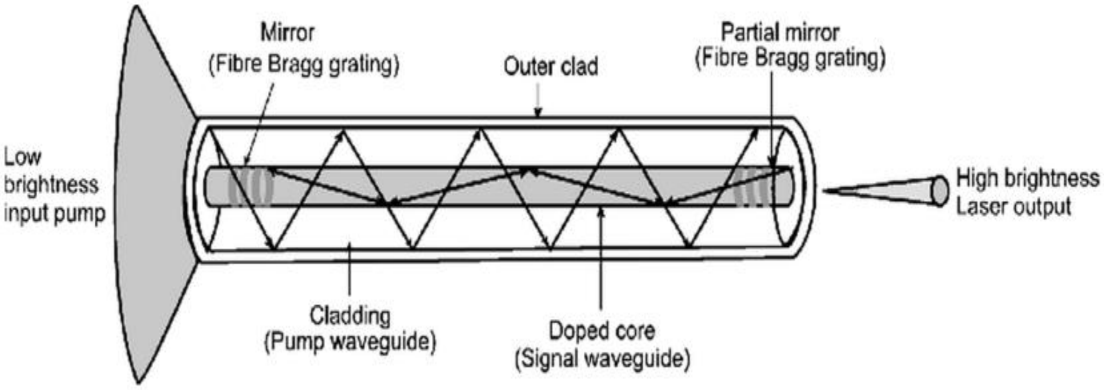

Figure 2.3 Schematic of a fibre laser indicating how the pumped light is reflected through the inner doped fibre core via cladding. This light is then used within the fibre core to stimulate the emission of photons that are subsequently released through a partial mirror at one end of the laser cavity to form the high brightness output beam (Maini, 2013).

The fact that the beam is confined into the fibre provides the first advantage of the fibre laser over traditional lasers. In particular, the confinement results in an easy delivery of the beam to a moveable focusing element. This also means that fibre lasers are more stable because the set-up that exists in a solid state laser to generate the beam such as finely aligned mirrors can easily move if knocked, whereas the beam created from a fibre laser is generated within the fibre core. Another advantage of the beam confinement within the fibre is that it leads to generating a beam of very high quality. This causes the creation of a beam that can be focused into a very small spot which can be effective for laser applications such as cutting. Another advantage of such lasers is that the fibre can be bent or coiled reducing the systems overall dimensions compared to a traditional laser. There are many more advantages associated with fibre lasers such as high power production and their power conversion efficiency.

At the same time fibre lasers also exhibit some disadvantages. These include undesired nonlinear optical effects when operated at higher pulse energies such as Raman scattering. This process occurs when the photons within the gain medium interact with matter resulting in inelastic scattering of the incident photon. This results in the frequency of the photon being changed, usually lowered. A large amount of these collisions can limit the achievable peak power of the laser. The benefits of fibre lasers are reflected in their sales growth. At the close of 2011, fibre laser sales had grown by 38% compared to a 14% growth in CO2 laser systems. This growth was led by the sales of high-power laser systems for the use of metal cutting (Overton et al, 2012).

Fibre lasers are used in many industrial sectors to cut, drill and weld a variety of materials (Dietrich and Kelbassa, 2012 and Quintino et al, 2007). They are also utilised for engraving, micromachining (Gabzdyl, 2010) and even processing of thin films such as Indium Tin Oxide (SPI Lasers, 2008). Kleine and Watkins (2004) applied a fibre laser to conduct micro cutting operations in metals for instance. Cutting tests were undertaken to investigate the influence of pulse shape, pulse length and pulse frequency on the cutting quality performed on stainless steel. It was concluded that fibre lasers produce beams that result in good quality cutting with low surface roughness and low taper of sidewalls, when the process parameters were optimised. Metals are not the only material that fibre lasers are suitable to machine. Hendow et al (2010) reported on the use of a 10 ns fibre laser to machine silicon. Cutting, drilling and scribing were investigated and it was concluded that the ability to tune and refine the pulses from a master-oscillator-power-amplifier (MOPA) fibre laser output leads to being able to optimise the machining process of silicon. The flexibility that MOPA fibre lasers offer also lends them to the machining of thin films like Molybdenum for use in photovoltaic cells.

Even though fibre lasers offer the flexibility to be able to process materials in many industrial sectors, the parameters of the laser system need to be optimised to attain the desired result for the application chosen. This optimisation can be achieved through experimental observations and theoretical modelling of the underlying physical phenomena driving the process. In the remaining parts of this chapter, a literature review is provided to summarise 1) published research studies that investigated the parametric optimisation of the ns laser machining process, 2) experimental efforts into laser material interaction, 3) investigations of the laser processing of bulk metallic glasses and 4) theoretical model developments of the laser ablation process. Conclusions are then made on the general assumptions made in the investigations and also on the remaining gaps there appear to be in the reported body of literature.

2.2 Process Optimisation

2.2.1 Introduction

When aiming to remove material from a workpiece through laser processing, there are many parameters that can be considered important such as the energy, peak power, spot size and frequency of the laser pulses. Laser ablation parameters influence the process in different ways. The energy (J) of the pulse, for example, is important because this is the energy that is transported into the workpiece, via thermal conduction, in order to process the material. The peak power (W) can be influential because it must be large enough to heat the material above its melting point in order for removal to occur. Ion (2005) states that in the context of machining ceramics, a high peak power can be used to cause the onset of vaporisation faster, bypassing melting and resulting in a smaller heat affected zone. The amount of energy contained within the laser pulse affects the temperature to which the material substrate is raised. There is an energy threshold for different materials, below which no melting/vaporisation and thus no material removal will occur (Chen and Yao, 2000). The frequency (Hz) of the applied pulses is important to ensure efficient removal of material. It is also a factor in determining the degree of overlapping for successive pulses which in turn influences the material removal rate and the achieved surface roughness of the final product. Pulse duration (s) is also an essential factor to consider when optimising the laser machining process. Not only do different categories of pulse width (i.e µs, ns, fs and ps) cause different material responses, but varying the pulse duration within one category such as in the nanosecond regime, can also affect the machining outcomes due to the variation in effective heat penetration as the pulse lengthens and shortens (Schaaf, 2010).

2.2.2 Process optimisation using single factor experiments

Stafe et al (2006) investigated the effect of the laser fluence *(F)* on the ablation rate of aluminium using an Nd:YAG laser system operating at 4.5 ns. It was concluded that the ablation rate increases with laser fluence as a function of $F^{1/2}$. Gounaris et al (2010) also used an Nd:YAG laser to complete experimental investigations on the effect of energy on the ablation rate. The conclusion was that an investigation of the energy influence on ablation rate would not be particularly useful because the work showed a 'sweet-spot' at approximately 4.5 mJ for the highest ablation rate for steel, possibly due to the possibility of unwanted thermal effects such as plasma occurring at higher values of energy. This is in-line with the work of Voisey et al (2003), who stated that the ablation rate increases with power density up until a certain point before decreasing. The point at which the sign of the gradient between power density and ablation rate changes is dependent on the material being processed.

Deladurantaye et al (2009) investigated the influence of a pulse-shaping 2.5 ns fibre laser on the laser machining process. By using a Yb-doped ns fibre laser, experiments were carried out on aluminium and stainless steel. The conclusions for aluminium were that the augmentation of the pulse duration increases the efficiency ($\mu m^3.\mu J^{-1}$) up until a specific value after which it begins to decrease. These optimum values are said to correspond to the plasma ignition values for the region. In subsequent experiments, these authors then utilised the identified pulse duration that achieved the highest removal rate for the majority of machining then switched to a pulse duration that resulted in a better surface roughness, in the same vain as Gounaris et al (2010) did with mixed-mode ablation.

When processing stainless steel with a fibre laser that had an adjustable pulse duration from 10 ns to continuous wave, Herfurth et al (2007) kept the energy per pocket machined constant but varied other parameters throughout to see their effect on the material removal rate and the surface quality. The experimentation found that, at lower pulse repetition rates, the material removal rate (MRR) increases as the pulse duration increases up to a certain value. The same behaviour is seen at higher pulse repetition rates, where it becomes more pronounced. The conclusion drawn was that the maximum MRR occurs at longer pulses for lower repetition rates compared to higher repetition rates. This is expected because if the pulse duration is longer, the material is subjected to energy from the beam for longer and thus the amount of pulses needed to remove the same amount of material compared to shorter pulse duration is less. However, with a higher repetition rate of pulses, the accumulation of damage begins to occur as investigated by Liu et al (2010). In particular, these authors investigated the morphological changes when applying pulses from an Nd:YAG 20 ns laser to stainless steel. The main conclusion reached was that with the application of an increased number of pulses the morphological changes such as micro cracks and droplets due to re-solidification become more pronounced. These studies illustrate the precedent for the necessary compromise needed when optimising the process for two separate machining outcomes such as MRR and low surface roughness.

2.2.3 Scanning strategies

Other investigations have been completed on the effect of scanning strategies on material machining responses. It has been concluded by Genna et al (2010) that the scanning strategy is secondary in importance compared to other parameters. Bartolo et al (2006) investigated the influence of scanning strategies when machining tempered steel with an Nd:YAG laser integrated within the G900 system manufactured by FOBA North America Laser Systems. The considered strategies were defined by different hatch angles, hatch spacing and initial angles. It was found that the best surface roughness was generated by having a small angular increment between machined layers. The second conclusion from Bartolo's work (2006) was that the surface roughness is minimised for a certain value of hatch spacing. This conclusion is in agreement with Selada et al (2011) who, whilst investigating the effect of laser machining on moulds for micro-injection moulding, also concluded that the roughness first decreases with increasing hatch spacing and then it begins to increase. This behaviour could be due to the inefficient removal of material from the previous machined track. Yasa and Kruth (2010) attempted to explain this behaviour by relating the hatch spacing to the overlap factor by:

$$Hatch\ spacing = (1 - overlap) \times spot\ size \tag{2.1}$$

This means that a high overlap factor corresponds to low scan spacing. They concluded that for lower overlap factors (high hatch spacing), the roughness is higher because there is insufficient removal of re-distributed material from the previous track. For higher overlap factors (low hatch spacing) the roughness again is high because of the detrimental effects of higher energy per unit of surface area. Thus it seems that there is a critical threshold value for achieving the lowest possible surface roughness with respect to hatch spacing.

2.2.4 Design of experiments studies

Although single factor analysis is adequate for finding the ideal regimes to machine with and to perform initial investigations of the process, it is a time-consuming procedure, which does not necessarily take into account any interactions that may exist between different factors. A way to investigate the influence of different process parameters and to observe possible interactions between them is to use a design of experiment (DOE) approach. In this case, the parameters are applied in specific combinations and then the results are analysed statistically. Both methods; single factor and DOE, can be used in combination, to identify the most influential parameters and their associated values to optimise the MRR and the surface roughness (Gournaris et al, 2010, Deladurantaye et al, 2009).

Campanelli et al (2007) investigated the effect of different parameters with respect to the depth of removed material and to the achieved surface roughness by using the experimental design approach. Following preliminary testing, a number of parameters such as pulse duration, pulse power and peak power were set to constants in order to obtain an acceptable MRR. For the analysis of the depth, two factors were investigated namely, the overlapping of consecutive pulses and their frequency. For the surface roughness analysis, the overlapping and frequency were also studied along with a third parameter for the scanning strategy. The results showed that, for surface roughness, the main influential parameter is the overlap between consecutive pulses and the least influential parameter is the scanning strategy. Using the single factor method, the effect of these parameters was found to be identical. This shows that the DOE method can give the same results as the single factor method while being less time consuming. The DOE approach is also superior in some ways because it can provide additional information on the interaction between parameters, thus giving a more extensive view of the reasons behind the behaviour observed. Campanelli et al (2007) did not include the scan speed in the reported investigation while Saklakoglu and Kasman (2011) found that this was the most influential parameter when machining on steel with a 30W fibre laser marking system. However both studies were completed on different metals. Thus, differing conclusions may be reached when attempting to optimise the laser machining process because the variety of parameters affecting the machining response does not only include the machine parameters but also the material properties. This is demonstrated in work by Chen and Darling (2005) where a frequency tripled Nd:YAG laser was used to machine on sapphire and silicon. The ablation efficiency for sapphire was shown to increase up to a certain point, where any increase in fluence did not enhance the ablation rate. This behaviour was the same for silicon except that the ablation rate did not decrease like the sapphire; it began to reach a plateau. This plateau is attributed to a plasma shielding effect. The other difference between the materials was that the effect of the scan speed was more pronounced when processing the silicon workpiece. The slower ablation rate for the sapphire was reported to be due to the difference in its material properties compared to the silicon, primarily due to the higher melting temperature (2054 ^{o}C compared to 1414 ^{o}C for silicon) and lower conductivity (0.30 W.(cm.K)$^{-1}$ compared to 1.50 W.(cm.K)$^{-1}$ for silicon) of the sapphire.

2.2.5 Summary

The main conclusion that can be drawn from the above section is that numerous process factors can influence the machining outcomes of laser ablation. Two main experimental methods are employed to optimise the process. The first is the single factor method, where parameters are investigated separately. This approach can take a substantial amount of time for completion. The second method, design of experiments, is not only faster but it also enables the identification of any interaction that may occur between different process parameters. Another conclusion that may be drawn is that there is no factor combination that will give both an optimised material removal rate and an optimised surface roughness. There has to be a compromise between these two process outcomes. In order to address this issue, authors have proposed a mixed-mode method of ablation: using factor combinations for high material removal rate for the first part of machining, then a different set of factor values for achieving a good surface finish as the last machining operation. Finally, it is also observed that published studies on experimental process optimisation using nanosecond lasers seems to be dominated by Nd:YAG systems. Thus, such investigations using fibre lasers are scarcer, even though the use of fibre lasers in industry is going from strength to strength.

2.3 Laser Material Interaction

Many researchers have attempted to quantify the mechanisms of material removal during the laser ablation process. Some of these investigations include high speed imaging, probing laser to analyse the plasma plume produced at high fluence values and measurement of weight loss before and after ablation (Mele et al 1996, Kuper and Brannon 1993 and Gamaly et al 2001). These methods have enabled a picture to be built of the complex mechanisms involved in the removal of material during laser ablation. It is understood that once the temperature of the processed material has reached melting point, it can be removed via vaporisation or explosive melt ejection. When low fluence values are used, the temperature reached by the surface is only enough to facilitate melting meaning that the resulting topography of the generated crater is comparably smooth. When the fluence is increased, the high temperature will facilitate vaporisation which will leave a more pronounced crater shape in the material being machined (Maul et al 2006). If the fluence is further increased, the evaporated material produces plasma, which will hinder the ablation by consecutive pulses. This is demonstrated in the work of Semerok et al (2002) where the ablation rate of craters in metal irradiated by a ns Nd:YAG laser begins to decrease after a certain fluence.

Fishburn et al (2006) studied the interplay of these mechanisms with respect to the applied fluence of the laser pulse. Using a MOPA copper vapour laser, single 30 ns pulses were applied to aluminium at varying fluence values and the resulting craters were subsequently analysed. The results showed that at low fluence (0.7 J.cm^{-2}), the crater depth was low and there was no sideways displacement of the material. Also, the diameter of produced craters was significantly smaller than the diameter of the incident beam. As the fluence was increased (around 4-5 J.cm^{-2}), substantial material removal began and the diameters of the craters reached that of the incident beam and their depth increased with the increasing fluence. Rims formed around the craters also became more pronounced. At the maximum fluence (~ 9 J.cm^{-}

^{2}), not only were these phenomena observed, but solidified droplets were also noticed around the craters suggesting the onset of melt ejection. This was verified by using high speed imaging where liquid material could be seen to leave craters in droplet form.

György et al (2002) also reported a similar behaviour with respect to the resulting crater topography when irradiating a titanium target with an Nd:YAG laser with pulse durations from 130 to 220 ns. These authors kept the energy constant and varied the intensity of the beam. They found that, at low intensities, the material in the irradiated area only melted and the ablated depth was negligible. As the intensity applied increases, the craters became deeper and the material removal was more efficient resulting in a rim around the craters that consisted of re-solidified molten material that had been ejected. As the intensity reached higher values, again, droplets began to appear around the irradiated area. Identifying these intensity and fluence regimes that result in specific material responses can be useful when completing certain types of machining operations such as polishing where only melting of a thin layer is needed.

By studying the volume and shapes of craters irradiated by single pulses and then by applying an accurate theoretical model, ablation behaviours can be determined which can give information on the transfer efficiency of the laser energy that is absorbed into the target material. These behaviours can also give information about the shock wave that propagates into the material upon irradiation by the pulse. Borodziuk et al (2003) found that the biggest craters were produced by the pulses with the highest energy and that most of the craters had a hemispherical shape.

It is not just the beam parameters that can affect the behaviour of the craters machined but also the characteristics of the material being irradiated. Quintana et al (2009) studied the difference in the machining behaviour between amorphous and crystalline nickel. They concluded that the material ejection from the craters was more pronounced in the amorphous material than in the crystalline counterpart. This was explained by the difference in the thermal properties of the amorphous nickel as a result of its disordered atomic structure. In particular, amorphous materials have a lower thermal conductivity which lessens the amount of heat conduction within the bulk leading to a more localised heating and a more violent melt ejection process.

Not only are single pulses useful to study laser material interaction as reported above, they are also being utilised in order to texture surfaces for various industrial purposes and for enabling subsequent experimental investigations. In particular, Schwarz-Selinger et al (2001) found that single pulsed nanosecond laser texturing is a ‘convenient and flexible’ way to treat silicon and change its morphology. In the study reported, they were able to apply the surface textured silicon in follow-up experiments, such as in crystal growth investigations. Voevodin and Zabinski (2006) used single 35 ns pulse to form arrays of micro-dimples (c.f. Figure 2.4) in order to investigate the optimum diameter and area coverage for the creation of reservoirs for solid lubricants. Even though single pulse craters are useful for surface texturing, most of the studies in this area utilise multiple pulses per crater to create deeper and wider cavities (Etsion, 2005).

The materials used in many of the single pulse investigations are of high industrial importance. Silicon is widely used in many industries from circuit boards in computers to the waterproof exteriors of buildings. Due to this, many researchers have investigated its machining potential. One such study, conducted by Yoo et al (2000), discussed the mass removal from pure silicon at high irradiances using a 3 ns Nd:YAG laser operating at 266 nm. It was concluded that the mass removal mechanisms vary depending on the fluence applied during machining, and that explosive boiling is present if the fluence is high enough. O’Neill and Li (2009) conducted a preliminary study on the micromachining potential of silicon using a MOPA Yb fibre laser

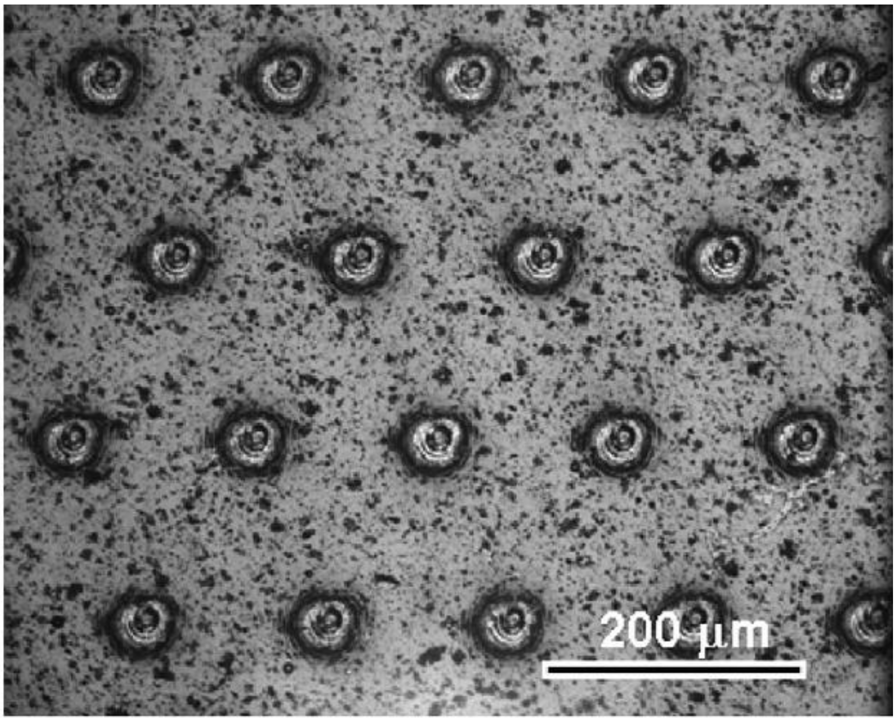

(a)

Figure 2.4 An array of micro dimples machined in TiCN coating surface using an $Nd:VO_4$ *laser operating at 355 nm and a pulse duration of 35 ns. The dimples have a diameter of around 20 µm and are surrounded by thermal oxidation rings which occur due to the localized heating introduced by the laser (Voevodin and Zabinski, 2006).*

operating at 1064 nm. The results showed that the use of this specific laser resulted in high quality micromachining without the usual detrimental effects seen when processing silicon at 1064 nm such as micro cracking and a recast layer. The properties of the compound of silicon and carbon, silicon carbide, include high hardness, good resistance to extreme temperatures and its high thermal conductivity. These properties make this material an ideal candidate for armour plates, brake discs and mirrors in astronomical telescopes. In the context of laser micromachining, Chen and Darling (2008) effectively machined silicon carbide for microfluidic applications using an Nd:YAG laser operating at 266 and 355 nm. Kruger et al (2007) also machined silicon carbide using UV lasers in the nanosecond regime to create through-wafer and blind holes for use in high-electron-mobility-transistor (HEMT) products. Titanium, unlike silicon and silicon carbide is a metal used in industries such as aerospace, sport equipment and medical. Its lightness makes it ideal for the production of sport equipment such as tennis rackets and golf clubs and the biocompatibility of titanium also makes it an ideal replacement for hard tissue in the human body (Liu et al, 2004). The cell resopnse of titanium can be improved by micromachining with a laser source to improve integration with the surrounding tissue. Fasasi et al (2009) demonstrated this ability using an Nd:YVO_4 laser at UV, green and IR wavelengths. It was concluded that the nanosecond laser operated at 355 nm produced the optimised structures with the required dimensions and lack of thermal degradation.

Summary

The above section suggests that studying crater formation by single pulses is important in order to investigate material removal phenomena occurring during laser material interaction without the need for theoretical models.

The main observations to be drawn from the studies reported are:

- The diameter and the depth of craters increase as the amount of energy applied from the beam is increased.

- The material goes through different phase changes depending on the range of fluence values applied.
- As the fluence reaches a specific level, the ablation of the crater is hindered by the production of a plasma plume from the evaporated material.

The identification of these fluence regimes is relevant for different industrial applications. The lower fluence regimes where only melting is taking place can be used for welding while the higher fluence regimes, where evaporation is the main material removal mechanism, can be employed for laser cutting. In addition, the accuracy of thermal models can be verified using empirical data gathered from single pulse experiments. Important process parameters can also be quantified such as threshold values for ablation through the use of mathematical relationships between parameters.

Because the machining of material via laser ablation is based upon the overlap of single pulses, the topography of a single pulse can affect the topography of the overall piece being machined. Thus, the study of single craters can also be used in order to foresee the final surface topography of a machined part. However such types of studies are limited to the observation of results post-machining and thus they need to be complemented by theoretical modelling efforts in order to enable the simulation of the laser ablation process and the prediction of machining outcomes for different types of workpiece materials and process parameters.

2.4 Laser Processing of Bulk Metallic Glass

The studies previously reported in this chapter have mostly involved crystalline materials. Although these are widely processed engineering materials, a new class of materials, known as bulk metallic glasses has emerged that offers superior qualities that make them attractive alternative candidates for use in many applications (Inoue et al 2008). Table 2.1 displays a comparison between the properties of metals, glasses and metallic glasses. Crystalline materials have a structured alignment of atoms in their lattice which means that the atoms are ordered periodically in three dimensions. Amorphous materials, on the other hand, display a lattice with no long-range order and a disordered atomic structure. Amorphous metals have a morphology which is a combination of both crystalline and amorphous materials. This results in a material with the metallic elements and bonds whilst the internal structure is amorphous. This glassy structure combined with the properties of metal that are inherent to these metallic glasses results in superior properties such as, high-strength, high elastic strain limit coupled with a superior corrosion resistance (Peker and Johnson, 1993). These materials are also specifically suited to micro and nano-scale processing as a result of their short range atomic order which allows the formation of grain sizes that range from 10-100 nm (Kumar et al, 2009).

The first reported metallic glass alloy was the produce of work by Klement et al (1960) at the California Institute of Technology. Further glassy metals were reported by Chen et al in the 1970’s. Figure 2.5 displays different types of bulk metallic glass ingots (Inoue and Takeuchi, 2011). The formation of bulk metallic glasses (BMGs) takes advantage of the difference in atomic sizing of all the elements present in the alloy system, which results in atomistic confusion upon cooling. This means that during the process used to cool down the liquid phase of the alloy, the different atoms do not organise themselves into an ordered structure in sufficient time before they become “frozen” in place. However, to avoid crystallisation when

Property	**Metal**	**Glass**	**Metallic Glass**
Structure	Crystalline	Amorphous	Amorphous
Bonding	Metallic	Covalent	Metallic
Yield Stress	Non-ideal	Almost-ideal	Almost-ideal
Workability	Good – ductile	Poor - brittle	Good – ductile
Hardness	Various	Very high	Very high
Optical Nature	Opaque	Transparent	Opaque
Conductivity	Good	Poor	Very good
Resistance	Low	High	Very low
Corrosion Resistance	Various	Very good	Very good
Magnetic Properties	Various	None	Various

Table 2.1 Comparison of the properties of metals, glasses and metallic glasses.

(Adapted from Anantharaman 1984).

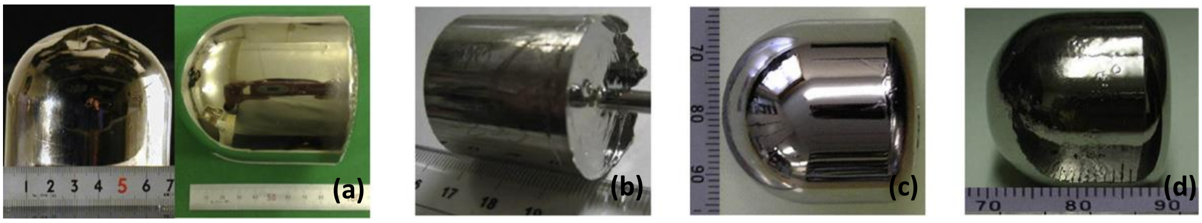

Figure 2.5 Different types of bulk metallic glass ingots (a) Pd-Cu-Ni-P, (b) Zr-Al-Ni-Cu, (c) Cu-Zr-Al-Ag and (d) Ni-Pd-P-B (Inoue and Takeuchi, 2011).

synthesising a metallic glass from its liquid state, it is essential that the cooling rate applied is higher than the critical cooling rate of the particular alloy system processed. As a result, early fabrication attempts were limited to the formation of samples with very thin dimensions as such specimens enabled the required fast heat dissipation rate.

The first metallic glasses to buck this trend, were reported in the 1990's with the creation of alloys with a glass forming ability, defined as the speed at which an alloy must be cooled to frustrate crystallisation, high enough to allow 1 mm diameter rods or larger to be formed fully amorphous (Axinte, 2012).

One of the most studied bulk metallic glass due to its superior glass forming ability was created in 1992 by Peker and Johnson (1993) and named Vitreloy 1, for which the composition is $Zr_{41.2}Ti_{13.8}Cu_{12.5}Ni_{10}Be_{22.5}$. This type of metallic glass exhibits a critical cooling rate of ~2 $K.s^{-1}$ (Kim et al, 1996) and has a critical casting thickness of 3 to 4 cm (Johnson et al, 2011). It also exhibits excellent thermal stability, meaning it can withstand crystallisation well above the glass transition temperature, and displays superior properties, which gives it a large potential for many applications as an advanced engineering material.

The attractive mechanical and chemical properties of BMGs have made them candidates for a number of applications as reported by Inoue et al (2008). These include parts for consumer goods, improved components for scientific instruments and automotive pressure sensors. Using BMGs for the production of micro-electromechanical systems (MEMS) parts with enhanced performance has also been an application of interest (Schroers et al, 2007). The amorphous structure of a material with the properties of metal results in the unique ability to form bulk metallic glasses like plastic. Schroers et al (2007) were able to process BMG with thermoplastic forming for MEMS fabrication by raising the temperature of the material in the super cooled liquid region for a duration short enough to avoid the onset of crystallisation. They concluded that being able to replicate 100 nm features in a similar way to plastic but with a material that has a high-strength, produces a wide range of applications for microstructures and MEMS fabrication. This ability to be formed like plastic also provides interesting prospect to the biomedical industry, as BMGs exhibit a strength and elasticity that exceeds most biomaterials. In particular, Schroers et al (2009) conducted biocompatibility tests and concluded that a number of BMGs could be used successfully as biomedical implants.

As mentioned earlier, in the context of employing BMG to produce miniaturised devices, one of the advantageous characteristics of such alloys relies on the fact that the absence of grain boundaries and crystal defects in their structure creates favourable processing conditions for generating micro and nano-scale surface features (Kumar et al, 2009). A number of material removal techniques have been investigated to structure micro and sub-micro features on as-cast BMGs including mechanical cutting (Zhu et al, 2012) and focused ion beam (Li et al, 2007) respectively. Micro-machining of BMGs with a high power laser system has also gained increased attention in recent years due to the inherent fast processing of such an approach.

Crystallisation of amorphous metals can be avoided if the liquid phase of the material is cooled fast enough to stop the nucleation and the subsequent growth of the crystalline phase. If the molten metal is cooled rapidly, the atoms do not have sufficient time to re-arrange themselves into the ordered atomic arrangement which defines a crystalline structure. The crystallisation temperature of bulk metallic glasses offers the maximum temperature at which the material can be processed without affecting the amorphous structure of the material (Suryanarayana and Inoue, 2011). Due to the dependence of the crystallisation kinetics on the temperature of the BMGs, processing using a laser needs to be studied due to the large temperature gradients experienced when applying a heat source of such magnitude. A large amount of the research into laser processing of BMGs has been centred on the laser welding process. Using a welding scanning speed from 2 to 8 m.min^{-1} and a peak output power of 1200 W, Li et al (2006), investigated the effect of processing parameters on the crystallisation of the weld bead and the heat affected zone when joining two pieces of a ZrCuAl metallic alloy. They concluded that the higher welding speed resulted in a cooling rate that was high enough to suppress crystallisation. This conclusion was supported by the development of a finite element heat source model. The temperature profiles created from this model showed that the samples which were scanned more slowly remained above the crystallisation temperature long enough for the sample to crystallise.

Wang et al (2012) also studied the crystallisation of BMGs during the laser welding process. In this case the bulk metallic glass studied was a TiZrNiCuBe substrate. The laser used had a power of 3.5 kW and the scanning velocity ranged from 6 to 10 $m.min^{-1}$. These authors observed that the crystallisation in the weld joint, where the material is melted, and crystallisation in the heat affected zone (HAZ), where the material stays solid, are dependent on different parts of the heating-cooling cycle. The authors conclude that the cooling rate from the melt temperature to the glass transition temperature is the decisive rate for the determination of the resulting microstructure of the weld zone. In this case, the cooling rate needs to be larger than 780 K/s to avoid crystallisation of the substrate. On the other hand, the change in amorphous structure in the HAZ, which has not changed phase, depends on the entire heating and cooling cycle. In particular, if the HAZ is subject to a temperature above the glass transition temperature of the material for a relatively large amount of time then it is likely to display crystallisation. In agreement with Li et al (2006), the faster scanning speeds resulted in retaining the amorphous structure whilst the slower scanning speeds led to the material being subjected to a large temperature gradient for longer, causing crystallisation to become apparent. These authors also showed that when fully amorphous, the welded joint exhibited a tensile strength close to that of the base material. Chen et al (2014) conducted laser welding tests on annealed $Zr_{55}Cu_{30}Ni_5Al_{10}$ plates using a Yb fiber laser in continuous mode. Interestingly, the study showed that the thermal annealing just above the glass transition temperature of the BMG prior to welding, has a beneficial effect on the weld quality, as well as on the micro hardness and bending strength of welded zones. This result was reported to be due to the fact that annealing favours nanocrystallisation while suppressing large crystal growth in the heat affected zone. Suppressing the crystallisation of bulk metallic glasses is imperative if the attractive mechanical properties of the material are to be retained. Controlling the crystallisation of bulk metallic glasses has been studied by Kim et al (2006) using an Nd:YAG laser system from 1 to 10 ms to weld a copper based bulk metallic glass. Transmission electron microscopy was used to analyse the crystallisation behaviour in the weld and the adjacent heat affected zone. Using both experimental and theoretical methods they concluded that the higher the pulse energy, the more likely the bulk metallic glass was to crystallise due to 1) the lower cooling rates achieved and 2) the variation in chemical composition of the material with the vaporisation of copper at the higher temperatures reached when the pulse energy increases. Another conclusion reported was that the single pulse crystallisation behaviour could not predict the multiple pulse crystallisation behaviour due to the pre and post-heating effects of the interacting laser pulses. This conclusion is important with respect to the theoretical modelling of crystallisation, because it means that a single pulse theoretical model will be insufficient and provisions will have to be made for overlapping, moving pulses.

Wang et al (2012) also studied how to retain the amorphous nature of a titanium based bulk metallic glass during the laser welding process. They indicated that the high heating rates ((2-3)10^4 Ks^{-1})) seen during laser processing result in a bypass of crystallisation completely due to the critical heating rate being around 200 Ks^{-1}. The different cooling rates experienced at varying welding speeds resulted in the material being subject to temperatures, above its crystallisation temperature, for longer leading to a higher likelyhood of crystallisation. Ikumoto et al (2008) also noted that varying the cooling rate affects the onset of crystallisation. These authors studied the crystallisation of a 2 mm thick $Zr_{55}Al_{10}Ni_5Cu_{30}$ substrate, using a diode laser with an output power of 500 W whilst varying the spot diameter to achieve different power densities. They observed crystallisation in the samples processed with large power densities (small spot diameter) at a slower scanning speed.

Laser processing of BMGs has also been reported for micro- and nano-surface structuring. Existing studies have mostly been relying on femtosecond or nanosecond laser systems. For example, Sano et al (2007) compared the ablation depths obtained between a Zr-based BMG ($Zr_{55}Al_{10}Ni_5Cu_{30}$) and its crystallised counterpart using a fs laser which delivered 100 fs pulses at 800 nm wavelength for a range of energy values comprised between 2 µJ and 900 µJ. It was found that, above 10 µJ, the ablation depth of the crystallised sample was lower than that of the BMG. This was attributed to the energy loss of hot electrons at grain boundaries that takes place during the fs laser processing of the crystallised metal. Ma et al (2010) also used a fs laser to process the same Zr-based BMG. In this case, the specific purpose of the research was to study the formation of micrometre-spaced concentric rings on the BMG. These periodic structures were induced by the accumulation of multiple de-focussed pulses irradiating a fixed location on the specimen surface. The system utilised was a Ti:sapphire laser delivering 50 fs pulses at 800 nm wavelength. These authors investigated the effect of a range of laser fluence values comprised between 0.18 $J.cm^2$ and 5.3 $J.cm^{-2}$ and a varying number of pulses on the process outcome. It was observed that, for lower laser fluence values, the concentric ring formation was driven by a non-thermal effect. In contrast, the formation of these circular features with higher fluence values appeared to be the result of a thermal process, i.e. the re-solidification of molten material. Chen et al (2013) also used a Ti:sapphire fs laser at 800 nm wavelength on a $Pd_{40}Ni_{40}P_{20}$ BMG target. The specific focus of these authors was to demonstrate the applicability of such a laser processing approach for generating periodic nanostructures on the workpiece, which could then be used as a nanoimprinting replication master. Reports of laser processing of BMGs in the ns regime include research from Lin et al (2012) who performed pulsed laser micro machining of Mg-based BMGs ($Mg_{65}Cu_{25}Gd_{10}$) with a 355 nm ultraviolet (UV) laser and a 1064 nm fibre laser. Both systems were operated with pulse durations of 30 ns and the fluence values considered were comprised between 6 $J.cm^{-2}$ and 12 $J.cm^{-2}$ for the UV laser and between 6.5 $J.cm^{-2}$ and 19 $J.cm^{-2}$ for the fibre laser. It was found that a higher micro machining rate was achieved using the UV laser due to the higher absorption rate of the Mg-based samples at 355 nm and the higher photon energy at such wavelength. It was also observed that the amorphous nature of the BMG samples could be retained when the lower and higher processing values were utilised for the laser power and the scan speed, respectively. Using single ns pulses, Liu et al (2011a) reported the formation of concentric surface ripple patterns on the edge of the irradiated areas for a Vitreloy 1 sample. More specifically, the experiments were conducted with a Q-switched Nd:YAG system generating a 532 nm laser beam with 10 ns pulses and an intensity of 2.5×10^{13} $W.m^{-2}$. This surface rippling phenomenon was attributed to the Kelvin-Helmholtz instability effect taking place at the interface between the laser-induced plasma plume and the molten Vitreloy 1 pool. In a subsequent study, the same authors also performed single pulse ns laser ablation of Vitreloy 1 but this time in a water environment (Liu et al, 2012). The laser system used was the same as that in Liu et al (2011a) and a fixed fluence of 238 $J.cm^{-2}$ was employed. In this case, it was observed that the strong interaction between the generated plasma plume and the molten layer led to the formation of rough starfish-shaped surface structures around the ablated area which are shown in Figure 2.6. This result was reported to be due to a hydrodynamic instability phenomena referred to as the Saffman-Taylor fingering. Surface ripples formed on the edge of the ablated area during single pulse ns laser irradiation in air were also observed by Liu et al (2011b) when processing a different type of Zr-based BMG ($Zr_{47.7}Cu_{31}Ni_9Al_{12.3}$). In this study, the authors used a KrF excimer laser operating at a wavelength of 248 nm and with a pulse duration of 10 ns under 3.45×10^{11} $W.m^{-2}$ of beam intensity.

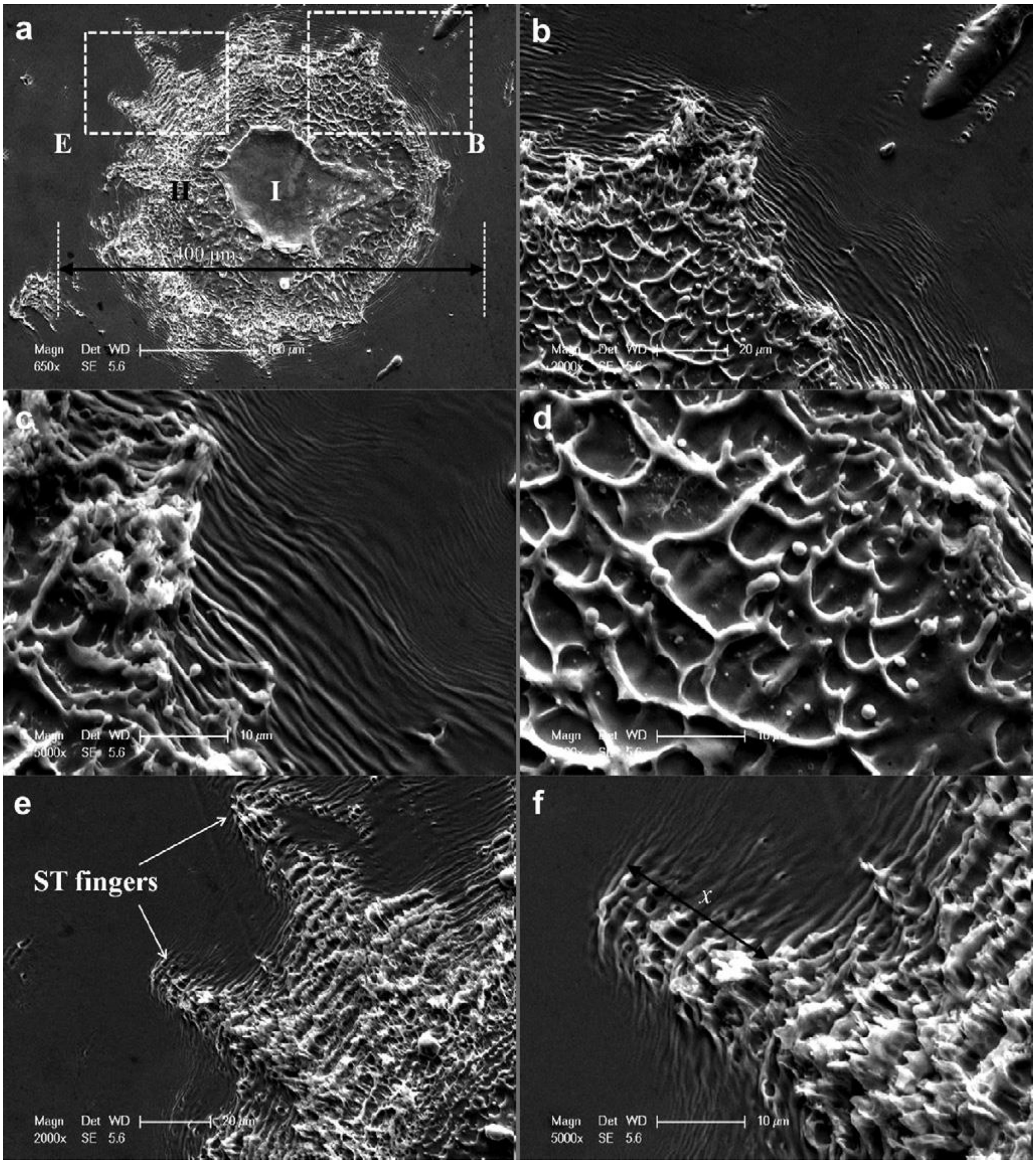

Figure 2.6 Images of the surface morphology formed when the bulk metallic glass, Vitreloy 1, is ablated using a nanosecond laser, operating at 532 nm, with a single shot under water. The morphology is named 'Saffman-Taylor fingering' and is reported to occur due to the occurrence of an interface between the molten Vitreloy 1 layer and the expanding plasma plume which becomes unstable and causes the perturbation of waves within the original molten pool (Liu et al 2012).

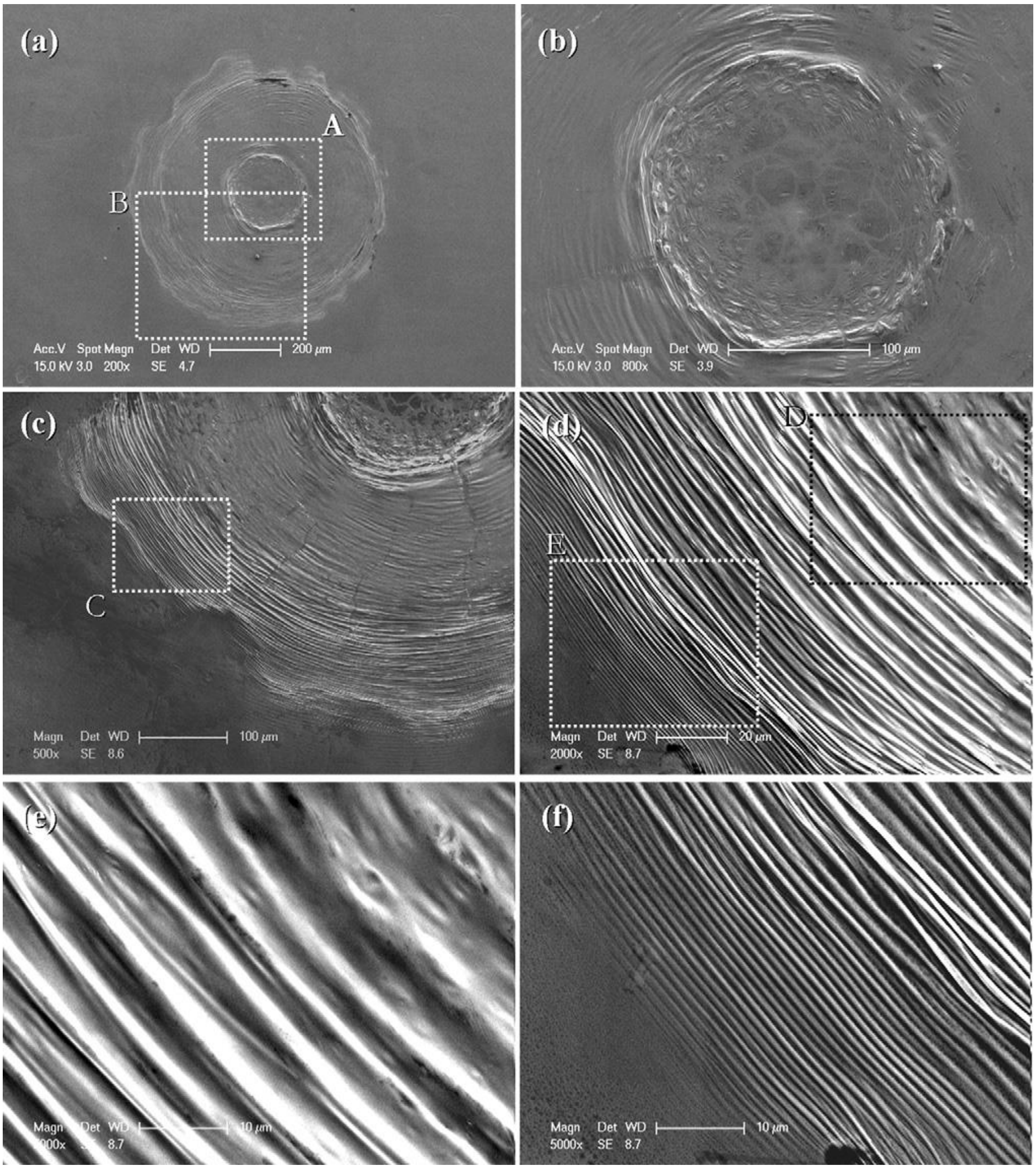

Figure 2.7 Morphology of Vitreloy 1 after being irradiated by a nanosecond laser operating at 532 nm and a pulse duration of 10 ns. The ripples are reported as being due to eh interplay of two fluid layers with different density and horizontal velocity; the molten layer induced by the laser heating and the subsequent plasma plume generated by ionisation of vaporised molecules (Liu et al, 2011(a)).

The literature review presented above and in particular, the reported investigations on the micro and nano structuring of BMGs, reveal that very little attention has generally been paid to study the single pulse laser processing of BMGs. This is in spite of the fact that the topographical analysis of single pulse crater is beneficial for developing a better understanding of laser ablation phenomena over a range of applied process parameters. In particular, such an approach can provide important information with respect to the different thermal processes taking place during laser material interaction such as melt ejection and vaporisation. For this reason, one of the aims of this research is to study the single pulse machining of Vitreloy 1, which is arguably the most popular type of BMGs, with a ns fibre laser, which possesses a flexible operating window with respect to the pulse duration compared to ns Q-switched DPSS systems. This section also presented reported research into the laser processing regimes that result in crystallisation, or lack there-of, in bulk metallic glasses. Even though there has been much interest in this phenomenon, the results using a nanosecond laser, which will induce ultra-high heating and cooling rates, have not been thoroughly researched leaving a gap in the knowledge for laser processing of bulk metallic glasses.

2.5 Laser Ablation Modelling

2.5.1 Introduction

Laser material interaction is a complex process that draws on many areas of physics including: heat transfer for describing the initial transfer of energy into the lattice of the substrate, fluid mechanics for representing the flow of molten material, gas dynamics for studying the flow of vaporized material and plasma physics for modelling cases when ionized particles produce plasma at very high intensities It is necessary to understand these processes so as to be able to machine optimally. Theoretical models can be used to identify various stages of the laser ablation process. For instance, temperature profiles can be employed to identify when phase changes occur as a function of various input parameters such as heat flux or with different beam shapes and machining paths. Most of the laser material interaction is physically un-observable so the creation of a theoretical model can also support the study of processes that cannot be quantified experimentally.

A comprehensive laser material interaction model needs to simulate the energy absorption of the laser irradiance at the surface of the work piece, the energy transfer from the surface through to the material lattice, the phase change upon temperature evolution of the material, the mechanisms of material removal, the occurrence of plasma and the absorbance of the incident irradiation by the plasma (Tani et al, 2007). The earliest reported models used analytical solutions of the heat conduction equation to simulate one-dimensional heating of a material target. These models were limited because they only served a purpose in one-dimension, and only considered temperature independent properties. Even though they are rather simplified, these have become the basis of more complicated models and are still used to validate these (Hu and Argyropoulos, 1996).

With the development of computers, numerical methods became available to simulate source heating. Even though these were more accurate than earlier analytical models, they were still limited in their description of phase change. This changed with the advent of faster computers and the more sophisticated numerical models of today created the ability to take into account the effect of the above mentioned physical processes.

2.5.2 Physical Processes

When a laser beam strikes a substrate material, the laser irradiation is partially reflected and partially absorbed into the electronic subsystem of the material. This absorbed radiation is transferred to the lattice. The energy that is transferred causes a rise of temperature until it reaches the melt temperature within the substrate material provided enough energy is delivered. This melt region expands through the process of heat conduction into the surrounding area of the initial point of irradiation. If the intensity is high enough the temperature rises to the vaporisation temperature of the material causing vaporisation of the melt. If the intensity is even higher this causes the onset of plasma formation as the irradiation continues to heat the vaporized material. These processes can be visualised in Figure 2.8. These phenomena correspond to the possible mechanisms of material removal within the process. In addition, when dealing with non-metallic workpieces, the mechanisms occurring to remove material may not be purely thermal and may be due to the chemical breaking of bonds through pyrolithic processes (Russo et al, 2002).

Thus, when considering modelling the laser material interaction on metallic work pieces, the process without plasma formation can be split into the following three stages:

- First the laser beam is incident on the material. This causes the temperature of the solid to increase with time as it absorbs the thermal energy. As the energy continues to be absorbed, the temperature of the material carries on rising until it reaches the melting temperature.

- The second stage, when the material is above the melting temperature results in melting. The temperature within the molten pool continues to rise as the radiation of the laser beam continues to be absorbed.
- The third stage occurs when the temperature of the melt is high enough to cause vaporisation of the molecules within the molten material. Unlike melting, which occurs in a specific temperature range, vaporisation in laser ablation can occur at any temperature from the vaporisation temperature up to the critical temperature of the material.

The first and second stage can be treated analytically, but the third stage needs to be tackled using a finite difference method as conduction, melting and vaporisation all occur at the same time. Because the beam intensity varies over its radial position, the three stages can happen at the same time at different locations along the materials surface. Fluid and gas dynamics may also be incorporated to address the recoil pressure added by the vaporised plume of material as well as the ionisation of the molecules evaporated from the molten surface.

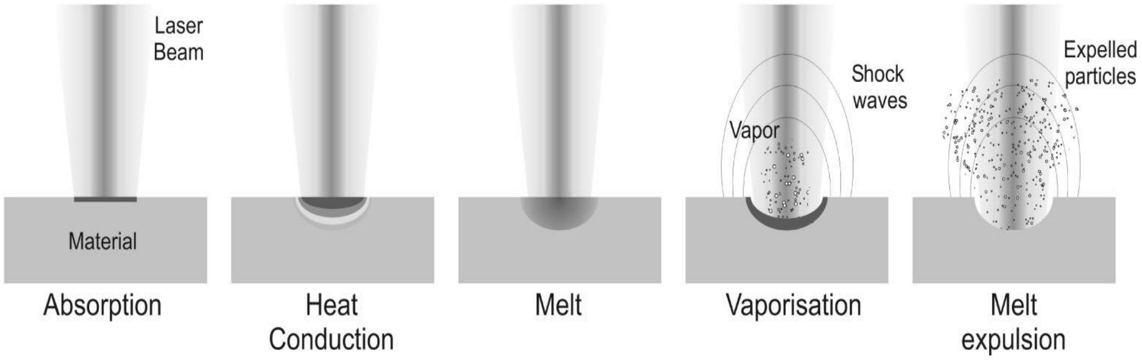

Figure 2.8 Visualisation of the processes occurring during laser material interaction that need to be incorporated if a complete theoretical model is to be recognised. First the material absorbs a percentage of the incident laser radiation. This radiation will be transferred through the material via heat conduction and when the temperature is high enough the material will melt. Molecules from this molten pool will be vaporised and the vaporised plume will exert pressure on the molten pool aiding in material ejection. If the incident laser intensity is high enough the vapour plume will form a plasma plume shielding the material surface from further irradiation from the laser beam (Bartolo et al, 2006).

2.5.3 Modelling Basics

Models can be incomplete in their treatment of laser-material interaction. This is purely due to the complexity of the process and the lack of understanding of its underlying dynamics. The first modelling studies were conducted upon the creation of the first Ruby laser in the 1960's. As Anisimov and Khokhlov (1995) pointed out, they were related to the moderate intensity region (10^5-10^9 W.cm^{-2}) and despite their simplification they give a good overview of the interaction. But as lasers have developed, there is an increasing need for more comprehensive models.

Stafe et al (2006) stated that in order to achieve an accurate theoretical description of the laser ablation process, the heat equation used to describe it needs to be an extension of the classical heat equation so that all of the phenomena encountered during laser-material interaction can be accounted for. This leads to a wide variety of models, some of which are simplified by making assumptions such as discarding certain phenomena that can occur or keeping material properties constant and not temperature dependent. The different phenomena that should be taken into account when developing a comprehensive model can be accounted for by including supplementary terms within the classical heat equation. Governing equations then need to be formed for other fundamental physical phenomena such as fluid flow and plasma formation. This is the usual starting point for most laser-material interaction models. The next step then consists in solving the governing equations. A range of techniques can be employed when solving these equations.

Typical calculation results of a model based on the thermal conduction equation with a melting and vaporisation phase change predict the temperature distribution inside the target, the depth of the molten material and the rate of evaporation. The maximum temperature occurs at the surface and the area of maximum temperature expands with time due to thermal conduction (Bogaerts et al, 2011). The results of such models can also show that the melt depth extends much deeper into the material compared to the evaporation depth which exists only on the surface layer.

Ready (1965) introduced the effects due to the absorption of laser radiation in 1964. He concluded that, on timescales of 10^{-9} s, the temperature was still a valid concept and the usual equations for heat flow could be used because the electrons receiving the energy from the laser source have relaxed enough to assume equilibrium within this timescale. Ready's model assumed the thermal properties of the material to be independent of temperature and also neglected the melting of the material and only considered vaporisation.

The simplest model of laser material processing can be viewed as a one dimensional heat transfer model with a stationary source. This model neglects phase change, temperature dependence of material properties and plasma generation, whilst assuming the heat transfer in only one direction. This approach can simulate the heat conduction into the material with one stationary pulse without phase change. In this way, the change in temperature at different depths at different times can be simulated up until the melting temperature of the material.

The one dimensional heat diffusion equation can be used to describe the heat transfer within the material upon irradiation by a laser beam. The equation can also include a term to account for the heat source from the laser beam and the heat sinks due to phase transformations. The equation with temperature dependent material properties can be written as:

$$\rho C \frac{\partial T(z.t)}{\partial t} = \frac{\partial}{\partial z}\left[k(T)\frac{\partial T(z,t)}{\partial z}\right] + S(z,t) \tag{2.2}$$

C being the heat capacity of the required phase, *k* being the thermal conductivity, *ρ* is the density of the material, *T* is the temperature, *z* is the depth from the surface and *S(z,t)* is the heat source from the laser irradiation.

For a heat source that varies with time, the heat conduction equation can be solved analytically by integrating the temperature distribution at previous times. If the heat source is in the form of a Gaussian distribution, the solution can still be found analytically by integrating over different areas.

Yilbas (1996) solved this model by using the heat transfer limited to conduction only for a Gaussian pulse irradiating a surface. The governing equations were solved using analytical methods to obtain the temperature distribution at the surface of the material over the pulse. Sami and Yilbas (1998) also studied the 3D laser heating of a moving Gaussian heating source using the electron-kinetic theory. The temperature profiles in the material were determined using a finite difference approach to the governing equations.

2.5.4 Phase change - melting

When a solid material is heated past its melting point it will experience a phase changes to liquid. In this case, the model of the laser material processing needs to account for phase change within its governing equations. The properties of different phases for a given material are not the same so the rates of energy, mass and momentum transfer vary from one phase to another. The position of the boundary between the two phases evolves during the process and this movement cannot be determined in advance so it has to be identified from the solution. There are a few different ways of doing this. One possibility is to use the classical approach of phase change equations and then find a solution to the Stefan problem. This means that the solid and liquid phases are separated by a sharp boundary. For this approach, the Fourier equation is applied to both the solid and liquid phases separately with different thermal properties for different phases. An energy balance is then applied at the boundary.

Assuming constant thermal properties and no surface heat loss, Xie and Kar (1997) studied the heat conduction in solid and liquid regimes of a laser irradiated sample. An analytical solution was found by applying appropriate boundary conditions and led to describing relationships between the melting depths, the power density of the laser and the time during which it irradiates the surface. These relationships could show the dynamics of the melting process. Shen et al (2001) also approached the melting process in a similar way – by treating the material heat conduction before and after melting separately. They applied the analytical solutions to four materials to obtain the melting depth, the temperature profiles and the time for the surface to melt and evaporate.

For models that need to count for ablation and thus for the change in shape of the domain due to the removal of material from the surface, the problem can to be modified to show that the changes in phase are separated by a thicker region called the mushy zone. This zone is a mixture of the two phases being analysed. The solid and liquid phases have the same conduction equation applied to them and an energy balance is applied to the mushy zone that includes the laser intensity.

Yilbas and Mansoor (2009) considered both types of thermal properties when simulating laser pulse heating. They solved the energy equations for each phase and then coupled the equations over the interfaces of the two phases. This interface was not a sharp interface between phases but was treated as a mushy zone, where both phases co-exist. For the temperature independent properties, the heat conduction equation and the governing equations across the mushy zone were solved numerically. For the temperature dependent properties the governing equations were solved using a finite difference scheme and the energy method was used to identify the mushy zone. Based on this, the temperature variation along the surface and the size of the cavity formed was obtained. This allowed the identification of the effect of thermal properties on the results. Because the thermal properties are variable, the heat conduction as the temperature changes can vary also, leading to different results for the temperature dependent and independent properties. When considering constant thermal properties, the size of the cavity was twice larger than that simulated with temperature dependent properties. The prediction for the temperature dependant thermal properties showed a better agreement with the experimental results obtained.

Another way of dealing with two phases numerically is to integrate the latent heats of the various phases within the heat conduction equation. Otto et al (2011) used the latent heats and an enthalpy method to find solutions with phase change during laser processing. The latent heats were iteratively corrected for within the heat equation. These authors used a step by step calculation to estimate the latent heats by using the enthalpy. Eventually, convergence was reached and the solution was used to find the temperature profiles. The Navier-Stokes equation was used to study the fluid flow of the molten or gaseous material.

2.5.5 Phase change - vaporisation

The methods reported above are suitable for the solid-liquid interface but when the material is heated past its melting point it can also reach its vaporisation temperature in which case the cavity formed by melting becomes filled with vapour. The vapour pressure can be calculated from the surface temperature by integration of the Clausius-Clapeyron equation. Between the layer of liquid and vapour, there is a layer called the Knudsen layer where the particle properties are discontinuous. From kinetic theory – where gases are described as a large number of particles that are in constant random motion – the Knudsen layer can be defined as a thin layer on the boundary where liquid and vapour exist and thus, where the phase is considered to be between liquid and vapour. In numerical modelling, the Knudsen layer provides a boundary condition which couples the heat transfer equation in the target material with the gas dynamics of the vapour phase. In order to solve the equation at the liquid-vapour interface, the energy balance has to include incident laser energy, heat transfer, phase change and the mass flow of the melt and vapour. Considering that the liquid-vapour front is also moving the problem becomes even more complex. According to Anisimov et al (1999), the majority of theoretical investigations on laser ablation usually assume that the vapour produced from evaporation is an ideal gas and its flow can be described from an analysis of gas dynamics. The boundary conditions can be derived from a solution to the Boltzmann equation which describes the flow of vapour in the Knudsen layer.

Bogaerts and Chen (2005) investigated the influence of laser irradiation, pulse duration and wavelength when modelling nanosecond laser ablation of copper in a helium gas medium. The heat conduction equation was used separately for the different phases and the expansion of the evaporated material was modelled using the Navier-Stokes equation. All parts of the model were solved simultaneously using a numerical method. The results showed the influence of the parameters on responses such as temperature evolution and vaporisation behaviour. The results for the intensity were consistent with most other models and showed that the intensity has to reach a certain level in order to initiate melting and change the morphology of the material. As the intensity increases, the morphological changes become more pronounced and the material will start to evaporate. The effect of the pulse duration was found to be different for constant fluence and for constant irradiance. More specifically, when the irradiance is constant, the heating, melting and vaporisation increases with increasing pulse duration. For constant fluence the trend was the opposite because of the rise in laser irradiance with shorter pulse duration.

Alexiades and Autrique (2010) developed an enthalpy based model for the treatment of heating, melting and vaporisation during ns laser ablation of a target. These authors studied a Gaussian shaped pulse with a full width at half maximum (FWHM) of 10 ns and a peak intensity of the order of 10^{13} W.m^{-2}. They described the heat conduction and the phase changes through the energy conservation laws in terms of the enthalpy. Equations of state, which describe the pressure and internal energy of a macroscopic system as a function of density and temperature, were used to update the enthalpy every time there was a phase change. The finite volume method was employed to solve the partial differential equations. The model was applied to laser ablation of copper in a helium background. The results from the model showed the evolution of the melt and vaporisation depth over time. The results also described the evolution of plasma characterized by a decrease in the vaporisation temperature at around 16 ns. This decrease in temperature of the vaporized plume suggests that the plasma was blocking the irradiation from heating the plume.

When vapour is formed, it induces a pressure that causes the plume to be moved away from the surface of the material being irradiated. In addition to this, the liquid material, from which the vapour has been evaporated, is pushed away from the vapour causing it to be ejected from the area being irradiated by the laser pulse. Chan and Mazumder (1987) developed a one-dimensional model to describe the process of material removal in such cases. They included two moving boundaries in the model because of the changes in phase; one solid-liquid which could be treated with the Stefan problem and one liquid vapour, which is slightly more complicated and was treated with molecular dynamics. The heat conduction in the solid and liquid regions was modelled using the heat conduction equation and the Stefan problem for the boundary conditions. The pressure discontinuities in the Knudsen layer were obtained and gas dynamics were analyzed in the vaporized region. From these equations, the material removal rates and surface temperature could be found using a numerical solution. This modelling approach was applied for three different materials.

As mentioned earlier, because material is evaporated, this means that the incoming laser radiation may be absorbed by the vapour phase before it can reach the target material. Fahler and Krebs (1996) investigated this by describing a model that takes into account the heat conduction within the target, the evaporation of material, the cooling on the surface of the target by the heat of evaporation and the absorbance of the laser beam by the evaporated material. The thermal conduction equation, with heat source terms, was used to describe the temperature profile in the material. The evaporation was described simply by modelling it as thermal evaporation from a hot surface and this led to the estimation of the evaporated depth which was then used for calculating the cooling of the surface by heat of evaporation.

Ho et al (1995) attempted to predict the evaporation rates of the removed material as well as the properties of the ejected particles as a function of the laser beam parameters. Firstly the heat conduction due to the irradiation of the laser beam was calculated. If the irradiance was high enough to cause melting, a finite difference scheme, based on enthalpy balance was formulated to treat the melting of the substrate. The motions of the melt and vaporizing boundaries were then calculated. When movement of the liquid/gas interface occurred, the property changes were monitored using the conservation laws and a kinetic relation.

Many investigations into the nanosecond laser ablation process have found a sudden increase in the ablation rate of materials at specific laser fluence. This is the evidence for the transition from normal vaporisation of the material to a phase explosion regime. Phase explosion is a mechanism of material removal which can occur at high laser intensities. The molten material is superheated up to its critical temperature. At this temperature near the critical temperature large density fluctuations can result in vapour bubbles being formed (Yoo et al, 2000). Once these bubbles reach a specific radius they expand which can lead to the violent ejection of molten mass (Lu et al, 2002). Miotello and Kelly (1995) discussed the application of using phase explosion to describe the material removal in laser ablation. The large ejection of mass results in a steep increase in the ablation rate of the material, this can be seen in Figure 2.9 from work by Yoo et al (2000) where the craters formed in silicon using an Nd:YAG laser operating with a wavelength of 266 nm and a pulse duration of 3 ns were measured with varying laser intensities. The Figure shows the dramatic increase in crater geometry at an irradiance of about 2.2 W.cm^{-2}. The accompanying time-resolved images (Figure 2.10) reveal that the crater formation at this irradiance and higher is accompanied by a violent ejection of droplets, strengthening the postulation that phase explosion is present.

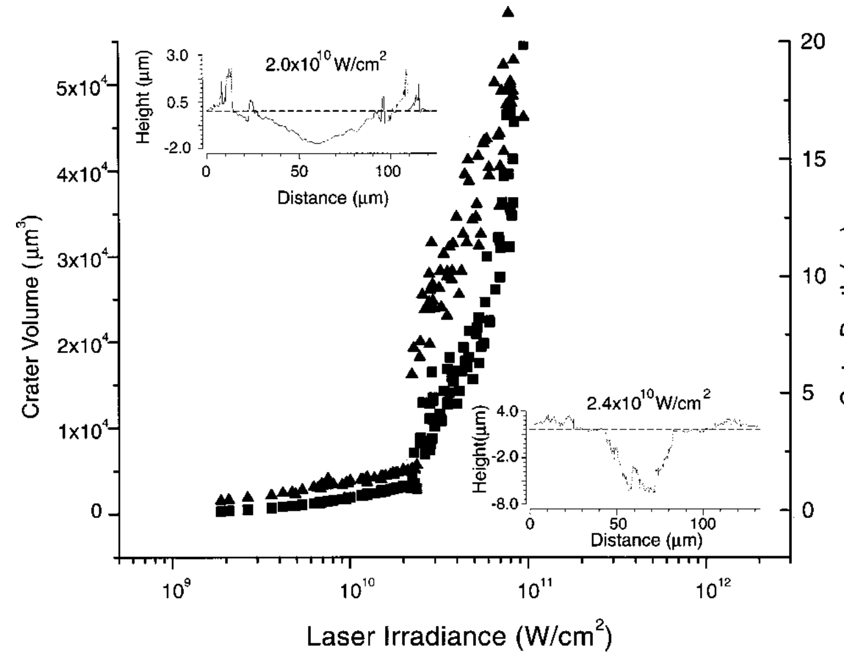

Figure 2.9 Measured crater volume and depth formed in silicon using an Nd:YAG laser operating at 266 nm and 3 ns pulse duration with varying laser irradiance (Yoo et al, 2000).

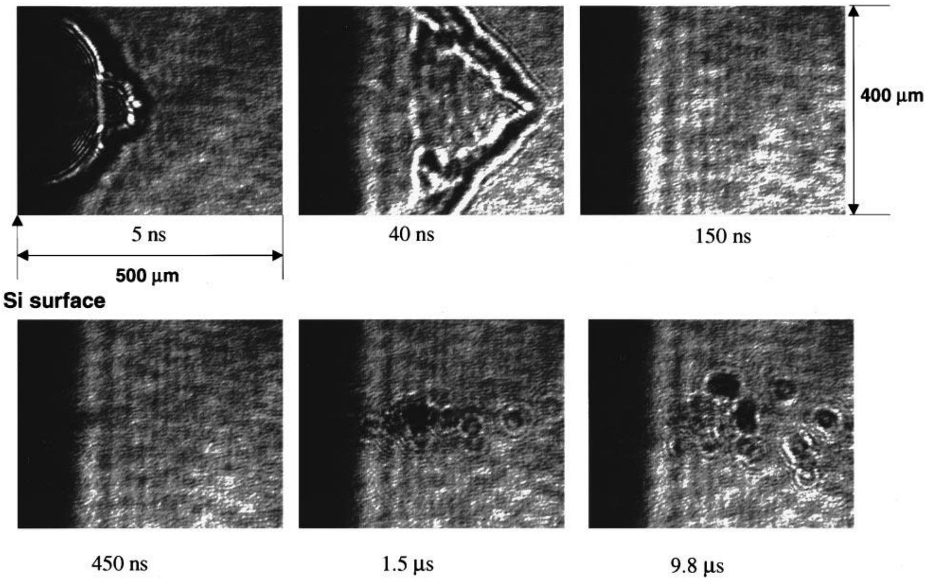

Figure 2.10 Images obtained via time-resolved spectroscopy showing the violent ejection of particles accompanying the sharp increase in crater removal at a laser irradiance above 2.2 W.cm^{-2} shown in Figure 2.1 (Yoo et al, 2000).

2.5.6 Plasma formation

If a complete model of laser material interaction and the laser machining process is to be realised, plasma formation needs to be taken into account. When a material is evaporated from its molten state it continues to be heated by the initial irradiation. This can cause ionization of the atoms or molecules within the vapour creating a state of matter with charged particles called plasma.

The state of plasma depends on the amount of laser irradiation absorbed by its plume and also the laser irradiation that subsequently reaches the workpiece through the plasma. Orazi et al (2010) described a model where both of these irradiation energy values were able to be evaluated through the production of empirical coefficients. Equations to describe the state of the plasma were recycled from previous work by the authors and the empirical coefficients were found using experimental work and the depth and width of craters machined with the laser pulse.

Because the plasma is created from the evaporated material, it exists above the surface of the target and thus it absorbs any incoming laser irradiation. Consequently, and due to the fact that the plasma consists of electrons and ions, the plume temperature and pressure increases causing it to accelerate in a direction perpendicular to and away from the target surface (Moscicki et al, 2010). Mazhukin et al (2007) described a model where phenomena such as back condensation, ionisation of plasma and absorption of the laser irradiation by the plasma were taken into account as well as the surface heating of a target by laser irradiation and the subsequent conductive heat transfer. They did not take into account the melting of the target material to simplify the model and because the melt was considered to be insignificant to the surface phase transition in the irradiation regimes that were being considered. The heat transfer to the target by the incident laser irradiation was described by the heat conduction equation. In the vapour region, the processes were described by gas dynamics and laser radiation transfer equations. Boundary conditions were created for evaporation and condensation. To solve the equations set out, the finite difference method was used while the heat conduction equation, with its convective term and temperature dependent coefficients, was solved using an alternating direction method. The laser used was a 1060 nm wavelength with a pulse duration of 20 ns and a pulse shape that was assumed to be Gaussian in time and space. The transmission coefficient of the plasma was modelled successfully over the time of the laser pulse. The results showed that, after the onset of evaporation, the plasma stayed transparent which means that it allowed radiation to be absorbed by the material for about 17 ns. After this time, the transmission through the plasma sharply decreases. The temperature on the surface of the material was also modelled and showed the onset of plasma as a decrease in temperature similar to the work reported by Alexiades and Autrique (2010). Lastly, the thickness of the removed layer was also analysed. The model showed that at lower intensities, plasma formation does not occur and the depth of the removed material is much higher. When plasma is present, at around 10^8-10^9 W.cm^{-2}, this depth decreases as the plasma is formed but begins to increase at higher intensities again because other processes such as subsonic evaporation, when the Mach number, which determines the vapour flow velocity is less than 0.8, take place.

Wu and Shin (2006) developed a thermal model to describe the nanosecond laser ablation process with plasma formation. The model was created by developing equations for the heat transfer and the gas dynamics in the vapour phase. The equations were coupled through the boundary conditions at the liquid vapour boundary using the Knudsen layer relations. Through a finite difference scheme, the equations were solved for a nickel substrate irradiated using a KrF excimer laser at 248 nm and with a FWHM pulse duration of 26 ns over a range of fluence values up to 5 J.cm^{-2}. The solutions showed that the plasma shields the laser energy reaching the target material. The predictions were compared to experimental results in order to verify the model which was only valid when phase explosion does not occur.

2.5.7 Molecular dynamics

When using computer simulations to model the laser material interaction during the laser machining process, one of the main challenges is to describe computationally the cascade of processes that occur after the material is irradiated with laser light. This can mean creating a model using many different techniques. Zhigilei et al (2010) described the techniques used for each phenomena taking place. They state that the heating, melting, evaporation and ablation processes are mostly described by using the solutions to a set of partial differential equations based on the energy of the laser beam irradiating a surface. The final stages of the laser material interaction can be incorporated by using a phase change model for re-solidification and surface vaporisation models for the removal of material. Molecular dynamics simulations have been introduced as a solution in cases when the classical models begin to fail.

When using molecular dynamics to model laser material interaction, it is often limited to short timescales because the simulation tracks the movement of single atoms, meaning when such a simulation model is implemented, it needs to track millions or more atoms at a time. For nanosecond molecular dynamics modelling, this causes a problem because the pulses are long causing simulation to run for large amounts of time. In order to overcome this problem, Zhang and Wang (2008) developed a hybrid molecular dynamics and macro-scale model, which resulted in the setting-up of two domains. Domain one would model the structural change through molecular dynamics and domain two would only be subject to heat conduction and a finite difference method was used to calculate the one dimensional heat conduction equation with temperature dependent material properties. Both domains were simulated at the same times.

Table A.1 in the appendix gives a condensed overview of a few of the important papers reviewed in this chapter.

2.5.8 Summary

The simulation of the laser ablation process is highly complex and many branches of physics including heat transfer, gas dynamics and plasma physics, need to be understood in order to achieve a comprehensive model. The heat diffusion equation can be used to model the ablation of material when irradiated by a laser beam. To make the model complete, modifications need to be made to this equation. These modifications include energy changes during phase transformations, changes in the surface topography due to ablation and the shielding of the surface due to the plasma (Marla et al, 2011).

The models reported in the literature show that, during laser material interaction, the material undergoes different phase changes depending on its temperature as a result of heating by the laser source. The material is then ejected from the target by different mechanisms. This ejected material can then block the incoming laser radiation by forming a dense plume of plasma.

Modelling of the laser material interaction and the laser ablation process provides insight into the physical phenomena that are occurring without the need for extensive experimentation. Modelling can also be used to optimise the laser machining process by determining the influence of particular parameters.

Modelling can be done in all dimensions, by taking into account temperature dependent thermal properties, with phase change or without phase change and by using many solution methods; analytically or numerically. Nearly all the models that are not based on molecular dynamics utilise the classical heat conduction equation in order to simulate the ablation process. The models that account for all phase changes are the most accurate, although simple models can still be used if the intensity of the incident beam is low enough.

2.6 Conclusions and identified knowledge gaps

The main gap identified in the reported research is the lack of investigations of Ytterbium-doped nanosecond fibre lasers in the field of micromachining. This could be due to the lack of availability of multiple laser sources within one academic institution or within a company that researches using their own laser systems. Thus, experimentation will be undertaken in this research on industrially relevant materials or materials that have not been previously investigated as well as with a laser source that may not be available to all researchers.

Based on the findings reported in this literature review, it can be seen that there is a vast number of process parameters that can affect the outcome of the laser ablation process. The need to find a compromise between a high material removal rate and a good surface finish was highlighted. When conducting experimental optimisation studies, single factor analysis can provide information about the effect of particular parameters on process outcomes. However, such type of analysis does not account for interactions between process parameters. Thus, it is mainly suitable as an initial research tool to become familiar with generic parameters' effects. Applying a design of experiments approach instead leads to more comprehensive results for process optimisation studies in a shorter amount of time and including additional information on the interaction between parameters. This method will be utilised in this PhD research to optimise nanosecond laser machining and thus to determine the best processing windows to achieve high material removal rate and a good surface finish for an industrially relevant material.

The issue with many of the reported studies in this review is that the influence of pulse duration is commonly investigated through the use of different laser systems. The particular laser system utilised in this research has the capability to produce different pulse durations, in the range of 15 to 220 ns. This is an advantage over existing studies as this allows saving time and also this adds robustness to the experimentations.

This review also showed that single crater experimentation is a valid way of investigating the influence of laser parameters on the achieved topography and on the physical phenomena. The characterisation of such resulting phenomena from single crater machining can provide guidance as to which process parameters can be used for optimum machining. In particular, the topography of single craters can affect the final topography of a produced part because machining is carried out via a set of overlapping craters. Analysis will be performed on the morphology of the irradiated craters by techniques such as electron microscopy which can give an insight into the thermal propagation of the laser radiation into the material.

Modelling of the laser ablation process has been thoroughly treated for the nanosecond laser machining regime in many reference works. In spite of that, modelling of the laser ablation process in this PhD research is still an important goal as it can be used in conjunction with experimental validation to optimise the process offline which in turn should save time and money for industrial implementations.

Laser machining of bulk metallic glasses has been reviewed with the conclusion that the studies on the ultra fast heating rates induced by nanosecond laser systems are lacking, with the majority of the literature based on the microsecond or longer laser welding of material. Secondly, the investigation of BMG materials processing through the use of single pulses has not been studied over the wide range of parameters available with the laser system employed within this research. An important conclusion made during the review is that single pulse investigations for BMGs cannot give enough evidence to predict the onset of crystallisation during multiple pulse processing. Thus, it is necessary to investigate this phenomena both from an experimental and theoretical perspective to obtain a clear view of the effect of laser processing on the crystallisation of bulk metallic glasses.

The nanosecond fibre laser machining of aluminium

3.1 Introduction

The latest advances in Yb fibre lasers based on a MOPA architecture provide an opportunity to investigate systematically a broad range of pulse durations and repetition frequencies on a single system and thus to study the influence of such parameters on particular machining outcomes. As concluded in Chapter 2, only a few reports are present in the literature with respect to the optimisation of machining operations using ns MOPA-based Yb fibre lasers. Instead, the literature is dominated by research with Nd:YAG laser systems. In this context, the main objective of this chapter is to conduct an experimental study of the nanosecond laser milling process with a 1064 nm Yb fibre laser in order to characterise the effect of various input parameters on the resultant material removal rate (MRR) and surface roughness when machining aluminium. In particular, this research aims to identify a window of process parameters which leads to a high machining throughput while maintaining a low surface roughness.

This chapter is organised as follows. The following section presents the experimental set-up utilised in this research. Then, the influence of the laser pulse length and repetition frequency on the achieved MRR and surface roughness is systematically investigated in section 3.3, for a range of laser pulse durations comprised between 25 ns and 140 ns. Next, in section 3.4, by employing the Taguchi parameter design method, experiments are conducted to optimise the process in relation to achieving high MRR and low surface roughness for a given pulse length. Finally, the conclusions reached are given in the subsequent section.

3.2 Experimental Set-up

3.2.1 Fibre laser system

The laser processing system utilised throughout this research was equipped with a 20 W Single Mode-Series fibre laser manufactured by SPI Lasers with the following specifications: emission wavelength 1064 ± 10 nm, continuous wave to 500 kHz, maximum pulse energy 0.56 mJ, maximum average power 20 W, PulseTune capability (pulse duration variable from 15 – 220 ns, each pulse duration possessing a frequency at which the peak power is optimized). The beam spatial profile is near-Gaussian with an M^2 of <1.2. This particular system is a MOPA-based laser which uses a seed laser equipped with two amplifiers in order to achieve a high power output pulse with its characteristics being determined by those of the seed laser. Unlike conventional diode-pumped solid-state (DPSS) lasers, whose average power drops off at higher repetition rates, the MOPA configuration results in full average power being maintained even as the repetition rate increases.

One of the unique features of this laser is the so-called "Pulse Tune" technology which allows precise tuning of the delivered pulses to form pre-programmed waveforms. The selection of these waveforms is a result of the directly-modulated seed laser whose output is amplified in the MOPA configuration. These waveforms are optimised for peak power at specific pulse repetition rates, with the MOPA configuration varying the output waveform to maximise the peak power. This can be seen in Figure 3.1 where the output waveforms are shown for different settings. It can be seen from this figure that the peak power is high even though the frequency reaches 290 kHz. The repetition rate at which the peak power is maximal is referred to as "PRF0" for each waveform. The waveforms considered in the research presented in this chapter along with their pulse duration and maximum pulse energy, E_{max}, at PRF0 are shown in Table 3.1.

Figure 3.2 illustrates the generic evolution of the average power and the pulse energy as a function of the pulse repetition rate for any waveform. While this behaviour remains consistent for every waveform, each of them has a specific PRF0 value where the power is at its highest. As it can be seen from this figure, when increasing the pulse frequency above the PRF0, the average power stays constant whilst the pulse energy decreases according to equation 3.1:

$$Pulse\ Energy = \frac{Average\ Power}{Frequency} \tag{3. 1}$$

Below PRF0, the average power decreases when reducing the pulse frequency for a given pulse duration. In addition, the pump laser diodes of the fibre laser system are modulated in order to prevent the energy within a pulse reaching levels that may be harmful to the workings of the laser. In this case, the pulse energy is constant and corresponds to its maximum value, E_{max}.

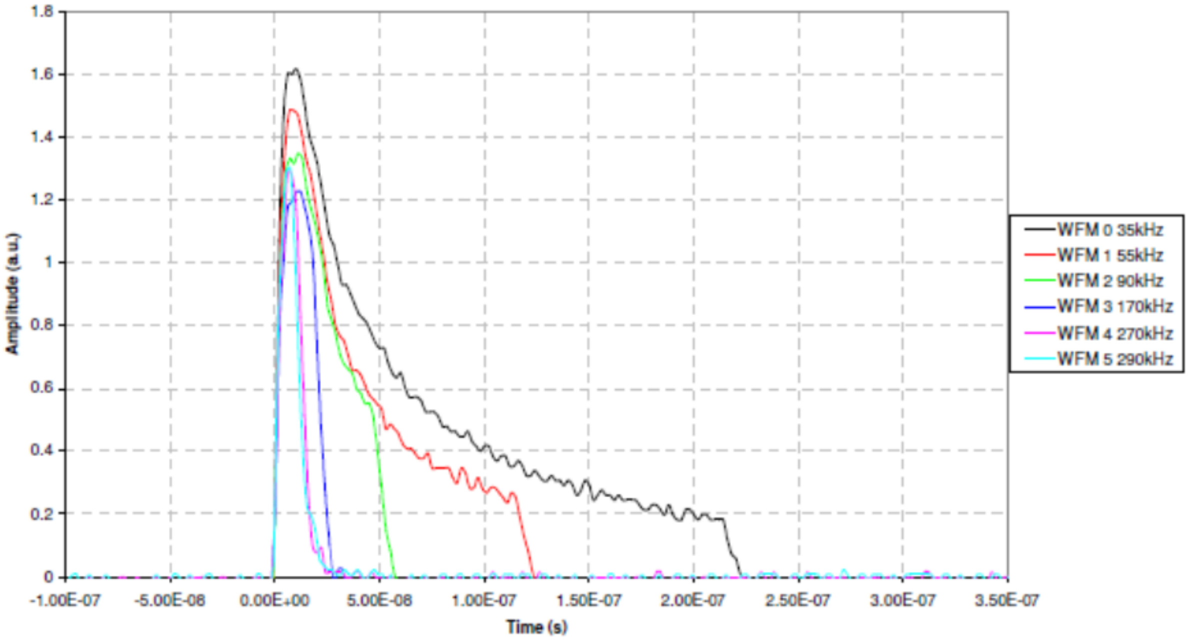

Figure 3.1 Output waveform variation at different frequencies. The configuration of this system allows maximum peak power as the frequency increases (Source: SPI manual for the G3 laser).

Waveform number	**Pulse duration (ns)**	**PRF0 (kHz)**	**E_{max} (mJ) at PRF0**
16	140	51	0.39
17	120	55	0.36
18	100	60	0.33
19	95	63	0.32
20	85	68	0.29
21	75	72	0.28
23	55	90	0.22
24	45	105	0.19
25	35	125	0.16
26	25	170	0.12

Table 3.1 Pre-set waveforms and their corresponding pulse duration, PRF0 and the energy at the PRF0 (Source: SPI Manual).

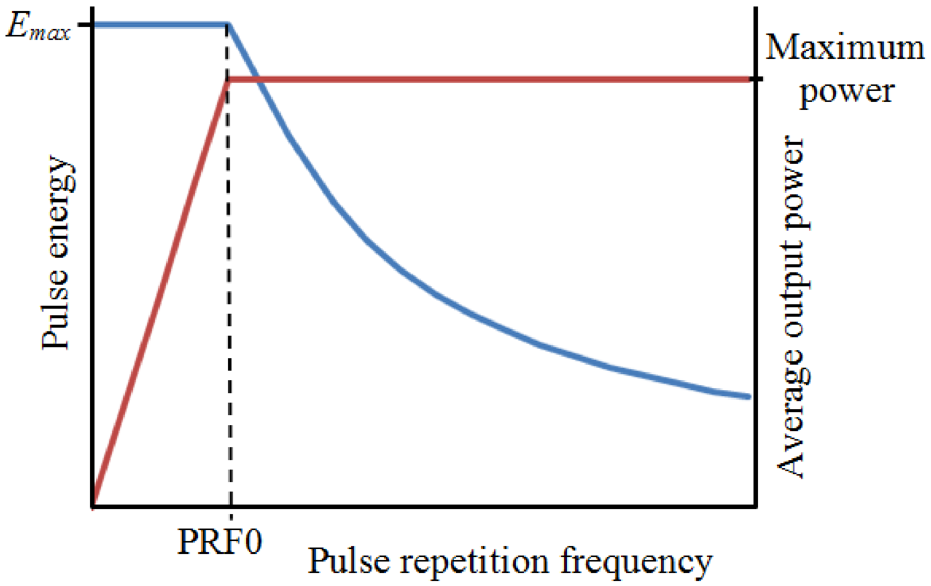

Figure 3.2 Evolution of the pulse energy and average power as a function of the pulse repetition frequency (Source: SPI Manual).

In order to be able to calculate the fluence and irradiance of the laser beam, the actual $1/e^2$ diameter of the laser beam needs to be evaluated. The method used here has been described by Bovatsek et al (2010) and can specifically be used to measure the beam diameter by processing a series of lines at varying pulse powers on a sample coated with a thin film which has a constant removal threshold. Several test series are necessary due to the experimental errors that can occur. The sample used for this experiment was a fused-silica coated with a thin chromium film. The value for the spot size determined from this method was 32 µm. The method and the subsequent data used to determine this value can be seen in the Appendix.

The SPI 20 W Single-Mode fibre laser is integrated into a system created by DMG named Lasertec which allows control of a 5-axis computer controlled rig on which material is placed to be machined by the laser. The computer system also controls the parametric set-up of the laser such as the choice of pulse duration and frequency. The delivery of the beam from the laser source onto specific points on the substrate material occurs through the use of galvanometric mirrors and a 100 mm F-Theta lens as shown in Figure 3.3.

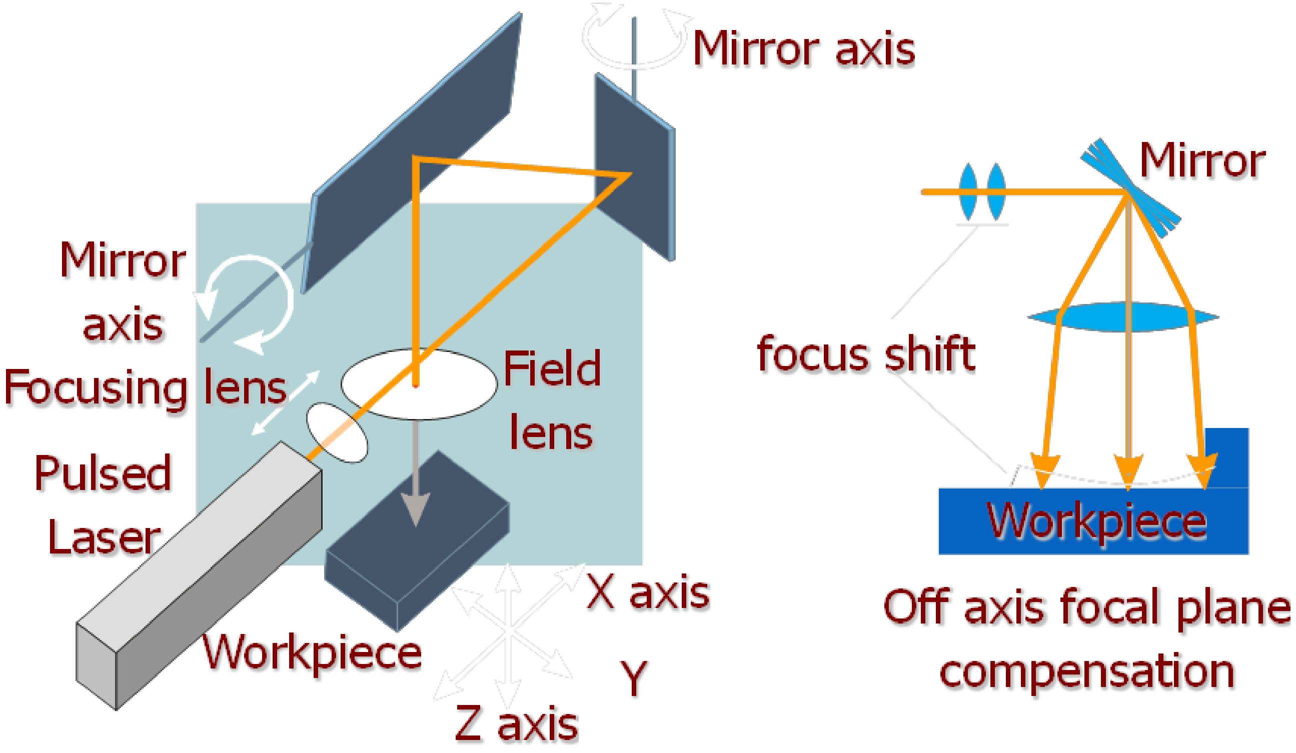

Figure 3.3 Image showing the optical set up of the optical beam delivery system. The beam from the source laser is reflected from moveable mirrors, through a 100 mm F-Theta lens, ontp the surface of the workpiece (Courtesy of Lasertec).

3.2.2 Measurement of machining outcomes

All experiments were conducted by producing 2 x 2 mm square pockets in aluminium 6082 with three replicates for each data point. The scanning speed of the laser system was kept constant at 600 mm.s^{-1} and the track displacement was also kept constant at 11 µm. 10 layers at the same parameters were machined in order to achieve a measureable depth. The thermal properties of this material are displayed in Table 3.2.

The MRR obtained during this study is defined as the volume of material removed (mm^3) per unit of time (minute). In order to determine the MRR for each parameter set, the depth of each of the machined pockets was measured using a touch probe integrated in the laser system. The MRR was then calculated by dividing the measured volume by the machining time for producing each pocket, which was recorded automatically.

In order to assess the repeatability of the touch probe used to measure the depth of each pocket machined, a test was conducted whereby the touch probe was used to measure the same spot ten times and this in eight different locations making for a total of eighty measurements to assess the repeatability. The average standard measurement error for all values was 14.7%.

The surface roughness at the bottom of each square cavity was measured with a white light interferometric (WLI) microscope microXAM from ADE Phase Shift. This microscope uses a CCD camera which records the intensity of the bright and dark fringes formed via recombination of the reflected light on the surface and the reference beam. Based on the recorded intensities, the topography of the surface under inspection can be built by using built-in algorithms. There are a number of different parameters that can be used to define the surface texture. These include amplitude parameters that represent changes in the height of a profile, spacing parameters that can capture the mean widths of profile peaks and valleys as well as statistical parameters that account for vertical and lateral characteristics of a profile. The parameter used to describe the roughness in this research is the arithmetical mean roughness (Ra). This value describes the average of all measured points from a profile mean line. For each pocket machined, a map of the surface topography was first obtained using the above mentioned WLI at three randomly selected locations. A constant vertical scan length of 35 µm was applied to obtain the maps of the surface topographies. These maps were then used to extract the roughness in accordance with the standard BS EN ISO 4288:1998. The sampling and evaluation lengths were 250 µm and 1.25 mm respectively. A high-pass filter was used to remove the waviness components of the obtained profiles. The waviness of a profile is due to the more widely spaced repetitive changes on an image defined as the low frequency component whilst the roughness is attributed to finer irregularities on the surface defined as the high frequency components. Figure 3.4 describes the overall topography as well as its separate roughness and waviness components. Brebbia and Klemm (2013) state that it is important to separate these frequency components in order to be able to evaluate the roughness properly. Algorithms provided by the WLI software were used to compute and to average the considered roughness value over five sampling lengths for each obtained topography map.

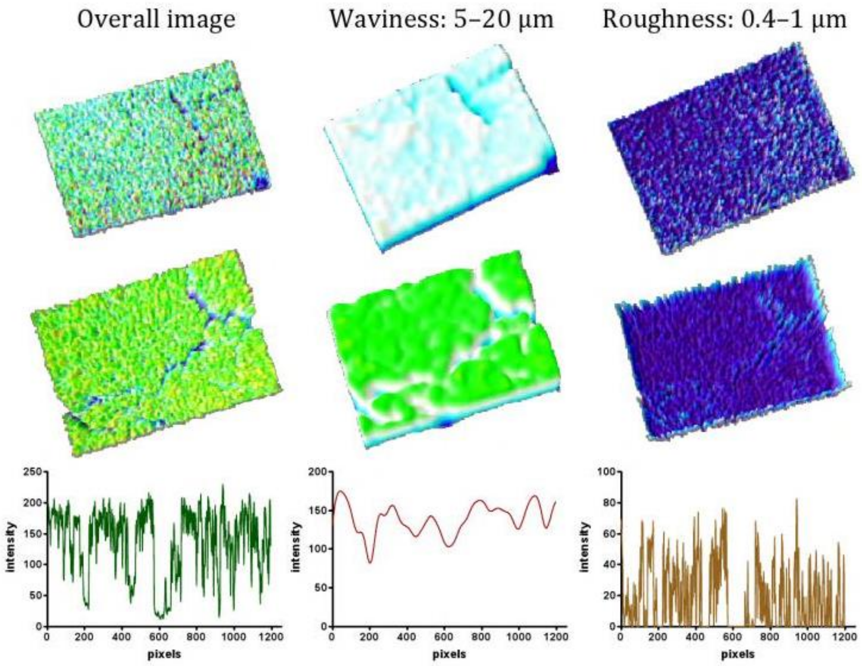

Figure 3.4 Sample images and their corresponding line profiles for the overall image and separated into its waviness (low-frequency) and roughness (high-frequency) components (Brebbia and Klemm, 2013).

Properties	**Units**	**Values**
Melting Point	K	934
Boiling Point	K	2520
Density	Kg.m^{-3}	2690
Specific Heat Capacity	J.(kgK)$^{-1}$	900
Thermal Conductivity	W.(mK)$^{-1}$	193
Latent heat of melting	kJ.kg^{-1}	400
Thermal Diffusivity	m^{2}.s^{-1}	6.35.10^{6}

Table 3.2 Thermal properties of the aluminium 6082 workpiece processed (Brandes and Brook, 1998).

3.3 Influence of pulse length and frequency on machining outcomes

In this first experimental study, pockets were machined at various frequencies for ten different pulse durations corresponding to the waveforms given in Table 3.1. The following sub-sections present and discuss the results obtained for the MRR and the surface roughness outcomes respectively.

3.3.1 Results – Material removal rate

As it can be seen from Figure 3.5, which illustrates the results obtained for the waveform having a pulse duration of 140 ns, and operating at 30% of the maximum available average power, the MRR increases with the augmentation of the pulse repetition frequency up to a certain value, after which it decreases. The frequency that corresponds to the highest MRR is 50 kHz which is close to the PRF0 value for this waveform: 51 kHz. As mentioned in the previous section, the pulse energy and average power exhibit different behaviour above and below PRF0 (see Figure 3.2). This can explain the MRR evolution observed in this figure. In particular, below PRF0, the energy is constant and the average power increases linearly, which results in the increase of the MRR. Above PRF0, the average power stays constant and the energy decreases, which results in lowering of the MRR.

The main conclusion that can be drawn from this figure is that the highest value of MRR occurs at the frequency which corresponds to the PRF0 of this specific waveform. This experimental method was systematically conducted for the remaining waveforms considered but this time when operating at 35% of their maximum available average power for a given frequency. The slight increase in average power was made due to the low removal rates witnessed at 30%. At this higher average power, the same observation could be made; that the MRR variation follows the behaviour reported above their respective PRF0 as a result of the evolutions of

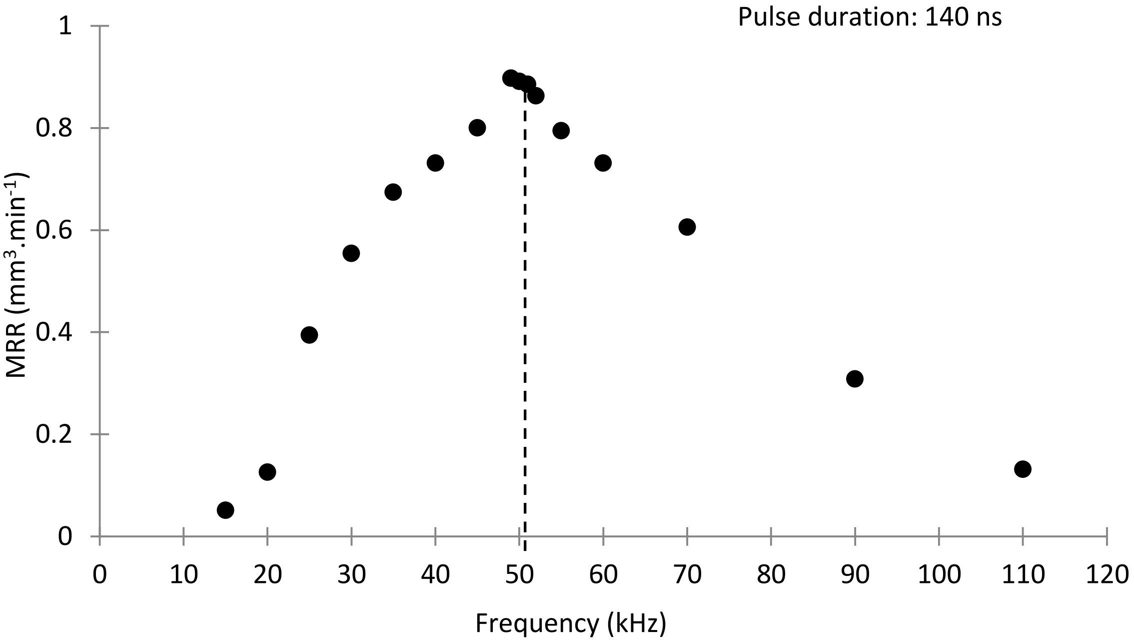

Figure 3.5 MRR evolution with the pulse repetition frequency for a pulse duration of 140 ns. The vertical dashed line indicates the PRF0 for this waveform which is 51 kHz.

energy and power. The results obtained for the three pulse durations of 95 ns, 100 ns and 120 ns, are shown in Figure 3.6. From this figure, it is also observed that, at the PRF0, the MRR decreases as the pulse duration becomes shorter. It should be noted however, that the results shown in Figure 3.5 may not be compared directly to the data plotted in Figure 3.3 because a different percentage of available power was used between the experiments, as stated previously.

As the pulse duration decreases, the laser beam is incident on the material surface for a shorter amount of time and thus, the depth of thermal penetration is reduced. In addition, as shown in Table 3.1, the delivered energy per pulse at PRF0 lessens as the pulse duration is reduced. Therefore, the observed decrease in MRR could be caused by a combination of both factors, namely a decrease in pulse energy and a decrease in pulse duration affecting the depth that the thermal energy can penetrate. Further investigations would be required to determine which of these two factors is more influential. In this case, the energy should be kept constant whilst varying the pulse duration at a specified frequency. A single pulse investigation would also be useful as it would enable a better understanding of the physical phenomena at play during material removal without the influence of heat accumulation, which is the case for laser milling.

Figure 3.7 shows the MRR obtained at PRF0 for the waveforms investigated between 25 ns and 120 ns pulse length. A trend can be observed in which the MRR at PRF0 generally increases as the pulse duration becomes longer. Figure A.2 in the Appendix displays the results of the other five waveforms studied during the course of this research.

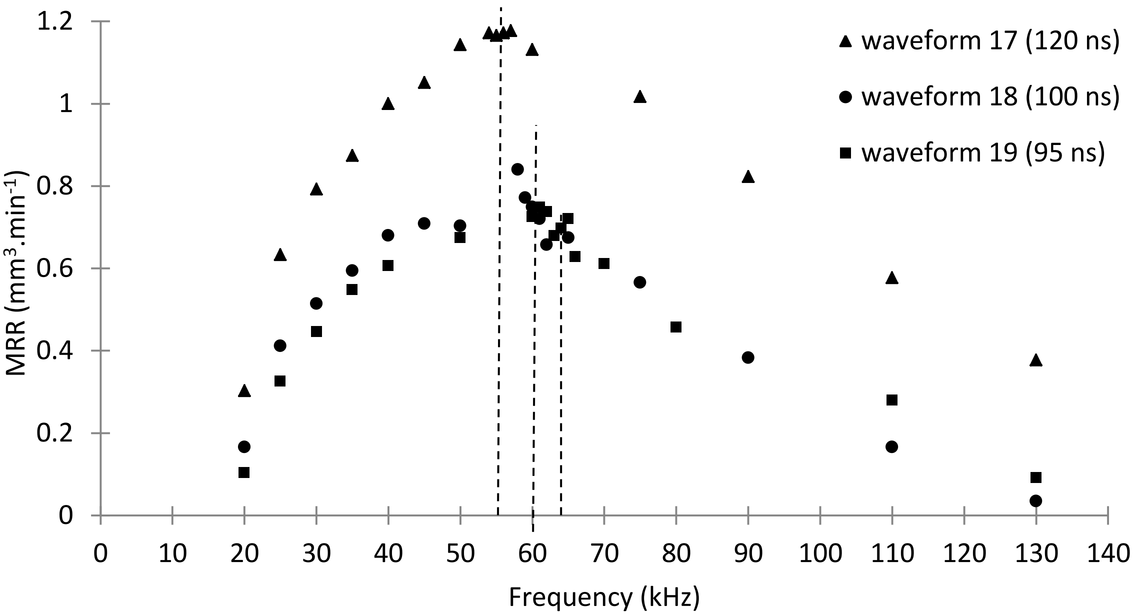

Figure 3.6 Evolution of the MRR with the frequency for three waveforms with different pulse durations. The vertical dashed lines represent the PRF0 for each waveform 55 kHz, 60 kHz and 63 kHz for waveforms 17, 18 and 19 respectively.

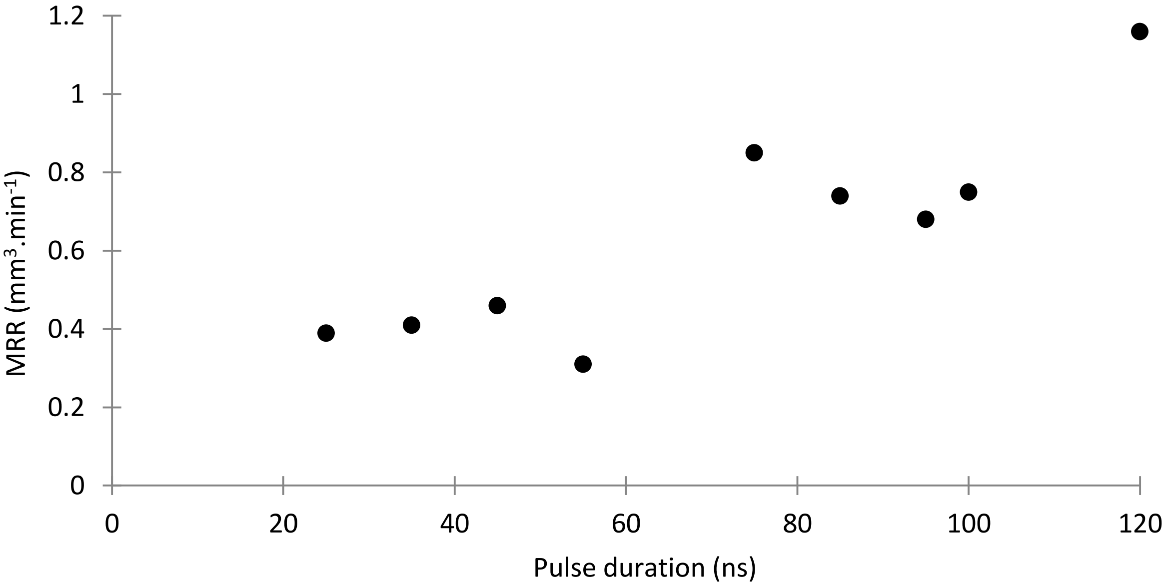

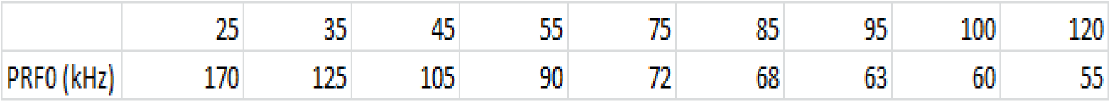

	25	35	45	55	75	85	95	100	120
PRF0 (kHz)	170	125	105	90	72	68	63	60	55

Figure 3.7 Variation of the material removal rate (MRR) at repetition rate, PRF0 for different waveforms at 35% of the maximal power. The table displays the pulse durations and their accompanying PRF0 value.

3.3.2 Results – Surface roughness

Figure 3.8 shows the results of the surface roughness, Ra, obtained at the bottom of the machined pockets for different repetition frequencies, again for the waveform with a pulse length of 140 ns used at 30% of available average power. From this figure, it can be seen that the surface roughness at PRF0 is relatively high. The same observation was also made for all waveforms investigated. Given that machining at PRF0 with any waveform leads to the maximum MRR, as reported in the previous section, a compromise has to be found when processing with a given pulse duration in order to achieve an acceptable level of MRR and a low surface roughness.

A second observation that can be drawn from this figure is that the lowest Ra value occurs at 30 kHz. This minimum follows higher values of surface roughness obtained between 15 kHz and 25 kHz although the average power in this range is lower than that delivered at 30 kHz. Unlike the effect on the MRR, the surface roughness does not increase linearly with the pulse energy increase below PRF0 as seen in Figure 3.2. This observation could be the result of the varying degrees of pulse overlap generated between different pulse repetition frequencies while the scanning speed is kept constant. In particular, the degree of overlap between pulses is defined by equation 3. 2 as follows:

$$Degree\ of\ overlap = \left(1 - \frac{v_s}{f.D}\right).100\% \qquad (3.\ 2)$$

where v_s is the scanning speed, *f* is the pulse repetition frequency and *D* is the diameter of the focused laser beam on the material surface. Based on this equation, the theoretical evolution of the degree of overlap between pulses for all the frequencies investigated is shown in Figure 3.9 for the particular values of scanning speed and beam diameter used in this experiment which were 600 mm.s^{-1} and 32 µm respectively.

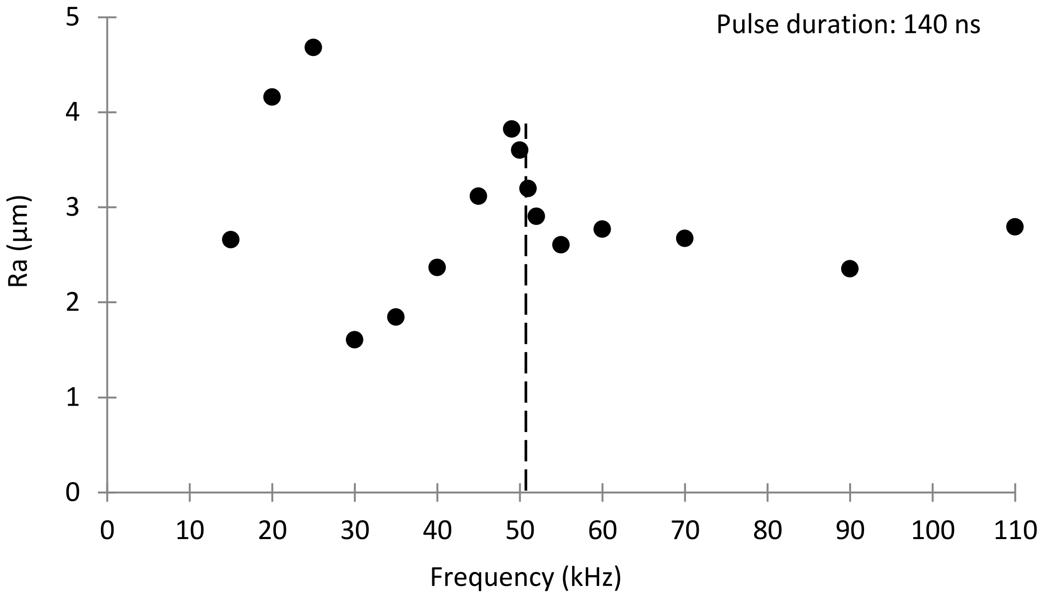

Figure 3.8 Evolution of the surface roughness (Ra) with the pulse repetition frequency for a pulse duration of 140 ns. The vertical dashed line indicates the PRF0 value for this waveform which is 51 kHz.

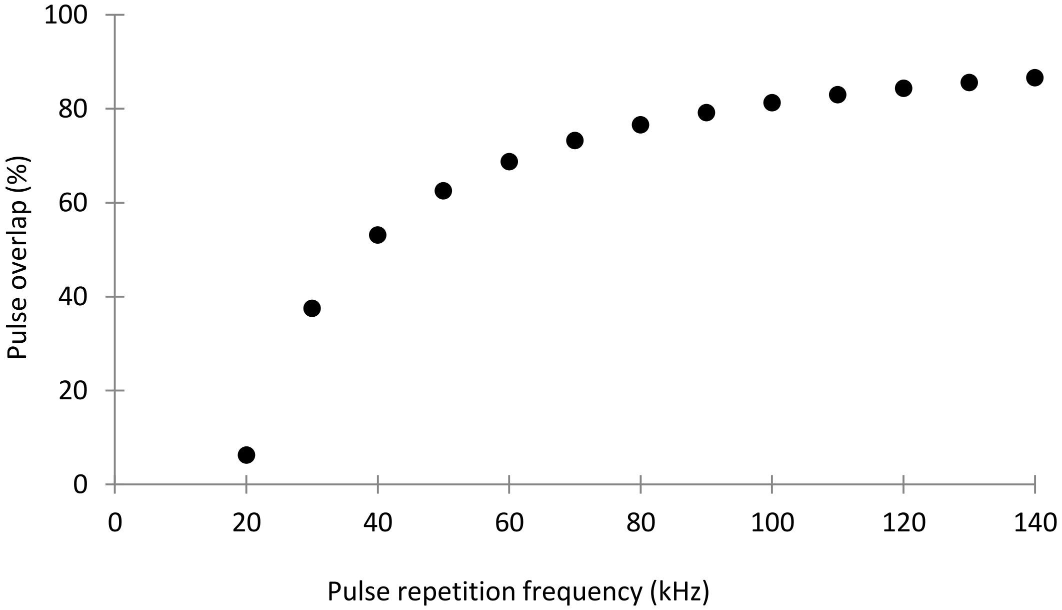

Figure 3.9 Percentage of pulse overlap as a function of the pulse repetition frequency for a scanning speed of 600 mm.s^{-1} and a spot diameter of 32 µm.

Based on Figure 3.9, it can be seen that, for frequencies below 30 kHz, the overlap is less than 40% and thus, most likely too low for a pulse to remove a significant amount of the surface topography of the crater created by the pulse delivered immediately before. This can be visualised in Figure 3.10(a) which shows a Scanning Electron Microscopy (SEM) micrograph of the bottom of the pocket machined at 15 kHz. In particular, this figure illustrates the presence of a substantial amount of material, which has not been removed between successive pulses creating pronounced peaks and valleys throughout the surface topography of a machined pocket. As the frequency increases to 30 kHz, the degree of pulse overlap reaches 40% which, for this particular pulse duration (i.e. 140 ns), led to the lowest surface roughness achieved. The SEM image for the pocket machined at 30 kHz can be seen in Figure 3.10(b). In comparison to Figure 3.10(a), the topography is smoother and does not exhibit pronounced craters.

Above 30 kHz, although the degree of pulse overlap becomes higher, its influence on the resulting surface roughness is lessened. More specifically, in spite of the increase in pulse overlap, the surface roughness is becoming worse as already reported with Figure 3.8. This could be due to the fact that the average power also increases with the augmentation of the pulse frequency until PRF0. Thus, these results show that there is an optimum frequency for achieving the lowest surface roughness and based on the data obtained for all the pulse durations investigated, it is observed that this frequency is always below PRF0 and comprised in the range 30 kHz to 40 kHz.

In order to investigate this further, single lines with different pulse to pulse overlaps were machined on the aluminium workpiece with 140 ns pulse durations and using the same settings as those utilised in the above experiment. The single lines were then imaged with the SEM instrument and their roughness measured on the WLI microscope. SEM micrographs for tracks machined at 20 kHz, 30 kHz, 60 kHz and 110 kHz are given in Figure 3.11 and it is observed that, as expected, when the frequency increases so does the overlapping of

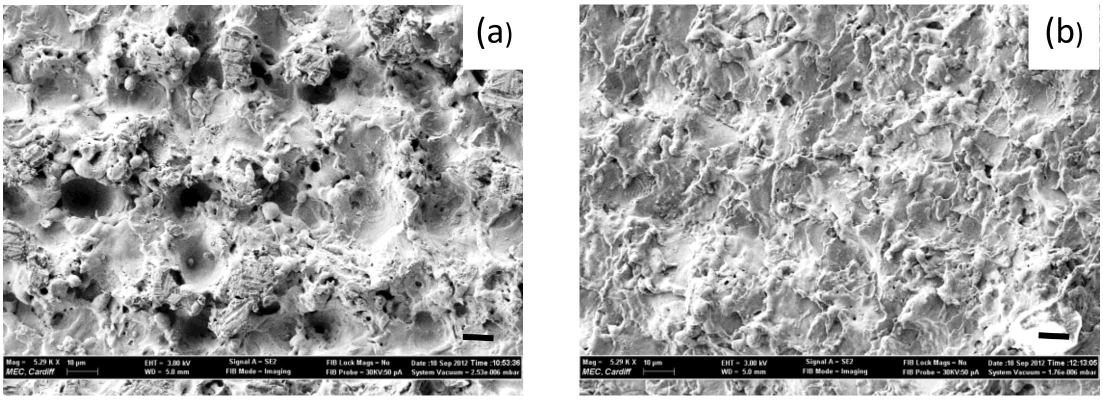

Figure 3.10 SEM images of the bottom of pockets machined at (a) 15 kHz and (b) 30 kHz

Scale bar: 10 µm.

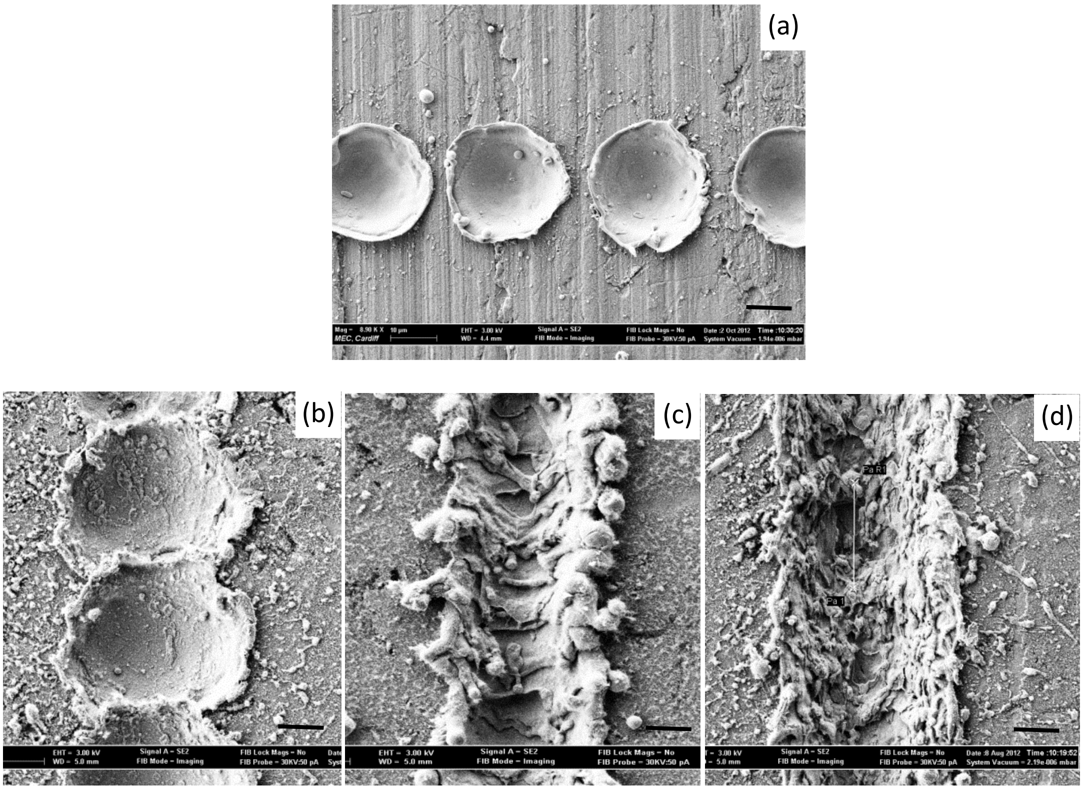

Figure 3.11 SEM images of single lines machined at various frequencies to achieve an increasing pulse overlap at (a) 20 kHz, (b) 30 kHz, (c) 60 kHz and (d) 110 kHz for a pulse duration of 140 ns.

Scale bar: 10 µm.

subsequent pulses, from separated pulses at 20 kHz to pulses with a large overlap at 110 kHz. Also the SEM images show an augmentation in material debris on the edges of the machined track as the pulse overlap increases. This was confirmed by measuring the height profile of the cross sections of these tracks with the WLI. This is a direct consequence of the fact that the pulse overlap results obtained at 60 kHz correspond to craters machined at a higher average power compared to those machined at 30 kHz. In addition, the measured surface roughness values at the bottom of the tracks increased from 1.38 µm Ra at 30 kHz to 3.3 µm Ra at 60 kHz. The roughness values of the single lines for this waveform are in relatively close agreement to those obtained for the machined pockets which were reported in Figure 3.8.

Figure 3.12 shows the surface roughness variation with the frequency for three other waveforms studied at 35% of the available average power. It can be concluded that, across the range of frequencies investigated, as the pulse duration is reduced, the surface roughness also generally decreases. As the pulse duration is reduced, the amount of time for the pulse to affect the material thermally decreases. This means that there is less time for melt ejection to cause debris and affect the roughness negatively. Also at shorter pulse durations, the peak power is higher which may result in the removal of material becoming driven by vaporisation resulting in a cleaner removal process. Experimental and theoretical evaluation of single pulses at different pulse durations may aid in the proper explanation of different removal mechanisms. The reasons for the multiple maximum and minimum roughness values are likely due to the differences in pulse overlap as witnessed in Figure 3.6. From this graph and based on the data given in Table 3.1, it is also observed that the highest surface roughness occurs around the PRF0 for each waveform. The other waveforms investigated during this research are shown in the Appendix in Figure A.3.

Figure 3.13 shows the variation of the surface roughness with pulse duration at the PRF0 for each waveform investigated at 35% available average power. It can be seen that the surface roughness generally becomes worse as the pulse duration increases. The augmentation in the delivered energy as the duration of the pulse increases causes the process of material removal to become more pronounced, which is reflected in the resulting surface finish.

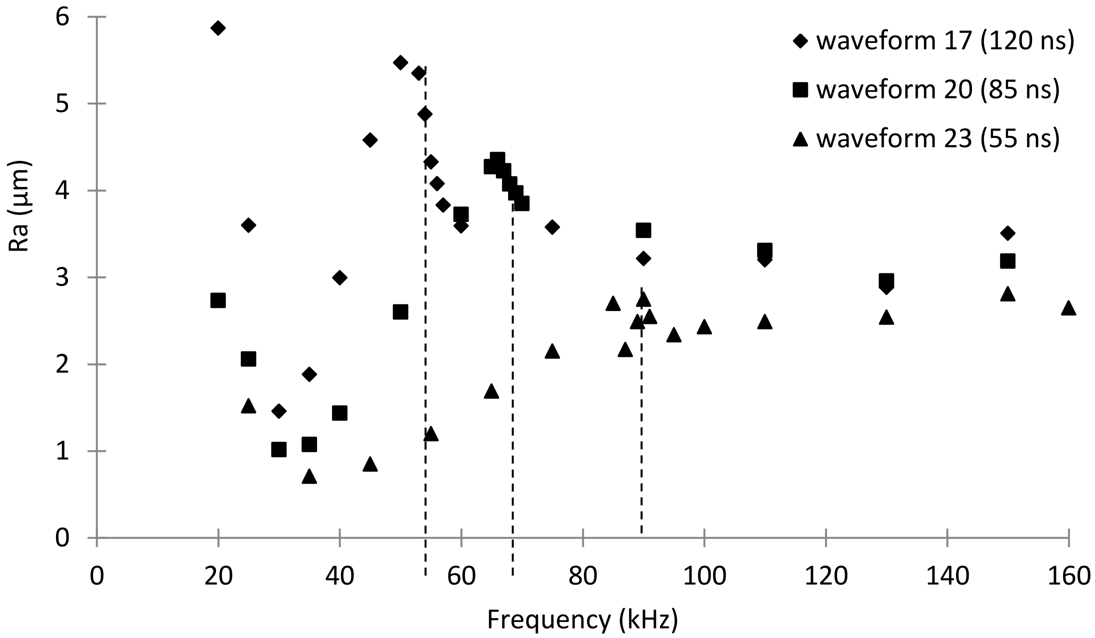

Figure 3.12 Surface roughness variation with the pulse repetition frequency for three different pulse durations. The vertical dashed lines represent the PRF0 for all the waveforms, 55 kHz for 120 ns, 68 kHz for 85 ns and 90 kHz for 55 ns.

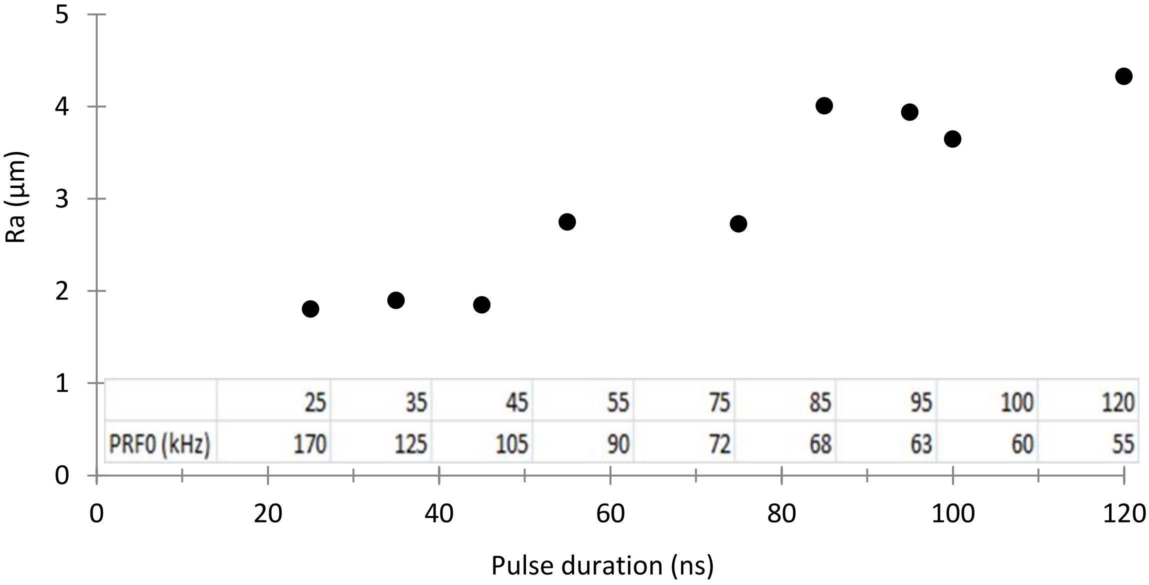

	25	35	45	55	75	85	95	100	120
PRF0 (kHz)	170	125	105	90	72	68	63	60	55

Figure 3.13 Surface roughness values at repetition rate, PRF0 for different pulse durations at 35% of the maximum power. The table displays the pulse durations and their accompanying PRF0 value.

3.3.3 Summary of the first set of experiments

From the experimental results presented, graphs were plotted to show the surface roughness obtained for each pulse duration used at 35% of the maximum available average power at their highest MRR (see Figure 3.14) and also the MRR for each of them at their lowest surface roughness achieved (Figure 3.15).

Figure 3.14 shows that generally the surface roughness increases with the augmentation in the maximum achievable MRR for each pulse duration. This graph can be used to identify possible regimes for optimisation. The results given in Figure 3.15 for the MRR at the lowest Ra values achieved for different waveforms tend to follow the trend shown in Figure 3.14 as the MRR increases with the augmentation of the best surface roughness obtained. This graph can be used in a similar way as Figure 3.14 to select pulse durations that result in the desired machining outcome or that could be further optimised.

The experimental work reported in section 3.3 shows that for all the investigated pulse durations, the highest MRR occurs at the frequency where the pulse energy and average power are the highest. This particular frequency is referred to as PRF0. Not surprisingly, machining at PRF0 leads to high levels of surface roughness. In particular, the best roughness achieved at PRF0 was Ra 1.8 µm, for a pulse duration of 25 ns, which is relatively high. The lowest surface roughness reported in this study is Ra 0.4 µm again for the waveform delivering 25 ns pulses. However, in this case, the MRR is reduced by a factor of 10 in comparison to that achieved when operating this waveform at its PRF0, highlighting the necessity of achieving a compromise to attain specific machining outcomes and the complexity of the laser-material interaction process. Thus, in the next section, a design of experiments is conducted in order to identify the influence of additional parameters on the machining outcomes when laser milling the aluminium workpiece with a given waveform at its PRF0. In particular, the ultimate objective of this further investigation is to identify an optimised processing window where the best compromise is found between the resulting MRR and surface roughness.

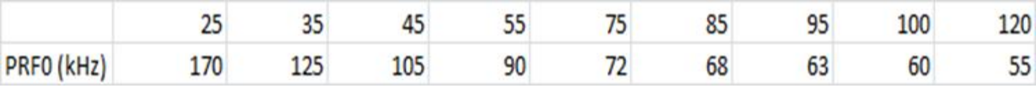

	25	35	45	55	75	85	95	100	120
PRF0 (kHz)	170	125	105	90	72	68	63	60	55

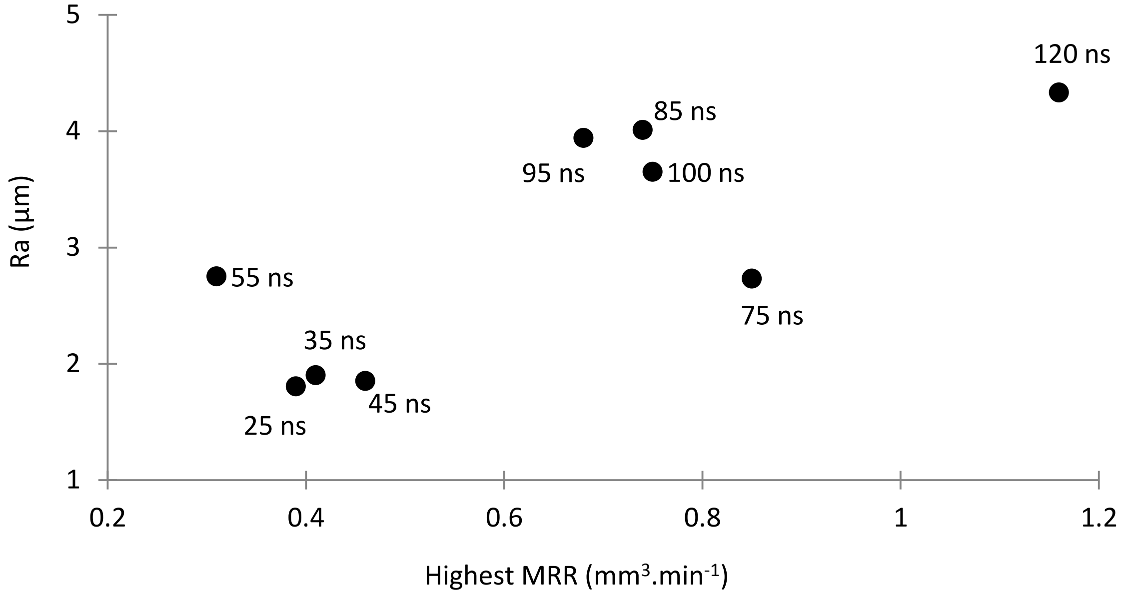

Figure 3.14 Surface roughness values at the highest material removal rate (MRR) for different pulse durations using 35% maximum power and various frequencies.

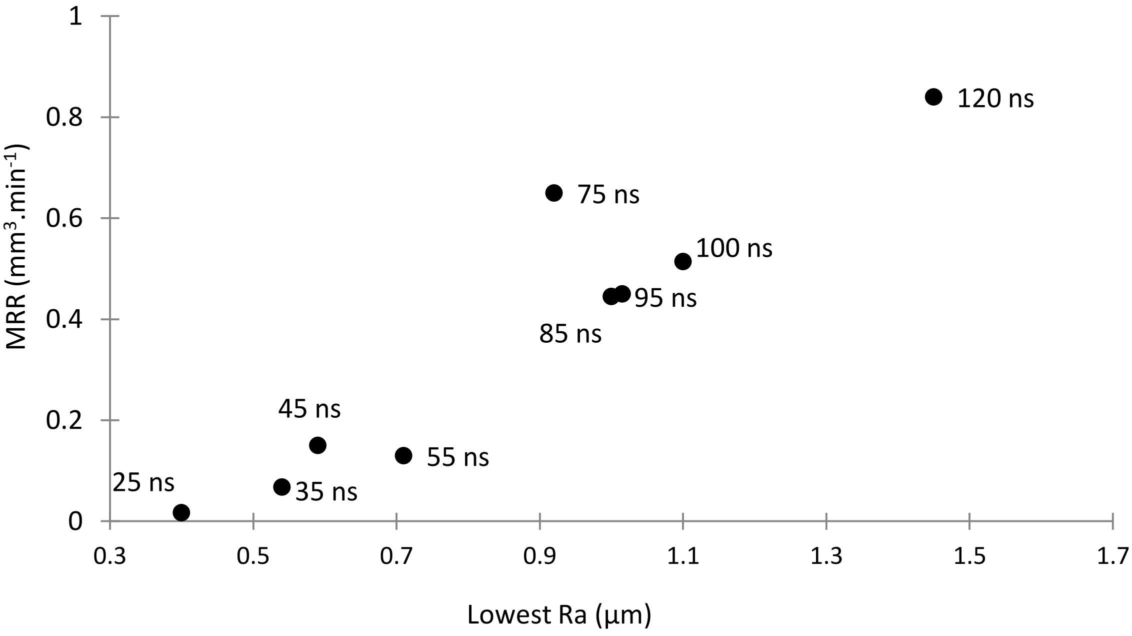

Figure 3.15 Corresponding MRR values for the lowest measured surface roughness for different pulse durations machined using 35% of the maximum power and at various frequencies.

3.4 Process Optimisation

3.4.1 Experimental design

Waveform 23, which has a pulse length of 55 ns, was chosen for further optimisation through the use of a systematic experimental design approach. This waveform was selected because of the high value of surface roughness generated compared to other pulses with similar MRR (see Figure 3.14). The pulse repetition frequency chosen for the machining experiments was the PRF0 because this frequency leads to the highest MRR. The following parameters were selected in order to investigate their influence on the particular laser machining outcomes of interest, i.e. the achieved MRR and surface roughness:

- *Pulse overlap.* This parameter corresponds to the percentage of pulse to pulse overlap in each machined track.
- *Track displacement.* This parameter represents the distance between each track of pulses.
- *Scanning strategy.* This parameter relates to the angle with which each layer is machined with respect to the previous layer.

The pulse overlap was chosen because it has been shown in the previous section to have an effect on the surface roughness achieved. The last two parameters were considered because they were not investigated in the initial study reported in the previous section. It is important to understand the effect of these additional parameters on the process output and also their optimum levels when attempting to achieve a combination of high MRR and low surface roughness. The values chosen for each parameter level are given in Table 3.3. The scanning strategy indicates how the layers are rotated with respect to an angular base. The first scanning strategy used is labelled ‘four angles’ which means that the orientation of each layer is rotated by 45 degrees compared to the previous layer until this has happened four times and then the rotation strategy repeats itself. The second scanning strategy is labelled ‘random’ which means that each layer is rotated at a random angle.

The third strategy is referred to as ‘Moiré’ which is similar to the ‘four angles’ approach where one full rotation is completed after machining four layers. The angles defined in this case were 18°, 72°, 0° and 45°. This approach is borrowed from inkjet printing applications where the values of these four angles used have been experimentally found to eradicate Moiré patterning (Gatter, 2005). A Moiré pattern is produced in a printed image when any two, or more, repeating patterns of dots overlap each other. The overlapping pulse crates can be analogous to the dots produced in inkjet printing. The selection of these particular scanning strategies was based on data from Yasa and Kruth (2010) where the 45° angle variation strategy was concluded to achieve the lowest Ra when machining with an Nd:YAG nanosecond laser and on the intention to investigate the Moiré approach, which is not traditionally employed for laser machining.

Due to the fact that three parameters were selected at three levels each, a Taguchi L9 orthogonal array was utilised for this optimisation study and thus, the number of trials was nine. As per the guidance in Roy (2001), the L9 array was chosen due to it being the smallest array that satisfied the number of factors and level assigned to each factor. This set of nine experiments was repeated three times in a random order in order to increase the robustness of the experiment. Each individual trial consisted of machining a 2 x 2 mm square pocket by applying one of the parameter combinations provided in Table 3.4. The MRR and Ra values were obtained using the measurement procedures described in section 3.2.2.

Parameter	**Code**	**Level 1**	**Level 2**	**Level 3**
Pulse overlap (%)	A	65	75	85
Track displacement (µm)	B	20	35	50
Scanning strategy	C	Four Angles	Random	Moiré

Table 3.3 The three system parameters chosen to be represented in the L9 Taguchi orthogonal array and their corresponding values for each level used in the design.

	Parameter Levels			Experimental run order		
Experiment No.	A	B	C	First Repetition	Second Repetition	Third Repetition
1	1	1	1	4	9	8
2	1	2	2	7	1	2
3	1	3	3	2	8	6
4	2	1	2	5	2	4
5	2	2	3	1	5	9
6	2	3	1	9	3	3
7	3	1	3	6	6	7
8	3	2	1	3	4	1
9	3	3	2	8	7	5

Table 3.4 Combination of each parameter's three levels for all nine experimental runs (A being the pulse overlap, B the track displacement and C the scanning strategy). And the last three columns of this table represent the random experimental run order for the three repetitions used to ensure the least possible error is introduced into the design.

3.4.2 Experimental result and analysis

The surface roughness and MRR values recorded for each experimental run are given in Table 3.5.

For each combination of parameters, the signal to noise (S/N) ratio value was calculated. The S/N ratio gives a measure of the sensitivity of the control factors to external factors not built into the experimental design. For the surface roughness results, the following formula was used to calculate the S/N ratio values for each combination of parameters given that the smallest possible value of Ra is the desired process outcome (Roy, 2001):

$$S/_N = -10\log_{10}\left(\frac{Ra_1{}^2+Ra_2{}^2+Ra_3{}^2}{3}\right) \tag{3. 3}$$

When analysing the achievable MRR, the highest possible value was the desirable outcome and in this case, the following formula was adopted to calculate the S/N ratio related to these results for each combination of parameters:

$$S/_N = -10\ \log_{10}\left(\frac{\frac{1}{MRR_1{}^2}+\frac{1}{MRR_2{}^2}+\frac{1}{MRR_3{}^2}}{3}\right) \tag{3. 4}$$

	First Repetition		**Second Repetition**		**Third Repetition**	
Experiment No.	**Ra_1 (µm)**	**MRR_1 ($mm^3.min^{-1}$)**	**Ra_2 (µm)**	**MRR_2 ($mm^3.min^{-1}$)**	**Ra_3 (µm)**	**MRR_3 ($mm^3.min^{-1}$)**
1	1.08	0.5	1.10	0.52	1.15	0.57
2	3.57	0.23	3.49	0.28	3.60	0.28
3	5.37	0.12	5.40	0.2	5.25	0.16
4	1.39	0.57	1.44	0.6	1.36	0.65
5	9.10	0.17	9.15	0.2	9.01	0.21
6	5.65	0.15	5.85	0.2	5.64	0.2
7	4.69	0.68	4.75	0.7	4.80	0.75
8	9.06	0.22	9.15	0.24	8.85	0.31
9	6.88	0.2	6.99	0.23	6.50	0.26

Table 3.5 Surface roughness and MRR values for each experimental run and repetition.

3.4.2.a Optimum parameter levels

Figure 3.16 shows the graphs of the S/N ratios for each parameter level and for both process outcomes. From Figure 3.16(a), the optimum combination of parameters for the lowest surface roughness is found to be:

- Pulse overlap: 65%;
- Track displacement: 20 µm;
- Scanning strategy: random.

The result obtained with respect to the optimum pulse overlap is in-line with the findings reported by Bartolo et al (2006) and Selada et al (2011) where the best value of pulse overlap when machining steel was found to lie in the range 60% to 70%. From Figure 3.16, the behaviour of the surface roughness can also be observed with the variation of the parameters within their investigated range of values. The surface roughness increases linearly with the augmentation in pulse overlap from 65% to 85%. Unfortunately, the particular laser system set-up used in this research did not allow the study of pulse overlaps lower than 65% when operating at PRF0. Thus, it could be that the best level for this parameter lies outside the studied range. For the second parameter, the track displacement, the optimum level corresponds to the lowest value considered, 20 µm. Given that the diameter of the focal beam used in this research is 32 µm, it can be said that the best surface roughness was achieved for a track displacement equals to 62% of the diameter of the focussed laser spot. This is somewhat in-line with the conclusions reached in the study from Selada et al (2011), who processed stainless steel with a 10 ns laser system and where it was observed that in general, the surface roughness decreases as the track displacement decreases. The value of track displacement reported by these authors which resulted in the lowest surface roughness, was a third of a 32 µm spot diameter. However, given that the material processed and the range of track displacement values studied by Selada and co-workers (2011) do not match those

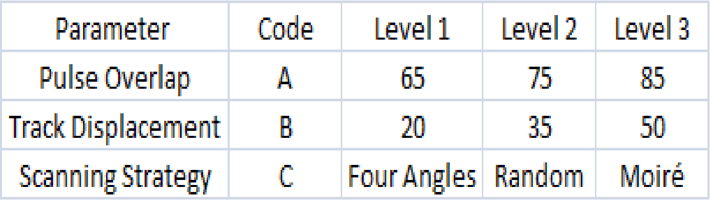

Parameter	Code	Level 1	Level 2	Level 3
Pulse Overlap	A	65	75	85
Track Displacement	B	20	35	50
Scanning Strategy	C	Four Angles	Random	Moiré

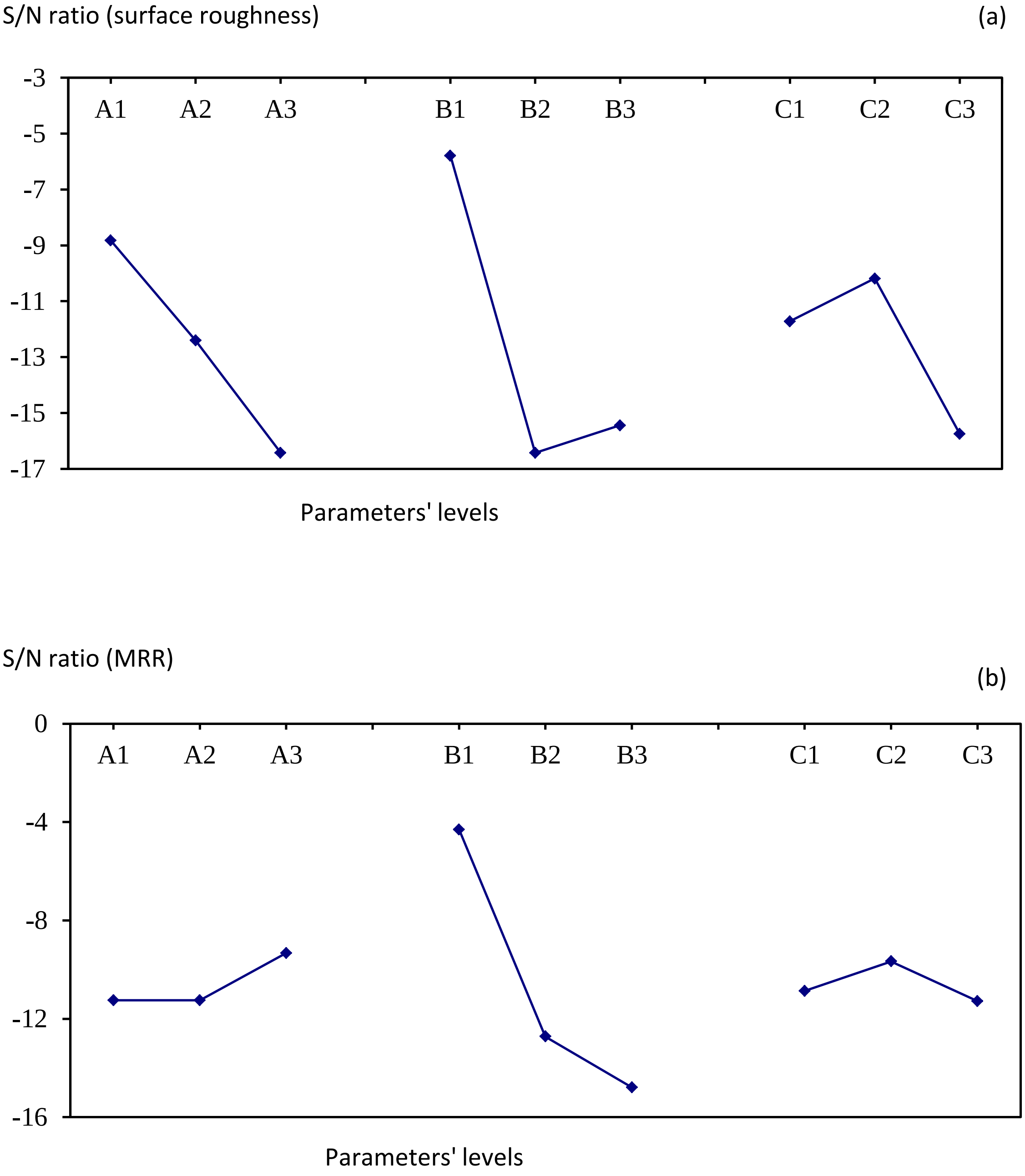

Figure 3.16 Average values of S/N ratios associated with (a) the surface roughness and (b) the MRR results for the three parameters at the three levels selected.

considered in this research, direct comparisons cannot be made. The optimum scanning operation identified is the random strategy.

This result was expected because the utilisation of a repetitive strategy such as a set of four angles repeated every four layers could lead to the creation of islands of material not processed effectively between different layers.

Similarly, based on Figure 3.16(b), the optimum parameters for the MRR are identified as follows:

- Pulse overlap: 85%;
- Track displacement: 20 µm;
- Scanning strategy: random.

This set of parameter values only differs for the pulse overlap when compared with those found for the surface roughness. In particular, more efficient material removal is achieved with an overlap of 85% rather than 75% or 65%. This should be due to the fact that an increase in the pulse overlap value results in more pulses being delivered in one track and thus leads to a higher accumulative material removal. It is also observed that an increase in track displacement will decrease the MRR. This is explained by the fact that a greater distance between tracks means that a smaller number of lines are machined within one layer and thus, less material can be processed in the same sized pocket. These finding are also observed in the work of Bartolo et al (2006), where it was concluded that a decrease in pulse overlap, leads to a decrease in the material removal rate.

3.4.2.b Significant parameters

In order to analyse the significance of each studied parameter on the process outcomes of interest, an analysis of variance (ANOVA) was conducted. The ANOVA results are given in Table 3.6 for the first response variable, surface roughness, and in Table 3.7 for the second response, the MRR. These tables also include the percentage contribution of each factor studied on the variation of the results. For the surface roughness, the track displacement is the largest contributor (60%) and thus causes the most variation for this process outcome while the percentage of pulse overlap contributes 25% and the scanning strategy contributes the least (14%). These results are in-line with the findings presented by Campanelli et al (2007) where it was found that the scanning strategy had less influence on the achieved surface roughness compared to other parameters when processing an aluminium-magnesium alloy workpiece with a pulse length of 5 ns. For the achieved MRR, the results show that the pulse overlap and the scanning strategy do not contribute significantly toward its variation. This is note-worthy because it means that those parameters can be varied in order to improve the surface roughness without having a significant effect on the MRR.

For both tables, the variance ratio value, obtained for each parameter was compared with the values from standard F-tables for given statistical levels of significance. In this way, it was concluded that:

- The parameters “pulse overlap” and “scanning strategy” had no statistical significance on the achievable MRR. However, they are significant for the resulting surface roughness at 97.5% and 95% confidence levels for the pulse overlap and scanning strategy respectively.
- The parameter “track displacement” has the highest statistical significance both for the surface roughness, 99% confidence level, and the MRR, a confidence level of 97.5%.

The aim of this optimisation study was to investigate whether the surface roughness of machined pockets could be improved for a given pulse duration (55 ns) while operating at its PRF0.

Based on the data reported in Table 3.5, the lowest average surface roughness achieved was Ra 1.1 µm and in this case, the average MRR was 0.53 $mm^3.min^{-1}$. If these values are compared against those reported in Figure 3.13 in the previous section where Ra values were given for different pulse durations when processing at PRF0, this corresponds to a decrease in the surface roughness of 60% (i.e. from 2.75 µm to 1.1 µm) while at the same time the MRR was increased by 46% from 0.36 $mm^3.min^{-1}$ to 0.53 $mm^3.min^{-1}$ (see Figure 3.5). The highest average MRR obtained was 0.71 $mm^3. min^{-1}$, which is above that achieved at PRF0 in the previous experiment but, the corresponding surface roughness was also a lot higher. If experiment number 4 is taken into account, the average MRR is 0.6 $mm^3.min^{-1}$ and the average surface roughness is a fourth of that seen at the highest MRR of 0.71 $mm^3.min^{-1}$.

This study shows that the design of experiment method can be used to identify process parameter values that can optimise the desired responses. In this case, using an L9 orthogonal array, it was found that, the surface roughness can be decreased by 60% whilst the material removal rate experiences an increase of 46%. The statistical analysis performed using the orthogonal array output measurements concluded that the track displacement is significant for both outcomes of material removal rate and the surface roughness, whilst the other two parameters of pulse overlap and scanning strategy only have significance when considering the surface roughness. This means that these values can be varied to affect the surface roughness output whilst not affecting the material removal rate. The signal to noise ratios calculated from the measurements contributed the values of each parameter necessary to achieve a high material removal rate and those necessary to achieve a low surface roughness. Those values are given in Table 3.8.

Parameters	DoF	SS	V	Variance Ratio	Percentage contribution	Statistical significance
A	2	86.74	43.37	42.3	25.06	97.5%
B	2	207.74	103.87	100.9	60.03	99%
C	2	49.54	24.77	24.06	14.32	95%
Error	2	2.06	1.03		0.59	
Total	8	346.08			100.00	

Note: DoF is the degree of freedom, SS is the sum of squares, V is the variance.

Table 3.6 ANOVA for the values of surface roughness obtained from each experimental run and repetition specified in the L9 orthogonal array.

Parameters	DoF	SS	V	Variance Ratio	Percentage contribution	Statistical significance
A	2	7.35	3.67	3.20	3.69	-
B	2	184.96	92.48	80.48	93.01	97.5%
C	2	4.26	2.13	1.85	2.14	-
Error	2	2.30	1.15		1.16	
Total	8	198.86			100.00	

Note: DoF is the degree of freedom, SS is the sum of squares, V is the variance.

Table 3.7 ANOVA for the values of the material removal rate obtained from each experimental run and repetition specified in the L9 orthogonal array.

Parameter	Value for highest material removal rate	Value for lowest surface roughness
Track Displacement	20 µm	20 µm
Pulse Overlap	85%	65%
Scanning Strategy	Random	Random

Table 3.8 The value for each parameter necessary to achieve both the highest material removal rate and the lowest surface roughness as determined from the signal to noise ratio analysis performed using the data collected in the L9 orthogonal array.

3.5 Conclusions and Summary

As well as providing an alternative to Q-switched DPSS lasers, recent developments in MOPA-based Yb fibre lasers open the opportunity to investigate a relatively broad range of pulse durations and repetition frequencies within one system. As a result, this reduces the uncertainty associated with studying processing outcomes from different laser machines. Thus, the main distinguishing characteristic of this chapter lies in the systematic investigation of a number of pulse durations in the nanosecond regime when performing milling operations on an aluminium workpiece with a 1064 nm wavelength Yb fibre laser. An investigation of the influence of pulse repetition frequency on the machining outcomes, specifically the MRR and the surface roughness, was initially conducted for ten different pulse lengths between 25 ns and 140 ns. The conclusions with respect to the material removal rate are as follows:

- For all the waveforms investigated, the highest MRR occurs at the PRF0 frequency which corresponds to the frequency with the highest pulse energy and average power.
- An increasing pulse duration generally leads to an increase in the MRR for pulse frequencies at the PRF0.

When considering the surface finish of the machined pockets, the following conclusions can be drawn:

- The surface roughness is relatively high at the PRF0. This leads to the need to compromise when a high MRR is necessary along with a low surface roughness.
- Across the range of frequencies investigated, as the pulse duration is reduced, the surface roughness also decreases.
- The surface roughness varies over the pulse repetition frequency range with a specific minimum comprised between 30 kHz and 40 kHz for all the waveforms studied. In this range, the pulse overlap appears to be high enough so that material is removed in a

uniform manner across the whole pocket while the energy levels are sufficient to induce ablation and at the same time low enough to minimise the amount of melt ejection generated by each pulse. Besides, it was also observed that the surface roughness variation with the pulse repetition frequency is not linear. There are two frequencies at which the surface roughness is at a maximum and the physical phenomena behind these two local maxima are different. The first maximum, at a low frequency, occurs because of a lack of sufficient material removal due to the small pulse overlap. The second maximum takes place at the PRF0 for each waveform. This is due to the volatile nature of the material removal at the high power that occurs at this particular frequency.

In addition, an experimental design was employed to investigate the influence of the pulse overlap, the track displacement and the scanning strategy on process outcomes of interest when machining with a pulse length of 55 ns operating at its PRF0. For the surface roughness, it was found that the track displacement was the most statistically significant parameter with the scanning strategy being the least. With regard to the MRR, the only statistically significant parameter was the track displacement. Finally, it was shown that this optimisation study could result in identifying a combination of parameters leading to a 60% decrease in the achieved surface roughness while still processing at the pulse repetition frequency that corresponds to the maximum MRR achievable.

During the studies reported in this chapter, multiple, overlapping pulses were used in order to mill the required shaped pocket to investigate the response of the MRR and surface roughness to variations in parameters. The use of multiple, overlapping pulses can disguise the actual behaviour of the material when subjected to a laser pulse even though the understanding of this process may lead to further optimisation of laser machining. For this reason, the next chapter will focus on the single pulse machining of materials in order to gain a better insight into the physical phenomena occurring during laser material interaction.

Theoretical and experimental study of laser material interaction with single pulses

4.1 Introduction

Chapter 3 investigated the machining response of aluminium during nanosecond laser milling and when varying a number of process parameters. While the optimisation results were satisfactory, with a 60% decrease in surface roughness for a given pulse duration, the possibility that the effects experienced, when using multiple pulses, hindered the understanding of physical phenomena occurring during laser material interaction was raised. As seen in Chapter 2, optimising the laser material interaction process is a non-trivial task to undertake as it involves understanding the effect of multiple parameters and phenomena, which are not directly controllable by the user. The optimisation of the outcome of laser machining depends on the understanding of both the effect of parameters and the phenomena apparent during the laser beam interaction. There are two main methods available when attempting to characterise the laser material interaction process; namely a theoretical or an experimental approach. Modelling the interaction of a laser beam with a workpiece material can be a very useful tool when trying to understand the laser machining process. An accurate model of this interaction can also be utilised in trying to predict, control and optimise the process without the waste of resources associated with experimental investigations. At the same time, experimental investigations can give a more accurate view of the machining process and the phenomena at its core. For this reason, both approaches are followed in this chapter for studying the single pulse processing of a number of engineering materials using the nanosecond laser system employed in this research.

The chapter is organised as follows, section 4.2 details a theoretical model that has been created in order to estimate the geometry of a single crater. This model accounts for temperature dependent material properties as well as for the phase change dynamics, from solid to liquid, and was solved using a partial differential equation solving software called FlexPDE. Next, the focus of section 4.3 is on the single pulse response of three different materials when processed with the nanosecond laser. These different materials consist of a pure metal (titanium), a ceramic (silicon carbide) and a semiconductor (silicon). An analysis is presented on the observed laser material interaction phenomena when varying the pulse duration, fluence, peak power and material properties.

In order to verify the predictions of the theoretical model, section 4.4 consists of a comparison of the experimental and theoretical diameters and depths for the three materials at four waveforms. A discussion of the accuracy of the model and its strengths and weaknesses is also included.

4.2 Theoretical Study

4.2.1 Theoretical model development

In addition to the better understanding of the laser material interaction process, the objective of the developed model is also to predict the geometry of the obtained craters when subjected to an incident laser beam of varying pulse duration and delivered energy. For this theoretical study, the assumption was made that the workpiece can be represented by a semi-infinite body due to the fact that the laser spot size, the optical absorption length and the thermal penetration depth are very small compared to the workpiece dimensions. In addition, convection and radiation losses from the top surface of the material, on which the laser beam is incident, were neglected because of the high intensity of the laser beam utilised, which is of the order of 10^{12} $\mathrm{Wm^{-2}}$ (Grigoropoulos et al 1993). At a nanosecond time scale, the absorption of the transmitted laser beam energy by electrons within the material lattice occurs at a time length which is shorter than the duration of the pulses. This means that the energy absorption can be treated as being transformed directly into heat creating a thermal process to be modelled. Thus, the evolution of the temperature, T (K), in time, t (s), and in a two-dimensional space (x, z) (m), resulting from the energy absorption of a pulse into the lattice can be described using the classical Fourier heat equation:

$$\rho c_p(T)\frac{\partial T(x,z,t)}{\partial t} - \frac{\partial}{\partial z}\left(k(T)\frac{\partial T(x,z,t)}{\partial z}\right) - \frac{\partial}{\partial x}\left(k(T)\frac{\partial T(x,z,t)}{\partial x}\right) = Q(x,z,t) \tag{4.1}$$

where $Q(x, z, t)$ represents a volumetric heat source generated by the laser beam incident on the top surface of the substrate. The variable z is the distance into the target from its top surface with a direction perpendicular to the surface while x is an axis parallel to the surface of the workpiece. The heat source is formulated according to the Beer-Lambert law using the following equation:

$$Q(x,z,t) = \alpha \times (1 - R) \times I(x,t) \times e^{-\alpha z} \tag{4.2}$$

where $I(x, t)$ describes the incident beam intensity, which is assumed to have a Gaussian profile in time and space, and α (m^{-1}) is the optical absorption coefficient of the material. Using this assumption, the equation describing the spatial and temporal shape of the pulse input is as follows (Hitz et al 2012):

$$I(x,t) = I0 \times e^{-2\left(\frac{x}{\omega_0}\right)^2} \times e^{-4.\ln 2.\frac{(t - t_0)^2}{t_{pulse}^{\,2}}} \tag{4.3}$$

where ω_0 is the radius of the laser beam at the focal point (m), t_0 is the time at which the pulse starts (s), t_{pulse} is the duration of the pulse (s) at full width half maximum (FWHM) and $I0$ is the peak output power of the laser pulse (W m^{-2}), which is described with:

$$I0 = \frac{E}{\tau \pi r^2} \tag{4.4}$$

where E is the pulse energy (J), τ is the pulse duration (s) and r is the beam radius (m). Melting of the material is taken into account in this model, which means that the contribution of the latent heat of fusion, L_h (J kg^{-1}), is also considered. This is achieved using the 'temperature formulation' method, which introduces a function, $f_l(T)$, denoting the liquid volume fraction (Fachinotti et al, 1999). In this study, the liquid volume fraction is described by a ramp function, which is assumed to vary linearly between the solidus and liquidus temperatures as follows (Abderrazak et al, 2009):

$$\left.\begin{array}{l} T < T_s, \quad f_l(T) = 0 \\ T_s \le T \le T_l, \quad f_l(T) = \dfrac{T - T_s}{T_l - T_s} \\ T > T_l, \quad f_l(T) = 1 \end{array}\right\} \tag{4.5}$$

where T_s and T_l are the solidus and liquidus temperatures, respectively. Thus, this function is added to the heat conduction equation along with the latent heat of fusion and the density to account for the latent heat contribution:

$$\rho c_p(T)\frac{\partial T(x,z,t)}{\partial t} + \rho L_h\frac{\partial f_l(T)}{\partial t} - \frac{\partial}{\partial z}\left(k(T)\frac{\partial T(x,z,t)}{\partial z}\right) - \frac{\partial}{\partial x}\left(k(T)\frac{\partial T(x,z,t)}{\partial x}\right) = Q(x,z,t) \qquad (4.6)$$

The following initial and boundary conditions are also adopted:

- Before pulse irradiation, the whole substrate is assumed to be at ambient temperature, i.e. $T(x, z, 0) = 293$K.
- The bottom surface of the workpiece is kept at ambient temperature, i.e. $T(x, -\infty, t) = 293$K.
- As mentioned above, the top surface is considered adiabatic, which means that:

$$k\left.\frac{\partial T(x,z,t)}{\partial z}\right|_{z=0} = 0 \qquad (4.7)$$

This theoretical model was implemented in the FlexPDE software using a fixed mesh finite element discretisation scheme.

4.2.2 Results of the theoretical modelling

Table 4.1 shows the properties of the three materials used in the experimentation (values in parenthesis represent liquid properties).

The theoretical model presented in the previous section, enables the prediction of the temperature distribution in two dimensions; radially across the surface and in the z-direction through the material. Equation 4.6 was used to track the melting evolution through the material so as to be able to predict the size of the resulting crater for comparison with experimental results.

Before conducting such comparison for the materials of interest in this research, the model output should first be validated against published theoretical predictions, which have followed the same modelling approach as that described in the previous section. Figure 4.1 shows a comparison of the results obtained with the model developed in this thesis and the model developed by Bleiner et al (2006) using an Nd:YAG laser at 266 nm, with a Gaussian profile in time and a FWHM of 5 ns. The spot size used was 100 µm and the intensity was 1 GW.cm^{-2}.

Only the results obtained for aluminium were compared due to the other six metals reaching vaporisation, which is not taken into account in this thesis. The predictions of the peak temperature of around 3500 K at about 10 ns agree well, with the small difference being perhaps due to different numerical techniques, through a variation in computing software.

	Silicon	**Silicon carbide**	**Titanium**
Thermal conductivity ($W. m^{-1} .K^{-1}$)	156 (22) Hull (1999)	360 Harris (1995)	20 (35) Welsch et al (1993), Wilkes et al (1996)
Specific heat capacity ($J .kg^{-1} .K^{-1}$)	694 (1032) Hull (1999)	700 Pierson (1996)	528 (700) Welsch et al (1993)
Density ($kg .m^{-3}$)	2340 (2560) Hull (1999)	3200 Harris (1995)	4500 (4140) Welsch et al (1993) HaiPeng et al (2012)
Diffusivity ($m^2 .s^{-1}$)	0.000086	0.00031	0.0000086
Optical penetration depth at 1064 nm (m)	15.10^{-4} (10.10^{-9}) Green (2008)	80.10^{-9} Larruquert et al (2011)	1.10^{-8} Welsch et al (1993)
Reflectivity (%)	0.3 (0.79) Green and Keevers 1995	0.2 Spritzer et al (1959)	0.7 Welsch et al (1993)
Latent heat of fusion ($J .kg^{-1}$)	$1.8.10^6$ Hull (1999)	$9.3.10^5$ azom.com	4.10^5 Welsch et al (1993)
Melt temperature (K)	1683 Hull (1999)	3103 Goodfellows data sheet	1940 Welsch et al (1993)

Table 4.1 Thermal and optical parameters for each material used in the theoretical analysis. Values in parenthesis represent the properties of the liquid material.

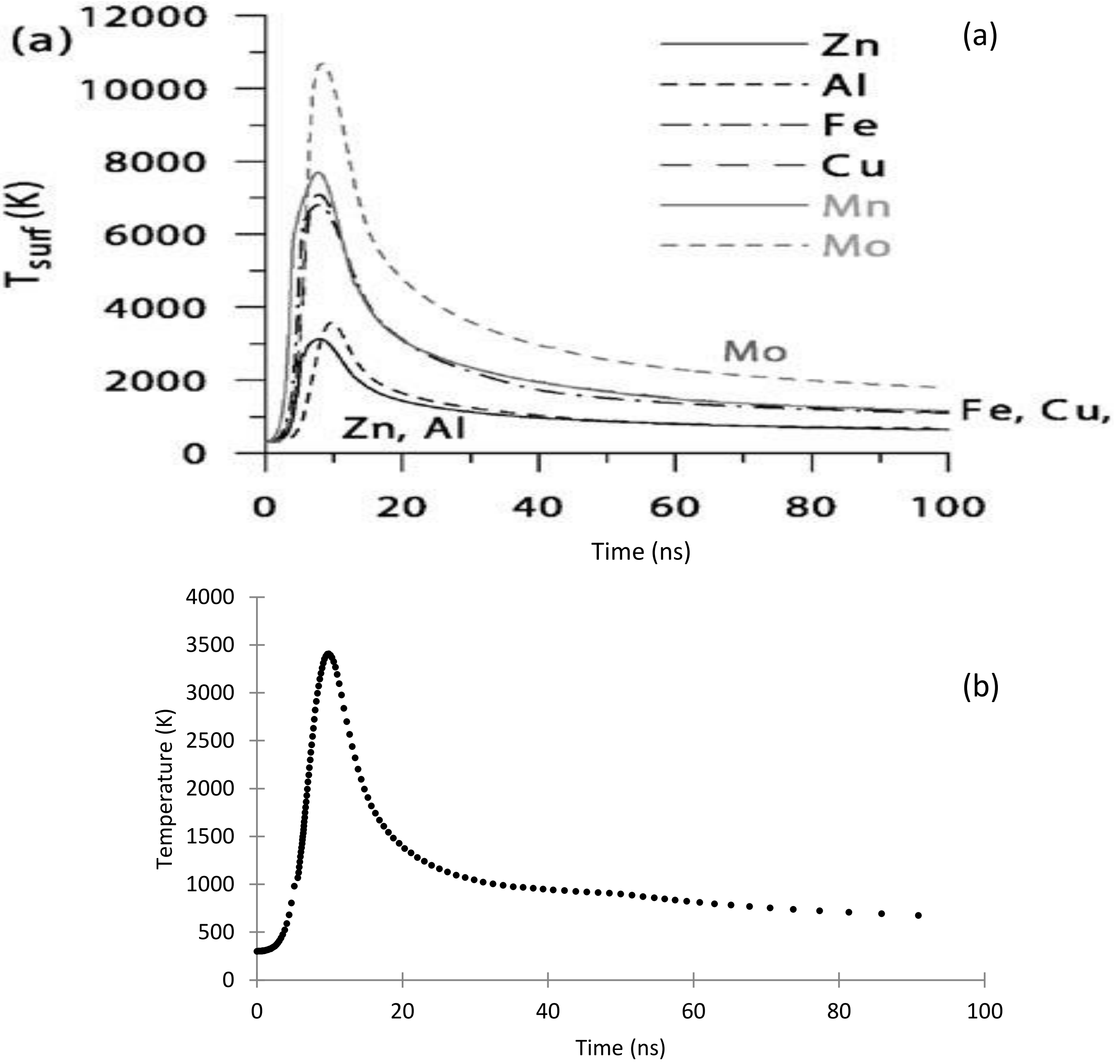

Figure 4.1 Comparison of the results of the theoretical modelling results for aluminium processing using a laser operating with a full-width-half-maximum (FWHM) of 5 ns and an intensity of 1 GW.cm^{-1}. (a) results from Bleiner et al (2006) (b) Results from the theoretical model developed in this thesis.

Temperature dependent and temperature independent values.

In order for the theoretical model to give as accurate predictions as possible, it is important that the material properties used are as reliable as possible. The nature of the thermal conductivity being that the free electrons in a metal facilitate the conduction, an increase in temperature decreases this value due to the augmentation in lattice vibrations resulting in a resistance to the flow of these free electrons (Thirumaleshwar, 2009). The heat capacity for metals on the other hand augments as the temperature increases (Cverna, 2002). Not only does the variation in temperature affect the thermal properties, a phase change also needs to be accounted for. The density of a material varies greatly with a phase change from solid to liquid or liquid to gas. For materials such as silicon, the large variation in optical properties with temperature also needs to be accounted for due to the metallic behaviour of the liquid silicon resulting in a large change in the optical absorption from cm value to the nm range (Sokolowski-Tinten et al, 1998). The reason behind this large variation is that the phase change of silicon from a solid to a liquid results in an increase in the amount of free electrons available for conduction causing the electrical conductivity of the molten material to rise from around 0.3 $\Omega^{-1}cm^{-1}$ to the a value close to that of a typical metal (~ 75 $\Omega^{-1}cm^{-1}$) (Grigoropoulos, 2009).

For example, the silicon temperature variation induced with a 140 ns pulse at 43.7 $J.cm^{-2}$ is shown in Figure 4.2 using a constant absorption coefficient. The result indicates that melting only just begins at this fluence and pulse duration which is not the case, as it will be seen in section 4.3 when the experimental single pulse experimentation is presented.

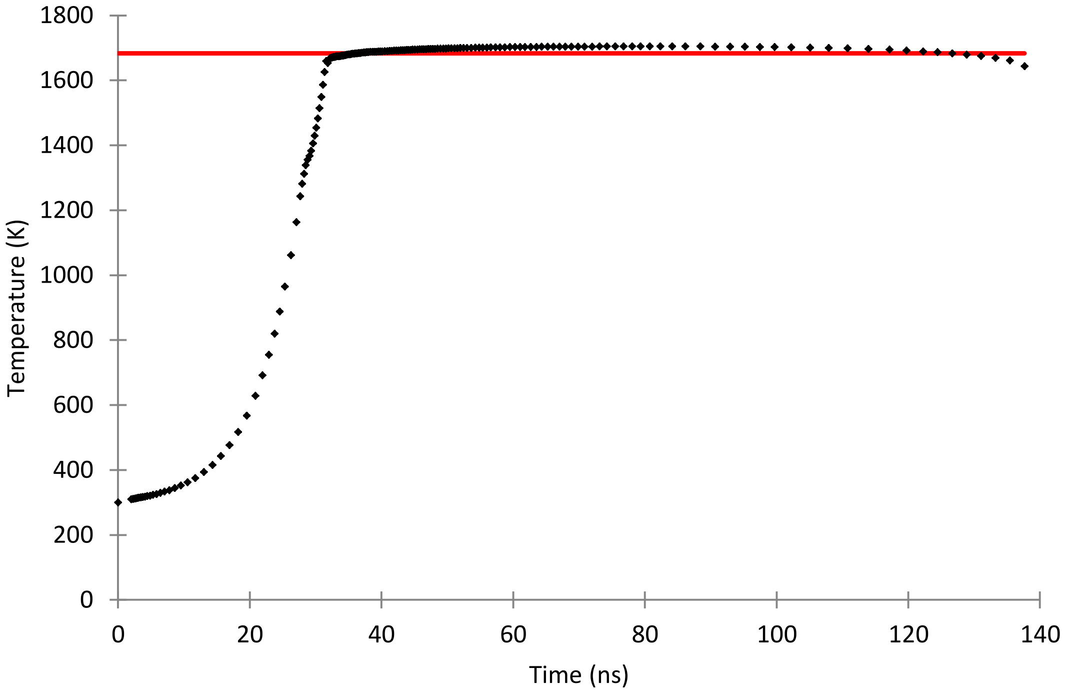

Figure 4.2 Graph of temperature variation with time for silicon processed with a 140 ns pulse having a fluence of 43.7 J.cm^{-2} when the temperature dependence of the material parameters is not considered. The horizontal line is the melt temperature of the silicon (1683 K).

4.2.2.a Heating and cooling cycles

Having validated the theoretical model, it is used to predict various behaviours, with respect to temperature variation, for three different materials; silicon carbide, silicon and titanium. Figure 4.3 shows the variation in temperature for a heating and cooling cycle from room temperature up until a time where the temperature has cooled back down to room temperature for a pulse duration of 140 ns and 43 $J.cm^{-2}$, for the three materials considered. These results can be used to identify at which temperature, or indeed phase, the material will be at when a subsequent pulse strikes in the case of multiple pulse machining.

The theoretical results of the cooling cycle obtained for silicon are of particular interest due to the large difference in absorption coefficient for different phases. For a 140 ns pulse at 43.7 $J.cm^{-2}$, the silicon does not solidify until about 1.7 μs after the end of the pulse. If the repetition rate of the laser used to machine silicon is high enough, then the next pulse will strike when the silicon is still molten. This would mean that the absorption coefficient would in that case be small and thus the laser irradiation would be absorbed only in a thin layer near the surface of the material. If the next pulse arrives after the silicon has reverted back to its solid phase, then the absorption coefficient would be higher and the laser irradiation would be absorbed within a larger depth.

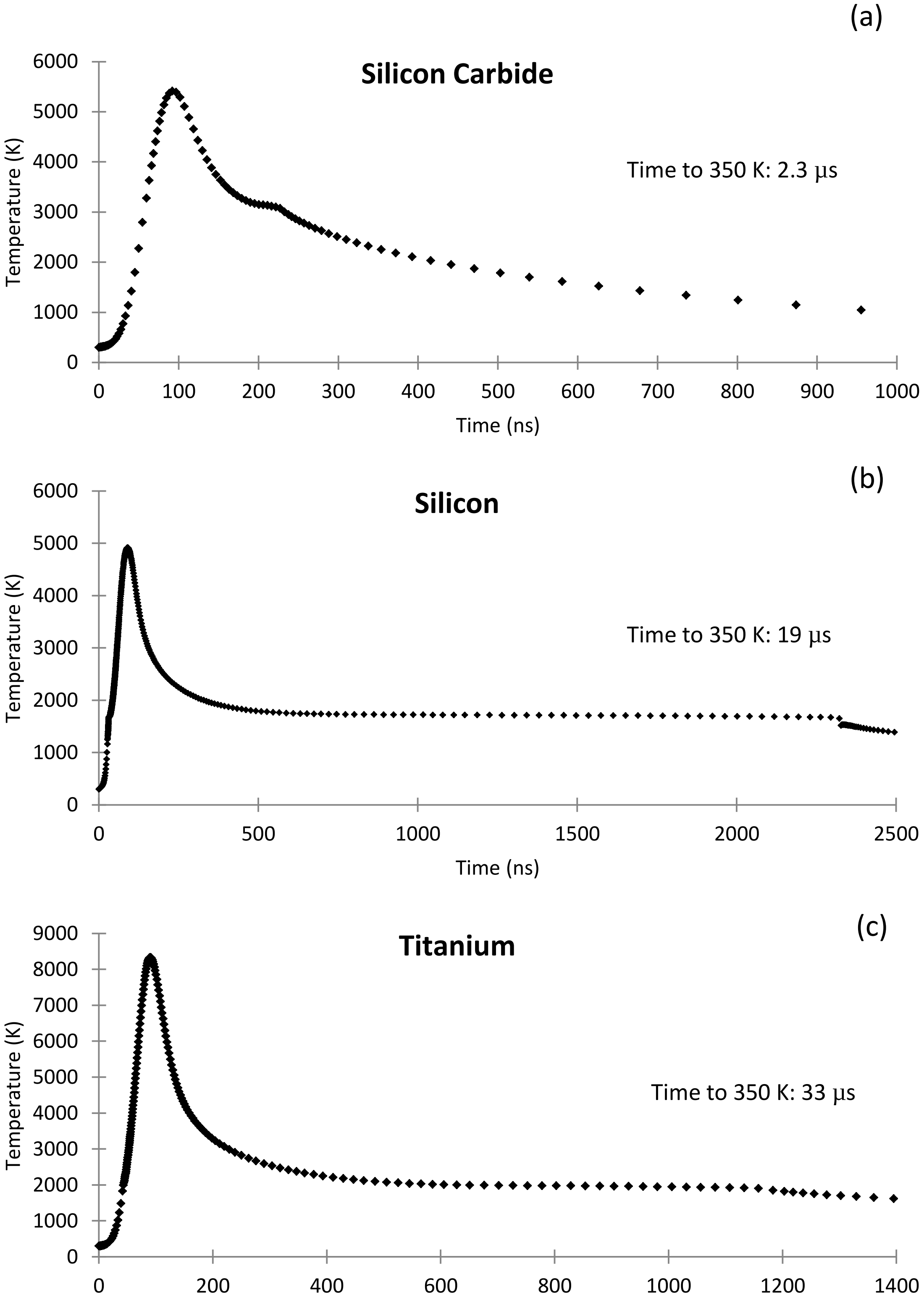

Figure 4.3 Variation of temperature with time for a complete single pulse heating and cooling cycle using a pulse width of 140 ns and at 43.7 J.cm^{-2} for (a) silicon carbide, (b) silicon and (c) titanium.

4.2.2.b Material parameter effects

The differing simulation results for each material when processed at the same fluence and pulse duration (see Figure 4.3), can be attributed to the differences in material parameters as given earlier in Table 4.1. The diffusivity parameter can be used as an indication of how fast a material can conduct heat. A low value of thermal diffusivity represents a restriction to the heat conduction within the substrate (Knopf and Otani 2012). The thermal diffusivity of silicon carbide is higher than that of silicon, which may be the reason for the higher overall temperature reached (i.e. 5500K for SiC and 5000K for Si). Even though the maximum temperature reached in the silicon carbide may still be viewed as similar to that of the silicon, this does not mean that similar amounts of material will be removed. In particular, the melt temperature of silicon carbide is almost twice that of silicon. So although it takes less energy to melt the silicon carbide compared to the silicon due to its lower heat of fusion, it will still take longer to reach the melt temperature of SiC. As mentioned earlier, the optical penetration depth of silicon is large at the beginning of processing, but this value reduces significantly upon its phase change to molten material.

The results obtained for titanium show that it reaches the highest temperature of all three materials at the same fluence and pulse duration. Even though the thermal conductivity of titanium is lower than the other two materials, its density is a lot higher due to its metallic structure. This means heat conducts well although not at the same rate within the same distance. Also, the absorption depth of titanium is smaller than both silicon and silicon carbide causing a more localised heating with the same fluence. Coupled with the lower melt temperature, and the not so large temperature dependence of its thermal properties, titanium displays more efficient heating and a larger temperature rise than silicon and silicon carbide.

4.2.2.c Threshold analysis

Figure 4.4 shows the prediction of temperature variation with time, for different fluence values, and for all the considered materials at a constant pulse duration of 140 ns. From this figure, an insight into the time needed to reach the onset of melting can be gained. It can be seen that an increase in fluence decreases the time taken to reach the melt temperature; which in turn leaves more energy available to aid in the subsequent removal of material. This can be beneficial to material removal but it can also be detrimental if the fluence is high enough to induce a plasma in the plume of vaporised material. In particular, the occurrence of plasma shields the incoming laser radiation from the surface of the material resulting in a loss of machining efficiency (Amoruso, 1999). The residual energy above the melt temperature is of particular significance to silicon due to the significant difference in absorption coefficient above this value. Table 4.2 summarises the predicted threshold fluence values required for the onset of melting and vaporisation for a pulse duration of 140 ns. Silicon carbide has the highest fluence threshold of all three materials with silicon having the lowest. The thermal diffusivity value for titanium is a factor of ten smaller than that for silicon. This larger value of thermal diffusivity for silicon means that it receives and conducts heat faster than the titanium, resulting in a lower energy needed to begin the melting process (Hahn and Necati Ozisik 2012).

The heat conduction mechanisms in conductors and insulators are different. The conductors have electrons that are free to move in the lattice resulting in easier heat conduction than that of insulating materials that have a lack of free electrons to carry heat resulting in heat conduction that is primarily dominated by lattice vibrations (Cooper, 2001). Silicon carbide and silicon are both good insulators but silicon carbide has a large thermal conductivity. The status of insulator is attached to the electronic conduction which can only occur due to the charge carriers. This phenomenon is different to the thermal conduction which can occur due to both charge carriers and the vibrations of the lattice.

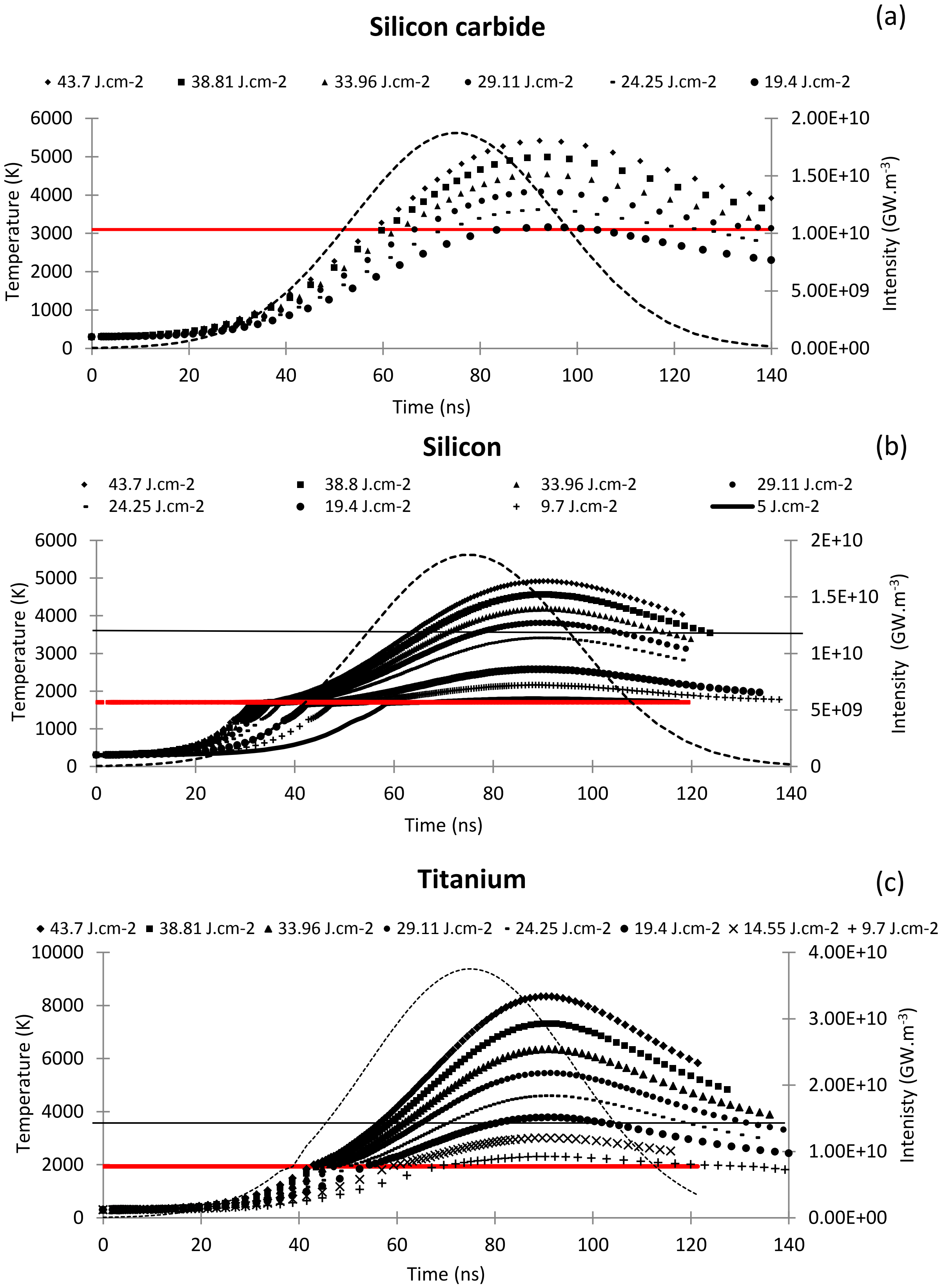

Figure 4.4 Temperature variation with time for varying fluence values and for a constant pulse duration of 140 ns for (a) silicon carbide, (b) silicon and (c) titanium. The horizontal lines are the melt temperature for each material and the vaporisation temperature for titanium and silicon. The dotted curve represents the intensity evolution for the highest fluence in GW.m^{-3}

	Theoretical Melt Threshold	**Theoretical Vaporisation Threshold**
Silicon	5 J.cm^{-2}	24 J.cm^{-2}
Silicon carbide	19 J.cm^{-2}	N/A
Titanium	Just under 9 J.cm^{-2}	19.4 J.cm^{-2}

Table 4.2 Predicted fluence thresholds for reaching melting and onset of vaporisation for all three materials for a pulse duration of 140 ns.

This means that electronic insulators can also be good thermal conductors. Being a good thermal conductor would suggest easier melting compared to insulating materials. This may not be the case though due to the optical penetration of the materials affecting the value of the volumetric intensity which in turn affects the temperature evolution. Silicon carbide has an optical penetration depth larger than that of titanium resulting in a dilution of the same value of laser intensity over a larger area. Coupled with a melt temperature that is a lot higher than titanium, this results in the time taken to reach the melt temperature to be longer for identical processing conditions between titanium and silicon carbide.

The different peak temperature reached with an identical increase in fluence between the considered materials suggests that different removal mechanisms may be present. Silicon carbide experiences a different process for material removal compared to silicon and titanium. In particular, due to the compound nature of the material, the process can include the melting and subsequent vaporisation of the silicon resulting in a carbon-rich surface (Salama et al, 2005). The temperatures predicted for silicon carbide in Figure 4.4 suggest that the craters created above a fluence of around 25 J.cm^{-2} may experience a vaporisation of the molten silicon component because the vaporisation temperature of silicon is 3514 K. At a fluence of around 30 J.cm^{-2}, the carbon component may melt or sublimate, changing phase directly from the solid phase to gas, and both molten material are pressurised by the vaporised components to eject from the crater. This should result in fine debris being deposited around the edges of the craters. If the thermodynamic critical temperature of silicon carbide is taken as the same as that of silicon (5200 K) then the phase explosion of the material is predicted not to take place in the range of fluence values considered. In particular, even though the material reaches this temperature, it is not held for long enough for the critical radius of nucleation bubbles to be reached. More specifically, this critical time was calculated to be around 70 ns for silicon (Lu et al, 2002). The results for titanium indicate that the material experiences melting at a value slightly lower than 9 J.cm^{-2}. The temperature then reaches the vaporisation point at about 19 J.cm^{-2}, suggesting any molten ejection resulting from vapour pressure will be observed above this fluence value. The temperature profiles for silicon also suggest that vaporisation will be present, at a similar fluence of 24 J.cm^{-2}.

4.2.2.d Material removal

A longer time needed to reach the melt temperature leaves less incident laser intensity to affect the material removal after the phase change has begun over the same pulse duration. Titanium, not only has the largest effective laser intensity, but also reaches the melt temperature in less time than the silicon carbide resulting in a higher peak temperature and larger material removal. The ejection of melt is primarily due to the pressure exerted by the vaporised material. For silicon carbide, the vaporisation of the molten silicon begins at around 3500 K which occurs at 60 ns for a fluence of 43.7 J.cm^{-2}. The titanium substrate on the other hand reaches its vaporisation temperature at about 50 ns leaving the majority of the pulse, which has a higher effective intensity originally, for the vaporisation pressure to increase as the temperature continues to rise. This increase in vaporisation pressure causes more volatile melt ejection. Gao et al (2011) determined that the material removal effects in silicon carbide irradiated by a 200 ns 1064 nm fibre laser, with a varying fluence from 11 to 100 J.cm^{-2}, were dominated by surface vaporisation followed by an ejection of the molten silicon. They also concluded that phase explosion was highly unlikely due to the temperatures of the surface not reaching values near the critical temperature of silicon carbide.

The results of the theoretical model can give an insight into the behaviour of the material when subjected to laser interaction. From the results in Figure 4.4, it is suggested that all the materials display different rates of removal as well as removal through different mechanisms. This theoretical model can therefore be used to predict the outcome of machining single pulses with different laser parameters for a variety of materials.

In Figure 4.5, a prediction of the depth and diameter of single pulse craters machined at varying fluence values for a pulse duration of 140 ns is given for all three materials. It is predicted that the

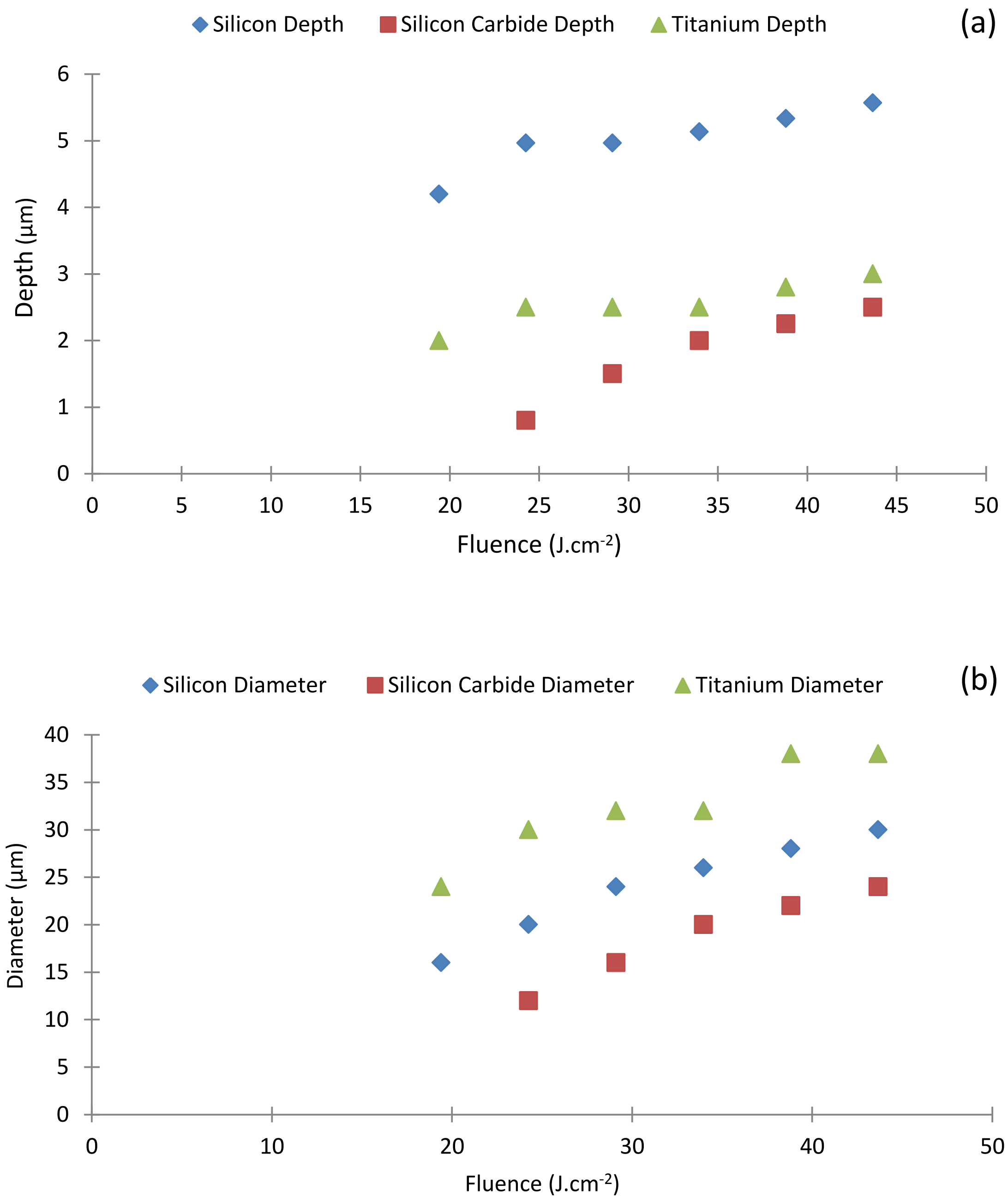

Figure 4.5 Predicted depth (a) and diameter (b) of craters machined at 140 ns pulse duration with varying fluence.

deepest craters are formed with silicon while the shallowest are created on the silicon carbide, whilst the widest craters are formed on the titanium substrate.

Figure 4.6 shows a comparison of the temperature evolution as a function of peak power for a given fluence of 14 J.cm^{-2}. Shorter pulse durations at the same fluence display a larger peak power. Pulses with higher peak power result in more available power above the threshold of removal of the material resulting in a larger processed area. Figure 4.6 predicts that for larger peak powers, the temperature rises higher in a shorter amount of time at the centre of the laser irradiated surface of the substrate. Figure 4.7 shows the temperature rise at the centre of the irradiated surface of titanium for two different pulse durations, 140 ns and 25 ns, at 14 J.cm^{-2}. As it can be seen from the difference in the temperature variation along the surface of the workpiece, the higher peak power at 25 ns (4000 W) compared to 785 W at 140 ns results in larger area above the melt temperature of the material resulting in larger diameter of craters.

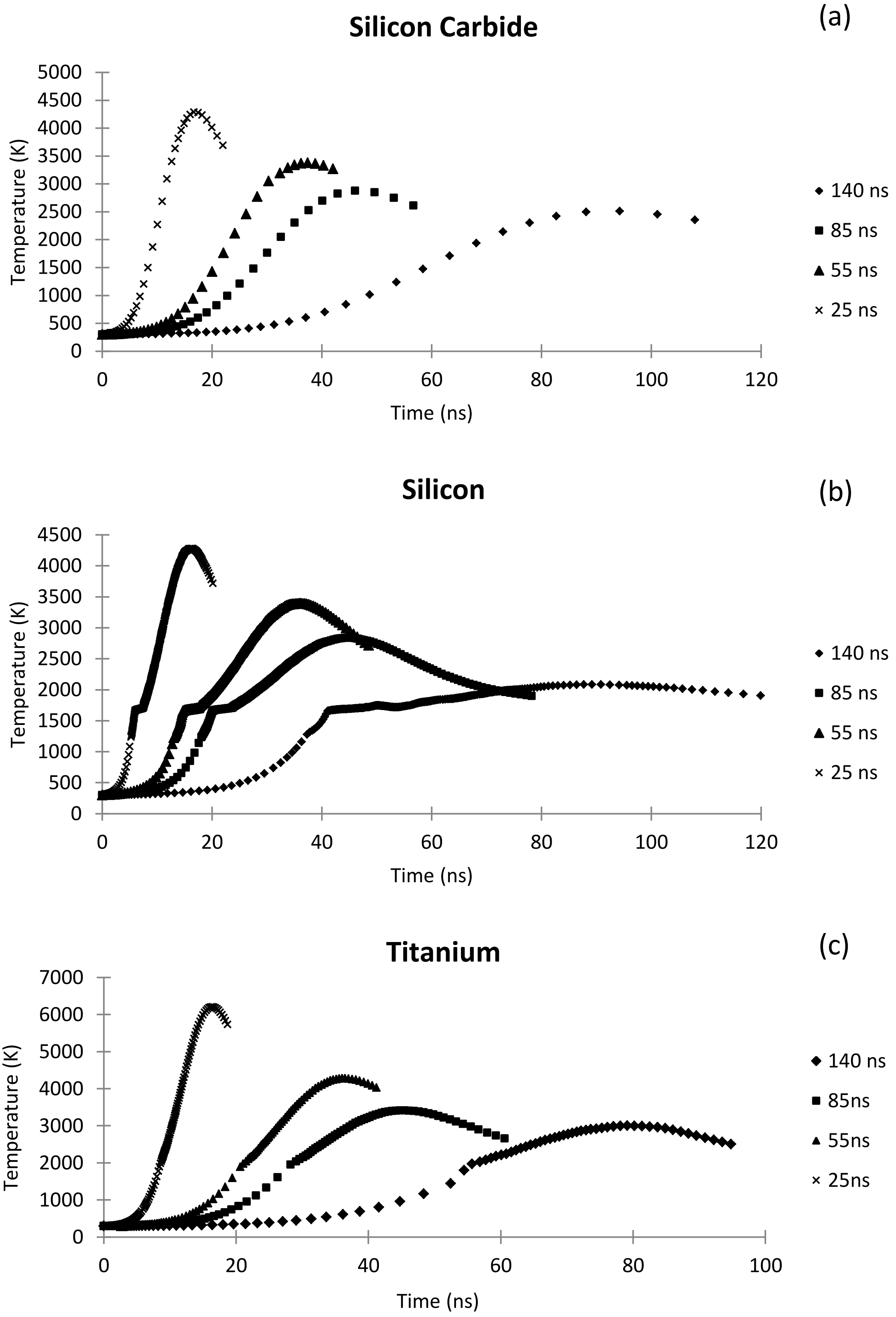

Figure 4.6 Temperature variation with time at 14 J.cm^{-2} at the centre of the substrate for a variety of peak powers for (a) silicon carbide (b) silicon and (c) titanium. The peak power varies with pulse duration according to; 140 ns – 785 W, 85 ns – 1294 W, 55 ns – 2000 W and 25 ns – 4000 W.

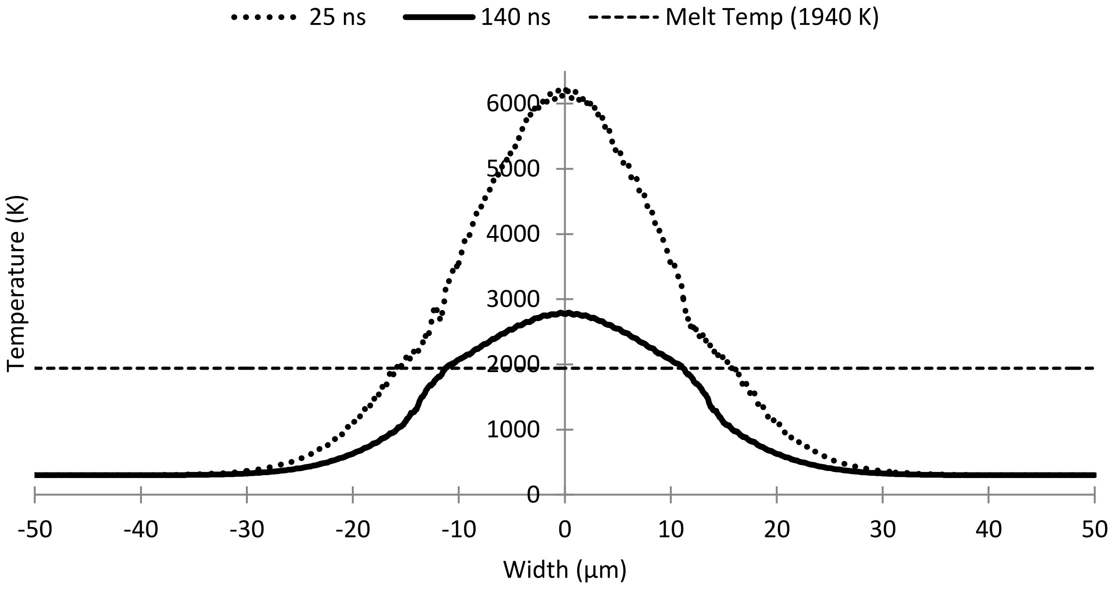

Figure 4.7 Variation of the temperature on the top surface of titanium for a fluence of 14 J.cm^{-2}, and for pulse durations of 140 ns and 25 ns. The higher temperature reached for the shorter pulse duration is a direct consequence of the higher values of peak power resultant at the shorter pulse duration.

4.3 Experimental Study

4.3.1 Methodology

In order to complement and validate the outcomes of the theoretical model reported in the previous section, the effects of three different parameters, namely the fluence, pulse duration and peak power on the laser processing of silicon, silicon carbide and titanium are now presented in this section through the machining of single craters.

Four different pulse durations were used, namely 25 ns, 55 ns, 85 ns and 140 ns at decreasing fluence values for each of them until no processing impact could be seen on the material substrate. The depth and diameter of the machined craters were measured using the White Light Interferometer, while their topography and the resulting material ejection were observed using the Scanning Electron Microscope already utilised for the study reported in Chapter 3. In addition, all material samples were polished using a procedure tailored for each material based on their hardness. The silicon and silicon carbide were categorised as hard materials whilst the titanium was treated as a soft material. Each material was initially levelled using a polishing pad made using tissidium with different grain sizes if categorised as a hard material and zirconia or silicon carbide if the material was soft. After the material samples were levelled, a diamond suspension varying from 9 µm to 1 µm was used with a matching polishing pad to achieve an acceptable surface. The titanium was treated using an additional suspension in order to achieve optimum polishing.

4.3.2 Fluence effect

The first set of results obtained provided the geometrical evolution, consisting of depth and diameter, of the single pulse craters when the fluence of the beam was varied. As an example for the 140 ns pulse duration, Figure 4.8a shows the experimental data for the generated crater depths as a function of the fluence for silicon, titanium and silicon carbide. Figure 4.8b shows the associated experimental data for the crater diameter, as measured with the optical microscope, for all three materials. The results obtained for all pulse durations considered, consistently show that the diameter and depth generally increase with an augmentation of the fluence. As the energy contained within the beam diameter increases, the electrons within the subsystem of the material become more energetic, transferring higher amounts of energy to the material lattice. This energy transfer increases the temperature past the melting point of the material. This elevation in temperature with higher incident energy results in an augmentation in the volume of material removed. This observation is the same for all the materials, the difference being in the geometric values of the craters. The minimum fluence required to initiate crater formation for a 140 ns pulse duration can be calculated for each substrate material. To achieve this, the procedure, as described by Liu (1982) is followed. In particular, the experimental data plotted in Figure 4.9 are fitted to the following equation:

$$D^2 = 2.w_0{}^2.\ln\frac{E}{E_{th}} \tag{4.8}$$

Where w_o is the spot size, E is the fluence and E_{th} is the minimum fluence for generating craters.

In this way, the values for the fluence threshold was calculated to be around 14 J.cm^{-2} for silicon carbide, 12 J.cm^{-2} for titanium and 11 J.cm^{-2} for the silicon substrate. The fluence thresholds reported in literature for these materials appear to be lower than those reported here. For example, Wang et al (2010) reported a threshold of just under 5 J.cm^{-2} for silicon irradiated with an Nd:YAG laser operating at 10 ns, and Duc et al (2013) reported a threshold of just under 8 J.cm^{-2} for silicon carbide using and Nd:YAG laser operating at 6 ns. The differences may be due to different measuring techniques aswell as the much shorter pulse durations used. Vladiou et al (2008) reported a fluence threshold of 4.5 J.cm^{-2} for titanium using an Nd:YAG laser operating at 4.5 ns. The shorter pulse durations and the subsequent larger peak powers may result in a difference in the absorption coefficient of the material. A higher absorption coefficient may lead to a lower value of the threshold fluence. There may also have been a difference in the definition of the threshold, when melting is witnessed on the surface or only when there is damage to the surface. It may also be possible that during this investigation the minimum fluence value used for machining was not low enough to achieve accurate enough values for the threshold from Figure 4.9.

Silicon carbide has the highest fluence threshold of all the materials, and exhibited the smallest craters formed. This is more than likely due to its high melt temperature and the fact that the material removal is dominated by vaporisation rather than melt ejection which is a result of its ceramic nature. The ceramic nature of silicon carbide results in decomposition of the material into different compounds at high temperatures with a recast layer of molten silicon (Gupta 2008). This fact is also supported by SEM images of the craters machined in silicon carbide at high fluence values. In particular, the electron micrographs of craters created at increasing fluence and for a pulse duration of 140 ns for all three materials can be seen in Figures 4.10 i, ii, and iii. As it can be seen in Figures 4.10.iii for silicon carbide, there is a significant lack of debris compared to the craters for the titanium shown in Figure 4.10.ii, suggesting vaporisation is dominant. Although the silicon also presents cleaner craters at high fluence compared to the titanium, melt ejection is a dominant feature at lower fluence unlike for the silicon carbide.

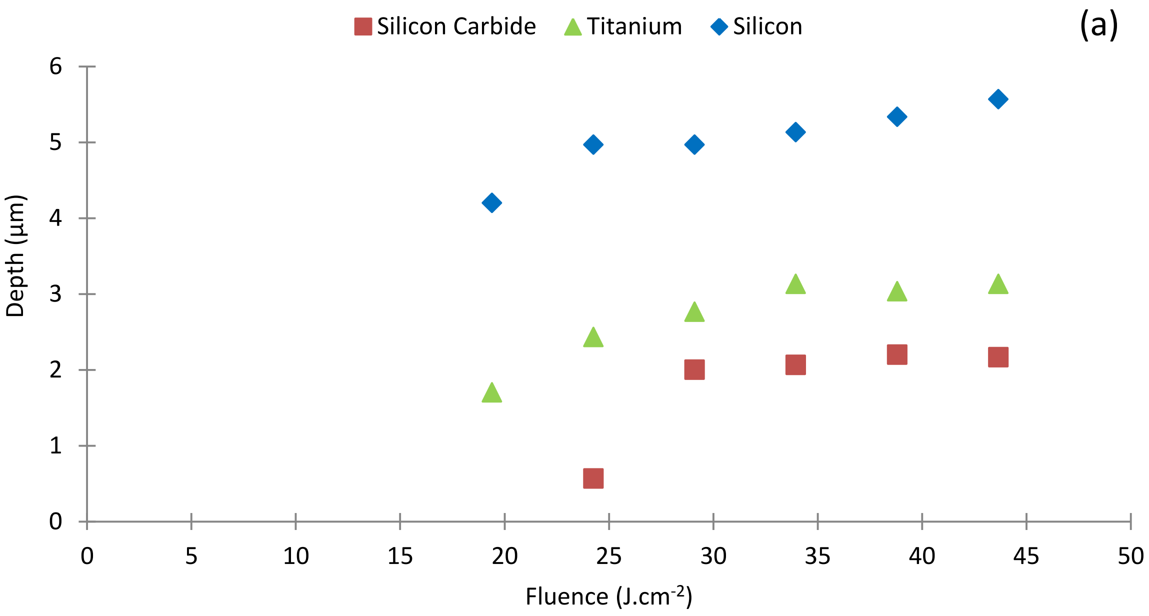

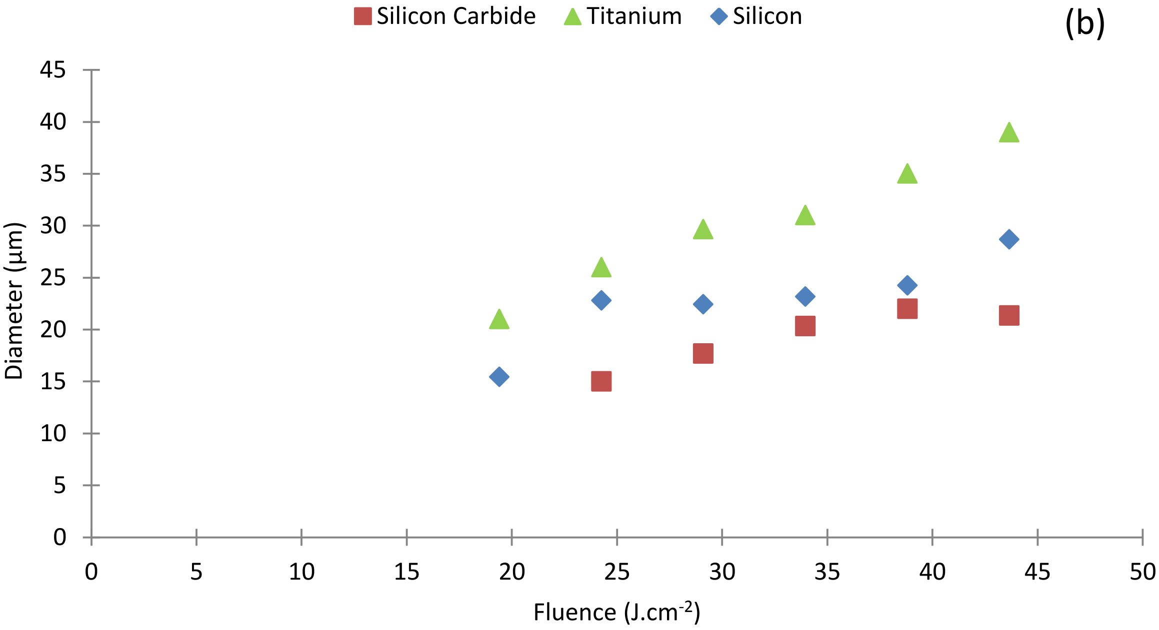

Figure 4.8 a) Depth and (b) diameter variation with fluence for three materials investigated at 140 ns

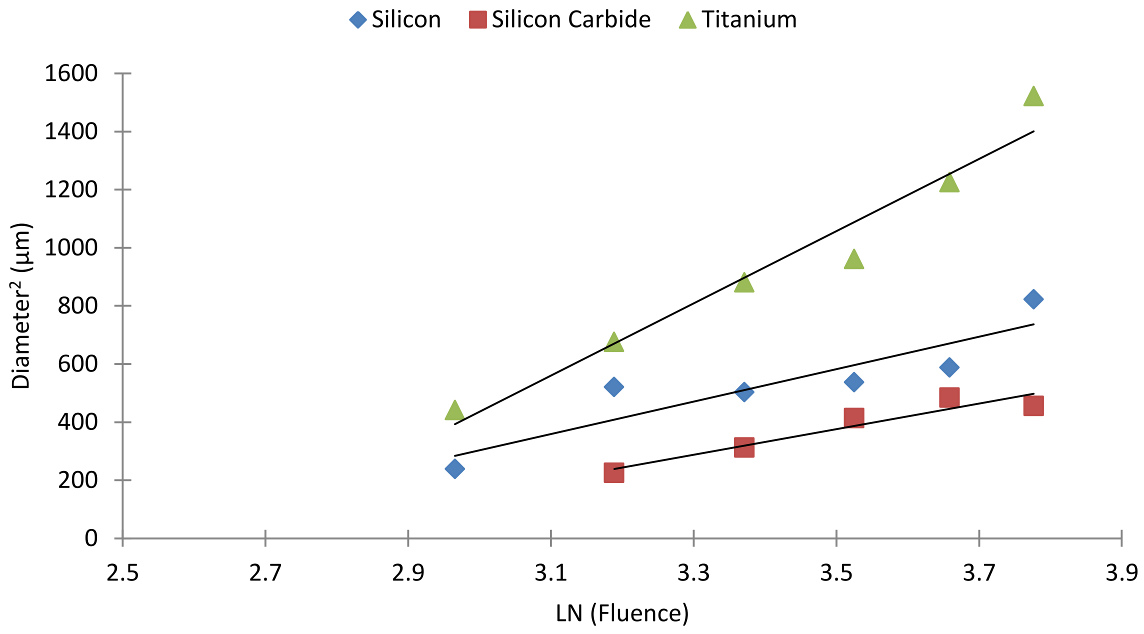

Figure 4.9 Semi-log graph used to determine the threshold for material removal at a pulse duration of 140 ns.

Figure 4.11 shows a comparison between craters obtained at the same fluence of 29.1 J.cm^{-2} for the three materials. The main observation is that the silicon carbide single pulse machining leads to a smaller, cleaner crater. Given that vaporisation is less efficient than melt ejection (Voisey et al 2003) volumetric removal is smaller for the same fluence applied. This observation is supported by the plots already reported with Figure 4.8. More specifically, another difference that can be stated for the silicon carbide, compared to the other two materials, is that the depth and diameter values reach a plateau at the higher fluence values applied. This occurs because vaporisation becomes the dominant mechanism with an increase in fluence and this proves to be a lot less efficient. This saturation is not as pronounced in the results for the other materials.

It should be noted however that because of the excessive melt that has re-solidified around the rim of the metallic craters, measuring the exact diameter is difficult. This could introduce higher uncertainty for the titanium results compared to the silicon carbide for which the defined crater edges are easier to measure.

An observation that can be made for all of the materials investigated is that the material ejection is generally symmetrically deposited around the edges of the crater, especially in the case of the silicon and silicon carbide. This is a result of the high M^2 (<1.3) value of the laser used in the experiments which allows the peak of the laser intensity distribution to be consistently positioned in the centre of the crater allowing the material to be processed in a symmetrical manner with respect to the axis of the laser beam.

Silicon displays the deepest craters between the three materials and also the lowest threshold, 10 J.cm^{-2}. As it can be seen in Table 4.1, silicon has a thermal conductivity almost seven times higher than titanium. This suggests that for a given fluence the heat conducts further into the material resulting in a larger depth removed.

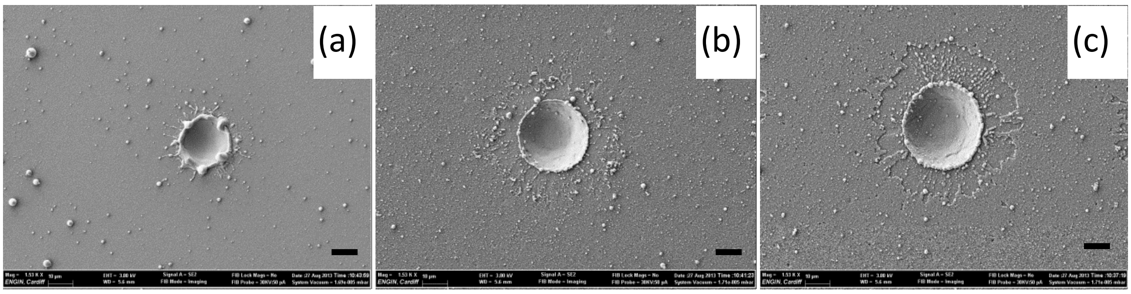

Figure 4.10i SEM images of three single pulse craters machined in silicon at 140 ns and at: (a) 19.4 J.cm^{-2} (b) 29.1 J.cm^{-2} and (c) 43.67 J.cm^{-2}. Scale bar: 10 µm

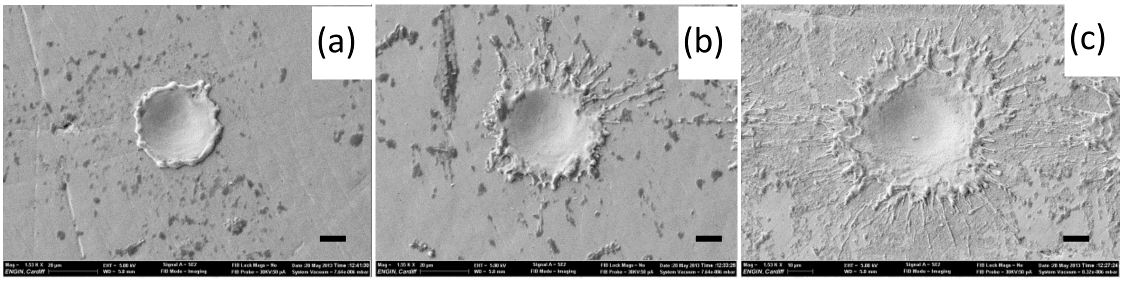

Figure 4.10ii SEM images of three single pulse craters machined in titanium at 140 ns and at: (a) 19.4 J.cm^{-2} (b) 29.1 J.cm^{-2} and (c) 43.67 J.cm^{-2}. Scale bars: 10 µm

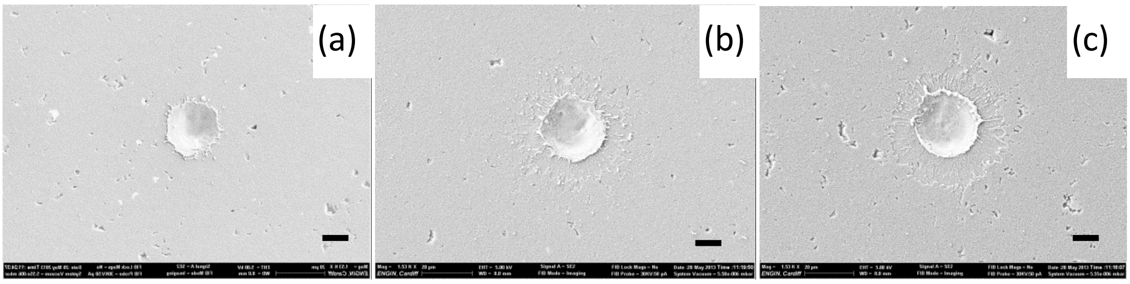

Figure 4.10.iii SEM images of three single pulse craters machined in silicon carbide at 140 ns and at: (a) 24.26 J.cm^{-2} (b) 33.96 J.cm^{-2} and (c) 43.67 J.cm^{-2}. Scale bars: 10 µm

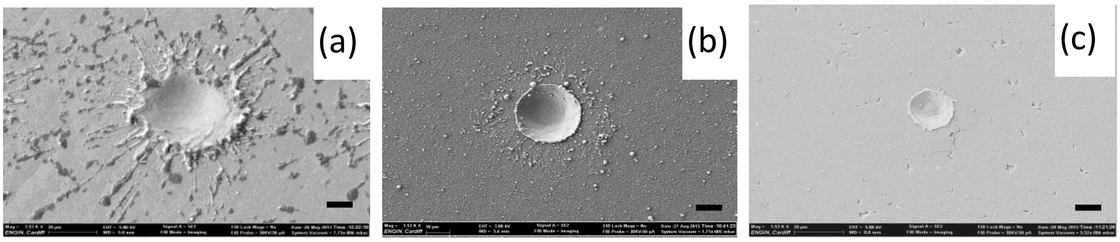

Figure 4.11 SEM images of three single pulse craters machined at 140 ns with the same fluence 29.1 J.cm^{-2} for (a) titanium (b) silicon and (c) silicon carbide. Scale bars: 10 µm

The optical penetration depth of silicon at varying temperatures has been the subject of many publications due to the large decrease that occurs when the silicon reaches the melt temperature. When silicon undergoes a phase change from solid to liquid, the optical penetration becomes that of a metal rather than the value associated with the original semiconductor. A phase change of this nature results in a larger concentration of phonon population causing an increase in the likelyhood of electron phonon interactions, hence an increase in absorption. This results in the laser irradiation being absorbed in a much smaller volume which raises the temperature to higher values. At higher fluence, the diameter increase becomes less pronounced. This change is most likely due to the mechanism of material removal becoming dominated by vaporisation rather than melt ejection, as stated previously in this thesis.

Titanium resides in the middle of the three materials for the depth of the craters but has the largest diameter removed for all the materials used for experimentation. From the SEM images shown in Figure 4.10, laser machining of titanium results in craters which display more melt ejection in the form of splashes around its rim. Compared to the semiconductor materials, this material displays the least clean removal, especially at high fluence. Having a low thermal conductivity compared to the other two materials, the heating due to the laser beam is more localised close to the surface of the material, aided by the easier heat conduction of the closely packed electrons apparent in the metallic structure. At the same fluence, of 29.1 J.cm^{-2} between all materials, Figure 4.11 shows that the ejection of melt around the edges of the titanium craters is still apparent whereas the silicon and silicon carbide are displaying craters with cleaner edges and insignificant melt re-solidified. Metal removal mechanism as apparent from the SEM images for titanium in Figure 4.10.ii (a) suggests that at a low fluence, the material has melted and hydrodynamic motion of the liquid material crates a crater with an edge of re-solidified material. As the fluence increases, the molten material reaches the vaporisation temperature and the material will be ejected through the effect of the vapour pressure, increasing in volatility as the pressure increases with an augmentation in temperature (see Figure 4.10.ii (b)). As the fluence increases further, a second material ejection may occur due to the effect of subsurface heating of a layer underneath the original molten material. This phenomenon presents itself as a second wave of re-solidified material within the craters as seen in Figure 4.10.ii(c).

The removal mechanism apparent in silicon follows the same pattern as the titanium at the beginning, with the material melting and droplets being ejected due to vapour pressure and then solidifying around the edges (see Figure 4.10.i (a)). The droplets are large compared to those for titanium, possibly as a result of the thicker melt layer formed due to the longer penetration depth apparent at 1064 nm. Unlike the titanium, this process does not develop into volatile melt ejection as the fluence increases. The droplets actually decrease in size and the debris around the edges of the craters becomes finer suggesting the dominance of vaporisation as a removal mechanism at higher fluence (see Figure 4.10.i (b)). The temperature dependence of the optical properties of silicon is important and upon reaching the melting point, this results in drastic changes to both the reflectivity and the penetration depth of the material. The shortening of the penetration depth as the material melts leads to further heat conduction being limited to a thin layer near the surface of the material. This results in the vaporisation temperature being reached more quickly due to more localised heating and as a consequence the process becomes dominated by vaporisation with limited melt ejection (Figure 4.10.i (c)).

4.3.3 Pulse duration effect

The second set of results focuses on the effect of varying the pulse duration and pulse shape on the material response. As mentioned earlier, the laser system used allows the ability to choose pulse durations from 15 ns to 220 ns. These varying pulse durations form different pulse shapes over time, with the longer pulses exhibiting a fast rise time over the first part of the pulse with a tail of lower energy prominent for the remainder of the pulse. When using these pulses to machine, the variation in shape may have an effect on the resulting crater shape. The difference in pulse shapes for the laser system utilised in this research can be seen in Figure 3.1, section 3.2.1.

Figures 4.12 and 4.13 show the depth and diameter variation, with fluence, for a range of pulse durations for all three materials. As the fluence increases, both the diameter and the depth display an augmentation at a single pulse duration. In addition, for a given fluence value, the depth of the craters generally tends to increase with the augmentation of the pulse duration. The longer pulse durations result in deeper thermal penetration due to the relationship:

$$l_t \approx 2\sqrt{D\tau} \qquad (4.9)$$

Where l_t is the thermal penetration depth in m, D is the diffusivity expressed in m.s^{-1} and τ is the pulse duration in s. The deeper thermal penetration experienced at longer pulse durations results in a deeper crater being formed. Also, as seen in Figure 3.1, the longer pulses have an added tail of reduced energy after the initial fast-rise. This extra tail aids in the removal of material from the crater by slowing down the cooling rate of the material.

SEM images are given in Figure 4.14 i, ii and iii, of craters machined at the same fluence but differing pulse durations for silicon, silicon carbide and titanium. These suggest that the longer pulses are more suited for processes that require higher removal rates but where the quality is not as important. On the other hand, processes that require precise material removal and negligible debris need shorter pulse durations. The largest variation in the crater morphology is seen for the titanium. The crater shapes for silicon carbide and silicon have smaller variation between pulse durations, largely due to the lack of melt that occurs because of the ceramic response to laser irradiation and the vaporisation dominated mechanism.

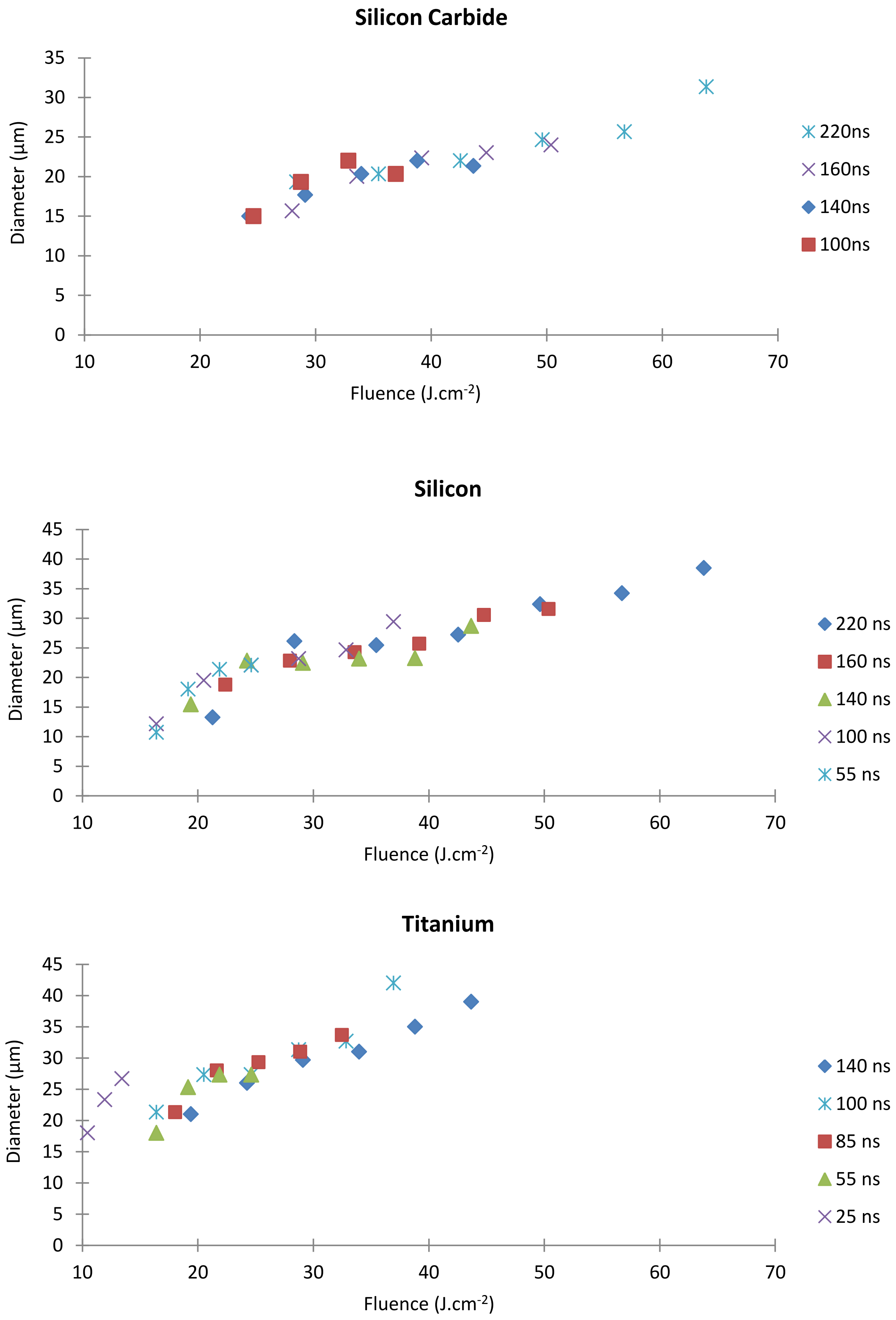

Figure 4.12 Crater diameter variation with fluence for varying pulse durations for a) silicon carbide, b) silicon and c) titanium

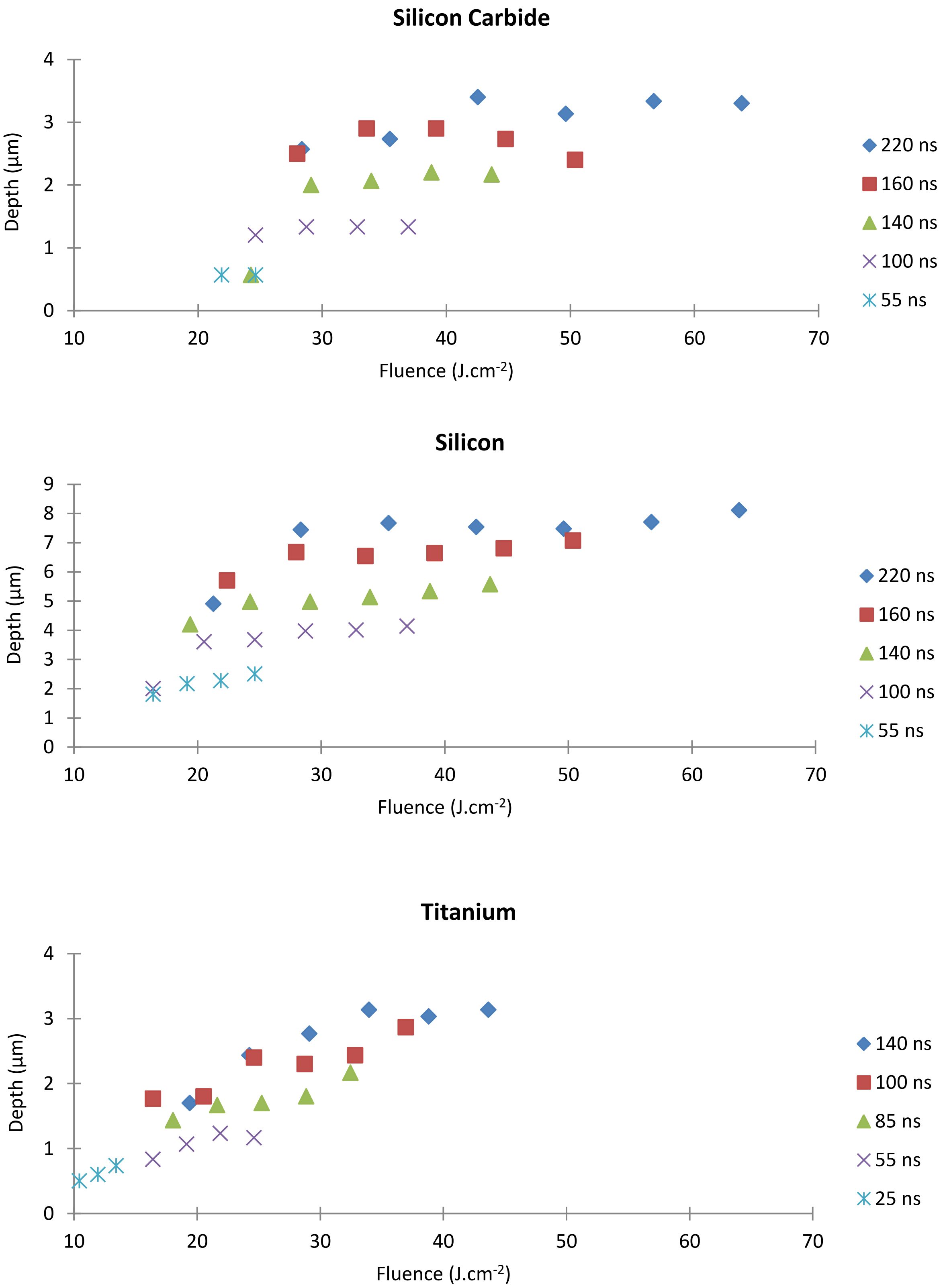

Figure 4.13 Crater depth variation with fluence for varying pulse durations for all a) silicon carbide, b) silicon and c) titanium

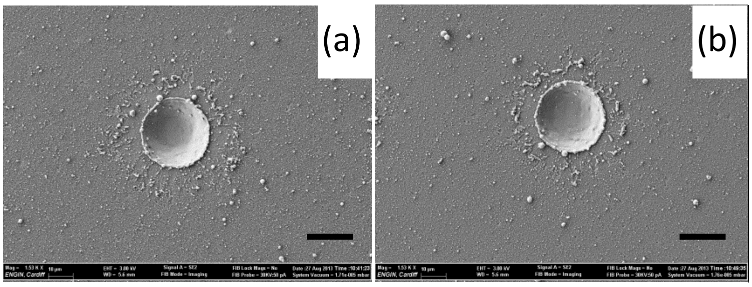

Figure 4.14.i Craters machined in silicon at 29 J.cm^{-2} and for a pulse duration of a) 140 ns and b) 100 ns. Scale bars: 20 µm

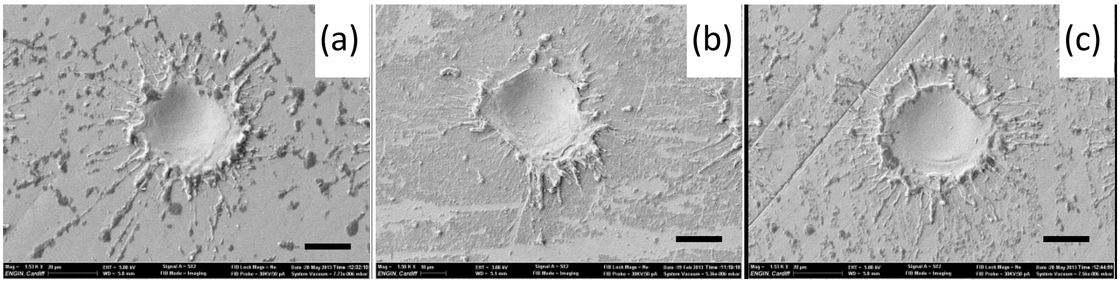

Figure 4.14.ii Craters machined in titanium at 29 J.cm^{-2} and for a pulse duration of a) 140 ns b) 100 ns and c) 85 ns. Scale bars: 20 µm

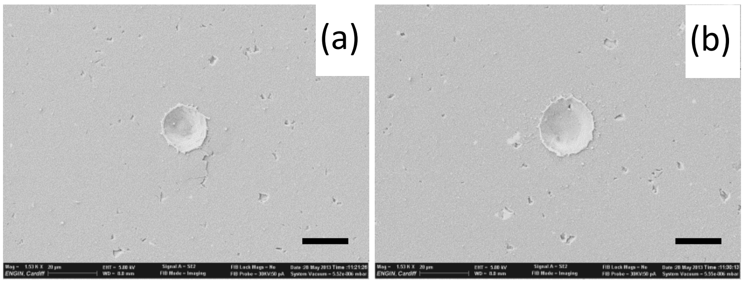

Figure 4.14.iii Craters machined in silicon carbide at 29 J.cm^{-2} and for a pulse duration of a) 140 ns and b) 100 ns. Scale bars: 20 µm

4.3.4 Peak power effect

For a constant energy delivered, different pulse durations exhibit different peak powers according to:

$$Peak\ Power = \frac{Energy}{Pulse\ Duration} \tag{4.10}$$

The graph shown in Figure 4.15 indicates that increasing the pulse duration results in a lower peak power for the same value of fluence. This change in peak power affects the thermal and thus, the geometrical and topographical response of the material. This effect can be seen experimentally with the results shown in Figure 4.16 for the diameter and depth variation at constant fluence with varying pulse duration. In particular, the diameters of the generated craters tend to decrease with a decrease in peak power. On the other hand, the results also indicate that an increase in peak power results in a decrease in depth. This suggests that variation in pulse duration drives the obtained crater depth while peak power variations drive the mechanism of removal. In order to support this statement SEM images are shown in Figure 4.17, 4.18 and 4.19 at varying peak powers for silicon, silicon carbide and titanium, respectively.

As it can be seen from the images, a higher peak power, at shorter pulse durations, result in larger diameters for the single pulse craters. At lower peak powers, there is less power available above the removal threshold to be used for ablation. In addition, because the power is defined as the rate of energy per second, it means that at higher peak powers, the energy is being delivered at a higher rate. Due to this variation in energy delivery and power above the removal threshold, different removal mechanisms take place for various peak powers for example, in the silicon substrate. At higher peak powers, the material removal is dominated by vaporisation and the resulting crater is clean but has a low removal rate due to the decrease in depth. Lower peak powers result in limited removal due to the low amount of power available above the removal threshold of the material. Identifying the machining regimes where different mechanisms occur can be useful when completing certain types of machining operations, such as polishing, where only melting of a thin layer is needed.

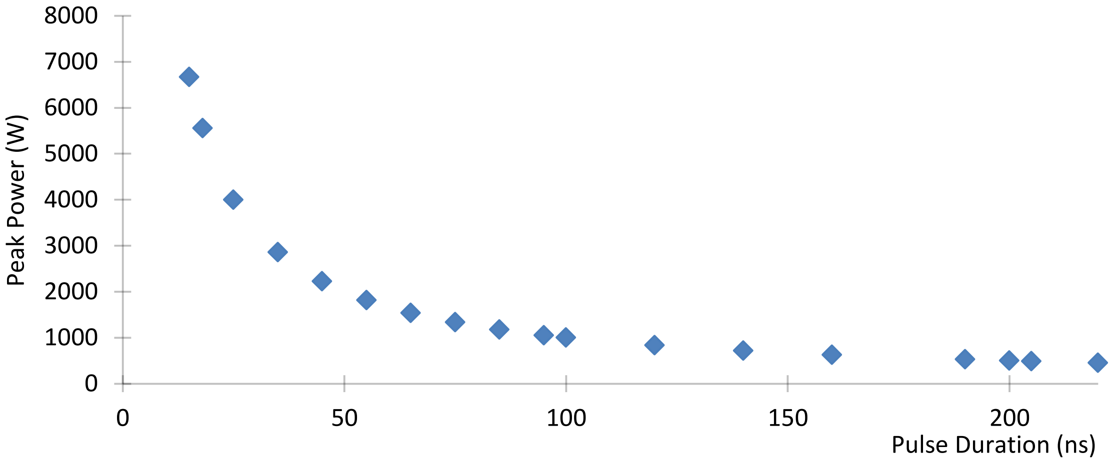

Figure 4.15 Variation in peak power with increasing pulse duration at 0.1 mJ

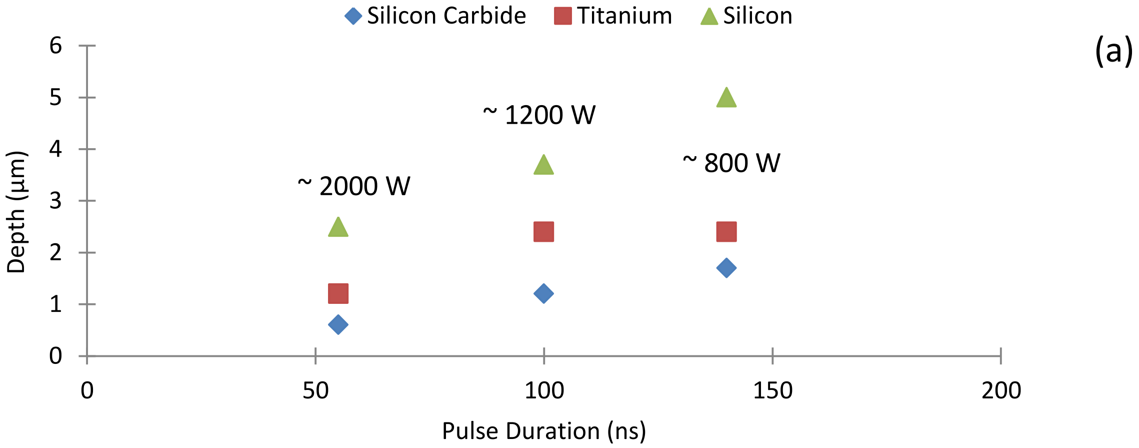

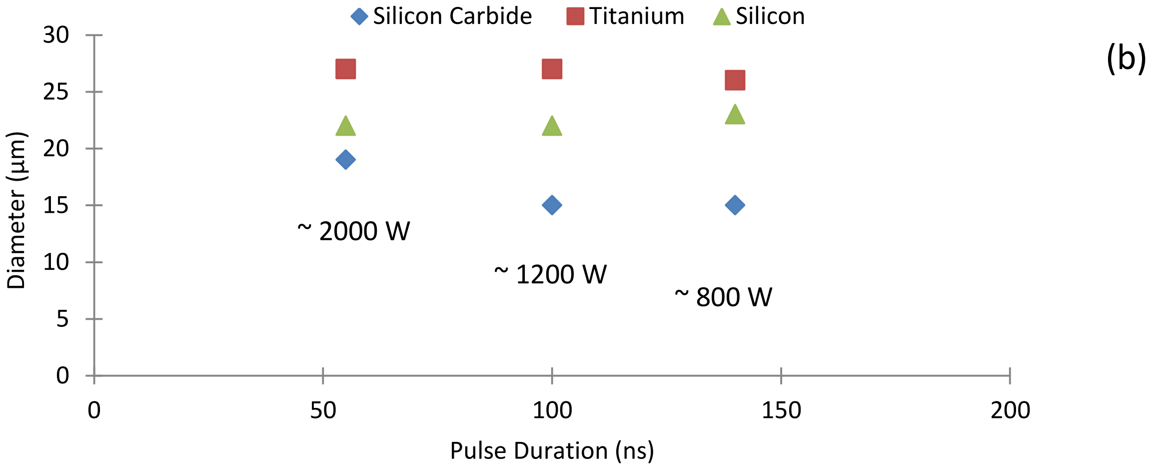

Figure 4.16 Variation of the (a) depth and (b) diameter with pulse duration for silicon carbide, silicon and titanium 24 J.cm^{-2}. The peak powers for each pulse duration are indicated as 2000 W for 55 ns, 1200 W for 100 ns and 800 W for 140 ns.

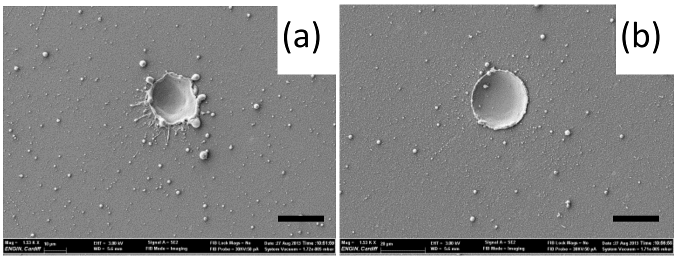

Figure 4.17 SEM images of single pulse craters machined in silicon at (a) 1.6 kW for 100 ns and (b) 3.2 kW for 55 ns. Scale bars: 20 µm

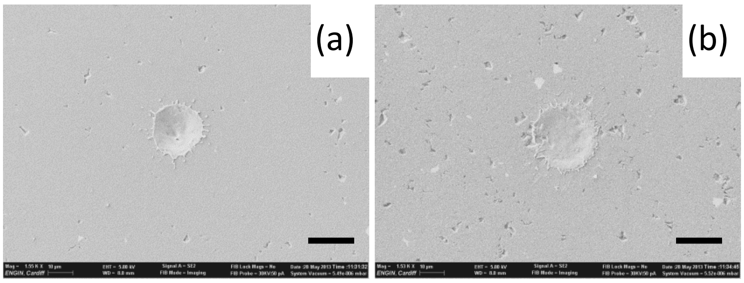

Figure 4.18 SEM images of single pulse craters machined in silicon carbide at (a) 1.98 kW for 100 ns and (b) 3.6 kW for 55 ns. Scale bars: 20 µm

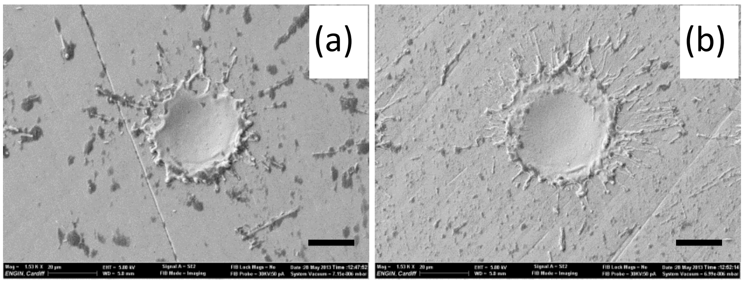

Figure 4.19 SEM images of single pulse craters machined in titanium at (a) 2.2 kW for 85 ns and (b) 3.5 kW for 55 ns. Scale bars: 20 µm

4.4 Comparison of theoretical and experimental investigations

Through the use of a theoretical model, predictions were made with respect to the melting thresholds i.e the minimum fluence required to induce melting for silicon, silicon carbide and titanium. Table 4.3 shows the comparison of the theoretical and experimental values obtained for the melting threshold for a given pulse duration of 140 ns.

The threshold for silicon carbide is the highest, more than likely due to the high melt temperature. The differences could be due to an abundance of melt ejection around the edges of some craters making them difficult to measure accurately as well as possible inaccuracy of values for thermal and optical parameters used in the theoretical model. The largest discrepancy between theory and experimentation is seen in the comparison of the results for silicon. This could be due to the slightly different modelling approach used for silicon due to the large dependency of its optical penetration depth on the temperature. Further work would be required to identify the source of this disagreement.

Predictions can also be made from the theoretical temperature profiles with regards to the generation of debris around the craters machined. For silicon carbide the vaporisation of silicon, melting of carbon and subsequent material removal was predicted to begin at above 30 J.cm^{-2}. SEM images of the crater generated at this fluence and above it are shown in Figure 4.20. As can be seen from these images, above 30 J.cm^{-2} there is a significant increase in ejected debris around the edges of the craters. This suggests that the model is correct in predicting that the molten material within the crater is ejected via pressure from the vaporised component of the silicon. The same comparison can be made for the titanium.

	Experimental Threshold	**Theoretical Threshold**
Silicon	11 J.cm^{-2}	5 J.cm^{-2}
Silicon carbide	14 J.cm^{-2}	19 J.cm^{-2}
Titanium	12 J.cm^{-2}	10 J.cm^{-2}

Table 4.3 Comparison of theoretical melting threshold predictions and those calculated experimentally for all three materials machined at 140 ns.

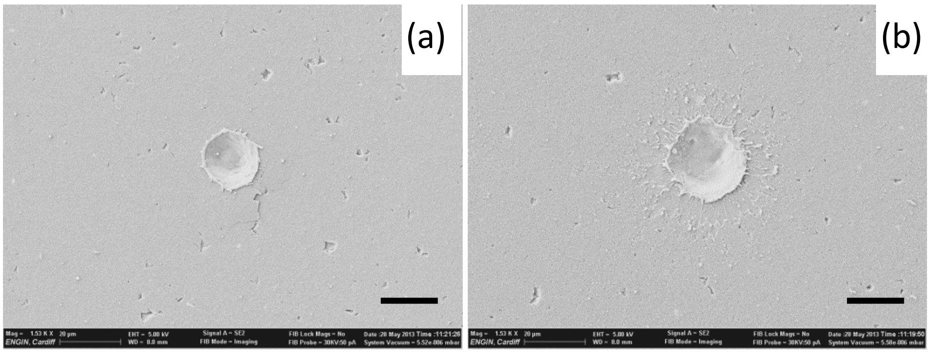

Figure 4.20 Craters machined at a pulse duration of 140 ns at a fluence of (a) 30 J.cm^{-2} and (b) 34 J.cm^{-2} in silicon carbide. Scale bars: 20 µm

It was predicted that at values of fluence above 19 J.cm^{-2}, vaporisation would start occurring and thus, that further fluence increases would cause sufficient pressure to eject molten material around the edges of the craters (c.f Figure 4.4). Figure 4.21 which shows the SEM images of craters obtained at this fluence and above, supports this prediction.

Table 4.4 summarises the average percentage differences obtained between the experimental values and the theoretical predictions for the diameter and depth of the single pulse craters for all three materials machined with a range of pulse durations. It can be seen that the experimental and theoretical values, in most cases, agree well, with only a few instances where the difference is over 10%. Considering the vast amount of pulses machined and the natural variation in the material removal through melt flow and the vaporisation process, the range of percentage differences is considered to be relatively small.

Not only could experimental measurement errors result in discrepancies, but inaccuracies in the theoretical modelling could also be a factor. For example, the vaporisation of the material was not accounted for in this particular model. This could result in larger disagreement at higher temperatures. Another issue may occur, not in the theory of the model itself, but in the data used for the thermal and optical properties. The properties for titanium are relatively well known which reduces the risk of inaccuracies becoming inherent in the model. The large variation in the thermal properties of silicon, especially its optical properties, can cause discrepancies.

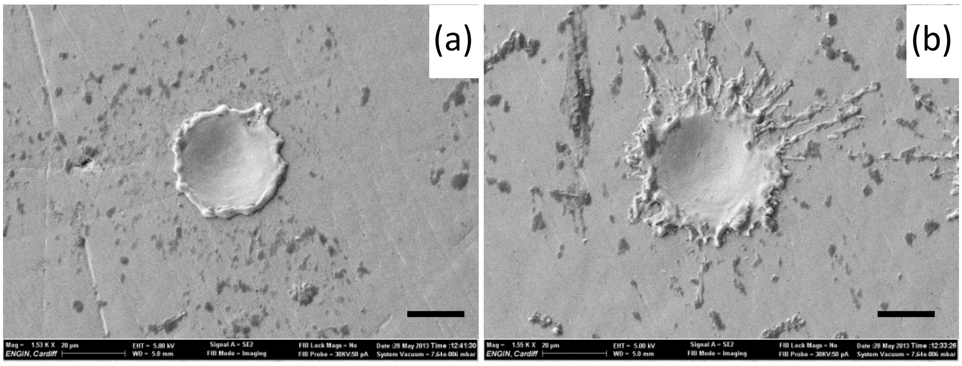

Figure 4.21 Craters machined at a pulse duration of 140 ns and a fluence of (a) 19.4 J.cm^{-2}and (b) 24 J.cm^{-2} in titanium. Scale bars: 20 µm

Pulse duration (ns)	**Average difference (%)**	
	Crater diameter	**Crater depth**
	Silicon	
140	9.2	6.0
100	4.8	8.2
55	6.0	6.8
	Silicon carbide	
190	1.6	7.1
140	9.6	16.3
100	14.6	22.0
	Titanium	
140	7.8	2.5
100	8.2	14.6
85	6.3	9.2
55	8.4	13.9

Table 4.4 Average percentage difference between the theoretical and experimental values for silicon, silicon carbide and titanium.

4.4 Summary

In this chapter, a theoretical model was developed in order to investigate the response of three engineering materials to laser irradiation. The model was able to predict the temperature variation with time as well as over a specified space within the substrate. For all three materials; silicon, silicon carbide and titanium, a full heating and cooling cycle was shown which predicted a higher temperature reached for titanium compared to the other materials. This result can be attributed to the difference in material parameters, namely the optical absorption coefficient and the thermal conductivity. A second result reported from the implementation of the theoretical model was the variation of the temperature with time for different fluence values. From the graphs presented, where possible, threshold values for melting and vaporisation were identified as well as an insight into the laser material interaction process. The theoretical model also gave the ability to predict the geometries of resulting craters. Being able to predict removal geometries as well as the interaction regimes, gives the ability to estimate the outcome of actual machining which aids in reducing the unnecessary waste of resources in pre trial tests. For example, the theoretical results predicted that the laser would remove comparable amounts of material for the titanium and the silicon. The difference being that the temperature profiles for the titanium predicted a shift into the vaporisation domain resulting in the, possibly volatile, ejection of molten material.

During this investigation, the three materials considered were also subjected to experimental laser irradiation at varying parameters with respect to the fluence and pulse duration used. The laser system machined single pulse craters which allowed the study of the laser material interaction without the effect inherent to multiple pulses, such as heat accumulation and molten deposits, which occur during laser milling as reported in Chapter 3.

The first set of experimental results showed the effect of fluence variation on the geometry and topography of the machined craters. The data indicated that an increase in fluence causes an augmentation in both diameter and depth of the craters, a conclusion which is consistent for all materials studied. The increase in fluence also causes a difference in the topography outcome of the craters. As the fluence is increases, this results in less clean crater edges with more prominent melt ejection around the rim, as a result of the increased pressure from the vaporisation of the molten material. The second parameter investigated was the pulse duration. The results indicate that longer pulses cause deeper craters to be machined, an observation related to the increase in the depth of heat conduction obtained at longer pulses. At constant fluence, a decrease in pulse duration causes an increase in crater diameter. This has been attributed to the higher peak powers apparent at shorter pulse durations which results in a larger amount of energy available above the threshold of removal for the material. The study into the peak power effects revealed that the fluence appears to drive the amount of material removed, whilst the peak powers appears to drive the removal mechanism.

In the context of industrial processes, the conclusion reached suggests that for machining processes that require large removal rates and where the crater quality is not an issue are suitable for long pulses with high fluence. On the other hand, high-quality machining requires the use of shorter pulses, where the removal rates are lower but the high peak power results in vaporisation driven material removal with less debris. Of the three materials studied, silicon carbide resulted in the cleanest material removal. This occurred due to the ceramic nature of silicon carbide causing direct phase change from solid to vapour with little or no solid-liquid phase change and its associated debris. Silicon also produced craters without significant debris around the edges but only at elevated fluence. The depth of removal for the silicon is the highest of all three materials, possibly due to the large penetration depth apparent before the melt temperature is reached. The titanium processing produced craters that displayed excessive re-solidified melt around the edges.

A comparison of the theoretical and experimental investigations was conducted in the final part of the chapter. The predictions from the theoretical model for the onset of melting and vaporisation were in agreement with the subsequent SEM images obtained from the experimental investigations. The geometries predicted with the theoretical model agreed well with the experimental measurements, over a variety of pulse durations and materials. The possible reasons for the discrepancies were discussed.

Figure 4.22 (a), (b) and (c), display graphs that summarise the data collected throughout this chapter for silicon, silicon carbide and titanium respectively. These graphs show how the results from the single pulse laser machining can be used in an attempt to identify machining regimes for a specified pulse duration. In particular, for the three materials investigated in this chapter, the graphs enable a direct comparison of the removal per pulse in μm^3, the peak temperature reached at each data point and the surface topography of the crater for a pulse duration of 140 ns, enabling a choice of fluence depending on the desired machining outcome.

Further work can be carried out to incorporate other material removal effects into the theoretical model, as well as the shielding effect created by the ionization of vaporised molecules above the surface of the material. This will increase the accuracy of the model at high fluence values. It is also necessary to be able to verify the thermal properties of each material studied over a large temperature range for the model to be able to achieve higher accuracy. Due to the nature of the model, it can be used to predict the laser material interaction of many different types of material over a variety of parametric ranges.

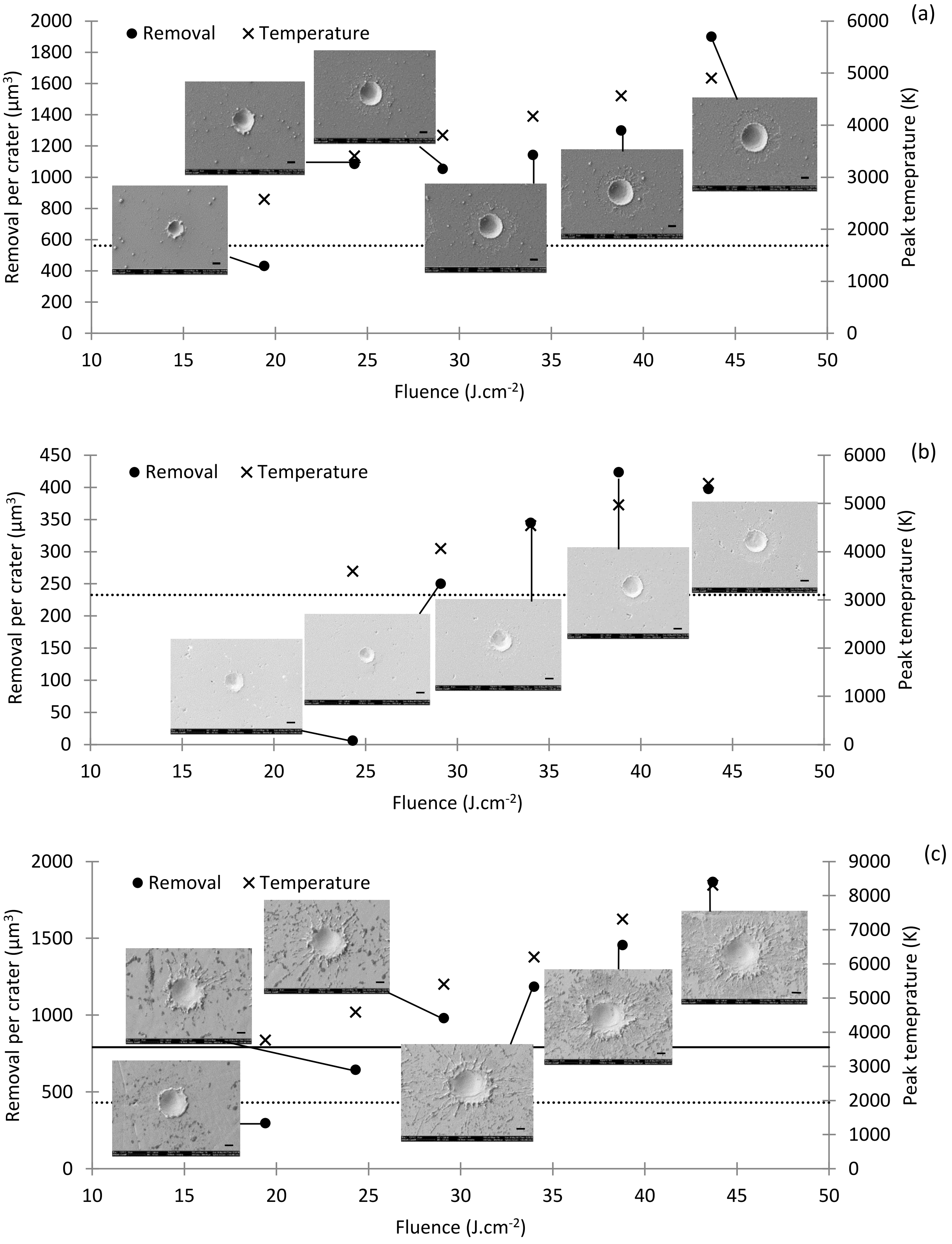

Figure 4.22 Removal per crater and the peak temperature for a variation in the fluence value, and the corresponding SEM images for, a) silicon, b) silicon carbide and c) titanium. The dashed horizontal line represents the melt temperature and the solid horizontal line represents the vaporisation temperature. Scale bars: 10 µm

Nanosecond laser machining of $Zr_{41.2}Ti_{13.8}Cu_{12.5}Ni_{10.0}Be_{22.5}$

5.1 Introduction

The literature review presented in Chapter 2 reported a number of investigations into the micro and nano structuring of BMGs, revealing that very little attention has generally been paid to the study of the single pulse nanosecond laser processing of BMGs. This is in spite of the fact that the topographical analysis of single pulse craters is beneficial for developing a better understanding of laser ablation phenomena over a range of applied process parameters. The research in Chapter 4 produced results that support the use of single pulses to aid in the understanding of the laser material interaction process for a variety of material types, both experimentally and theoretically. In particular, such an approach can provide important insights with respect to the different thermal phenomena taking place during laser processing such as melt ejection and vaporisation. In this context, the first objective of this chapter is to study the single pulse machining of $Zr_{41.2}Ti_{13.8}Cu_{12.5}Ni_{10.0}Be_{22.5}$, also known as Vitreloy 1, which is arguably the most popular type of BMGs, with the ns fibre laser utilised in this PhD study. The results of this investigation are presented in section 5.2. In particular, the generated craters are studied with reference to the variations in pulse energy, pulse duration and peak power. Following this, a theoretical study of single pulse processing, which also includes a comparison between the experimental and predicted results is presented in section 5.3. The second objective of this chapter is to investigate the crystallisation behaviour of Vitreloy 1 as a function of changing process parameters in order to contribute towards a better understanding of the crystallisation behaviour of bulk metallic glasses at the ultra high heating and cooling rates inherent to nanosecond laser ablation. To achieve this, the response of Vitreloy 1 to multiple, moving pulses, with specific attention paid to the crystallisation of the material is discussed in section 5.4 by combining both experimental and theoretical data.

5.2 Experimental observation of single pulse machining of $Zr_{41.2}Ti_{13.8}Cu_{12.5}Ni_{10}Be_{22.5}$

5.2.1 Experimental set up

As described in the previous chapter, the laser system used was equipped with a 20W fibre laser from SPI Lasers and allowed the precise tuning of the delivered pulses to generate waveforms at varying lengths. In particular, four different pulse durations were used, namely 25 ns, 55 ns, 85 ns and 140 ns at a number of decreasing fluence values until no topographical change could be observed on the BMG substrate. These experiments were conducted in ambient air and the focussed spot size (beam radius at $1e^{-2}$) was estimated to be 32 µm, as calculated by the method presented in Chapter 4. As with the previous chapter, the depth and diameter of the machined craters were measured using White Light Interferometery, while their topography and the resulting material ejection were observed using a Scanning Electron Microscope. The Vitreloy 1 material was purchased as a rod and cut into 3 mm thick disks using micro wire electro discharge machining. The optical and thermal properties of Vitreloy 1 are given in Table 5.1. Prior to the laser processing operations, the BMG samples utilised were polished using a procedure tailored for hard materials and their atomic structure was observed using X-ray diffraction (XRD) equipment (Bruker Discover d8, Bruker) using Cukα radiation.

Parameter	**Value**	**Reference**
Density (kg.m^{-3})	6100	Schroers et al 1999
Specific Heat Capacity (J.kg^{-1}K^{-1})	(1/M).(24.9+0.0075T+8.17e^{-6}/T^{2})	Demetriou and Johnson 2004
Thermal Conductivity (W.m^{-1}K^{-1})	0.0163T + 0.84	Demetriou and Johnson 2004
Molar Mass (kg.mole^{-1})	0.0603	Demetriou and Johnson 2004
Latent Heat of Fusion (J.(moleK)$^{-1}$)	6.6	Peker and Johnson 1993
Melt Temperature (K)	937	Peker and Johnson 1993
Glass Transition Temperature (K)	623	Waniuk et al 2007

Table 5.1 Optical and thermal properties of Vitreloy 1.

5.2.2 Effect of the delivered fluence

For a pulse duration of 85 ns, the results displayed in Figure 5.1 show that the diameter and depth of the craters increases with the augmentation of the fluence from 15 J.cm^{-2} to 32 J.cm^{-2}. This effect has been explained in Chapter 4, section 4.3.2, where it was stated that there is a higher energy inherent in the electrons within the lattice of the material when the energy contained within the beam diameter increases. However, it is also noted, for Vitreloy 1, that at fluence values above 25 J.cm^{-2}, the diameter and depth start to saturate. This change is most likely due to the mechanism of material removal becoming dominated by vaporisation rather than melt ejection. The absorption of a larger latent heat leads to vaporisation needing four times the amount of energy to remove the same amount of material as melt ejection, the result being less material removed during one pulse (Voisey et al 2003). Using the method described in section 4.3.2, the ablation threshold for Vitreloy 1 was determined to be around 10 J.cm^{-2}.

Figure 5.2 shows SEM images of craters machined within the processing window used to plot the graph on Figure 5.1. These SEM micrographs provide an indication about the different mechanisms that the material experiences when subject to different fluence values. At low fluence (Figure 5.2(a)), molten material has already begun to be ejected in the form of droplets that solidify around the edges of the formed crater. As seen from Table 5.1, Vitreloy 1 has a low thermal conductivity, which results in a large amount of confined volumetric heating which, coupled with the low melt temperature, creates a rapid onset of melting and relatively wide craters. Quintana et al (2009) also concluded that the amorphous structure of material results in more localised heating due to the lower thermal conductivity, which is a consequence of a lack of long range atomic ordering. As the fluence increases the vapour pressure from the evaporation process will increase and thus the ejection of melt becomes more volatile (see Figure 5.2(b) and (c)).

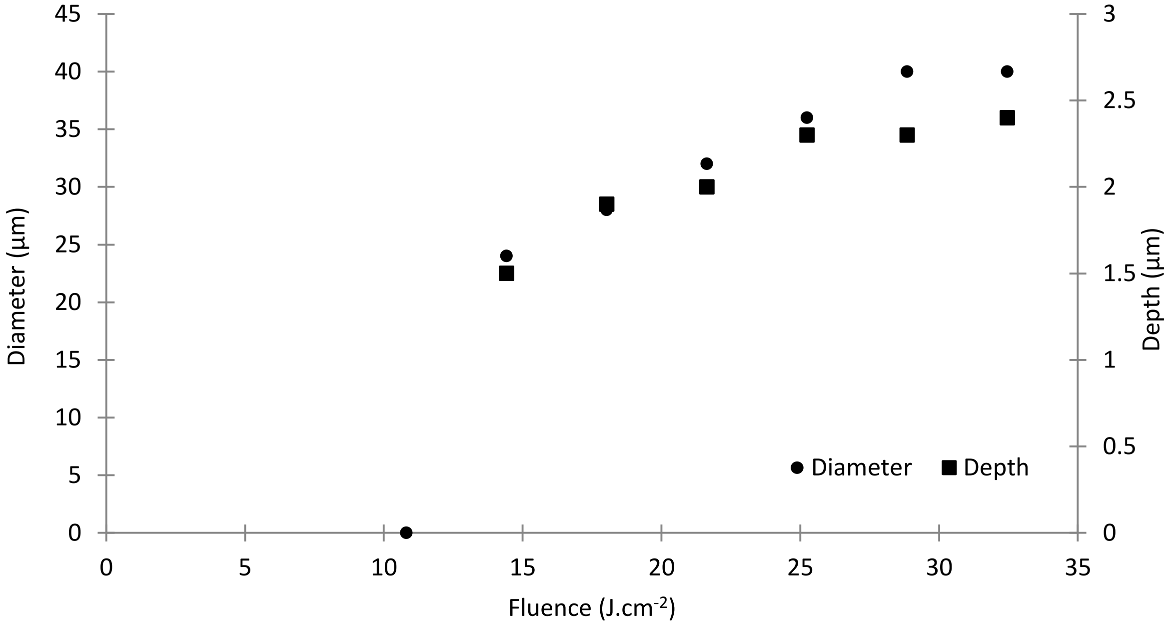

Figure 5.1 Measured depth and diameter for craters machined in Vitreloy 1 at 85 ns and varying fluence

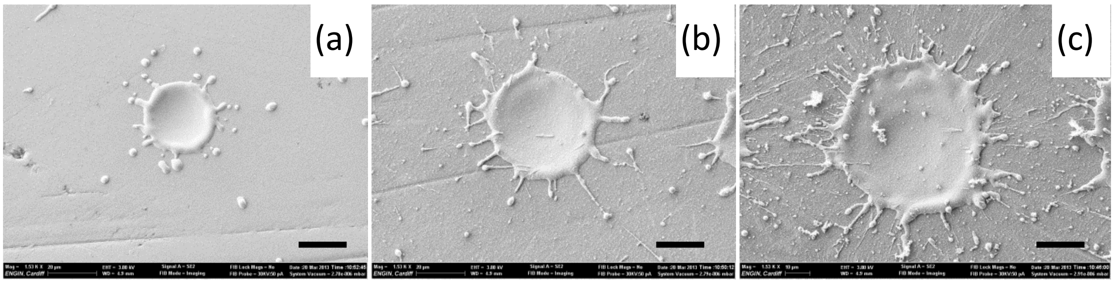

Figure 5.2 Craters machined in Vitreloy 1 showing the various mechanisms apparent at 85 ns with fluence (a) 14.4 J.cm^{-2} and b) 21.6 J.cm^{-2} and (c) 32.5 J.cm^{-2}. Scale bars: 20 µm

Figure 5.3 presents SEM micrographs of craters, for the considered pulse durations, at the respective highest possible fluence, which could be achieved with the laser system used. This figure shows that a large value of delivered fluence, for each of the pulse durations, causes volatile material removal, which results in increased melt ejection and poorly defined crater edges. This can especially be observed in Figures 5.3(a) and 5.3(b) for which the fluence used was larger than 25 J.cm^{-2}. In addition, ejected melt droplets for a generated crater can be seen to infringe on the preceding pulse indicating that the melt pool solidifies before the next pulse is incident on the surface. In Figure 5.3(a) and 5.3(b), several rings of solidification can be noticed suggesting that multiple waves of melt flow occurred. The highest fluence investigated for the 25 ns pulse was 13.4 J.cm^{-2} and, as it can be seen from Figure 5.3(d), this fluence is not high enough to cause significant explosive ejection. This suggests that the delivered fluence enables the onset of melting but the pulse duration is too short to allow enough time for the pressure within the molten layer to increase sufficiently to cause melt expulsion either through nucleate boiling or vaporisation pressure driven ejection.

As the fluence is decreased, the craters become cleaner and the material removal becomes less volatile. In particular, Figure 5.4 shows the craters machined at the same pulse durations as those reported in Figure 5.3 but this time, at the lowest fluence investigated. At these lower fluence values, the material ejection is in the form of droplets rather than explosive “splashes” and the ejection site does not spread as far as that observed for the higher fluence values. These droplets of material may be due to an initial burst of slow particles from the molten material, occurring because of the radial pressure gradients apparent in the molten pool of the crater. The craters also have better defined edges in the form of a ridge of molten material compared with the craters machined at a higher fluence value.

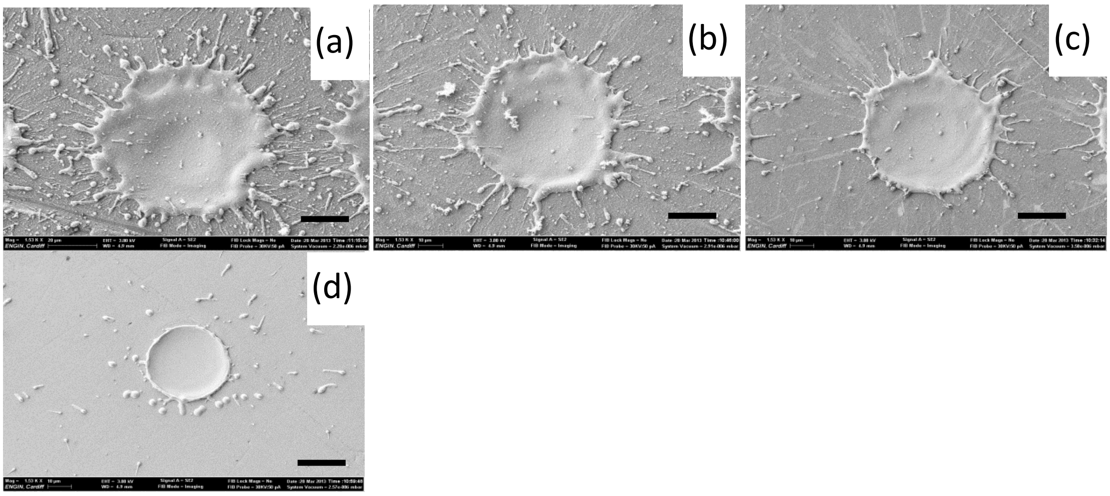

Figure 5.3 Craters machined in Vitreloy 1 for the highest achievable fluence at (a) 140 ns (43.7 J.cm^{-2}) (b) 85 ns (32.5 J.cm^{-2}) (c) 55 ns (24.6 J.cm^{-2}) and (d) 25 ns (13.4 J.cm^{-2}).

Scale bars: 20 µm

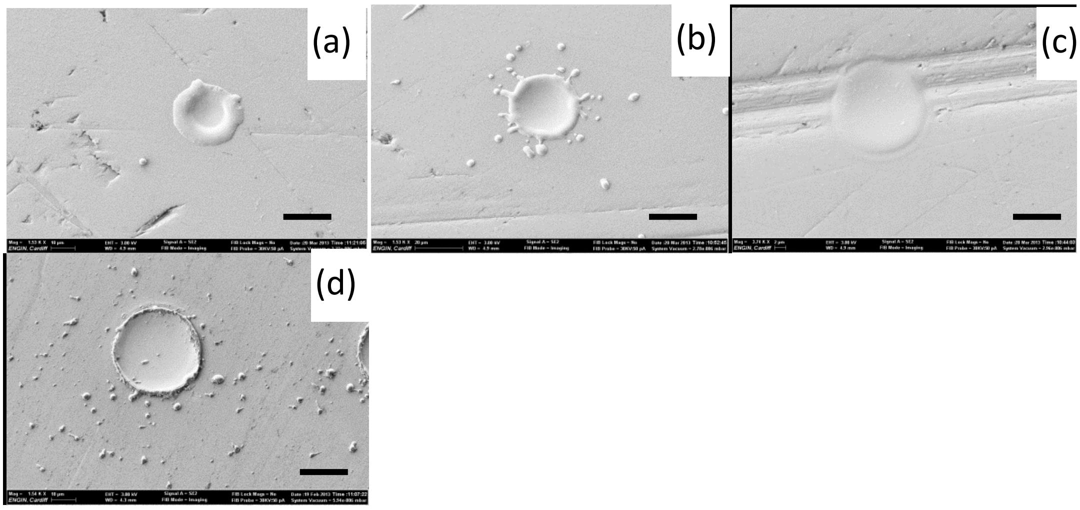

Figure 5.4 Craters machined in Vitreloy 1 for the lowest fluence at (a) 140 ns (14.6 J.cm^{-2}) (b) 85 ns (14.4 J.cm^{-2}) (c) 55 ns (11 J.cm^{-2}) and (d) 25 ns (12 J.cm^{-2}) .

Scale bars: 20 µm.

5.2.3 Effect of the laser pulse duration

The results displayed in Figure 5.5 (a) show that the depth of the craters increases with the augmentation of the fluence for all the pulse lengths investigated. This is due to the fact that, with the increase of the fluence, the workpiece is subjected to an increase of incident energy, which raises the temperature of the substrate and leads to an augmentation in the volume of removed material. The reported data also shows that, for a given fluence value, the depth of the craters increases with the augmentation of the pulse duration. As stated in Chapter 4, section 4.3.3, this is a consequence of the laser beam being incident on the material for longer at higher pulse lengths and thus, allowing more time for the heat to penetrate within the material and its temperature to increase above the melting point.

Figure 5.5 (b) shows the experimental data for the crater diameters generated for all pulse lengths as a function of the fluence. It can be observed that the diameter of the craters also increases with the augmentation of the fluence for all the considered pulse lengths. In addition, it is noted that, for a given fluence value, the diameter of the generated crater tends to increase as the pulse length reduces. This is attributed to the peak power effect. In particular, at constant beam energy, shorter pulses have a higher peak power. This leads to a higher surface area of the substrate within the spot size region to be above the ablation threshold. For example, Figure 5.6 shows two craters machined at the same fluence but with different peak powers. The crater in Figure 5.6(a) was machined at 1.4 kW peak power with a pulse length of 140 ns whereas the crater shown with Figure 5.6(b) was processed with a peak power of 3.6 kW at 55 ns. In this figure, the SEM micrographs are shown at the same magnification. It can clearly be seen that the diameter of the crater formed with the higher peak power is larger. On the other hand, this crater is also shallower because it was processed with a shorter pulse length, allowing less time for heat penetration.

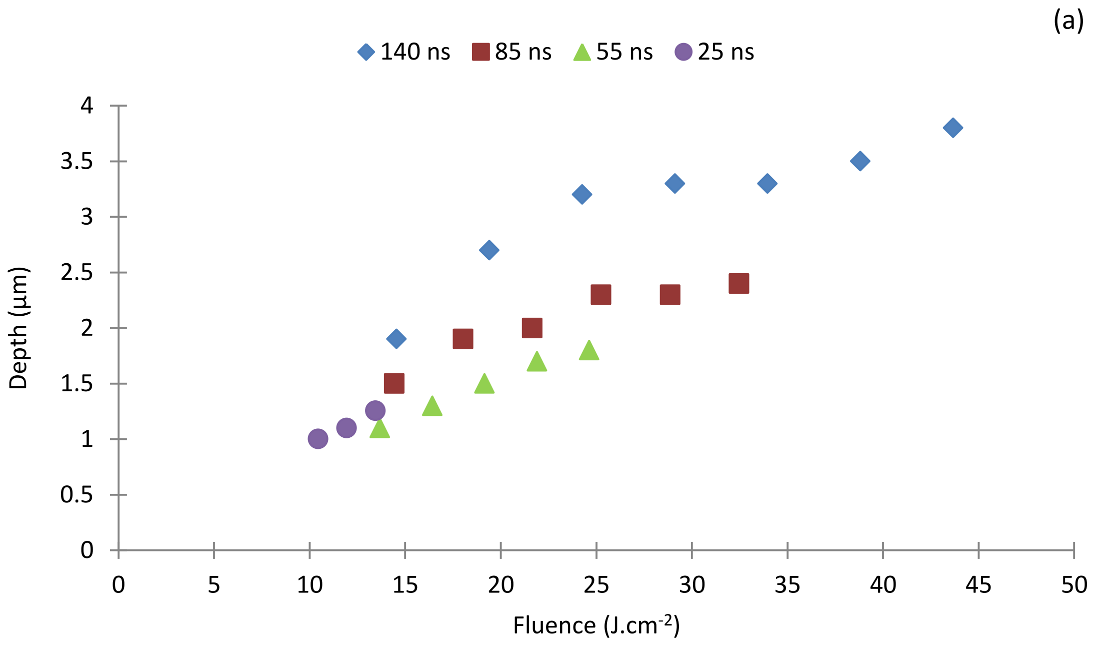

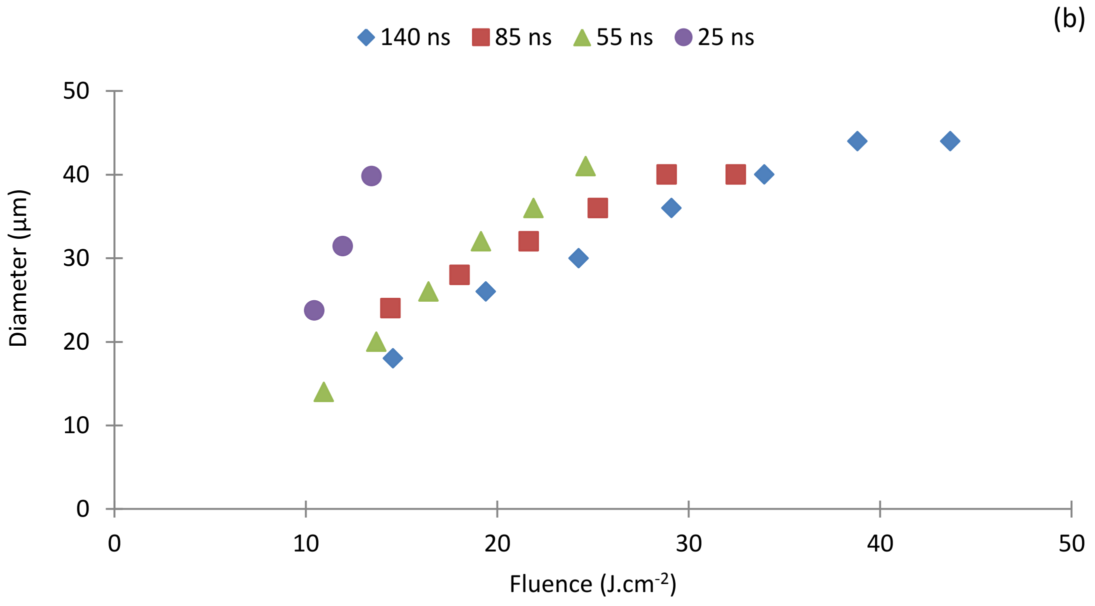

Figure 5.5 Measured crater (a) depths and (b) diameters, machined in Vitreloy 1, as a function of the fluence for the four different pulse durations investigated; 140 ns, 85 ns, 55 ns and 25 ns.

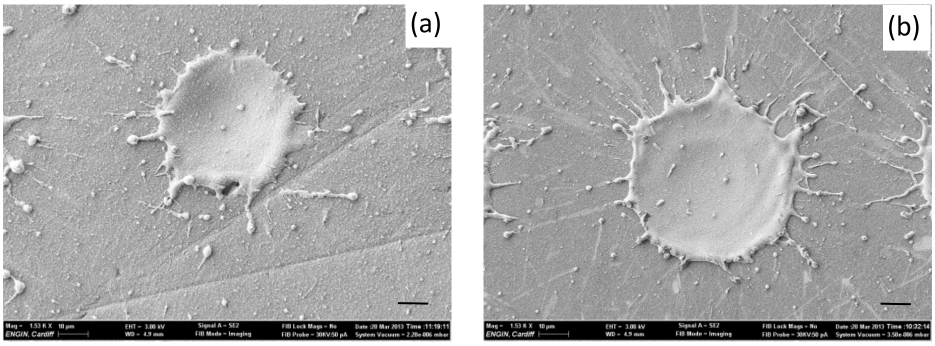

Figure 5.6 Craters machined in Vitreloy 1 at the same energy but different peak powers: (a) 1.4 kW at 140 ns and (b) 3.6 kW at 55 ns.

Scale bars: 10 µm.

Figure 5.7 shows the variation in peak power when the pulse duration is changed from 15 ns to 220 ns with an energy of 0.1 mJ. This figure also shows the corresponding SEM images for five of the pulse duration; 25 ns, 55 ns, 85 ns, 100 ns and 140 ns. At higher peak power, the material removal is dominated by vaporisation and the resulting crater is clean. However, the removal rate is low in this case due to the decrease in crater depth. A lower peak power results in the material removal process becoming dominated by melt ejection, as indicated by the increase in droplets surrounding the craters machined with a longer pulse duration in Figure 5.7. If the peak power is reduced any further, this could result in incomplete removal due to the reduced amount of power available above the removal threshold of the material.

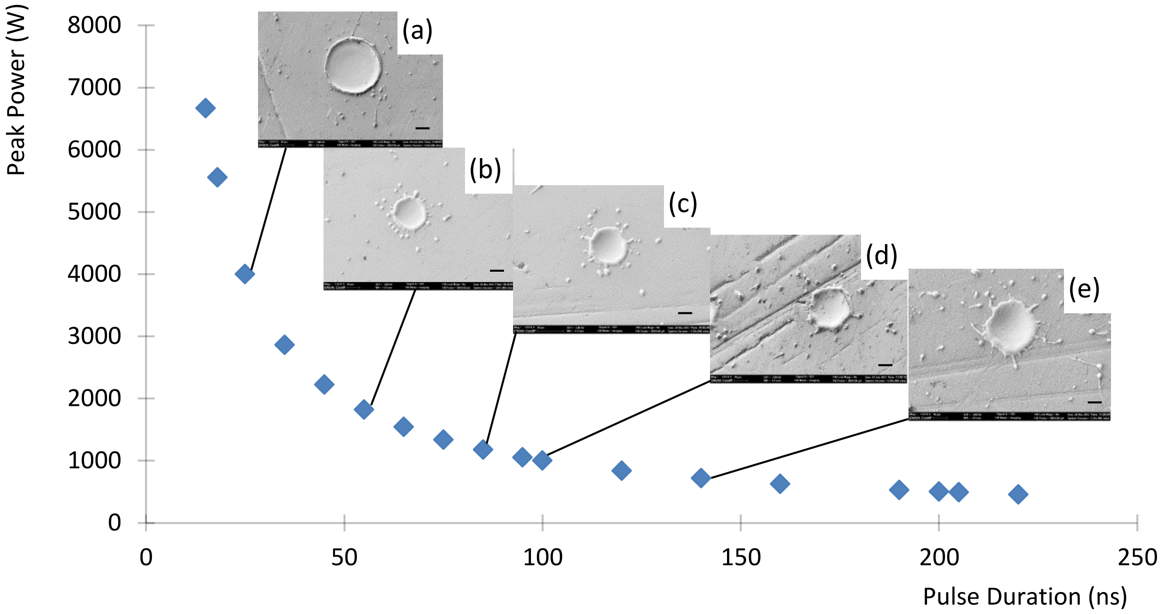

Figure 5.7 Peak power variation with pulse duration at 0.1 mJ, and the corresponding SEM images of craters machined in Vitreloy 1 with (a) 25 ns, (b) 55 ns, (c) 85 ns, (d) 100 ns and (e) 140 ns pulse length.

Scale bars: 10 µm.

5.3 Theoretical prediction of single pulse machining of $Zr_{41.2}Ti_{13.8}Cu_{12.5}Ni_{10}Be_{22.5}$

As mentioned previously in this thesis, the experimental investigation of single pulses is useful to shed light on some of the phenomena involved in laser material interaction such as the mechanisms of material removal or the threshold at which removal begins. Such a study however, can be long-winded and the analysis can be time consuming. In order to shorten the time required in the study of single pulses and also to investigate the laser material interaction process with additional details, a theoretical model has been developed for the single pulse processing of Vitreloy 1 based on the approach described in Chapter 4. The theoretical results gained can enhance the observations made during the experimental investigations. Besides, the model creates a platform with which the machining response of Vitreloy 1 could be anticipated when using laser systems with different parameters than those available in the system employed during the experimental investigation reported in the previous section.

Figure 5.8 displays the prediction of the temperature variation over a complete heating and cooling cycle for a single pulse of 140 ns in length and with a fluence of 43.7 $J.cm^{-2}$. The maximum temperature reached is around 2800 K. An interesting observation to be made from this theoretical result is the amount of time necessary for Vitreloy 1 to cool. If this material is processed through laser machining, it is highly unlikely that single pulses would be used. Instead, a series of overlapping pulses at a specified frequency and overlap distance should be employed. In this case, depending on the frequency used, a given crater machined by the laser may or may not be at a temperature higher than room temperature when the next pulse strikes. In the case of Figure 5.8, if a pulse hits within 0.8 µs after the previous pulse has ended, then the BMG crater will still be molten.

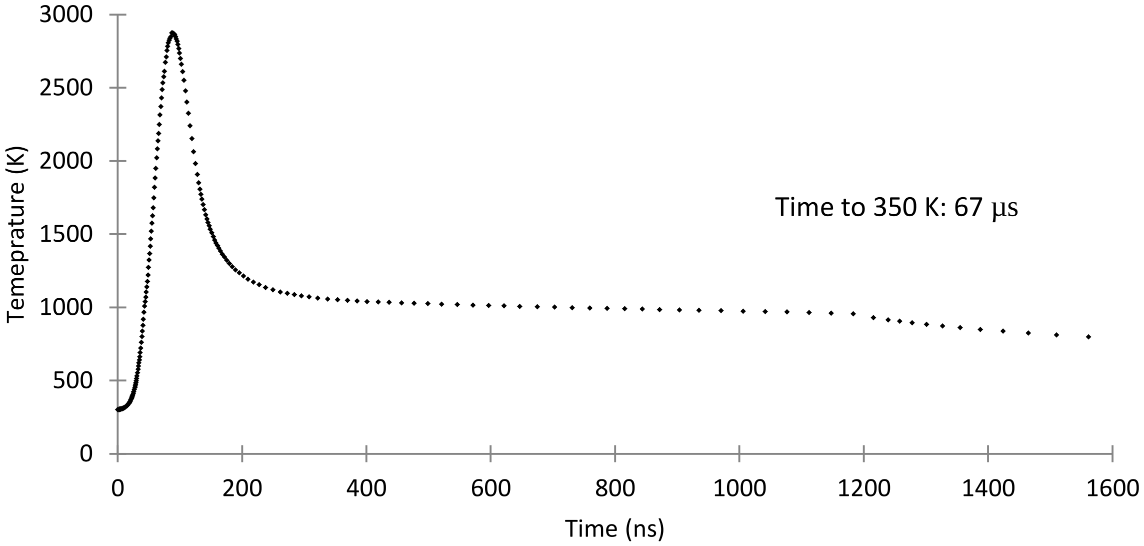

Figure 5.8 Theoretical temperature distribution with time for a heating and cooling cycle for a single pulse of 140 ns and with a fluence of 43.7 J.cm^{-2}*. The time taken for the material to cool down to 350 K is 67 µs.*

It takes 590 µs for the bulk metallic glass to cool down to room temperature so any pulse that hits before this time will cause some degree of heat accumulation within the substrate due to the amorphous nature of this material, any heat accumulation has the ability to change its microstructure.

Figure 5.9 shows the variation in temperature with time for various fluence values with a pulse duration of 140 ns. These results suggest that the fluence leading to the onset of melting in this material is around 10 J.cm^{-2} for this pulse length. This result is supported with the SEM images given earlier in Figure 5.4 (a) where the image shown at 14.6 J.cm^{-2} displays a crater that has melted and also where the melt has been displaced by the thermal and surface tension gradients, suggesting that the threshold for melting is lower than this fluence.

Figure 5.10 shows the theoretical temperature distribution for pulses with the same fluence but different peak power values. The graph indicates that, on the workpiece surface located at the centre of the beam, higher temperature values are reached with larger peak powers. In turn, this means that a wider region around that point on the surface of the workpiece should be subjected to temperature above the melting point of Vitreloy 1. This is in line with the experimental results showed earlier in Figure 5.7 where the effect of varying the peak power on the resulting crater geometry was illustrated. In particular, it was observed that, for a given fluence, an increase in peak power caused craters with larger diameters.

Figures 5.11 (a) and (b) show the theoretical prediction of the depth and diameter of the craters machined at varying fluence values for 140 ns, 85 ns, 55 ns and 25 ns. Table 5.2 summarises the difference between these results and the experimental values obtained in the previous section (see Figure 5.5). The theory and experimental measurements generally agree well with the maximum difference being 12 %.

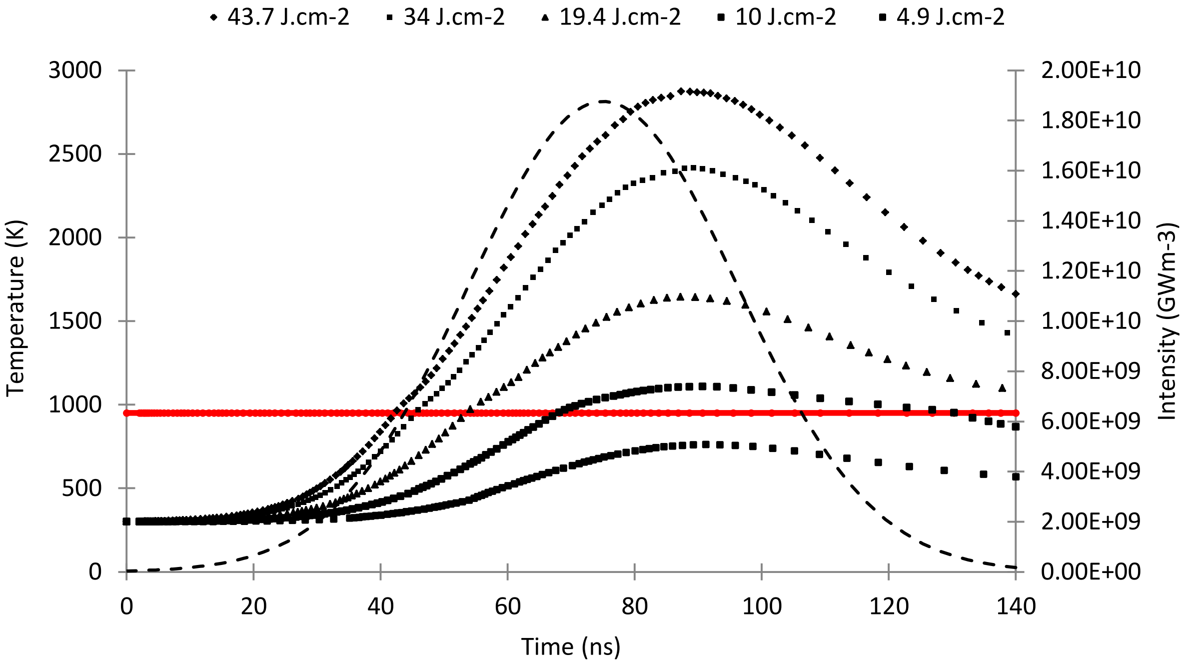

Figure 5.9 Theoretical temperature distribution with time for a variety of fluence values at 140 ns pulse duration. The horizontal line shows the melt temperature of the material at 937 K. The dotted curve represents the intensity distribution with time for the highest fluence of 43.7 J.cm^{-2}.

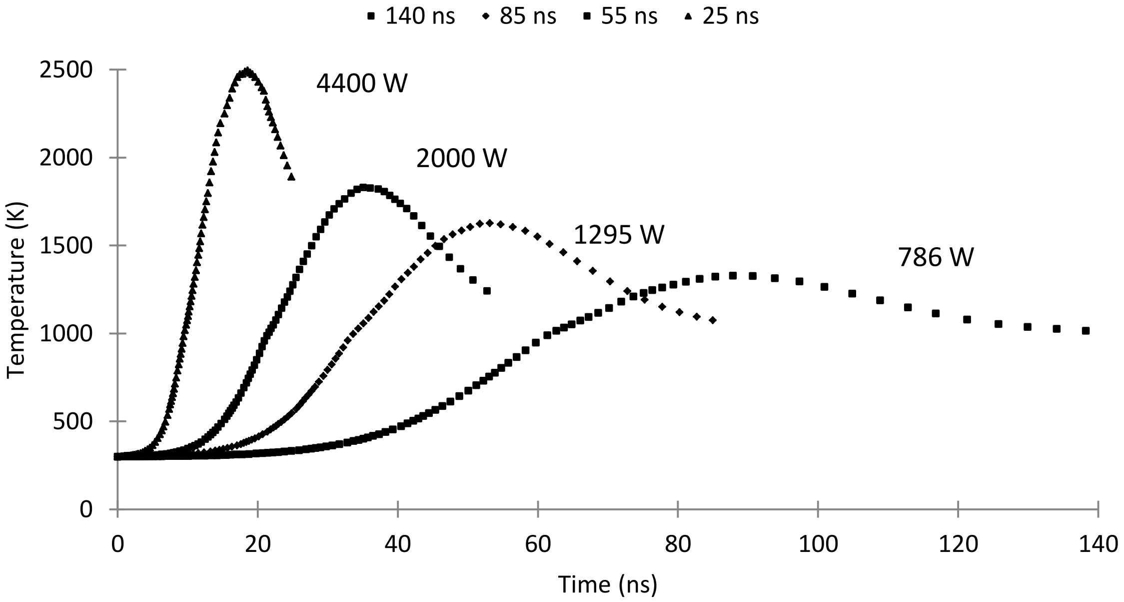

Figure 5.10 Effect of varying the peak power at the same fluence on the temperature variation with time for four different pulse durations; 140 ns, 85 ns, 55 ns and 25 ns and for a fluence of 14 J.cm^{-2}. The peak power value is also given for each curve.

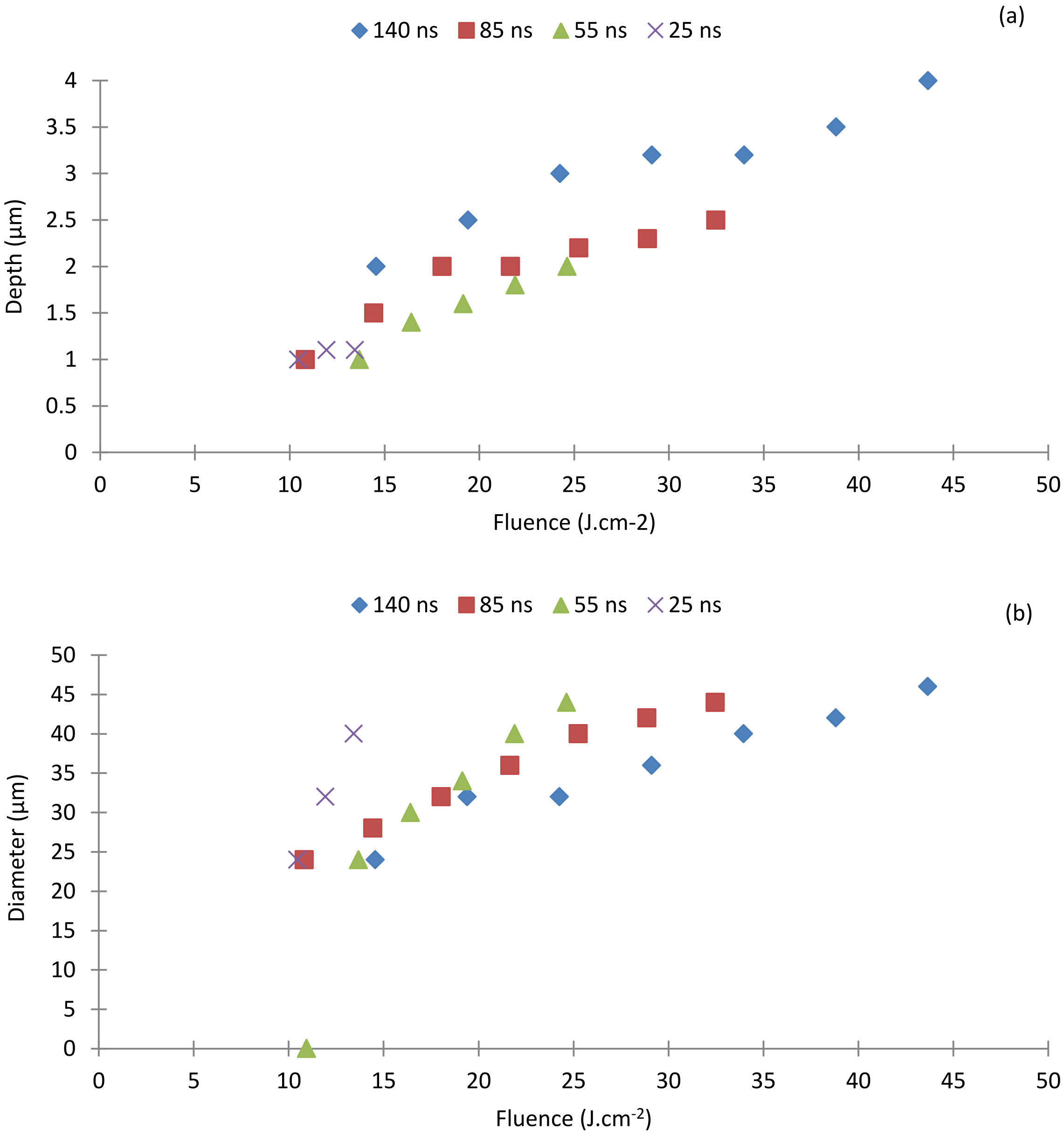

Figure 5.11 Predicted (a) depth and (b) diameter for craters machined in Vitreloy 1 with pulse durations of 140 ns, 85 ns, 55 ns and 25 ns at varying fluence values.

Pulse Duration (ns)	**Average Difference (%)**	
	Crater Diameter	**Crater Depth**
140	10.3	4.3
85	11.6	2.3
55	12.0	8.1
25	1.1	4.2

Table 5.2 Average percentage differences between the crater diameters and crater depths predicted by the theoretical model and those measured during the experimental investigation.

The discrepancies between theory and experiments could be due to errors in the measurements of the craters with large melt ejection and also they could possibly due to a lack of accurate values of material properties for Vitreloy 1 given that this material has not been studied as extensively as the more common engineering materials.

The results from the theoretical model can also aid in the interpretation of topographical features that can be witnessed in SEM images. In particular, Figure 5.12 shows a SEM micrograph of the crater machined at 15 ns with a fluence of 7.6 J.cm^{-2}. It can be observed from Figure 5.12 (b) that from the immediate edge of the crater to a value of about 2.5 µm radially outwards, surface deformations are present. This area may be referred to as the heat affected zone given that it is influenced by the heat distribution from the laser beam but has not reached the melt temperature. This is confirmed with the theoretical results shown in Figure 5.13 where it can be seen that a small region outside the edge of the crater, with a similar width to that observed in the SEM micrograph (Figure 5.12 (b)) is subjected to heating above the glass transition temperature of the material. This suggests that the material exhibited a viscous behaviour in this region and was deformed plastically by the pressure from the molten material flow coming from the centre of the crater. Liu et al (2011) also observed similar surface rippling effects when machining Vitreloy 1 with an Nd:YAG solid state laser with 10 ns pulses and a wavelength of 532 nm. They concluded that the created patterns were not due to light interference given that the spacing of the ripples was larger than the wavelength of the beam. Instead, they attributed the ripples to the Kelvin-Helmholtz instability arising from the differences in densities and velocities of the molten material and the plasma plume generated in the centre of the laser ablated region. This instability can occur when wind moves over water, two fluids of different densities moving with different velocities, resulting in the formation of waves on the water surfaces (Thomson, 1871).

Due to the lower intensities used for this investigation compared to that of Liu et al (2011) and the lower temperatures experienced, it is unlikely that plasma is formed at all suggesting that the ripples are due to a different effect. Lin et al (2012) also reported ripples outside grooves micromachined on an Mg-based bulk metallic glass using pulsed nanosecond lasers at 355 nm and 1064 nm. They attributed the formation of these wrinkles to the heat accumulation in the HAZ, causing heating above the glass transition temperature and leading to the softening of the material. Due to the results presented in Figures 5.12 and 5.13, it is likely that the ripples formed in Vitreloy 1 with these particular laser parameters are also due to the effect of heat accumulation and the subsequent plastic deformation of the heat affected zone.

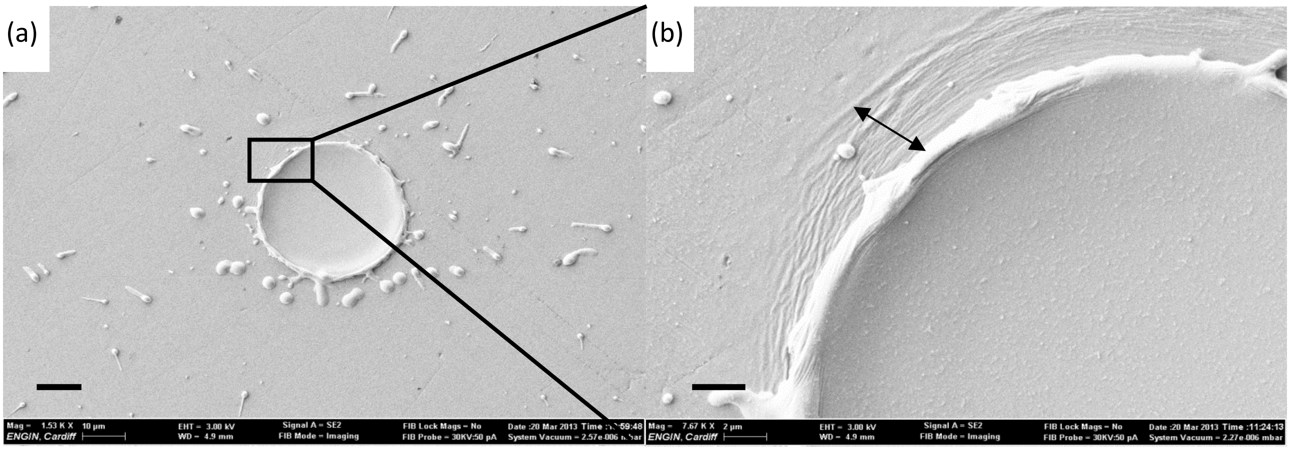

Figure 5.12 (a) SEM image of a crater machined at 15 ns with 7.6 J.cm^{-2} with (b) close up of the feature of interest. The arrows on image (b) measures 2.5 µm. Scale bars: (a) 10 µm (b) 2 µm

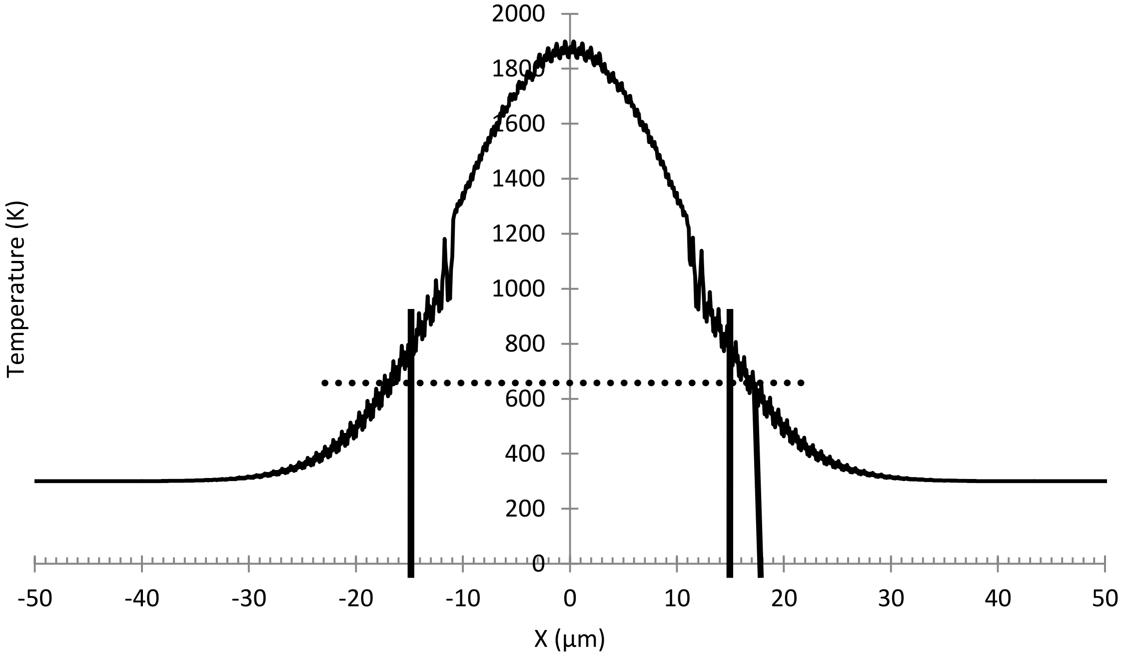

Figure 5.13 The theoretical temperature distribution on the surface of the crater shown above. The vertical solid line represents the edge of the crater which has a diameter of about 30 µm and the outside region of the material that is heated to the glass transition temperature, and the horizontal dotted line indicates the glass transition temperature of Vitreloy 1 which is stated to be 623 K (Waniuk et al, 2007).

5.4 Experimental and theoretical study on the crystallisation of $Zr_{41.2}Ti_{13.8}Cu_{12.5}Ni_{10}Be_{22.5}$

5.4.1 Introduction

The investigation using single pulses provided useful insights regarding the laser material interaction of Vitreloy 1. However, given that the outstanding properties of BMG materials in general are intrinsically linked to their amorphous nature, it is important to consider the thermal load induced during laser processing as the addition of heat to these substrates can result in a change in this nature. Crystallisation of amorphous material is expected to take place at, or above, the crystallisation temperature of the material being studied. Crystallisation itself takes place due to the processes of nucleation and crystal growth. It can either occur heterogeneously or homogeneously, depending on the role of foreign bodies within the material (Liu, 2000). To avoid the crystallisation of a material upon cooling, the amorphous structure must not be allowed sufficient time to re-arrange itself into a more ordered crystalline structure. This means that each amorphous material has a critical cooling rate which, if exceeded, results in the amorphous structure being “frozen in” (Suryanarayana and Inoue, 2011). As reported in the literature in Chapter 2, phase change upon cooling is the main reason for the formation of crystalline precipitates in the amorphous matrix of BMGs during nanosecond laser ablation. This is due to the high heating rate that exists well above the critical heating rate of BMG.

In this context, the crystallisation of Vitreloy 1 was studied in this section using multiple pulses with different laser processing parameters, namely pulse overlap, pulse energy and pulse duration. The laser operations consisted of milling identical 10 mm by 10 mm square cavities made of only one layer of parallel machined lines of overlapping pulses. The time taken to machine the square cavities varied depending on the scanning speed used. Whether the amorphous material had crystallised after processing was determined by comparing x-ray diffraction (XRD) patterns obtained before and after processing. The XRD machine used was a Bruker D8 Discover. The atoms within a crystalline structure are arranged in an orderly fashion and when an x-ray is incident on the structure the atoms will reflect the beams at various angle depending on their orientation. If the individual x-rays within a beam are reflected at the same phase from each atomic plane, then constructive interference will occur. Using an XRD, the incident angle of the incoming x-rays can be altered and the angle that the atomic structure reflects the incoming beams that have experienced constructive interference at can be detected. The detector that confirms the angle of the reflected x-rays can also measure the rate of outcoming x-rays. The result is a plot of the rate of x-rays reflecting off the atomic structure at varying angles. For amorphous materials, the atoms are not arranged with long-range order thus constructive interference of the incoming x-rays will not occur resulting in a lack of peaks in the XRD pattern.

5.4.2 XRD analysis

In total, seven Vitreloy 1 samples were processed using different laser parameters and machining a single layer. Table 5.3 shows the process values used for each sample. A relatively wide range of parameter combinations was used due to the lack of substantial research into parametric influence on the crystallisation of Vitreloy 1 during nanosecond laser machining.

The XRD patterns for the samples prior and post machining are given in Figures 5.14 to 5.20. If the material has an amorphous structure then there will be a lack of intensity peaks at specific angles within the XRD pattern. If the material has a crystalline structure then there will be peaks at varying intensities evident at different angles. The patterns for the un-machined samples are shown to validate the amorphous nature of the polished bulk metallic glass. The visual observation of the corresponding XRD patterns of the processed Vitreloy 1 specimen suggests that crystallisation occurred for samples 1, 6 and 7. The laser processing parameters used for these samples that displayed crystallisation are reported in Table 5.4.

Upon melting, the atoms within the amorphous structure attain translational motion. This means that they can form new bonds, either with other metal atoms or with oxygen from the air to form new crystalline phases. These crystalline structures form up until the material reaches its solidification temperature, where the atoms can no longer move freely. With many different elements within this specific metallic glass, the different possible pathways to crystallisation are complex. The elements themselves, namely zirconium, titanium, copper, nickel and beryllium, may form crystalline structures on their own, or they may bond with each other to form binary, stoichiometric compounds such as $CuZr_2$ or $BeZr_2$, or possibly compounds with larger numbers of elements. Martin et al (2004) identified the crystallisation pathways for Vitreloy 1 as being a multi-phase process with, firstly, the separation of the amorphous phase and icosahedral-phase (I-phase) structures followed by the formation of the compounds Be_2Zr and $CuZr_2$, as well as additional phases which were not identified by these authors. The atoms may also react with the oxygen present in the atmosphere before and after machining, resulting in crystalline oxides.

	Laser Processing Parameters					
Sample	**Pulse Duration (ns)**	**Fluence ($J.cm^{-2}$)**	**Frequency (kHz)**	**Scanning Speed ($mm.s^{-1}$)**	**Track Displacement (µm)**	**Pulse Overlap (%)**
1	220	70	35	100	5	91
2	75	4	125	100	15	97.5
3	220	70	35	600	10	46
4	220	6	250	1000	6	87
5	220	6	40	200	6	84
6	220	70	35	500	5	55
7	220	6	250	100	6	98.75

Table 5.3 Parameters for each sample machined in the crystallisation study.

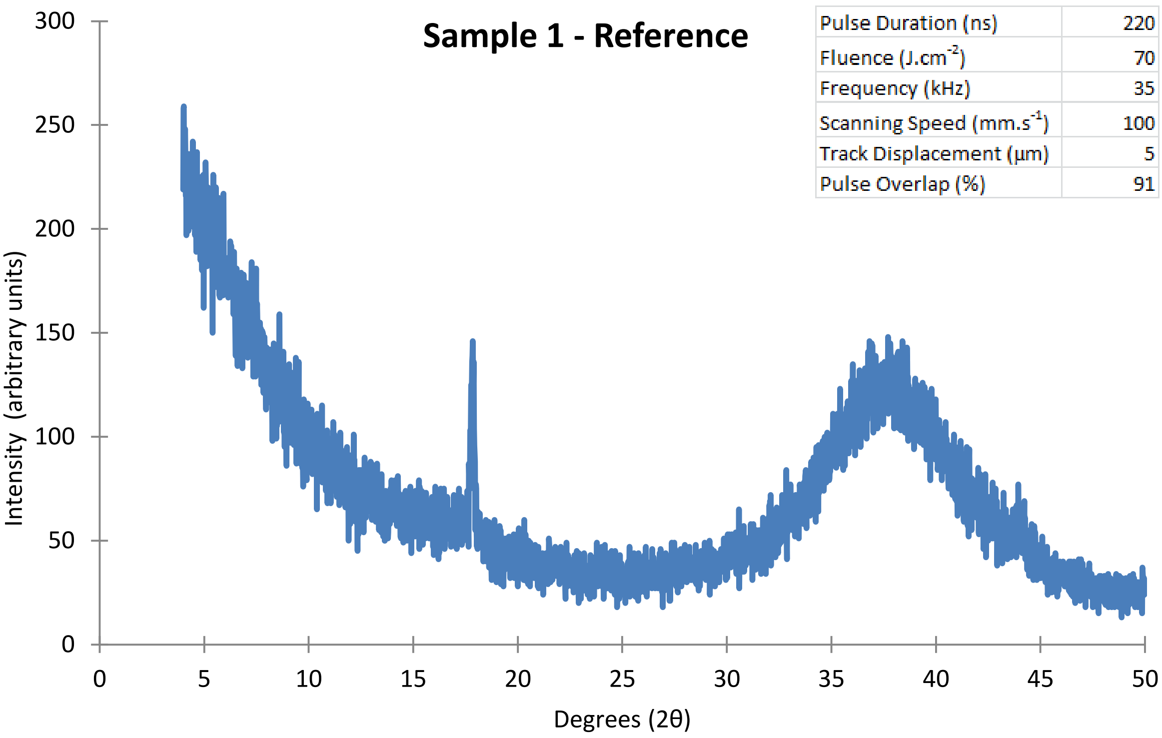

Pulse Duration (ns)	220
Fluence (J.cm^{-2})	70
Frequency (kHz)	35
Scanning Speed (mm.s^{-1})	100
Track Displacement (µm)	5
Pulse Overlap (%)	91

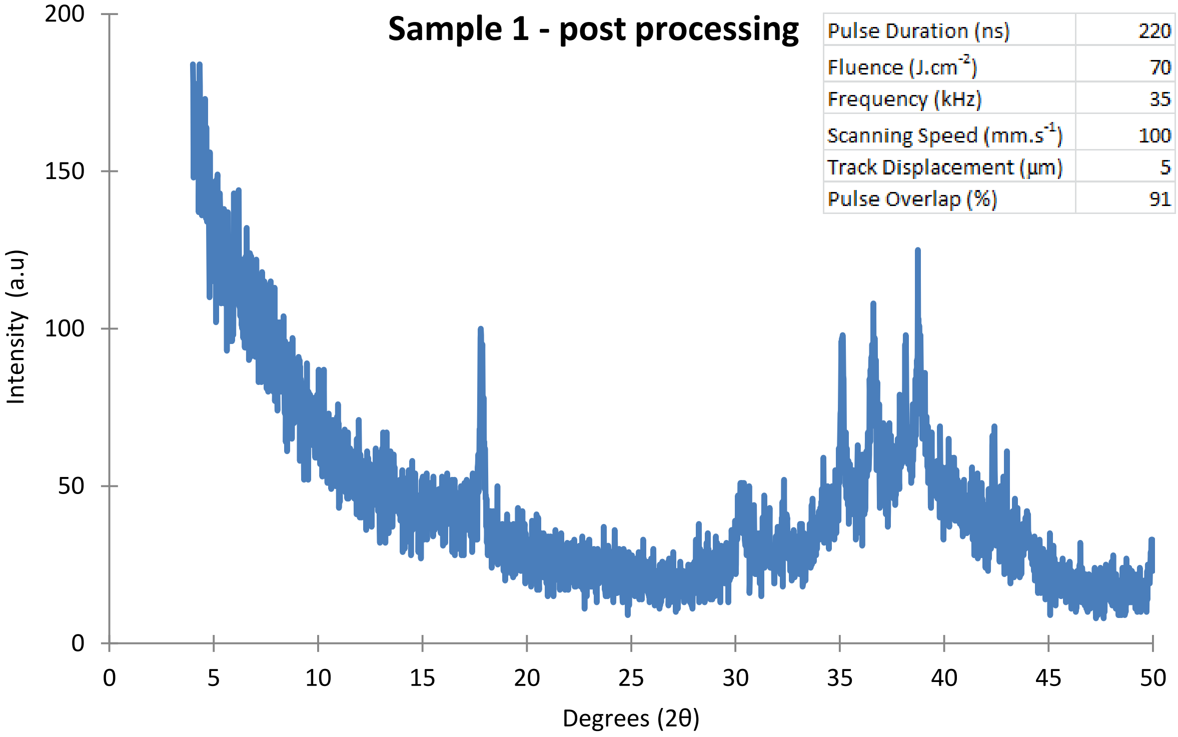

Pulse Duration (ns)	220
Fluence (J.cm^{-2})	70
Frequency (kHz)	35
Scanning Speed (mm.s^{-1})	100
Track Displacement (µm)	5
Pulse Overlap (%)	91

Figure 5.14 XRD patterns for sample 1 (a) pre-processing and (b) post laser processing. The processing conditions used are reported in the tables. The peaks that occur from 30-50 degrees indicate that these processing conditions cause crystallisation of the Vitreloy 1 material.

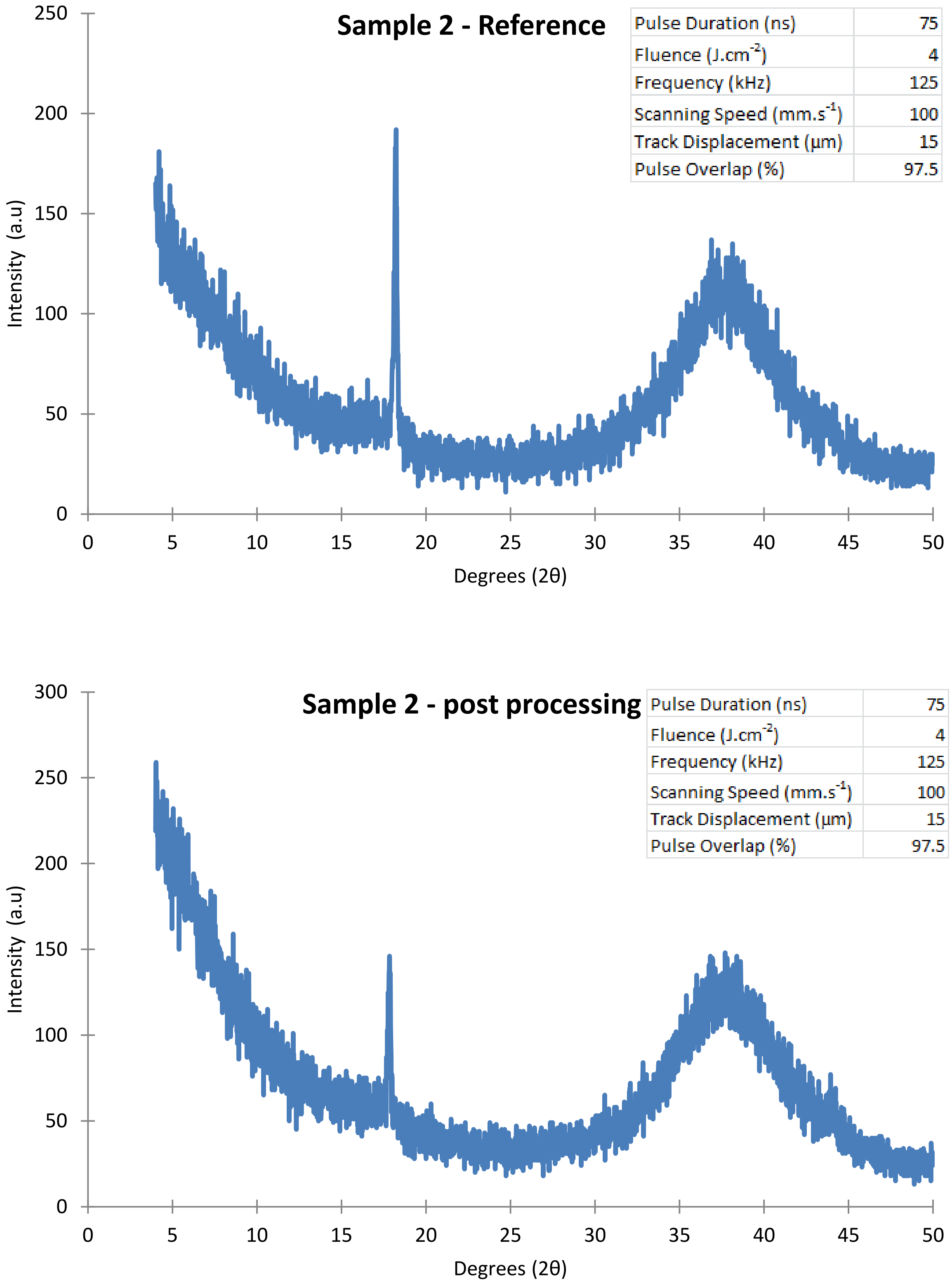

Pulse Duration (ns)	75
Fluence (J.cm^{-2})	4
Frequency (kHz)	125
Scanning Speed (mm.s^{-1})	100
Track Displacement (μm)	15
Pulse Overlap (%)	97.5

Pulse Duration (ns)	75
Fluence (J.cm^{-2})	4
Frequency (kHz)	125
Scanning Speed (mm.s^{-1})	100
Track Displacement (μm)	15
Pulse Overlap (%)	97.5

Figure 5.15 XRD patterns for sample 2 (a) pre-processing and (b) post laser processing. The processing conditions used are displayed in the tables. The similarities of the patterns suggest that these conditions do not change the amorphous nature of the Vitreloy 1.

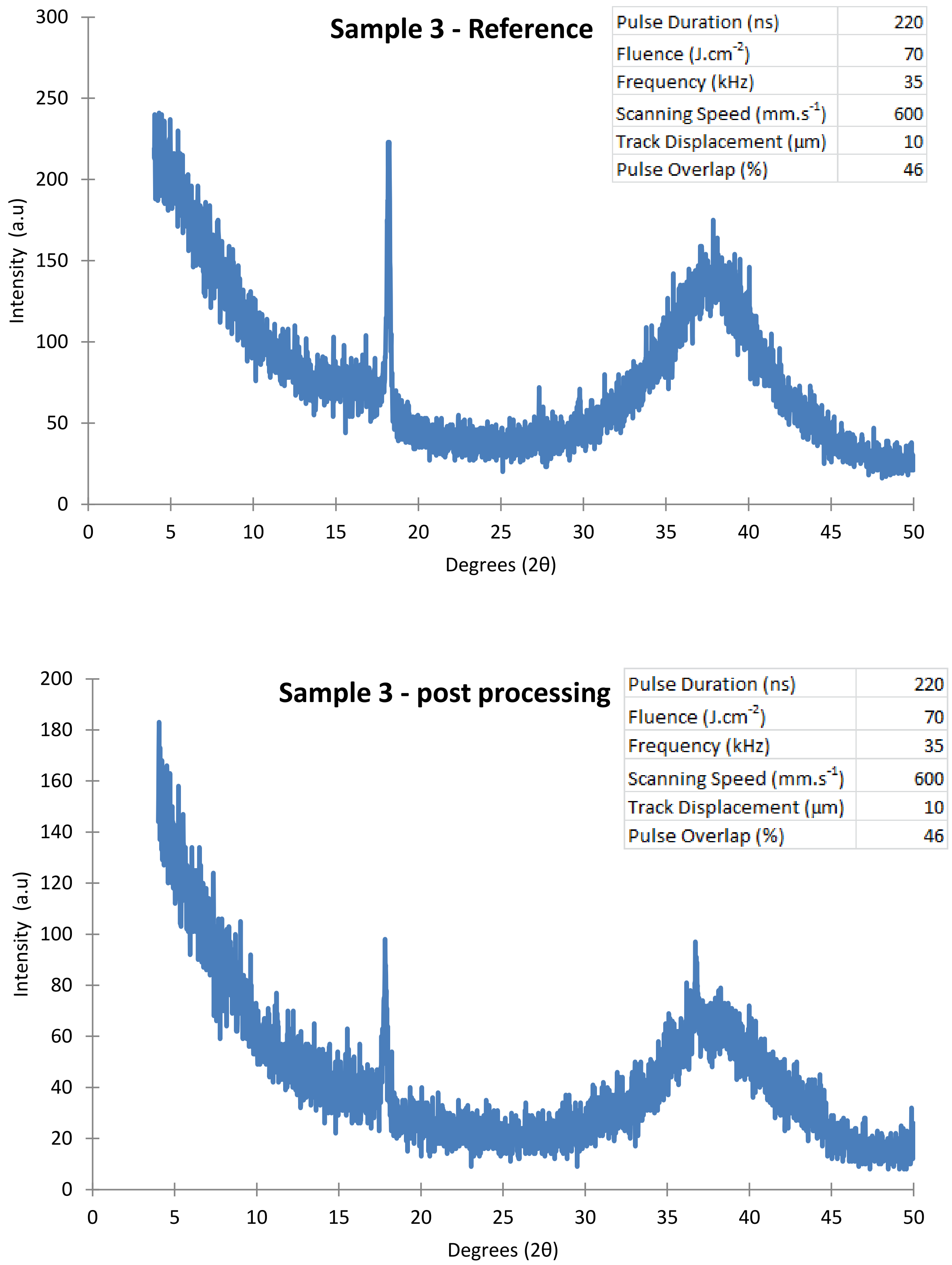

Pulse Duration (ns)	220
Fluence (J.cm^{-2})	70
Frequency (kHz)	35
Scanning Speed (mm.s^{-1})	600
Track Displacement (μm)	10
Pulse Overlap (%)	46

Pulse Duration (ns)	220
Fluence (J.cm^{-2})	70
Frequency (kHz)	35
Scanning Speed (mm.s^{-1})	600
Track Displacement (μm)	10
Pulse Overlap (%)	46

Figure 5.16 XRD patterns for sample 3 (a) pre-processing and (b) post laser processing. The similarities of the patterns suggest that the processing conditions specified in the tables do not induce a change in the amorphous structure of the Vitreloy 1.

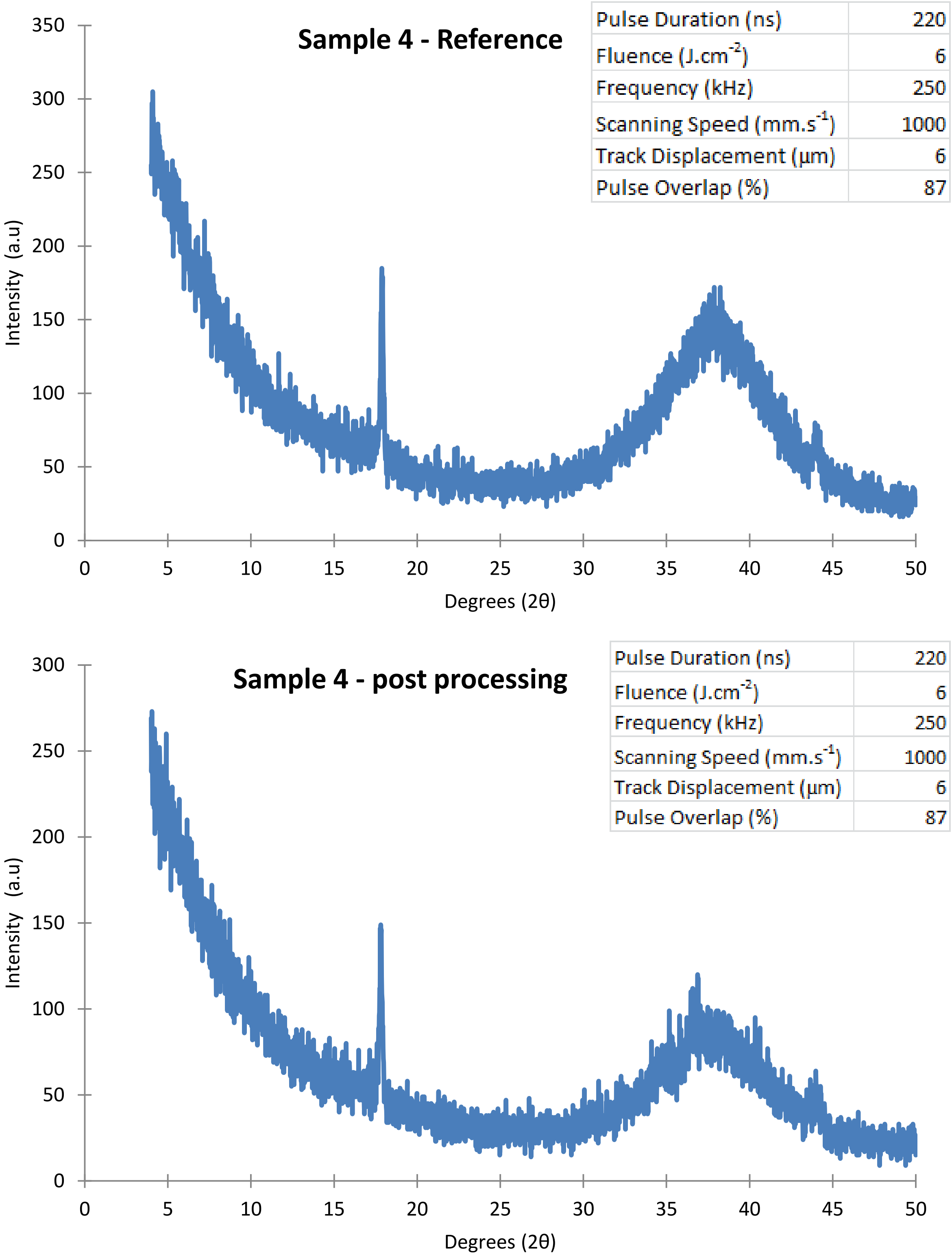

Pulse Duration (ns)	220
Fluence (J.cm^{-2})	6
Frequency (kHz)	250
Scanning Speed (mm.s^{-1})	1000
Track Displacement (µm)	6
Pulse Overlap (%)	87

Pulse Duration (ns)	220
Fluence (J.cm^{-2})	6
Frequency (kHz)	250
Scanning Speed (mm.s^{-1})	1000
Track Displacement (µm)	6
Pulse Overlap (%)	87

Figure 5.17 XRD patterns for sample 4 (a) pre-processing and (b) post laser processing. There are no additional peaks visible in the post processing pattern suggesting that the processing conditions specified in the table do not induce crystallisation within the Vitreloy 1 sample.

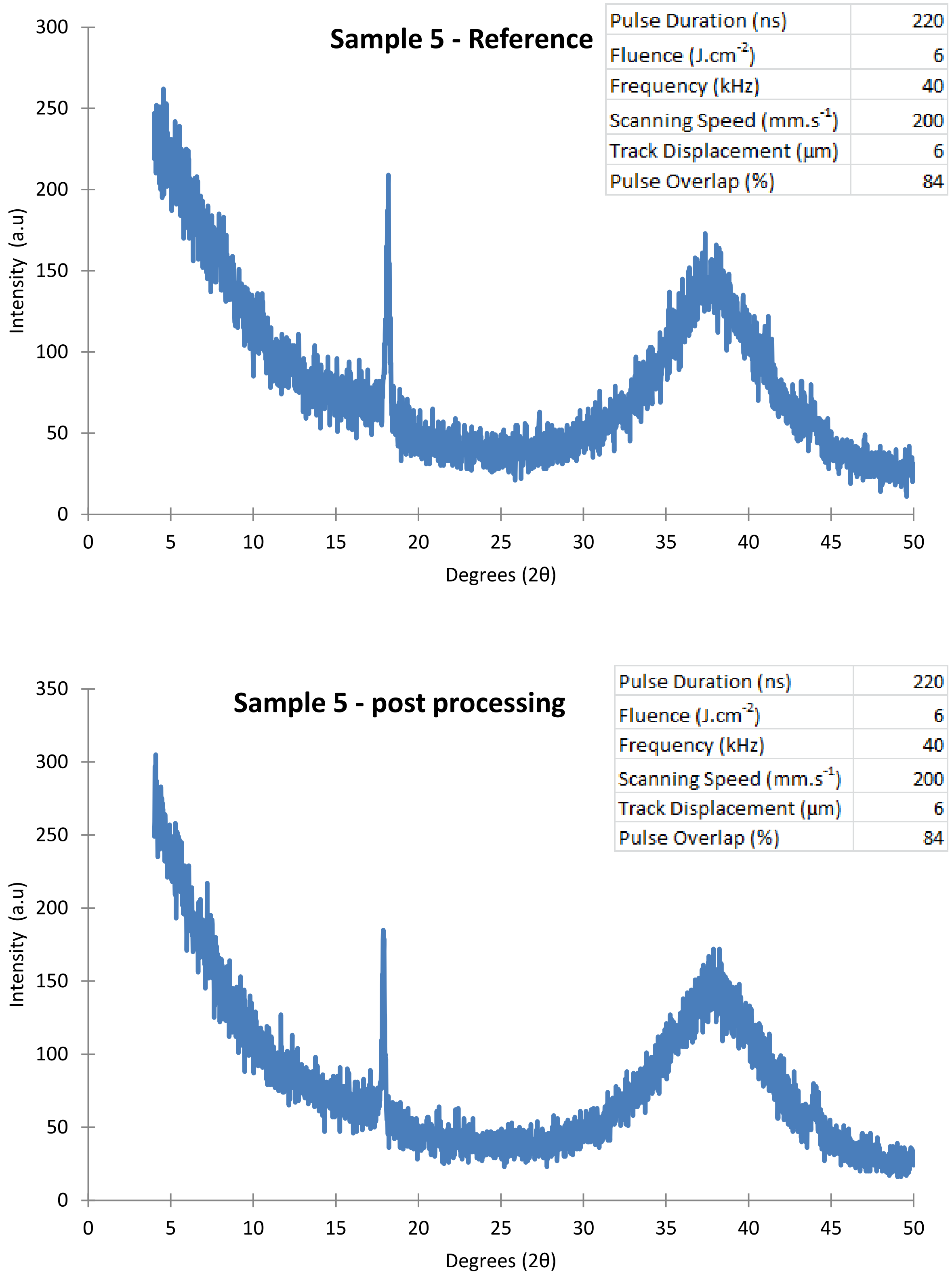

Pulse Duration (ns)	220
Fluence (J.cm^{-2})	6
Frequency (kHz)	40
Scanning Speed (mm.s^{-1})	200
Track Displacement (µm)	6
Pulse Overlap (%)	84

Pulse Duration (ns)	220
Fluence (J.cm^{-2})	6
Frequency (kHz)	40
Scanning Speed (mm.s^{-1})	200
Track Displacement (µm)	6
Pulse Overlap (%)	84

Figure 5.18 XRD patterns for sample 5 (a) pre-processing and (b) post laser processing. The lack of prominent peaks in the pattern produced after processing suggests that the processing conditions identified in the tables do not change the amorphous nature of the Vitreloy 1.

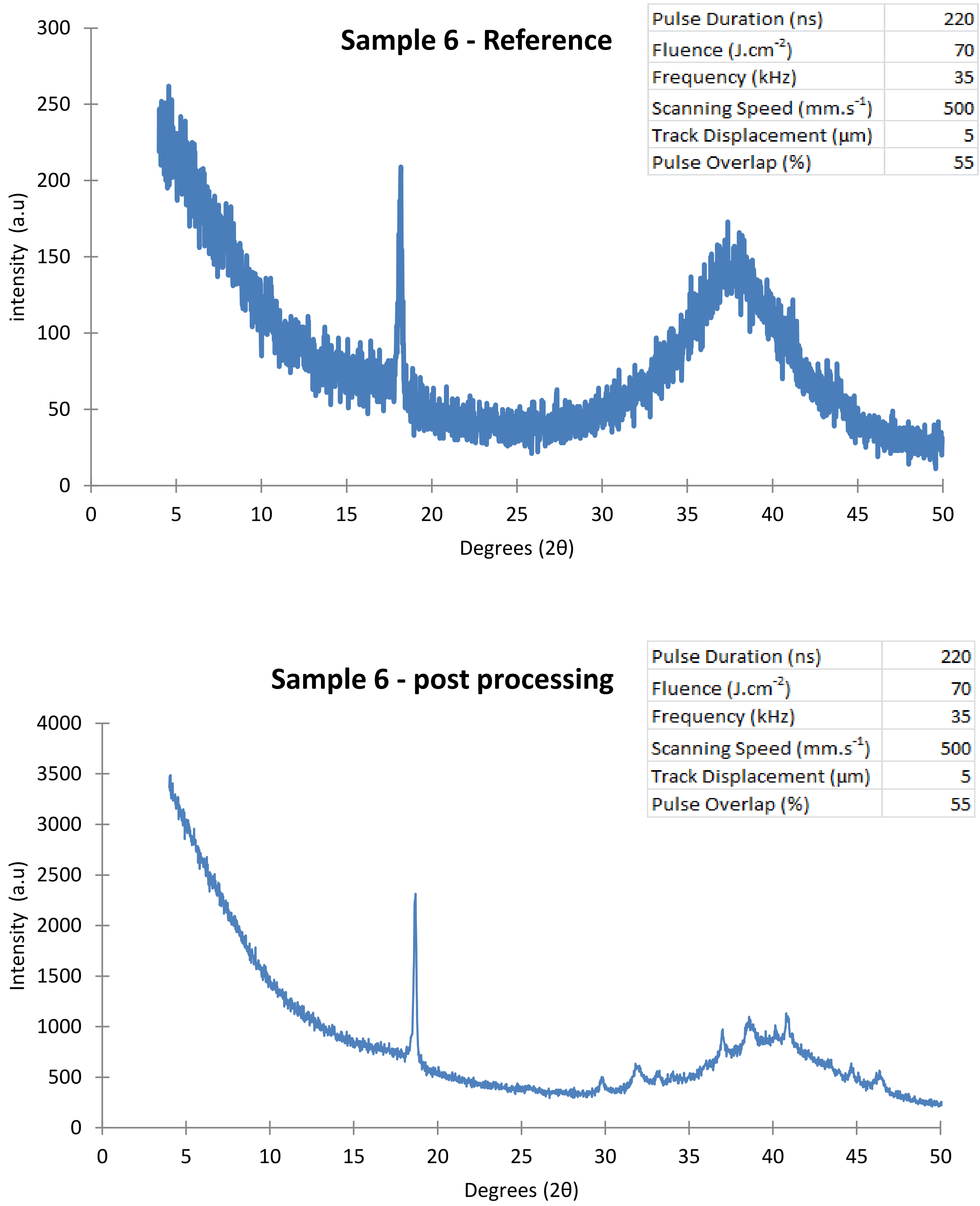

Pulse Duration (ns)	220
Fluence (J.cm^{-2})	70
Frequency (kHz)	35
Scanning Speed (mm.s^{-1})	500
Track Displacement (µm)	5
Pulse Overlap (%)	55

Pulse Duration (ns)	220
Fluence (J.cm^{-2})	70
Frequency (kHz)	35
Scanning Speed (mm.s^{-1})	500
Track Displacement (µm)	5
Pulse Overlap (%)	55

Figure 5.19 XRD patterns for sample 6 (a) pre-processing and (b) post laser processing. The additional peaks present in the pattern after processing with the conditions specified in the table suggest crystallisation has occurred within the Vitreloy 1 sample. The length of the XRD scan for sample 6 post-processing was extended so as to achieve a finer image of the peaks to aid in the identification of each crystalline phase.

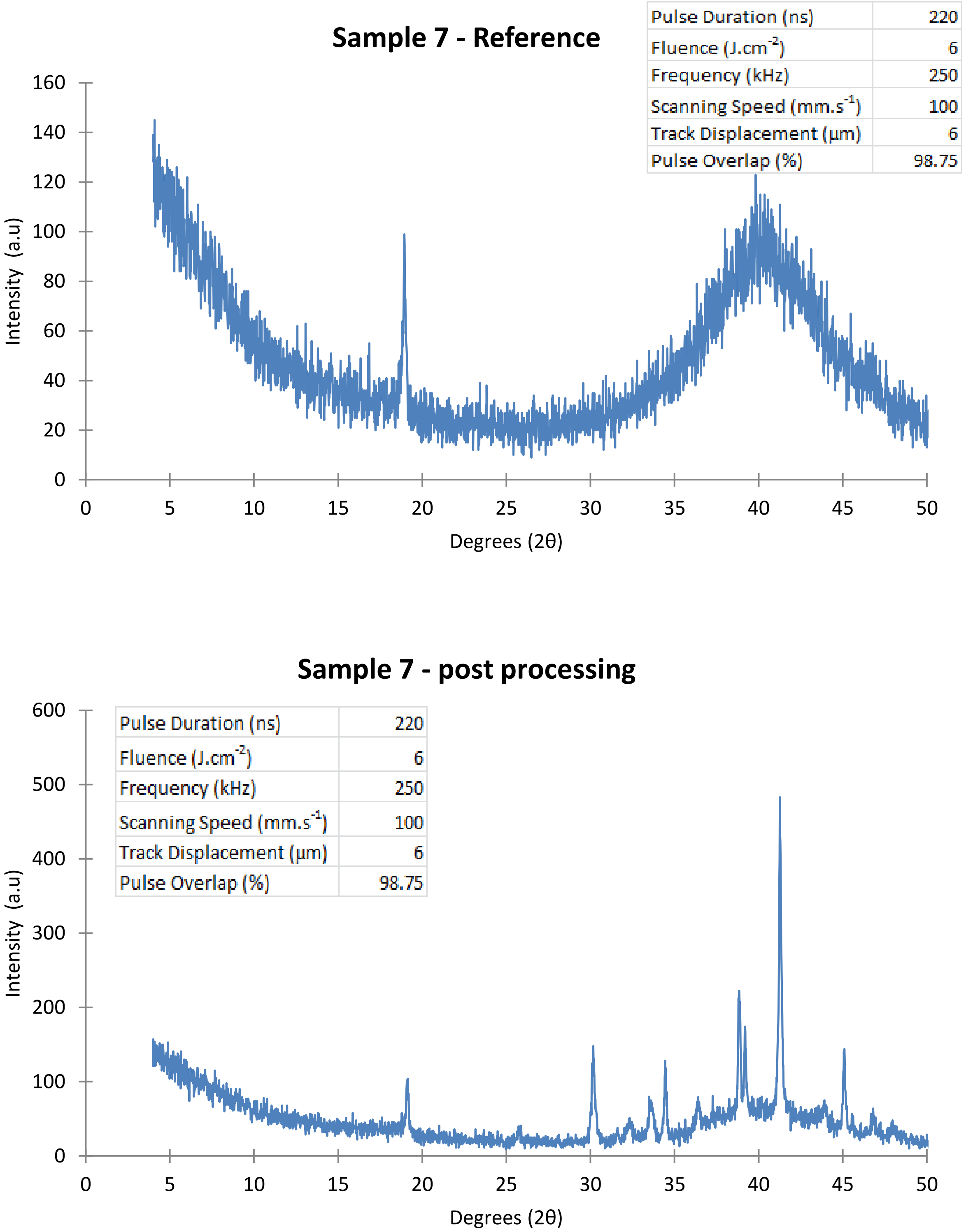

Pulse Duration (ns)	220
Fluence (J.cm^{-2})	6
Frequency (kHz)	250
Scanning Speed (mm.s^{-1})	100
Track Displacement (µm)	6
Pulse Overlap (%)	98.75

Pulse Duration (ns)	220
Fluence (J.cm^{-2})	6
Frequency (kHz)	250
Scanning Speed (mm.s^{-1})	100
Track Displacement (µm)	6
Pulse Overlap (%)	98.75

Figure 5.20 XRD patterns for sample 7 (a) pre-processing and (b) post laser processing. The additional peaks in the pattern produced after processing with the parameter values specified in the tables suggest crystallisation has occurred in the Vitreloy 1 sample. The length of the XRD scan for sample 6 post-processing was extended so as to achieve a finer image of the peaks to aid in the identification of each crystalline phase.

	Laser Processing Parameters					
Sample	**Pulse Duration (ns)**	**Fluence (J.cm^{-2})**	**Frequency (kHz)**	**Scanning Speed (mm.s^{-1})**	**Track Displacement (µm)**	**Pulse Overlap**
1	220	70	35	100	5	91
6	220	70	35	500	5	55
7	220	6	250	100	6	98.75

Table 5.4 Processing parameters for the samples that showed evidence of crystallisation as identified using the XRD analysis patterns pre and post processing.

The exact identification of all crystalline peaks for samples 1, 6 and 7 is a difficult task. Comparing the XRD patterns for the samples that showed evidence of crystallisation with diffraction powder patterns for many different compounds resulted in the identification of many phases within these samples. In this way, evidence of CuNi, ZrTi compounds including ZrTiNi and oxidation of the metallic elements such as NiO_2 and different variations of ZrO, was found for samples 1, 6 and 7. The peak that is displayed around 18° for all samples pre and post laser processing, is hypothesised to be an oxide, possibly of the form NiO_2, the powder pattern for which can be seen in Figure 5.21. This XRD pattern of the powder of NiO_2 was achieved using XRD analysis. These powder patterns can be used to verify the crystalline components within an XRD pattern of material through comparison of the placement of the peaks. It is thought that the sample experiences oxidation upon exposure to the ambient atmosphere, explaining the presence of the peak both before and after processing. The oxidation of the BMG sample, during processing, can favour the crystallisation of amorphous alloys that are based on the element Zirconium (Lin et al 1997). The resources necessary and the time needed to complete the precise characterisation of each peak are significant and should represent the focus of future work.

In summary, the observation of the XRD patterns concludes that sample 1, 6 and 7 display evidence of crystallisation, whilst the other samples do not. The difference in process parameters used to machine the samples that crystallise and those that do should be the reason for these results. In order to further investigate the effect of the variation in process parameters on the crystallisation of Vitreloy 1, the theoretical model, first presented in Chapter 4, was modified to be able to provide theoretical data regarding the temperature distribution for each of the seven parametric combinations utilised. The results of this additional study are the focus of the next section.

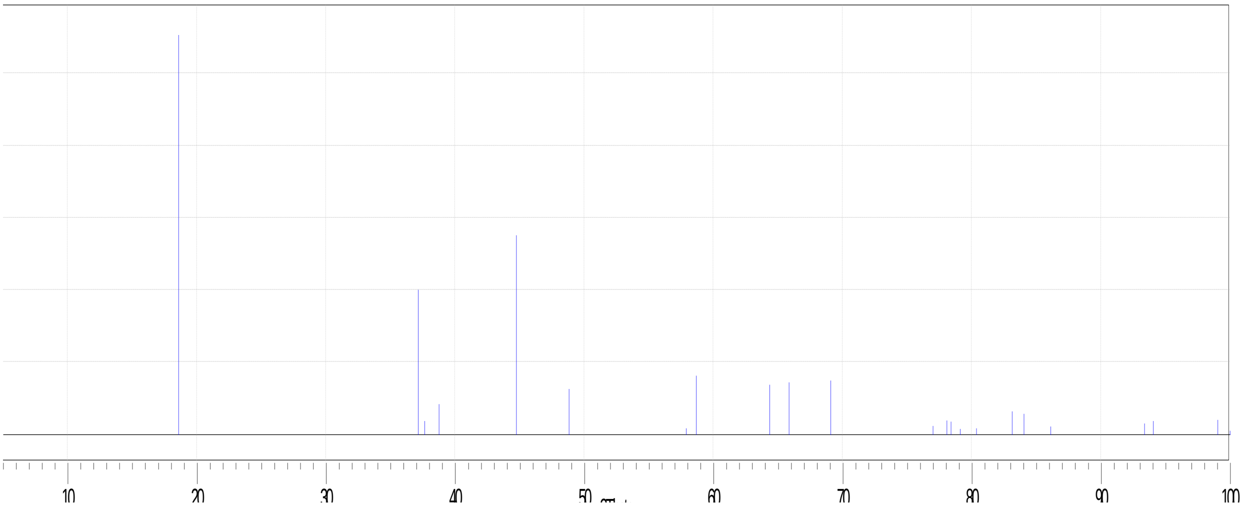

Figure 5.21 The pattern obtained using X-Ray powder diffraction for a sample of powder Nickel Oxide (NiO_2) displaying the peak at 18.55°. Data obtained from Hirano et al (1995).

5.4.3. Modelling of single pulses

The theoretical temperature evolution with time based on the model developed in Chapter 4 for single pulse heating and cooling cycles for each sample is presented in Figures 5.22 to 5.24. Results for samples 1, 3 and 6 share the same graph because they have the same pulse duration and energy. This is also true for samples 4, 5 and 7 while sample 2 has unique pulse length and fluence. This results in three different single pulses heating and cooling cycles for all 7 samples. From these theoretical predictions, it can be seen that samples 1, 3 and 6 reach a higher temperature than the other samples with a peak temperature above 3000 K. This high temperature could result in vaporisation of the molten material. There is uncertainty here however, due to the vaporisation temperature of Vitreloy 1 not being well documented. Vaporisation of molecules can alter the chemical composition of the material. Kim et al (2006) concluded that this could be a factor in increasing the likelyhood of crystallisation occurring upon cooling of the material. Samples 4, 5 and 7, experience a much lower temperature rise, with the peak only just reaching above the melt temperature of Vitreloy 1 (937 K). This is also apparent for sample 2, as a result of the low fluence delivered to the material substrate during single pulse laser processing.

The maximum temperature reached is not the only outcome that can be observed from the theoretical prediction. The model produces the complete heating and cooling cycle, thus giving results for the heating and cooling rates of the material during laser processing. The single pulse prediction for samples 1, 3 and 6, shows that they experience a heating rate in excess of 2.10^{10} $K.s^{-1}$. Their cooling rates are about 1.10^{9} $K.s^{-1}$ between the maximum temperature and the melting temperature. The other samples have lower heating rates of around 5.10^{9} $K.s^{-1}$ and cooling rates of about 1.10^{7} $K.s^{-1}$. If the samples are experiencing differences in both their cooling rates and the maximum temperature from which the cooling begins, this will affect the amount of time the material stays above the melt temperature until the next laser pulse is incident.

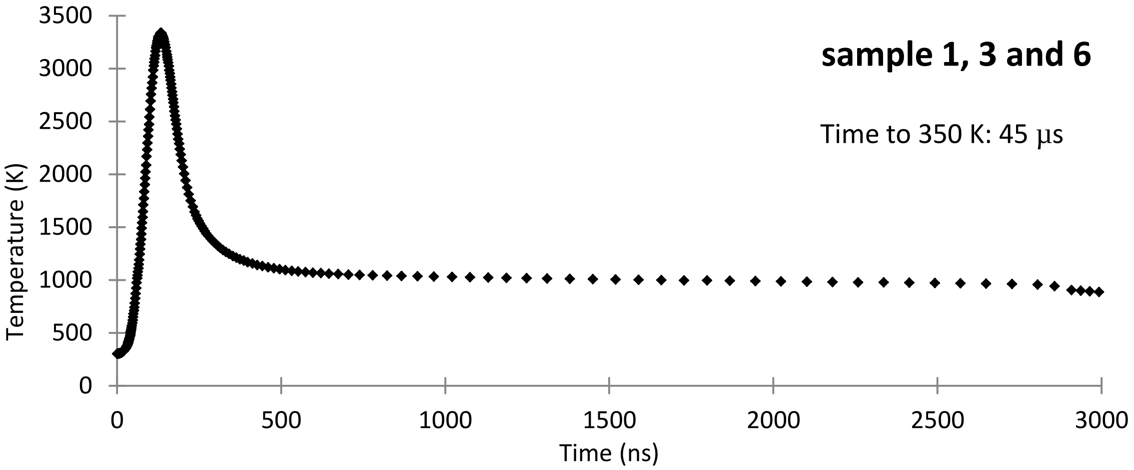

Figure 5.22 Single pulse heating and cooling cycle for samples 1, 3 and 6 for which the pulse duration is 220 ns and the fluence is 70 J.cm^{-2}.

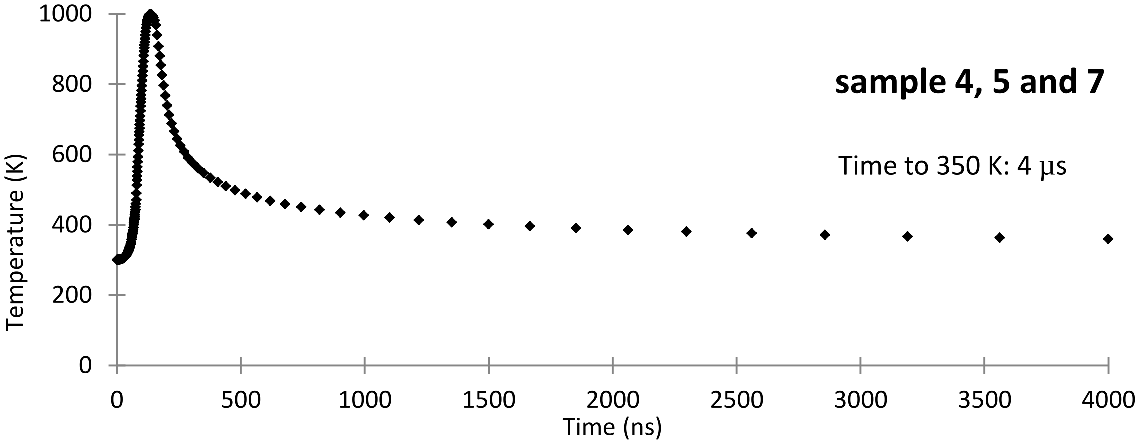

Figure 5.23 Single pulse heating and cooling cycle for samples 4, 5 and 7 for which the pulse duration is 220 ns and the fluence is 6 J.cm^{-2}.

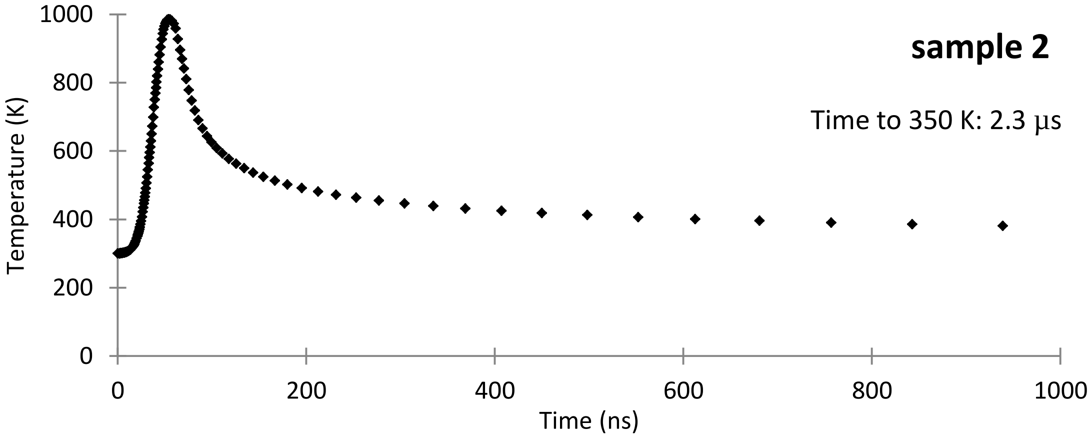

Figure 5.24 Single pulse heating and cooling cycle for sample 2 for which the pulse duration is 75 ns and the fluence is 4 J.cm^{-2}.

Even though the single pulse heating and cooling cycles are the same for some of the samples, differences between specimens occur with respect to the other parameters used for laser processing. In particular, for a fixed pulse repetition frequency, a sample scanned more slowly is subjected to more of the incident intensity overall as the Gaussian pulse moves from point to point less quickly as shown in Figure 5.25. This figure illustrates that, a faster scanning speed leads to less intensity being delivered at a given central point over a fixed amount of time.

The coupling of the applied scanning speed and the frequency leads to different pulse overlaps according to equation 3.2, and as reported in Table 5.3. Samples 1, 2, 4, 5 and 7 experience a high percentage overlap, over 80 %. This results in the subsequent pulse re-melting a large amount of the previously machined crater. A high overlapping could also result in larger heat accumulation.

The difference in frequency affects the period of the pulses. Sample 1 has a period of 28.10^{-6}s, and from the theoretical result presented in Figure 5.22, at this time the material will be at about 430 K, which is 130 K above room temperature. This means that, theoretically, every subsequent pulse could be incident on a surface which is 130 K hotter than the previous. Sample 4, on the other hand has a smaller period of 4.10^{-6} s, but also experiences a smaller single pulse temperature increase resulting in the material being close to room temperature of 300 K when the next pulse is incident.

During the investigations of Kim et al (2006), the authors studied the issue of crystallisation of the amorphous alloy $Cu_{54}Ni_6Zr_{22}Ti_{18}$ during multiple pulse interactions, using a ms Nd:YAG laser. They concluded that crystallisation within the heat affected zone of the laser interaction was due to the complete heating and cooling cycle whereas crystallisation within the weld was due to the cooling of the molten material. The authors also stated that the residual heat generation from one laser pulse can affect the heating cycle of the next pulse possibly causing crystallisation. How much heat accumulation that was experienced depends on the frequency and scanning speed of the laser pulses.

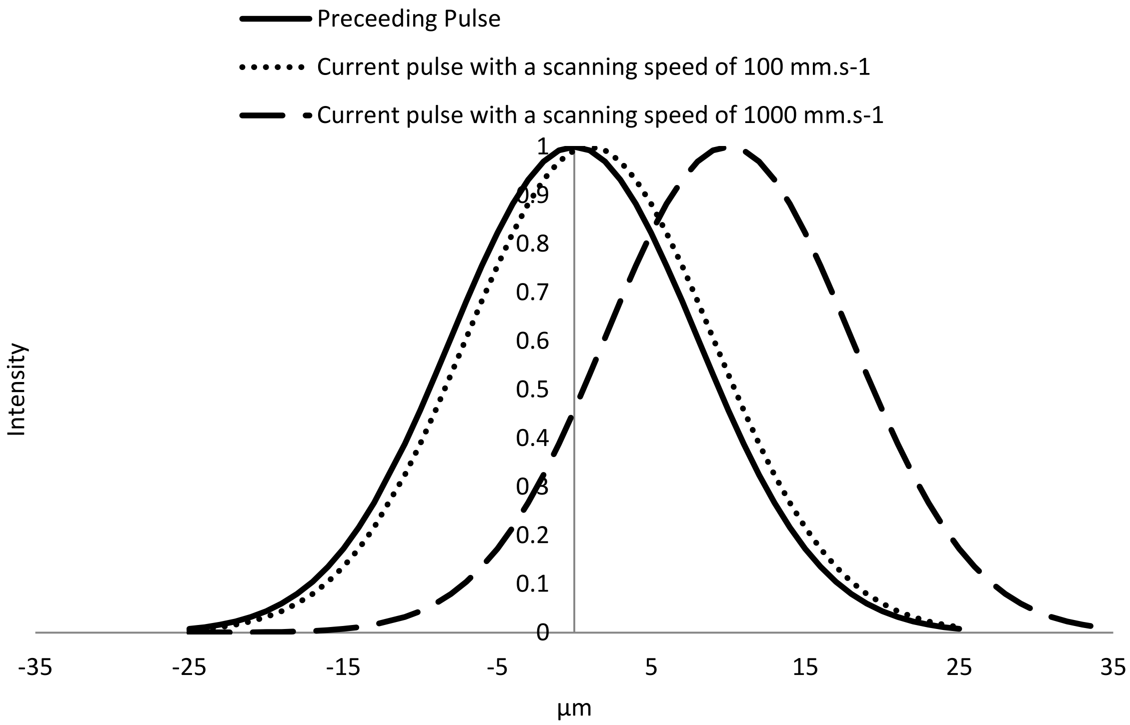

Figure 5.25 Illustration of the spatial intensity distribution on the top surface of the workpiece, for a current pulse with respect to the preceding pulse (solid line), when using two different scanning speeds: 100 mm.s^{-1} *(dotted line) and 1000 mm.s*$^{-1}$ *(dashed line).*

For example, as the frequency is increased, the heat input rate can become higher than the heat dissipation rate, allowing the temperature to reach higher values following the incidence of a number of pulses. The heating rates for all samples investigated in this study are over 1.10^9 K.s^{-1}. In comparison, the critical heating rate of Vitreloy 1 was reported to be 200 K.s^{-1} (Schroers et al, 1999). Therefore, it is suggested that the formation of crystalline precipitates observed for samples 1, 6 and 7 is likely due to the cooling cycle only.

Figure 5.26 shows the XRD pattern for a sample machined with an array of single pulses using the same parameters as those for sample 1, but in this case using a combination of scanning speed and frequency to ensure that the formed craters were spaced completely apart and thus to remove the effect of heat accumulation for overlapping craters. The data for the reference sample and for the laser processed sample do not show any discernible differences indicating that there is no crystallisation present following single pulse processing. In contrast, crystallisation did occur for sample 1 when such pulses were overlapped as reported earlier in Figure 5.14(b). Therefore, it is fair to assume that the accumulative heating occurring due to multiple pulses has an effect on the crystallisation mechanisms during laser machining. Even though the sample does not crystallise with the first pulse, it is possible that each subsequent separate pulse will introduce primary crystalline structures into the material sub system during its cooling cycle. Tang et al (2001) commented that during multiple pulse laser irradiation of amorphous silicon, using a 532 nm Nd:YAG laser with pulses at 3 ns, each subsequent laser pulse results in a much faster crystallisation process occurring, due to primary crystallisation structures having been introduced by the previous pulse. These crystalline structures may not melt during the subsequent pulse due to the higher melt temperature leaving them to act as facets for growth during further nucleation with the next pulses (Tang et al, 2001).

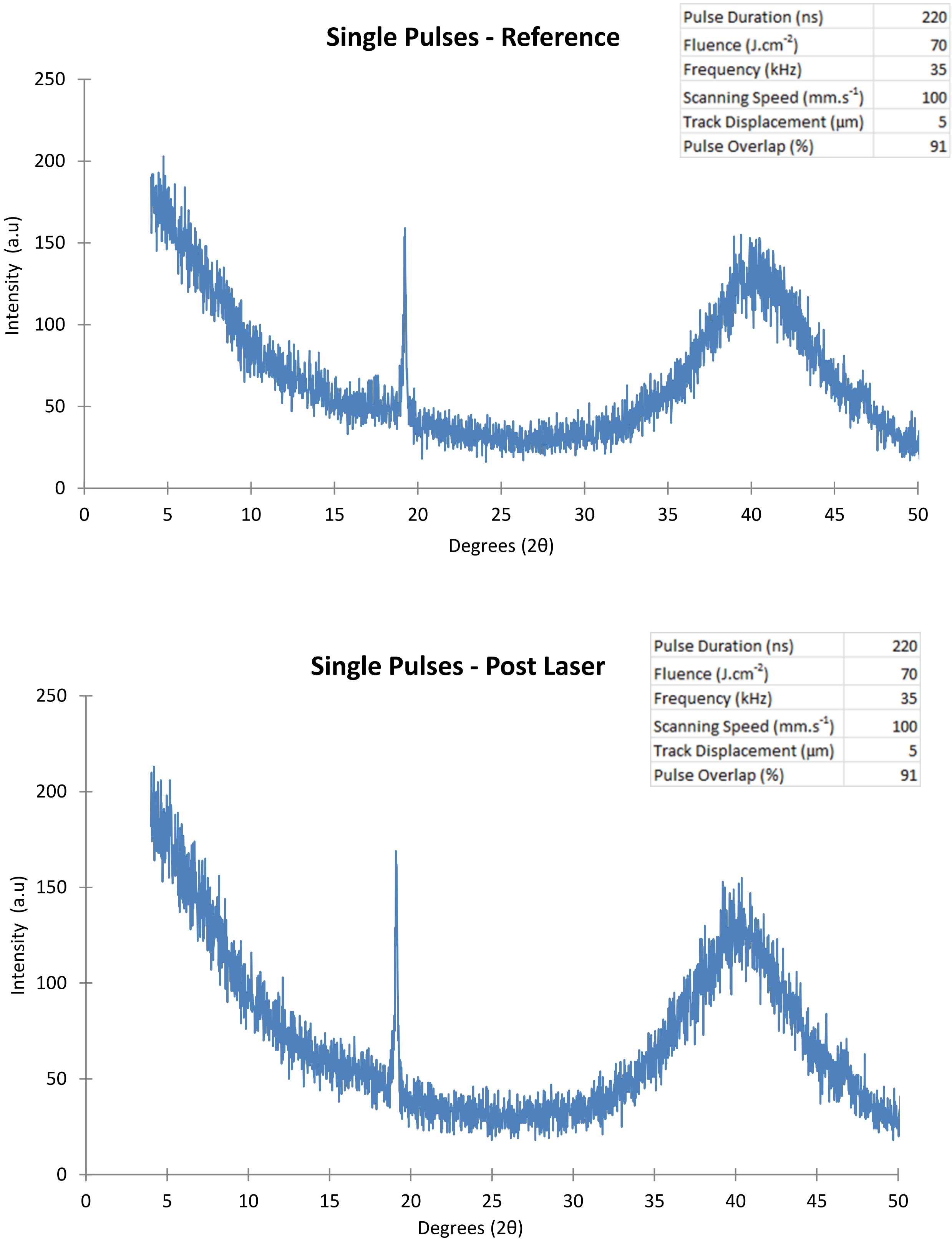

Figure 5.26 XRD pattern for a sample machined with single pulses (a) pre-processing and (b) post laser processing with parameters the same as sample 1.

5.4.4. Modelling of multiple pulses

The theoretical model that uses the software FlexPDE was presented in Chapter 4. In order to integrate multiple, moving pulses into the model, it was modified to include repetition of the Gaussian pulses, as well as movement of the pulse in space along the top surface of the material.

Samples 4 and 7 are of interest due to them being processed with identical parameters except for the scanning speed, which is 100 mm.s^{-1} and 1000 mm.s^{-1} for sample 7 and sample 4 respectively. Even though the scanning speed is the only difference, sample 7 crystallised yet sample 4 did not. In addition, compared to the samples that also showed crystallisation, sample 7 was processed with a fluence which was about ten times lower. The initial single pulse temperature profiles are the same for samples 4 and 7, as can be seen in Figure 5.23, yet the ten times difference in scanning speed affects the amount of effective source intensity available to process the material. The effect of this can be seen from the theoretical results in Figures 5.27 and 5.28 where the temperature variation with time for multiple pulses at the centre of the top surface for both samples is presented. Sample 4 experiences nine pulses that are effective in varying the temperature until the Gaussian pulse moves out of range of the central point as it scans the surface at 1000 mms^{-1}. The sample only reaches a temperature above the melting point for two of these pulses and the cooling time between the melt temperature and the glass transition temperature is very short, around 100 ns. This fast cooling does not give atoms in the melt enough time to organise themselves into crystal structures so when the material solidifies it stays in its amorphous phase. The cooling for sample 7 is different, due to the source moving more slowly along the surface and being effective for a longer period of time. As a result, after the pulse that raises the temperature above the melting point for the last time, the material takes over 1700 ns to cool down to the glass transition temperature where there will no longer be atoms that can move in a translational direction. Tang et al (2001) concluded that at low powers, a large number of

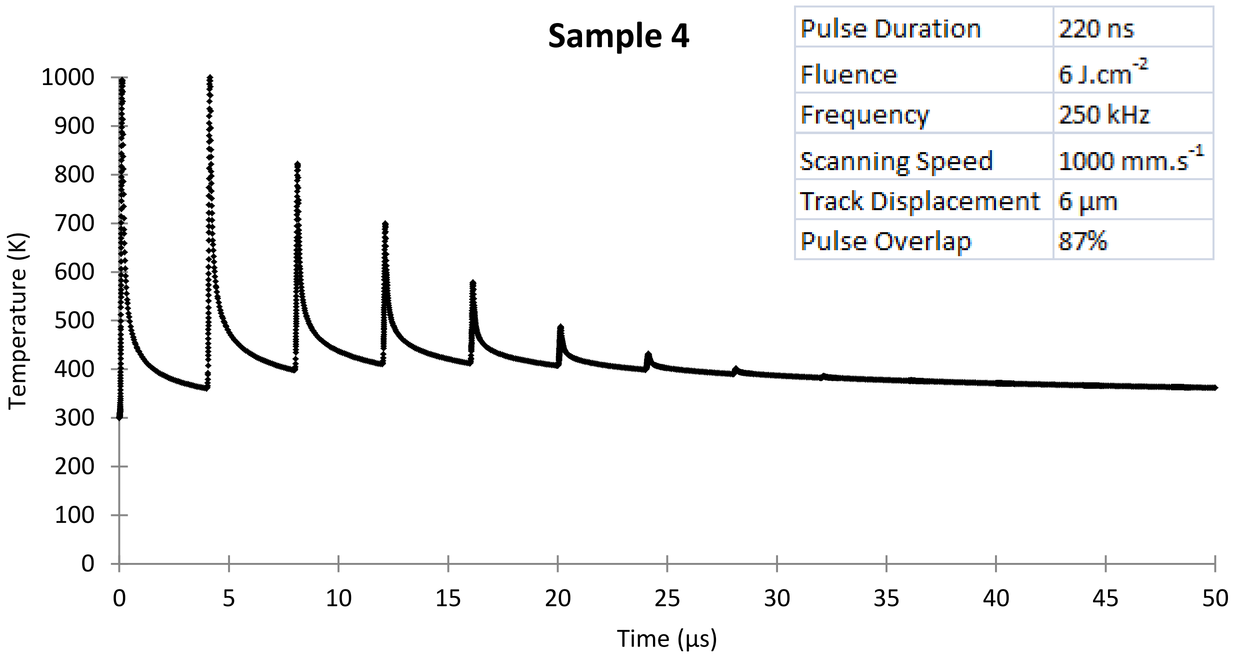

Figure 5.27 Predicted temperature distribution for multiple, moving pulses in the centre of the top surface of sample 4 over 50 µs.

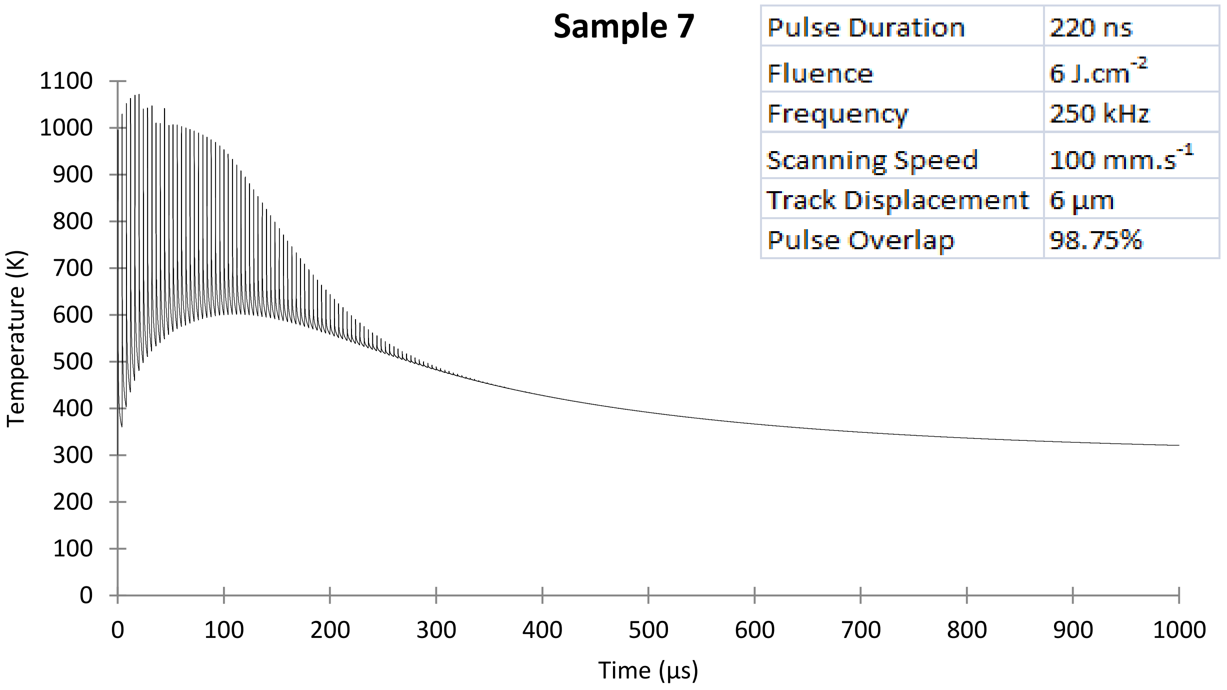

Figure 5.28 Predicted temperature distribution for multiple pulses in the centre of the top of sample 7 over 1000 µs.

pulses are needed to crystallise a sample of amorphous material, with each pulse causing precipitate growth on the back of the previous pulse. Both samples 4 and 7 have a large number of pulses at a low power, the difference being the amount of effective pulses is larger for sample 7 due to the much slower scanning speed. The important conclusion that can be made is that crystalline precipitate can be formed without large amounts of material removal which is associated with laser processing at higher fluence. This ability could be used in applications where the mechanical properties of a component need to be changed while it has already been processed into its net shape.

As shown with Figure 5.29, sample 3 only experiences two effective pulses due to the low frequency used. After the final effective pulse it takes 600 ns for the material to cool from the melt temperature to the glass transition temperature. Pulses for sample 6, on the other hand, move with a scanning speed which is 100 mm.s^{-1} less than that for sample 3. In this case the cooling time from the melting temperature to the glass transition temperature is close to 1600 ns as shown in Figure 5.30, which is a similar cooling period to sample 7 that crystallised. Sample 1 is processed using identical parameters to that used to machine sample 6, except that it is scanned at 100 mm.s^{-1} compared to the 500 mm.s^{-1} used for sample 6. Lin et al (2012) concluded that increasing the fluence whilst also reducing the scanning speed of the laser melting of an Mg-Cu-Gd bulk metallic glass, resulted in crystallisation. The theoretical results shown in Figure 5.31, predict a cooling time from the melt temperature to the glass transition temperature to be around 2000 ns for sample 1, an amount of time similar to the other samples that showed evidence of crystallisation. Figure 5.31 shows that sample 1 reaches a temperature that may vaporise the surface multiple times. The vaporisation of molecules from an alloy surface varies its composition. This can aid the crystallisation process. In particular, if the beryllium atoms vaporise due to being the lightest element, the zirconium and titanium and the copper and nickel may form crystalline structures more easily due to their proximity in the periodic table. Proper investigation of the crystalline products formed during each of the

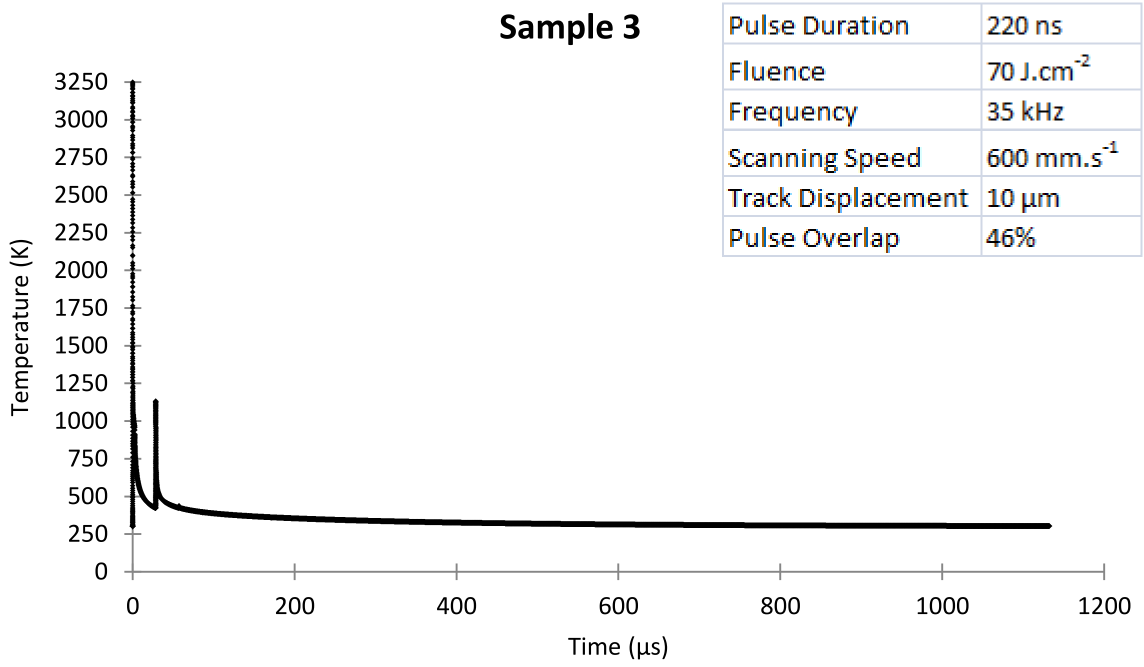

Pulse Duration	220 ns
Fluence	70 J.cm^{-2}
Frequency	35 kHz
Scanning Speed	600 mm.s^{-1}
Track Displacement	10 µm
Pulse Overlap	46%

Figure 5.29 Temperature distribution for multiple pulses in the centre of the top of sample 3 over 1200 µs.

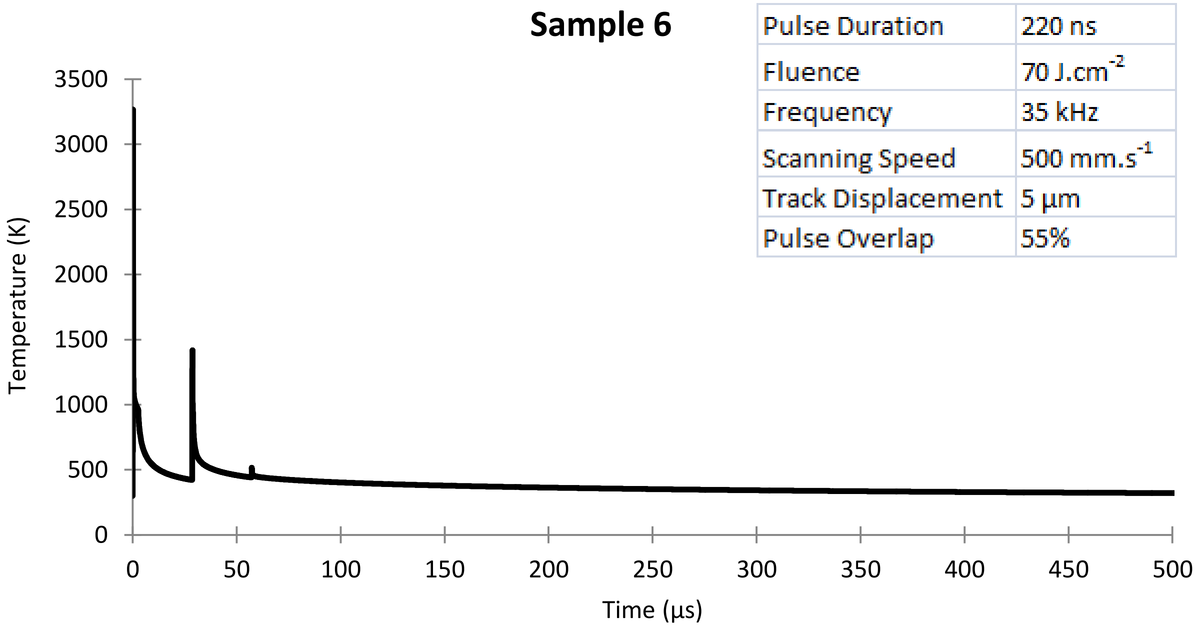

Pulse Duration	220 ns
Fluence	70 J.cm^{-2}
Frequency	35 kHz
Scanning Speed	500 mm.s^{-1}
Track Displacement	5 µm
Pulse Overlap	55%

Figure 5.30 Temperature distribution for multiple pulses in the centre of the top of sample 6 over 500 µs.

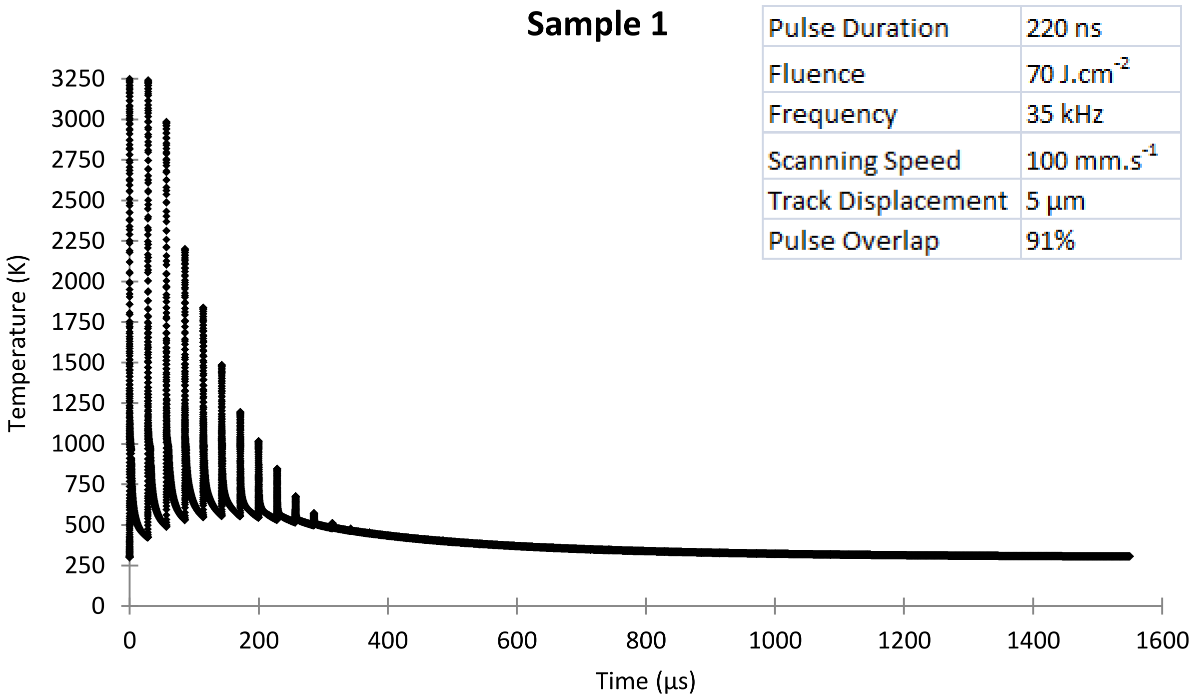

Pulse Duration	220 ns
Fluence	70 J.cm^{-2}
Frequency	35 kHz
Scanning Speed	100 mm.s^{-1}
Track Displacement	5 µm
Pulse Overlap	91%

Figure 5.31 The temperature distribution with time for multiple pulses for sample 1 over 1600 µs

samples processing may aid in the explanation of the reason for crystallisation, or lack thereof, for each parametric combination.

The cooling cycle for each sample can be seen in Figure 5.32. This figure indicates that each sample experiences different cooling rates as well as a different amount of pulses incident on the centre of the top surface of the material within the same amount of time. Figure 5.33 shows the comparison of the cooling cycle from the final pulse that induces phase change for all samples, with the time adjusted so that each final pulse begins at 0 ns, for comparison purposes. The samples that crystallise, (1, 6 and 7), display longer cooling curves than those that do not (3 and 4). The analysis above suggests the onset, or lack thereof, of crystallisation for each sample could be due to the differences in the time it takes for the sample to cool from the melting temperature (937 K) to the glass transition temperature (623 K). The values for this are taken from the final pulse that induces phase change from solid to liquid within the multiple pulses that are used to machine. Of course, the crystallisation could take place at any point within the accumulation of pulses. The crystallisation may even be due to the growth of crystals due to the nucleation occurring in previous pulses. This may be especially true for the sample that displays crystallisation at high frequencies and slow scanning speeds such as sample 7. This sample consistently cools at the same cooling rate as sample 1 in the final pulse that induces phase change, perhaps inducing larger vales of nucleation and growth. This effect can be seen in Figure 5.33 where sample 7 displays similar cooling curves to that of sample 1 but this cooling cycle occurs more frequently for sample 7.

The only fact known is that the samples that experience slower cooling rates between the melt temperature and the glass transition temperature, during each pulse under the multiple pulse envelope crystallises, and those that cool faster do not. So for the sake of analysis, the final pulse that induces phase change is chosen for discussion. The cooling rate that this final pulse induces within each sample, is shown in Table 5.5. These values suggest a critical cooling rate in between 0.21 $K.ns^{-1}$ (sample 6) and 0.52 $K.ns^{-1}$ (sample 3). If the sample is machined at rates slower than this it should exhibit crystallisation. The cooling curves that correspond to this table can be seen in Figure 5.34. The figure displays the part of the final pulse that induces melting, between the melt temperature and the glass transition temperature.

If the laser pulse results in a cooling curve that passes through the hypothetical boundaries of the dotted curve in Figure 5.34 within the time frame then crystallisation should occur. Any temperature variations outside of these boundaries should result in the retainment of the amorphous structure of the material. The curve is not an exact representation due to the lack of differential scanning calorimetry (DSC) data at these timescales and at these high heating and cooling rates. Addressing this lack of knowledge should be the focus of further work on the bulk metallic glass substrate, as well as the exact values for the thermal and optical temperature dependent properties of the material, in order to be able to increase the accuracy of the model and its assumptions. Schroers et al (1999) demonstrated the use of a DSC to detect the variation in the crystallisation temperature when varying the heating rate. It was concluded that as the heating rate was increased from 0.6 to 200 $K.s^{-1}$, the crystallisation temperature for Vitreloy 1 shifted to higher temperatures.

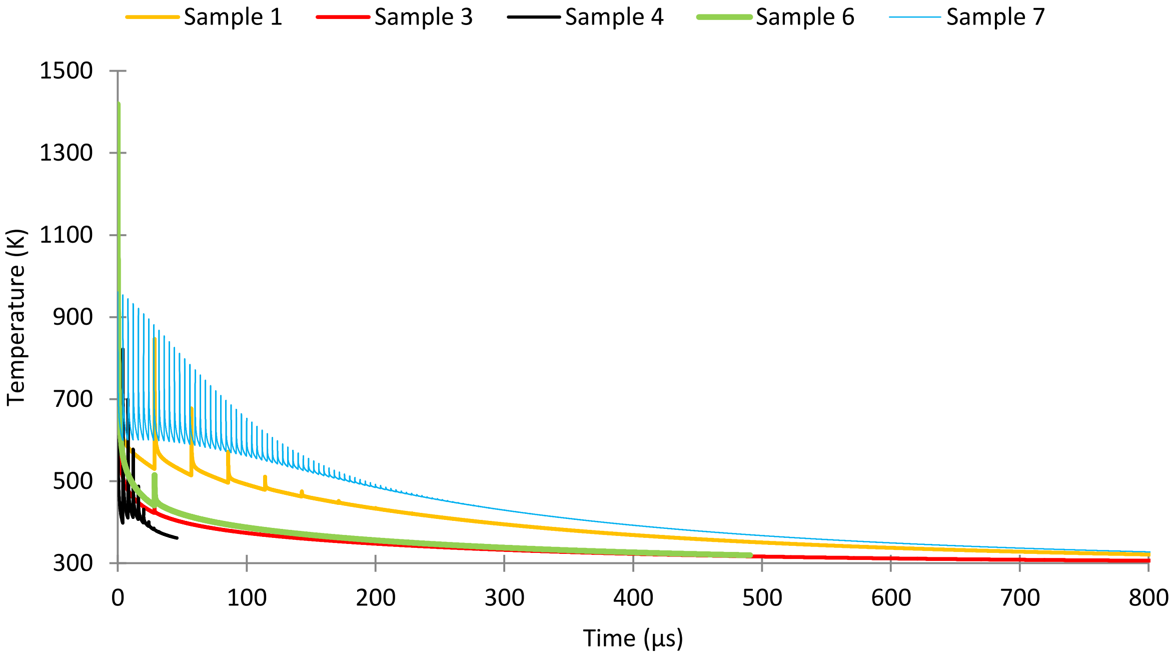

Figure 5.32 Theoretical heating and cooling curves for each sample in the centre of the top surface of Vitreloy 1.

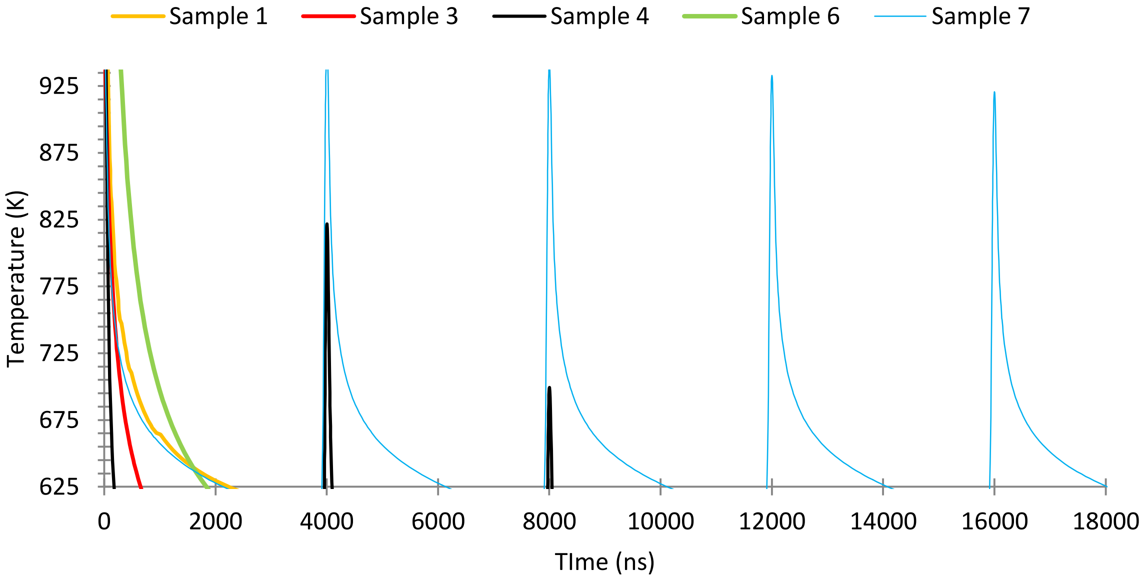

Figure 5.33 Comparison of effective cooling curves for the final pulse that causes phase change in the centre of the top surface of the substrate, between the melt temperature and the glass transition temperature for all samples processed.

Sample Number	Cooling Rate (K.ns^{-1})
1	0.16
3	0.52
4	2.13
6	0.21
7	0.16

Table 5.5 The cooling rates following the final pulse that induces a phase change for each sample between the melt temperature and the glass transition temperature obtained from the theoretical model.

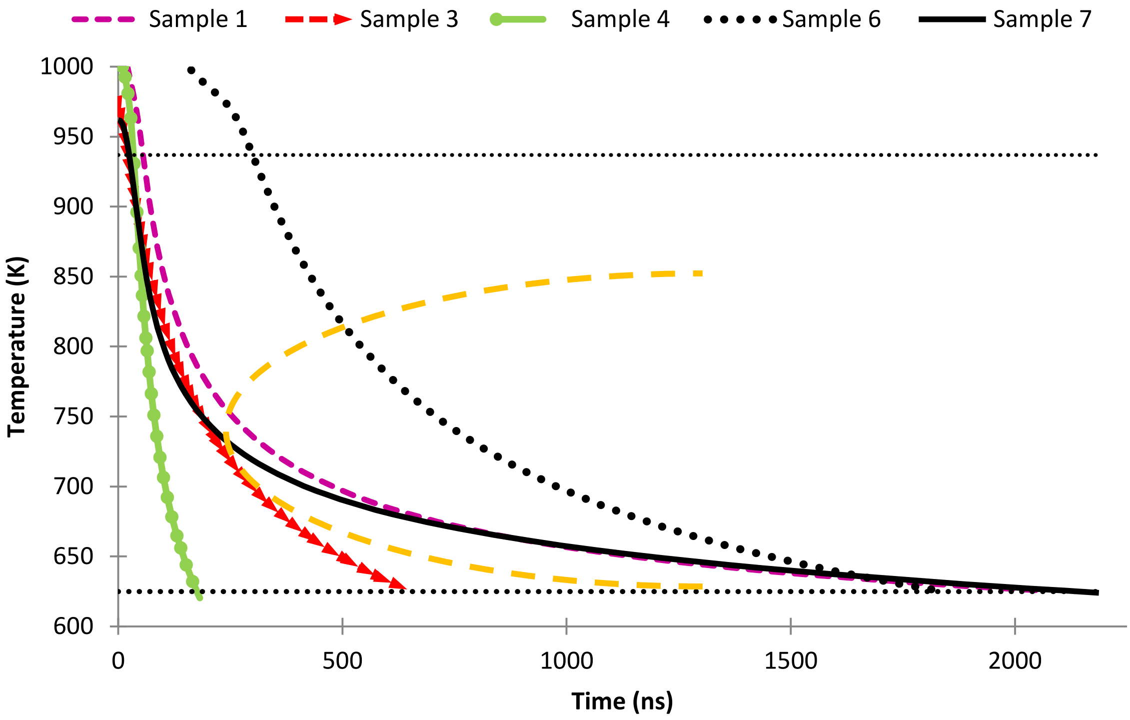

Figure 5.34 Cooling curve of the final pulse that induces phase change from solid to liquid for each sample machined between the melt temperature and the glass transition temperature. The dotted lines represent the melt temperature (937 K) and the glass transition temperature (623 K). The dotted curve represents a hypothetical version of the critical cooling curve for this material.

5.5 Summary

The experimental study reported on the single pulse nanosecond laser processing of a Vitreloy 1 BMG workpiece showed that an increase in the delivered fluence for each pulse length investigated results in an augmentation in both the diameter and the depth for the generated craters. For fixed fluence values, the increase of the pulse length led to an augmentation in the crater depth but it also resulted in a decrease in the crater diameter due to the peak power effect.

The single crater analysis also showed the various phases that the material goes through when the pulse parameters change. At higher fluence values, the melt ejection is significant and reaches far beyond the edge of the crater. At lower values of delivered fluence, i.e. between 13 J.cm^{-2} and 20 J.cm^{-2}, this material ejection is not as volatile and it occurs as droplets rather than "splashes" and the edges of the craters become more defined. At a fluence value below 12 J.cm^{-2}, the material is not ejected at all and the melt flows to the edges of the crater causing only a slight ridge.

A theoretical two-dimensional model of the interaction between the incident laser beam and the material was also developed. The prediction and the experimental results were found to be in good agreement with respect to the dimensions of the craters.

Further work was undertaken to expand the model for simulating repetitive pulsing at specific frequencies in order to predict the thermal load within the BMG work piece as a function of time. This is important in order to ensure that the processing parameters utilised during nanosecond laser milling do not lead to the crystallisation of the BMG material. It was shown that certain parametric combinations do lead to crystallisation of the material which was proven to be a result of heat accumulation. The crystallisation of certain samples milled with specific parametric combinations is hypothesised to be due to the slow cooling that these samples experience as shown in the theoretical model.

The experimental investigation of the milled samples showed evidence of crystallisation for samples that were machined at a high fluence, and also those machined at a low fluence but with a high frequency and low scanning speed. The XRD patterns were analysed and from then, it was determined that the crystallized components were many and varied from metallic components to oxides which have been proven to aid in the crystallisation of Zr-based amorphous alloys.

The chapter concludes that the crystallisation and retainment of amorphous structure can both be achieved through nanosecond fibre laser milling of a zirconium-based bulk metallic glass, with various removal rates. Further work needs to be carried out in order to complete the analysis using a larger range of laser parameters, as well as an in depth analysis of the material properties, especially those that are temperature dependent, to further increase the accuracy of the theoretical model. Due to the high heating and cooling rates apparent when using a nanosecond laser to mill the bulk metallic glass, the dynamic properties of the crystallisation and glass-transition temperature, have not been presented in research. Knowing these properties would greatly increase the ability to predict the behaviour of the amorphous alloy upon heating and cooling with ultra high rates.

Conclusions and Future Work

6.1 Knowledge Gaps

The literature review presented in Chapter 2 identified a number of knowledge gaps surrounding laser material processing using a MOPA-based nanosecond fibre laser. In particular these gaps were considered to be:

1. The opportunity to address the inherent uncertainty when using multiple laser systems for the investigation of the effect of the pulse duration on the machining outcomes.
2. The relatively scarce research efforts reported on the optimisation of machining operations using MOPA-based nanosecond lasers. Specifically, the gap in knowledge relating to the optimisation of machining outcomes results from the need to compromise between a high material removal rate, whilst retaining a low surface roughness. Thus, further investigations were identified to achieve both of these responses simultaneously in an efficient manner.
3. The need for complimentary theoretical and experimental investigations of the basic nanosecond laser material interaction for a wide range of engineering materials. Obtaining this understanding was also seen as beneficial in the selection of optimum process parameters.
4. The lack of studies using the relatively high heating and cooling rates induced when machining with a nanosecond laser on amorphous metallic glasses including investigations of the crystallisation behaviour.

6.2 Chapter 3: Nanosecond fibre laser machining of aluminium

6.2.1 Aim

The first issue that the literature identified could be tackled using a fibre laser system having the ability to vary the pulse duration over a wide range of values from 15 to 220 ns. The second knowledge gap was also addressed in Chapter 3 by aiming to 1) investigate the effect of varying the pulse repetition rate on the material removal rates and surface roughness values over a range of pulse durations and 2) optimise the process using a design of experiment approach that followed the Taguchi parameter design method.

6.2.2 Contributions

The main contributions from Chapter 3 lies in the systematic investigation of a number of pulse durations in the nanosecond regime when performing milling operations on an aluminium workpiece with a 1064 nm wavelength Yb fibre laser.

6.2.3 Conclusions

Two machining outcomes were investigated first, the material removal rate and the surface roughness, with respect to a variation in the frequency for ten different pulse durations. The conclusions from this part of the chapter are as follows:

1. At the frequency where the highest pulse energy and average power occurs (PRF0), the resulting material removal rate and surface roughness is high. This trend is consistent for the range of pulse durations investigated.
2. For each pulse duration, the surface roughness varies with the frequency with a minimum occurring at 30-40 kHz. This minimum has been attributed to the variation in the pulse overlap affecting the removal of material from pulse to pulse.

3. Generally, at a specific frequency, an increase in pulse duration leads to an increase in material removal rate and surface roughness.

The second half of the chapter focused on the Taguchi parameter design method to determine the effects of three other process parameters. This study revealed that:

4. After statistical analysis of the experimental data, it was found that the track displacement was the most significant parameter with regards to both machining responses.
5. Applying the Taguchi parameter design method led to a 60% reduction in the achievable surface roughness whilst retaining the high material removal rate for the particular pulse duration considered, 55 ns. This result illustrates the benefit of employing the design of experiments approach for optimising the laser machining process.

6.3 Chapter 4: Theoretical and experimental study of laser-material interaction with single pulses.

6.3.1 Aim

To focus on knowledge gap number 3, a single pulse machining method was applied in Chapter 4. This allowed the material interaction mechanisms occurring between the laser and the material to be investigated without the interfering effects, such as heat accumulation, of multiple pulses. In particular, the aim of Chapter 4 was to study the laser material interaction mechanisms on a wide range of materials, specifically silicon carbide, silicon and titanium, over a number of pulse durations and fluence values using both experimental and theoretical methods.

6.3.2 Contributions

In this chapter, a theoretical model was developed and employed as a useful tool for the prediction of material removal fluence thresholds and of the trend in material removal as the process parameters are varied. This theoretical model was validated against both published literature and experimental data collected in the second half of the chapter. These experimental observations contributed to the understanding of the laser material interaction for three different engineering materials. Using scanning electron microscopy and an optical measurement technique, the geometrical variation and the phase change behaviour was characterised when varying the system parameters. A thorough understanding of the processing response to parametric variation can aid in the efficient selection of parameters and materials for specific industrial applications.

6.3.3 Conclusions

The main conclusions from Chapter 4 can be summarised as follows:

1. Increasing the fluence of the laser beam increases the diameter and depth of the resulting craters for all the materials investigated.
2. As the fluence increases, the topography of the craters changes. The rims of the craters display re-solidified melt at lower fluence which then changes to eject melt around the crater edges as the fluence increases and the pressure from the vaporised material begins to have an effect.
3. All the materials investigated experience an increase in the depth of the single pulse craters as the pulse duration increases, an observation related to the augmentation in the conduction of heat at longer pulse durations.
4. It was found that processing with a long pulse duration and a large fluence results in large material removal values but with a lot of unwanted effects such as debris around the crater resulting in a low quality crater. When the materials are processed with a shorter pulse, the higher peak power results in a vaporisation driven process producing less melt ejection and debris.
5. The ceramic nature of the silicon carbide results in the cleanest craters when comparing with the silicon and titanium craters, especially at elevated fluence. This effect was thought to occur due to the direct transition of the silicon carbide from solid to vapour during the laser material interaction process.
6. A good agreement was generally found when comparing the theoretical investigation with the results from the experiments, across the range of pulse durations and fluence values considered.

6.3.4 Future Work

The future work identified from this chapter concerns the advancement of the theoretical model to include vaporisation and plasma shielding effects to be able to gain a clearer and more accurate insight into the laser material interaction process. It would also be useful to characterise the interaction for a wider range of laser systems, such as those at higher power or shorter pulse durations, and materials.

6.4 Chapter 5: Nanosecond laser machining of $Zr_{41.2}Ti_{13.8}Cu_{12.5}Ni_{10}Be_{22.5}$.

6.4.1 Aim

The aim of Chapter 5 was to address the lack of literature surrounding the response of a zirconium based bulk metallic glass, namely Vitreloy 1, to the laser processing using a 1064 nm MOPA-based nanosecond Yb fibre laser. The focus was on the behaviour of the bulk metallic glass when subjected to the ultra-high heating and cooling rates induced when operating the laser in single pulse and multiple pulse mode. For the latter case, the specific interest was on the study of the crystallisation behaviour.

6.4.2 Contributions

Due to the scarcity of literature surrounding the nanosecond laser processing of Vitreloy 1, the observations in Chapter 5 contribute to the basic understanding of the laser-Vitreloy 1 interactions. Specifically, the determination of the parametric combinations that did or did not lead to crystallisation and the possible explanations for this behaviour is an original contribution to the quest to understand the processing responses of this relatively young, yet remarkable, engineering material.

6.4.3 Conclusions

With respect to the single pulse processing of Vitreloy 1, the main conclusions include:

1. The topographical evolution of the single craters produced on the Vitreloy 1 surface when an increase in fluence is applied at a fixed pulse duration is the same as that for the materials presented in Chapter 4. More specifically, this increase in fluence also results in an augmentation in both diameter and depth of the craters.

2. For a fixed fluence value, an increase in pulse length results in a deeper crater, which is attributed to the same heat conduction effect as discussed in Chapter 4.
3. A rippling effect is seen just outside the edge of craters generated at a pulse duration of 15 ns. This phenomena is attributed to the temperature rise in this heat affected zone, which causes softening of the bulk metallic glass above its glass transition temperature without reaching the melt temperature while the pressure from the molten material flow coming from the centre of the crater causes the heat affected zone to deform plastically.
4. XRD patterns indicate that crystallisation does not occur when machining with ns single pulses in the range of fluence values considered. Therefore, it is suggested that crystallisation may occur in the laser milled samples due to the accumulation of heat, which is occurring when multiple, moving pulses are overlapped.

The complementary investigation into the multiple pulse milling of Vitreloy 1 concluded that:

5. Crystallisation can occur for different parametric combinations. The XRD patterns for the milled samples suggest that crystallisation occurs when the material is scanned slowly (100 mm.s^{-1}) at large frequencies (250 kHz) and at low fluence (6 J.cm^{-1}) but also when the surface is processed quickly (500 mm.s^{-1}) with large fluence values (70 J.cm^{-1}).
6. Within the processing widow considered, crystallisation was more likely to occur when the cooling cycle was slower as it allows more time for the nucleation and growth of crystal structure with the atomic base of the material. This conclusion was reached using an expansion of the developed theoretical model to integrate multiple moving pulses. The model predicts that a cooling rate lower than 0.21 K.ns^{-1} results in crystallisation.

6.4.4 Future Work

Further work was identified during the research reported in Chapter 5 including the necessity of obtaining the exact values for the temperature dependent thermal and optical properties of the bulk metallic glass used. It was also identified that due to the ultra-high heating and cooling rates, the glass transition temperature as well as the crystallisation temperature reported in the literature may not be accurate. During the analysis of the XRD patterns, the recorded crystallisation peaks varied depending on the parameters used. The comprehensive identification of these peaks may further illuminate the phenomena occurring during the laser processing of Zr-based bulk metallic glass.

Appendix

Table A.1 Overview of a few of the important papers reviewed in this chapter including the method used, the main conclusions reached comments on the strength of the model.

Name of paper	Method	Results	Comments
Analytical solution for time unsteady laser pulse heating of semi-infinite solid. Yilbas (1996)	Time unsteady analysis of heating with an analytical solution of the Fourier equation.	Temperature distribution on the surface including the maximum temperature. The lowest frequency below which, repetitive pulsing of the laser source will not produce a continuous wave-like effect on the material.	No melting or vaporisation was included in the model.
Laser pulse heating and phase changes in the irradiated region: Temperature-dependant thermal properties case. Yilbas and Mansoor (2009)	Heat conduction through solid and liquid modelled with the Fourier heat conduction equation. During phase change an energy balance is used to describe the enthalpy changes in the mushy zone with different latent heat values for different phases. The governing equations were solved using a finite difference method.	The temperature field, the formation of the mushy zones for solid-liquid and liquid-vapour were modelled, as well as the size of the cavity formed. These results were found for temperature dependent material properties and temperature independent material properties.	
Numerical simulations – a versatile approach for better understanding dynamics in laser material processing Otto et al (2011)	The basic heat equation is used with the latent heats iteratively corrected by use of the enthalpy. The latent heat of evaporation is used to calculate the mass flow and then the mass flow is used as a source term for the Navier –Stokes	The model gives the possibility of tracing the induced melt and vapour flow of laser beam welding, drilling and cutting.	The coupling of thermo-mechanics and the fluid dynamics has not been addressed.

	equation. The finite volume method is used to solve the equations.		
Effect of laser parameters on laser ablation and laser-induced plasma formation: A numerical modelling investigation. Bogaerts and Chen (2005)	The heat conduction equation is used to describe the heating of the solid and the liquid phases using different thermal data. Vaporisation temperature is calculated from the Clausius-Clapeyron equation.	The temperature distribution, the melt depth, and the evaporation depth were modelled as well as various properties of the plasma plume.	The model accounts for plasma expansion into a background gas and is mainly orientated to those working with laser induced breakdown spectroscopy.
Enthalpy model for heating, melting and vaporisation in laser ablation. Alexiades and Autriques (2010)	Description of the heat conduction and phase changes in terms of the enthalpy. Separate volumetric enthalpy equations are created for each phase. The finite volume method is used to discretize the equations.	The model is used to simulate laser ablation of copper. The melt and vaporisation depth as well as the vaporisation temperature over the pulse duration is modelled.	This model accounts for the entire laser ablation process and because it is dimensionless it can be applied in all three dimensions.
Computational study of heat transfer and gas dynamics in the pulsed laser evaporation of metals Ho et al (1995)	One dimensional heat conduction equation is used with enthalpy included to account for the changes in phase. This is solved by using a finite difference method. The dynamics of the vapour phase are described by the Euler conservation equations. These equations were solved using a compressible flow algorithm.	The surface temperature profile is modelled as well as the melt depth. Vapour properties such as its pressure and temperature are modelled.	
One dimensional steadystate model for damage by vaporisation and liquid expulsion due to laser material interaction	Conduction in the solid and liquid regions is modelled using a 1D heat conduction equation. The fluid flow of the molten material is	The surface temperature and the thickness of the molten layer is modelled with respect to the amount of	The vapour plume was assumed to be optically thin so that the absorption of the laser beam within it was negligible.

Chan and Mazumder (1987)	modelled with a 1D flow equation, and the vapour properties are modelled using gas dynamics. Some of the equations are solved analytically whilst the more complex are solved using the numerical Newton-Raphson method.	absorbed power. The total removal rate of material is modelled taking into account the vaporisation and the liquid expulsion.	
Mathematical modelling of laser induced heating and melting in solids Shen et al (2001)	Split the process into two parts – before melting and after melting. Before melting the thermal conduction is described by the heat conduction equation for solid phase. After melting there are two equations – one for the solid region and one for the molten region. The equations are solved analytically for a variety of materials.	The temperature profile over time and depth is modelled for many different materials and the melt depth is also calculated.	The material properties are assumed to be independent of temperature.
Calculations and experiments of material removal and kinetic energy during pulsed laser ablation of metals. Fahler and Krebs (1996)	The 1D heat conduction equation was used with extra terms to account for the absorption of the laser radiation and the heat of evaporation. The ablation mechanism was described by the kinetics of evaporation. A finite element procedure was used to solve the equations.	The temperature profiles in the target material were modelled this gave information on the mechanism of laser material interaction.	The absorption in the plume of evaporated material is assumed using the same optical properties as the bulk material. Plasma effects were neglected.
Modelling of plasma-controlled surface evaporation and condensation of Al target under pulsed laser irradiation in the nanosecond regime.	Heat transfer was described by the heat conduction equation. The processes and the movement in the vapour were described by gas	The optical characteristics of the plasma were modelled for two different wavelengths of the incident laser	Melting was not accounted for because of its added complication to the model and it was considered to not have a significant

Mazhukin et al (2007)	dynamics and the laser radiation transfer equation. The subsequent heating of the plume by laser irradiation and the thermal transfer was approximated by using energy balance equations. A finite difference technique was used to solve the differential model.	irradiation. The thickness of the layer of material removed is also modelled.	effect on the surface phase transitions.

Method for the determination of the spot size.

A thin chromium film was produced on a fused silica base. A line of overlapping pulses was machined at decreasing values of power. Each line was processed using the same short pulse duration of 15 ns and a low overlap value, achieved by using a frequency of 20 kHz (PRF0 of 170 kHz) and a scanning speed of 100 mm.s^{-1}, in order to ensure the limitation of unwanted thermal effects and the cleanest material removal possible so as to be able to achieve reliable, accurate data. The laser power for each line was reduced from 90% to 20% average power with material removal ceasing at 40%. Every average power value was repeated five times to increase the accuracy of the data. The actual average power output was measured using a powermeter, and the width of the resulting lines measured using an optical microscope. The resulting average power for each line series and the corresponding average line width, from the five repeated lines, can be seen in Table A.2.

Due to the assumption that the thin film has a constant removal threshold, a series of values for F_{th} can be obtained using the following equation and using the data produced from measuring the lines machined in the thin chromium film as the values for '*r*';

$$F_{th} = \frac{2.(1-e^{-2}).(pulse\ energy).exp^{\frac{-2.r^2}{w_0{}^2}}}{(\pi.w_0{}^2)} \tag{A.1}$$

Where F_{th} is the threshold fluence, *r* is defined as the width of the machined test lines and w_0 is the radius of the beam. Different values of w_0 can be used in order to find the value that gives the most constant value of F_{th} for all experimental lines produced in the thin film. Figure A.1 shows the results of the calculation using equation A.1 with the value of w_0 that gives the best fit, and a value that is too small. The value of w_0 that is too small, 10 µm, has a calculated maximum threshold fluence forty times larger than the minimum. At 16.25 µm, the variation is around three times from the minimum to the maximum calculated threshold fluence.

Percentage Average Power (%)	Actual Average Power (W)	Track Width (µm)
90	1	25.04
85	0.79	24.5
80	0.62	23.11
75	0.44	21.35
70	0.3	20.94
65	0.2	19.5
60	0.09	18.97
55	0.05	17.65
50	0.03	15.44
40	0.001	N/A
30	0	N/A

Table A.2. Values of actual average power corresponding to the percentage average power, as measured with a power meter at specific frequency of 20 kHz below the PRF0 which is 170 kHz.

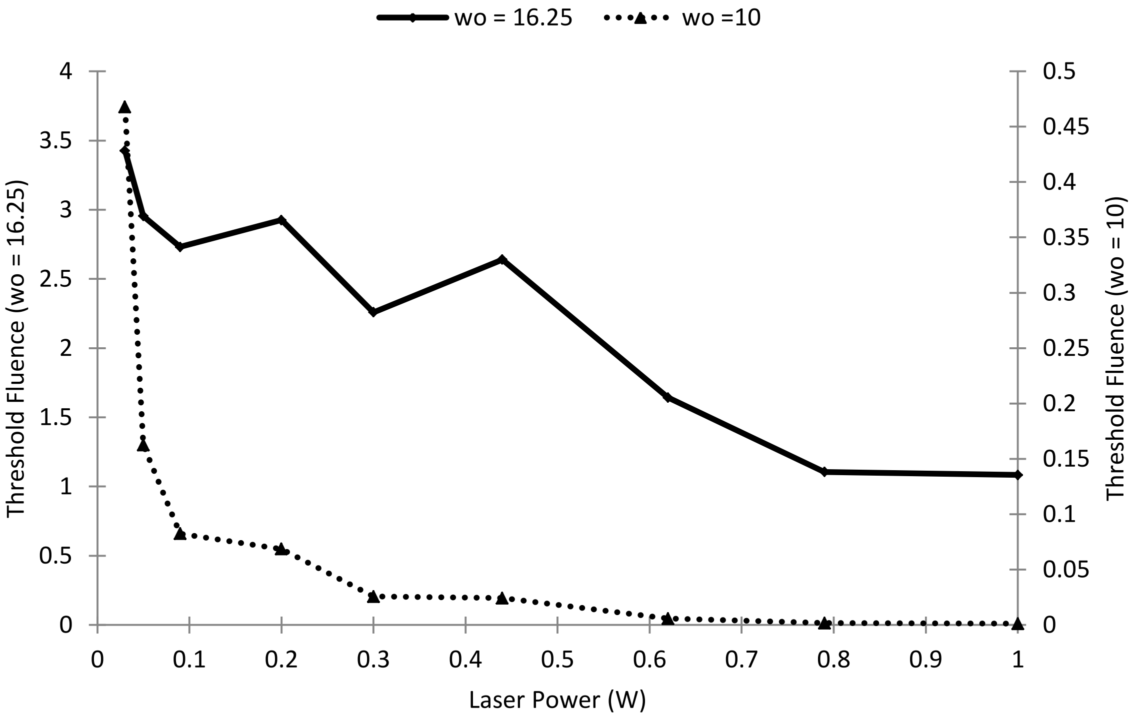

Figure A.1 A graphical representation of the best fit beam radius that results in the most constant value of the threshold fluence. The dotted line uses a value of radius too low and the solid line represents the value of radius for the best fit. The value of w_0 that results in the best fit for F_{th} can be assumed to be the radius of the laser beam.

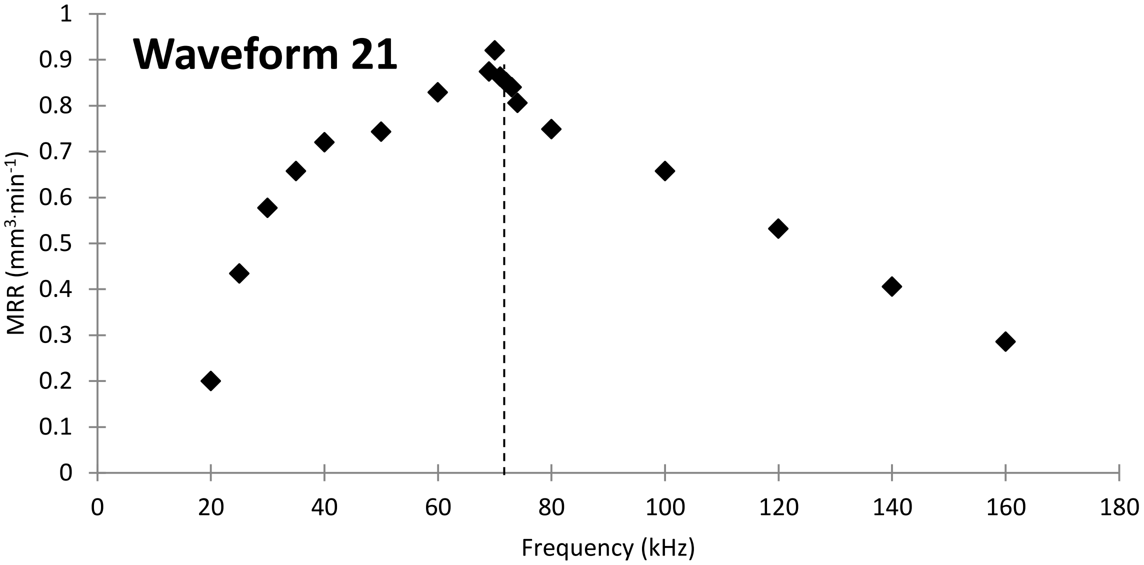
Waveform 21
MRR (mm^3·min^{-1})
1
0.9
0.8
0.7
0.6
0.5
0.4
0.3
0.2
0.1
0
0
20
40
60
80
100
120
140
160
180
Frequency (kHz)

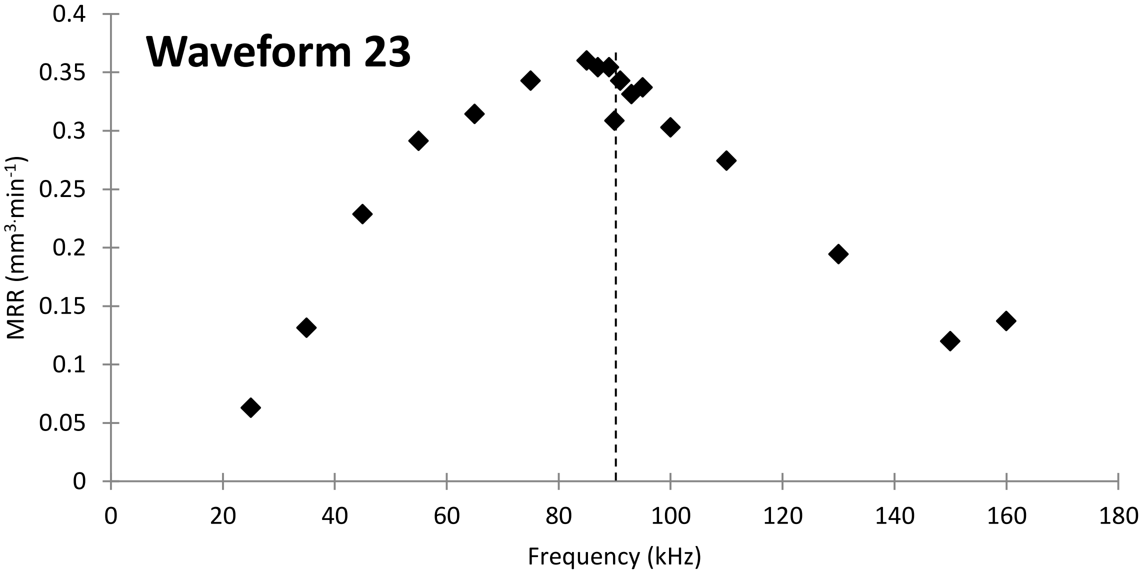
Waveform 23
MRR (mm^3·min^{-1})
0.4
0.35
0.3
0.25
0.2
0.15
0.1
0.05
0
0
20
40
60
80
100
120
140
160
180
Frequency (kHz)

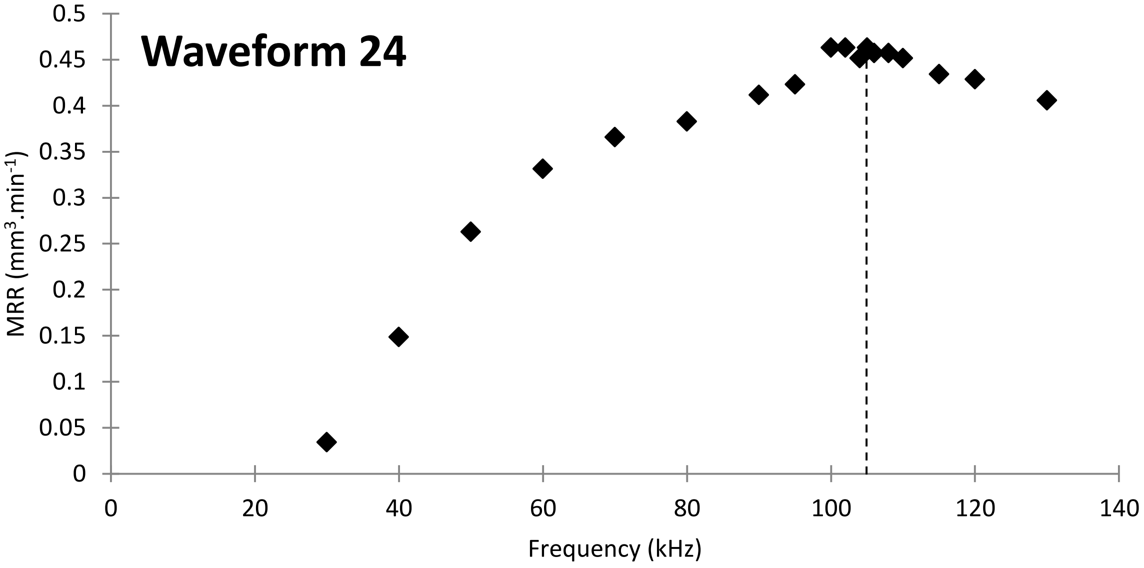
Waveform 24
MRR (mm^3.min^{-1})
0.5
0.45
0.4
0.35
0.3
0.25
0.2
0.15
0.1
0.05
0
0
20
40
60
80
100
120
140
Frequency (kHz)

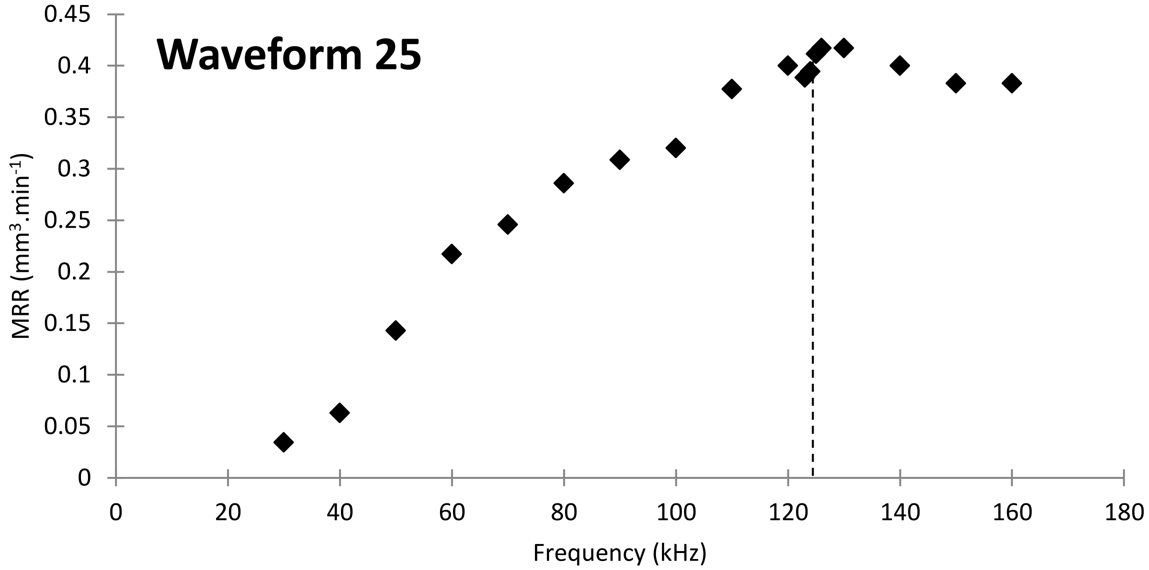

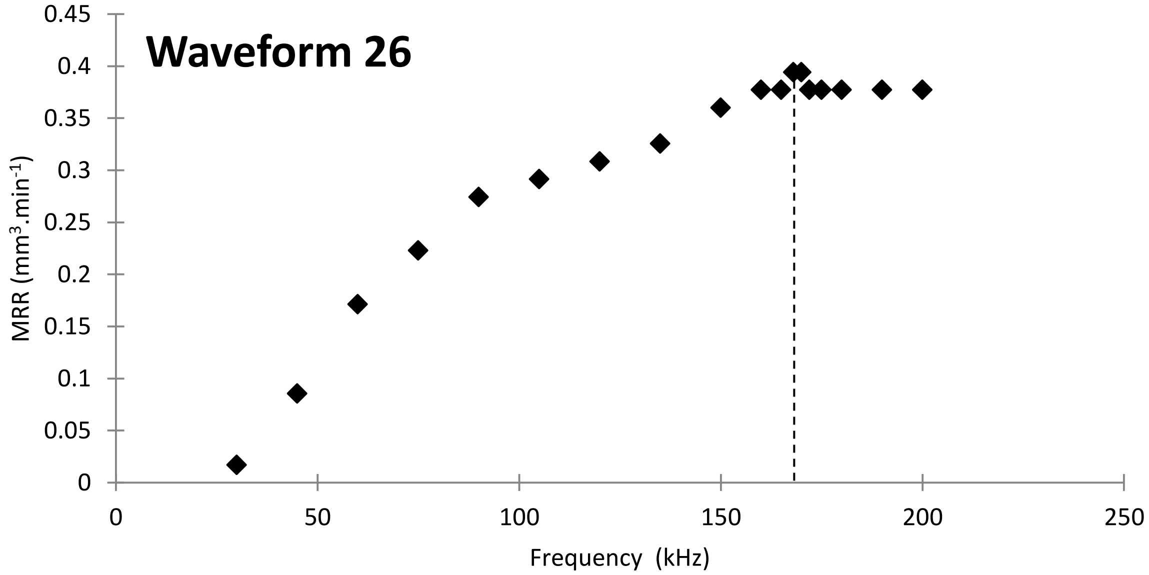

Figure A.2 The variation of the MRR with frequency change for waveforms 21 (75 ns), 23 (55 ns), 24 (45 ns), 25 (35 ns) and 26 (25 ns). The dashed vertical lines represent the PRF0 for each waveform, 72 kHz, 90 kHz, 105 kHz, 125 kHz and 170 kHz respectively.

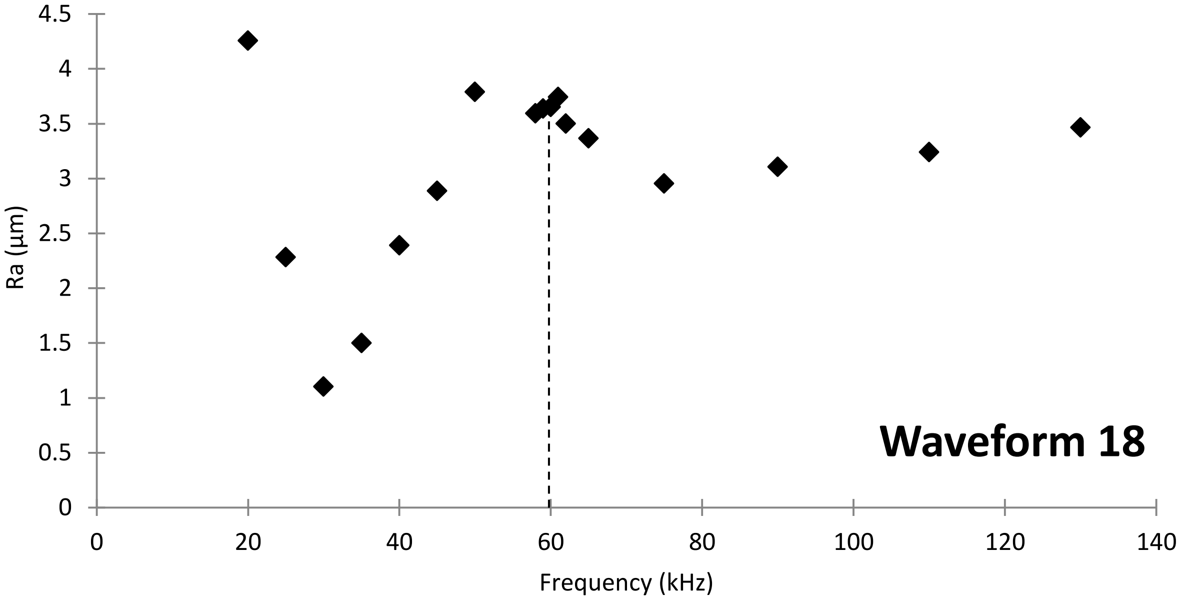
4.5
4
3.5
3
2.5
2
1.5
1
0.5
0
Ra (µm)
0
20
40
60
80
100
120
140
Frequency (kHz)
Waveform 18

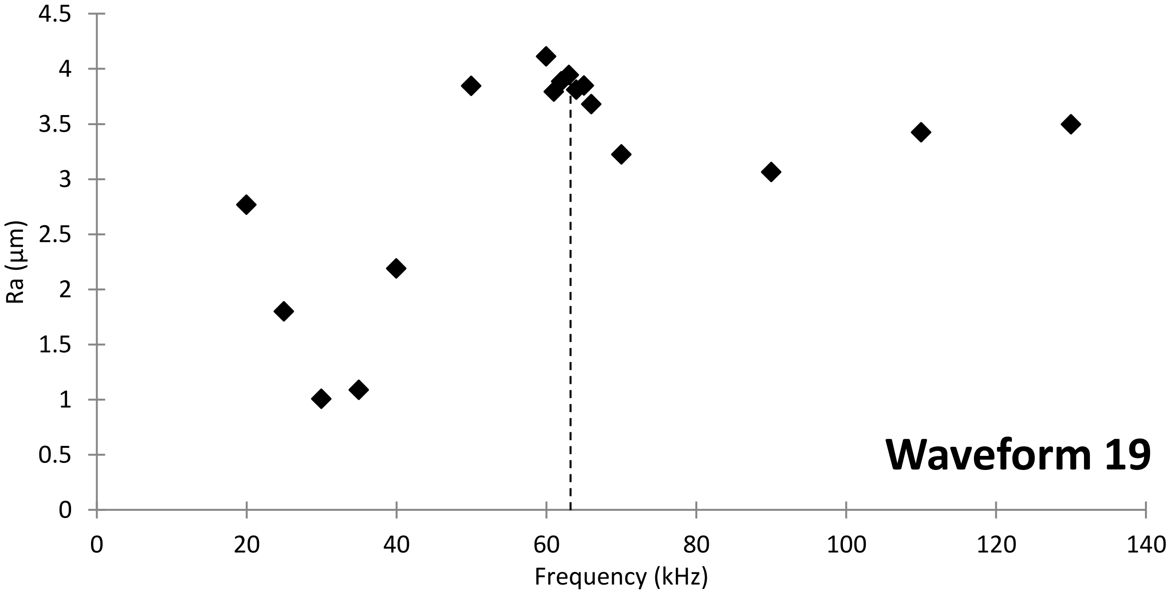
4.5
4
3.5
3
2.5
2
1.5
1
0.5
0
Ra (µm)
0
20
40
60
80
100
120
140
Frequency (kHz)
Waveform 19

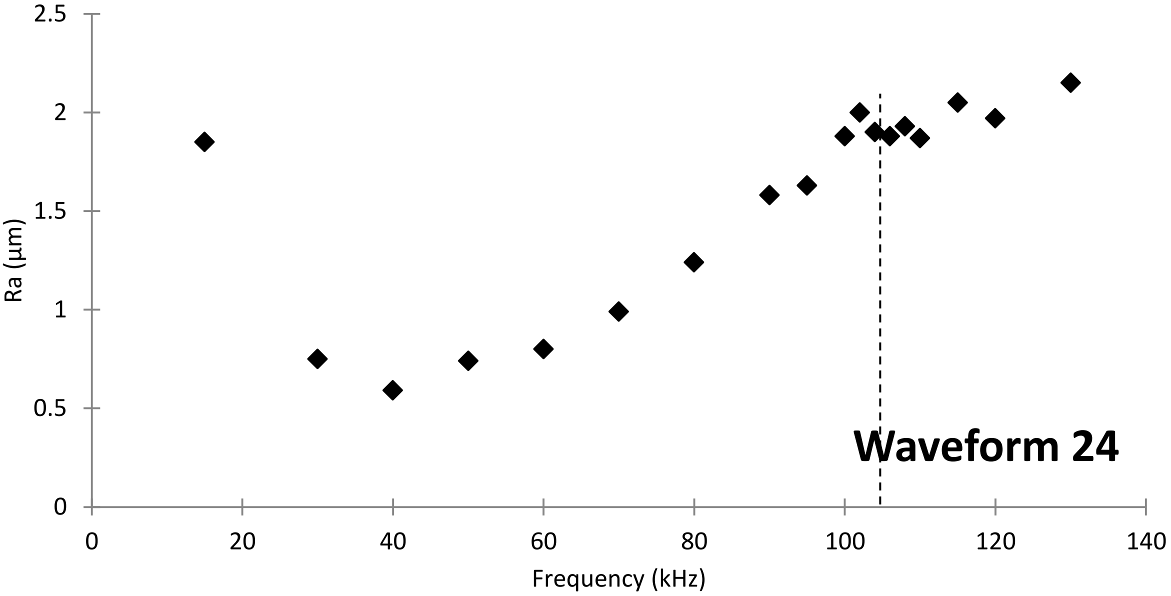

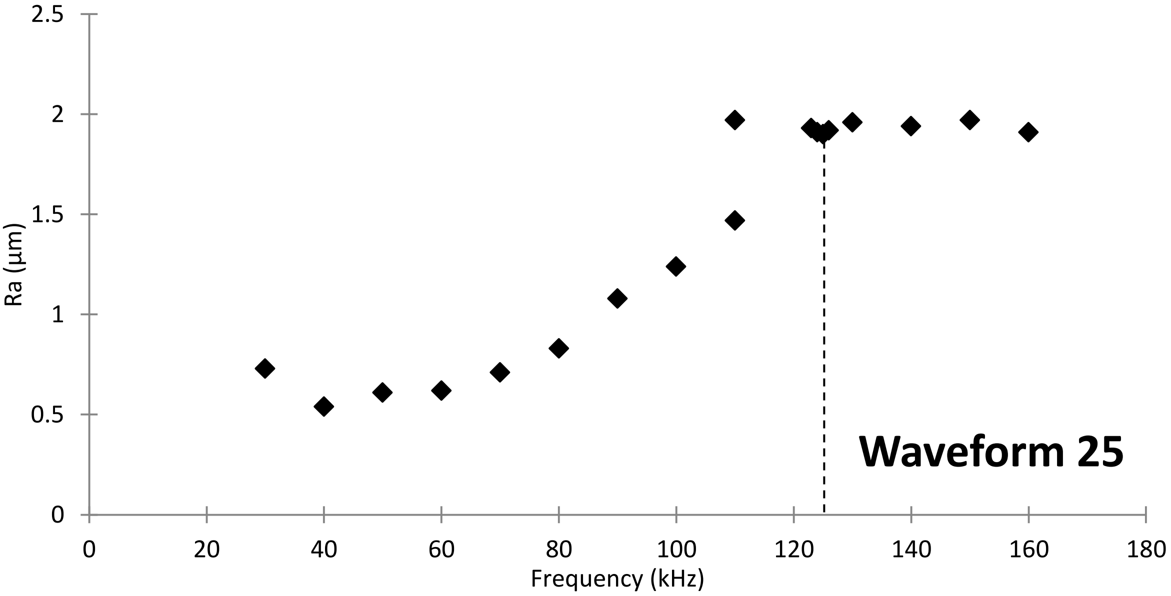

Figure A.3 Variation in the surface roughness with frequency for the four extra waveforms investigated. The dashed vertical lines represent the PRF0 for each waveform.

References

Abderrazak, K., Kriaa W., Ben Salem, W., Mhiri, H., Lepalec, G. and Autric, M. 2009. Numerical and Experimental Studies of Molten Pool Formation During an Interaction of a Pulse Laser (Nd:YAG) with a Magnesium Alloy. Optics &Laser Technology 41, pp. 470–480.

Alexiades, V. and Autrique, D. 2010. Enthalpy model for heating, melting and vaporization in laser ablation. *Electronic Journal of Differential Equations* Available at: http://ejde.math.txstate.edu or http://ejde.math.unt.edu ftp ejde.math.txstate.edu

Amer, M.S.,El-Ashry, M.A., Dosser, L.R., Hix, K.E., Maguire, J.F. and Irwin, B. 2005. Femtosecond versus nanosecond laser machining: comparison of induced stresses and structural change in silicon wafers. *Applied Surface Science* 242, pp. 162 – 167.

Amoruso, S., Bruzzese, R., Spinelli, N. and Velotta, R. 1999. Characterisation of laser-ablation plasmas. *Journal of Physics B* 32, pp. R131 – R172

Anantharaman, T.R. 1984. *Metallic Glasses – Production, Properties and Applications.* Trans Tech Publications Ltd.

Anisimov, S.I. and Khokhlov, V.A. 1995. *Instabilities in Laser-Matter Interaction.* CRC Press.

Anisimov, S.I., Inogamov, N.A., Oparin, A.M., Rethfeld, B., Yabe, T., Ogawa, M. and Fortov, V.E. 1999. Pulsed laser evaporation: equation-of-state effects. *Applied Physics A: Materials Science and Processing* 69, pp. 617 – 620.

Axinte, E. 2012. Metallic Glasses from “Alchemy” to Pure Science: Present and Future of Design, Processing and Applications of Glassy Metals. *Materials and Design* 35, pp. 518 - 556

Bartolo, P., Vasco, J., Silva, B. and Galo, C. 2006. Laser micromachining for mould manufacturing: I. The influence of operating parameters. *Assembly Automation* 26 (3), pp. 237 – 234

Belforte, D.A. 2014. Fibre laser revenues boost the 2013 laser market. *Industrial Laser Solutions for Manufacturing.* Available at: *www.industrial-lasers.com*

Bleiner, D., Chen, Z., Autrique, D. and Bogaerts, A. 2006. Role of laser-induced melting and vaporization of metals during ICP-MS and LIBS analysis, investigated with computer simulations and experiments*. Journal of Analytical Atomic Spectrometry* 21, pp. 910-921

Bogaerts, A. and Chen, Z. 2005. Effect of laser parameters on laser ablation and laser-induced plasma formation: A numerical modelling investigation. *Spectrochimica Acta Part B* 60, pp. 1280 – 1307.

Bogaerts, A., Aghaei, M., Autrique, D., Lindner, H., Chen, Z. and Wendelen, W. 2011. Computer Simulations of Laser Ablation, Plume Expansion and Plasma Formation. *Advanced Materials Research* 227, pp. 1-10.

Borodziuk, S., Kasperczuk, A., Pisarczyk, T., Rohlena, K., Ullschmied, J., Kalal, M., Limpouch, J. and Pisarczyk, P. 2003. Application of laser simulation method for the analysis of crater formation experiment on PALS laser. *Czechoslovak Journal of Physics* 53 (9), pp. 799 – 810.

Bovatsek, J., Tamhankar, A., Patel, R., Bulgakova, N.M. and Bonse, J. 2010. Effects of pulse duration on the ns-laser pulse induced removal of thin film materials used in photovoltaics. *Proceedings of SPIE* 7201 – 41

Brandes, E.A. and Brook, G.B. 1998. *Smithells Light Metals Handbook.* Butterworth-Heinemann

Brebbia, C.A. and Klemm, A. 2013. *Material Characterisation VI: Computational Methods and Experiments.* WIT Press

Bruening, S., Henning, G., Eifel, S. and Gillner, A. . Ultrafast Scan Techniques for 3D-μm Structuring of Metal Surfaces with high repetitive ps-laser pulses. *Physics Procedia* 12 (B), pp. 105 – 115

Campanelli, S.L., Ludovico, A.D., Bonseiro, C., Cavalluzzi, P. and Cinquepalmi, M. 2007. Experimental analysis of laser milling process parameters. *Journal of Materials Processing Technology* 191 (1-3), pp. 220 – 223.

Chan, C.L. and Mazumder, J. 1987. Onedimensional steadystate model for damage by vaporization and liquid expulsion due to lasermaterial interation. *Journal of Applied Physics* 62(11), pp. 4579 – 4586.

Chen B., Shi T.L., Li M., Yang F., Yan F. and Liao G.L. 2014. Laser Welding of Annealed $Zr_{55}Cu_{30}Ni_{5}Al_{10}$ Bulk Metallic Glass. *Intermetallics* 46, pp. 111-117.

Chen Y.C., Chu J.P., Jang J.S.C., Hsieh C.W., Yang Y., Li C.L., Chen Y.M. and Jeng J.Y. 2013. Replication of Nano/Micro-scale Features Using Bulk Metallic Glass Mold Prepared by Femtosecond Laser and Imprint Processes. *Journal of Micromechanics and Microengineering* 23(3), 035030.

Chen, K. And Yao, Y.L. 2000. Process Optimisation in Pulsed Laser Micromachining with Applications in Medical Device Manufacturing. *International Journal of Advanced Manufacturing Technology* 16 (4), pp. 243 – 249.

Chen, T-C. and Darling, R.B. 2005. Parametric studies on pulsed near ultraviolet frequency tripled Nd:YAG laser micromachining of sapphire and silicon. *Journal of Materials Processing Technology* 169 (2), pp. 214 – 218

Chen, T-C. and Darling, R.B. 2012. Fundamentals of Laser Ablation of the Materials Used in Microfluidics. In: Kahrizi, M. 2012. *Micromachining Techniques for Fabrication of Micro and NanoStructures.* InTech. Ch.3. Available from: http://www.intechopen.com/books/micromachining-techniques-for-fabrication-of-micro-and-nano-structures/fundamentals-of-laser-ablation-of-the-materials-used-in-microfluiducs

Chen, T-C., and Darling, R.B. 2008. Laser micromachining of the materials using in microfluidics by high precision pulsed near and mid-ultraviolet Nd:YAG lasers. *Journal of Materials Processing Technology* 198, pp. 248 – 253

Cooper, C. 2001. *Physics*. Taylor and Francis

Cverna, F. 2002. *ASM Ready Reference: Thermal Properties of Metals* ASM International

Data Sheet – Goodfellows – Material Information Silicon Carbide

Deladurantaye, P., Gay, D., Cournoyer, A., Roy, V., Labranche, B., Levesque, M. and Taillon, Y. 2009. Material micromachining using a pulsed fiber laser platform with fine temporal nanosecond pulse shaping capability. *In: Proceedings of SPIE Vol. 7195*

Demetriou, M.D. and Johnson, W.L. Modeling the transient flow of undercooled glass-forming liquids. *Journal of Applied Physics* 95 (5)

Dietrich, J. and Kelbassa, I. 2012. Drilling with fiber lasers. *Industrial Laser Solutions for Manufacturing* [online] Available at http://www.industrial-lasers.com/articles/print/volume-27/issue-1/features/drilling-with-fiber-lasers.html [Accessed 01 February 2012]

Dobrev, T., Dimov, S.S. and Thomas, A.J. 2006. Laser milling: modelling crater and surface formation. *Proc. IMechE. Part C: J. Mechanical Engineering Science* 220, pp. 1685 – 1696.

Duc, D.H., Naoki, I. and Kazuyoshi, F. 2013. A study of near-infrared nanosecond laser ablation of silicon carbide. *International Journal of Heat and Mass Transfer* 65, pp. 713-718

Etsion, I. 2005. State of the Art in Laser Surface Texturing. *Journal of Tribology* 127(1), pp. 248 – 253

Fachinotti, V.D., Cardona, A. and Huespe, A.E. 1999. A Fast Convergent and Accurate Temperature Model for Phase-Change Heat Conduction. *International Journal for Numerical Methods in Engineering* 44, pp. 1863-1884.

Fahler, S. and Krebs, H-U. 1996. Calculations and experiments of material removal and kinetic energy during pulsed laser ablation of metals. *Applied Surface Science* 96-98, pp. 61-65.

Fasasi, A.Y., Mwenifumbo, S., Rahbar, N., Chen, P., Li, M., Beye, A.C., Arnold, C.B. and Soboyejo, W.O. 2009. Nano-second UV laser processed micro-grooves on Ti6Al4V for biomedical applications. *Materials Science and Engineering C* 29, pp. 5 – 13

Fishburn, J.M., Withford, M.J., Coutts, D.W. and Piper, J.A. 2006. Study of the fluence dependent interplay between laser induced material removal mechanisms in metals: Vaporization, melt displacement and melt ejection. *Applied Surface Science* 252 (14), pp. 5182 – 5188

Fredriksson, H. and Akerlind, U. 2012. *Solidification and Crystallization Preocessing in Metals and Alloys*. J.Wiley and Sons.

Gabzdyl, J. 2010. Micro-machining with Nanosecond Pulsed Fiber Laser Beams. *PICALO 2010 #M606*

Gamaly, E.G., Rode, A.V., Perrone, A. and Zocco, A. 2001. Mechanisms of ablation-rate decrease in multiple-pulse laser ablation. *Applied Physics A* 73 (2), pp. 143 – 149.

Gao, Y., Zhou, Y., Wu, B., Tao, S., Jacobsen, R.L. and Goodman, B. 2011. Time-resolved experimental study of silicon carbide ablation by infrared nanosecond laser pulses. *Journal of Manufacturing Science and Engineering* 133, pp. 021006-1 – 021006-5

Gatter, M. 2005. *Getting it Right in Print: Digital Pre-press for Graphic Designers.* Laurence King Publishing.

Genna, S., Leone, C., Lopresto, V., Santo, L. and Trovalusci, F. 2010. Study of fibre laser machining of C45 steel: Influence of process parameters on material removal rate and roughness. *International Journal of Material Formation* 3 (1), pp. 1115 – 1118

Gounaris, E., Casioppo, D. and Denney, P. 2010. Mixed Mode Ablation Used for Improvements in Laser Machining. *ICALEO 2010 # M903*

Green, M.A. 2008. Self-consistent optical parameters of intrinsic silicon at 300K including temperature coefficients. *Solar Energy Materials and Solar Cells* 92(11), pp. 1305-1310

Grigoropoulos, C.P. 2009. *Transport in Laser Microfabrication: Fundamentals and Applications.* Cambridge University Press.

Grigoropoulos, C.P., Park, H.K. and Xu, X. 1993. Modeling of pulsed laser irradiation of thin silicon layers. *International Journal of Heat and Mass Transfer* 36 (4), pp. 919 – 924

Gupta, S. 2008. *Pulsed Laser Ablation and Micromachining of 4H and 6H Silicon Carbide Wafers for High-Temperature MEMS Sensors*. MSc Thesis ProQuest 2008 112 Pages, Iowa State University.

Gyorgy, E., Perez del Pino, A., Serra, P. and Morenza, J.L. 2002. Surface nitridation of titanium by pulsed Nd:YAG laser irradiation. *Applied Surface Science* 186 (1-4), pp. 130 – 134

Hahn, D.W. and Necati Ozisik, M. 2012. *Heat Conduction.* John Wiley and Sons

Harris, G.L. 1995. *Properties of Silicon Carbide*. IET

Hendow, S.T. and Shakir, S.A. 2010. Structuring materials with nanosecond laser pulses. *Optics Express* 18 (10), pp. 10188 – 10198

Herfurth, H., Patwa, R., LAuterborn, T., Heinemann, S. and Pantsar, H. 2007. Micromachining with tailored Nanosecond Pulses. In: *Proceedings of SPIE Vol. 6796.*

Heyl, P., Olschewski, T. and Wijnaendts, R.W. 2001. Manufacturing of 3D structures for micro-tools using laser ablation. *Microelectronic Engineering* 57-58, pp. 775-780.

Hirano, A., Kanno, R., Kawamoto, Y., Takeda, Y., Yamaura, K., Takano, M., Ohyama, K., Ohashi, M. and Yamaguchi, Y. 1995. Relationship between non-stoichiometry and physical properties in $LiNiO_2$. *Solid State Ionics* 78 (1-2), pp. 123-131

Hitz C.B., Ewing J.J. and Hetch J. 2012. *Introduction to Laser Technology*. Wiley, Hoboken, New Jersey.

Ho, J.R., Grigoropoulos, C.P. and Humphrey, J.A.C. 1995. Computational study of heat transfer and gas dynamics in the pulsed laser evaporation of metals. *Journal of Applied Physics* 78 (7), pp. 4696 – 4709.

Hu, H. and Argyropoulos, S.A. 1996. Mathematical modelling of solidification and melting: a review. *Modelling Simul. Mater. Sci. Eng* 4, pp. 371 – 396.

Hull, R. 1999. *Properties of Crystalline Silicon*. IET

Ikutomo, R., Tsujikawa, M., Hino, M., Kimura, H., Yubuta, K. and Inoue, A. 2008. Crystallization by laser for Zr based bulk metallic glass. *International Journal of Cast Metals Research* 21 (1-4), pp. 148-151

Inoue, A. and Takeuchi, A. 2011. Recent developments and application products of bulk glassy alloys. *Acta Materialia,* 59 pp. 2243–2267.

Inoue A., Wang X.M. and Zhang W. 2008. Developments and Applications of Bulk Metallic Glasses. *Reviews on Advanced Materials Science*, 18(1) pp. 1-9.

Ion, J. 2005. *Laser Processing of Engineering Materials: Principles, Procedure and Industrial Application.* Butterworth-Heinemann.

Jellison, G.E. Jr and Lowndes, D.H. 1982. Optical absorption coefficient of silicon at 1.152 μ at elevated temperatures. *Applied Physics Letters* 41(7), pp. 594 – 596

Johnson W.L. Kaltenboeck G., Demetriou M.D., Schramm J.P., Liu X., Samwer K., Kim C.P. and Hofmann D.C. 2011. Beating Crystallization in Glass-Forming Metals by Millisecond Heating and Processing. *Science*, 332 pp. 828-833.

Keevers MJ and Green MA. 1995. Absorption edge of silicon from solar cell spectral response measurements. *Applied Physics Letters* 66 (2) pp. 174-176

Kim Y.J., Busch R., Johnson W.L., Rulison A.J. and Rhim W.K. 1996. Experimental Determination of a Time–Temperature-Transformation Diagram of the Undercooled $Zr_{41.2}Ti_{13.8}Cu_{12.5}Ni_{10.0}Be_{22.5}$ Alloy Using the Containerless Electrostatic Levitation Processing Technique. *Applied Physics Letters*, 68, pp. 1057-1059.

Kim, J., Lee, D., Shin, S. and Lee, C. 2006. Phase evolution in $Cu_{54}Ni_{6}Zr_{22}Ti_{18}$ bulk metallic glass Nd:YAG laser weld. *Materials Science and Engineering A* 434, pp. 194-201

Kleine, K.F. and Watkins, K.G. 2004. Pulse Shaping for Micro Cutting Application of Metals with Fiber Lasers. In: *Proceedings of SPIE Vol. 5339: Photon Processing in Microelectronics and Photonics III. San Jose, CA, USA, January 2004.*

Klement W., Willens R.H. and Duwez P. 1960. Non-Crystalline Structure in Solidified Gold–Silicon Alloys. *Nature*, 187 pp. 869-870.

Knopf, G.K. and Otani, Y. 2012. *Optical Nano and Micro Actuator Technology*. CRC Press

Knowles, M.R.H., Rutterford, G., Karnakis, D. and Ferguson, A. 2007. Micro-machining of metals, ceramics and polymers using nanosecond lasers. *International Journal of Advanced Manufacturing Technology* 33, pp. 95 – 102.

Kruger, O., Schone, G., Wernicke, T., John, W., Wurfl, J. and Trankle, G. 2007. UV laser drilling of SiC for semiconductore device fabrication. *Journal of Physics: Conference Series* 59, pp. 740 – 744

Kumar G., Tang H.X. and Schroers J. 2009. Nanomoulding with Amorphous Metals. *Nature*, 457 pp. 868-872.

Kuper, S. and Brannon, J. 1993. KrF-Laser Ablation of Polyurethene. *Applied Physics A* 57, pp. 255 – 259.

Larruquert, J.I., Perez-Marin, A.P., Garcia-Cortes, S., Rodriquez-de Marcos, L., Aznarez, J.A. and Mendez, J.A. 2011. Self-consistent optical constants of SiC thin films. *Journal of the Optical Society of America A.* 28(11), pp. 2340-2345

Lee, S., Yang, D. and Nikumb, S. 2008. Femtosecond laser micormilling of Si wafers. *Applied Surface Science* 254 (10), pp. 2996-3005

Li B., Li Z.Y., Xiong J.G., Xing L., Wang D. and Li Y. 2006. Laser Welding of $Zr_{45}Cu_{48}Al_7$ Bulk Glassy Alloy. *Journal of Alloys and Compounds*, 413(1-2) pp. 118-121.

Lin H.K., Lee C.J., Hu T.T., Li C.H. and Huang J.C. 2012. Pulsed Laser Micromachining of Mg–Cu–Gd Bulk Metallic Glass. *Optics and Lasers in Engineering*, 50(6) pp. 883–886.

Lin, X.H., Johnson, W.L. and Rhim, W.K. 1997. Effect of Oxygen Impurity on Crystallization of an Undercooled Bulk Glass Forming Zr-Ti-Cu-Ni-Al Alloy. *Materials Transactions JIM* 38 (5), pp. 473 – 477

Liu W.D., Ye L.M. and Liu K.X. 2011(b). Micro-nano Scale Ripples on Metallic Glass Induced by Laser Pulse. *Journal of Applied Physics* 109(4), 043109.

Liu Y., Jiang M.Q., Yang G.W., Chen J.H., Guan Y.J. and Dai L.H. 2012. Saffman-Taylor Fingering in Nanosecond Pulse Laser Ablating Bulk Metallic Glass in Water. *Intermetallics* 31 pp. 325-329.

Liu Y., Jiang M.Q., Yang G.W., Guan Y.J. and Dai L.H. 2011(a). Surface Rippling on Bulk Metallic Glass under Nanosecond Pulse Laser Ablation. *Applied Physics Letters* 99(19) 191902.

Liu, J.M. 1982. Simple technique for measurement of pulsed Gaussian-beam spot sizes. *Optics Letters* 7(5), pp. 196-198

Liu, X., Chu, P.K. and Ding, C. 2004. Surface modification of titanium, titanium alloys, and related materials for biomedical applications. *Material Science and Engineering R* 49, pp. 49 – 121

Liu, X.Y. 2000. Heterogeneous nucleation or homogeneous nucleation? *The Journal of Chemical Physics* 112 (22), pp. 9949- 9955

Liu, Y.H., Hu, J.D., Zhao, L., Guo,Z.X., Chumakov, A.N. and Bosak, N.A. 2010. Accumulation morphology on the surface of stainless steel irradiated by a nanosecond Nd:YAG pulsed laser. *Optics and Laser Technology* 42 (4), pp. 647 – 652

Lu, Q. Mao, S.S., Mao, X. And Russo, R.E. 2002. Delayed phase explosion during high-power nanosecond laser ablation of silicon. *Applied Physics Letters* 80 (17), pp. 3072-3074

Lu, Q., Mao, S.S., Mao, X. and Russo, R.E. 2002. A thermal model of phase explosion for high power laser ablation. *Proceeding of SPIE* 4760, pp. 959 – 964.

Ma F.X., Yang J.J., Zhu X.N., Liang C.Y. and Wang H.S. 2010. Femto Second Laser-Induced Concentric Ring Microstructures on Zr-based Metallic Glass. *Applied Surface Science* 256, pp. 3653-3660.

Maini, A.K. 2013. *Lasers and Optoelectronics: Fundamentals, Devices and Applications.* John Wiley and Sons.

Marla, D., Bhandarkar, U.V. and Joshi, S.S. 2011. Critical assessment of the issues in the modelling of ablation and plasma expansion processes in the pulsed laser deposition of metals. *Journal of Applied Physics* 109, pp. 021101 1-15.

Martin, I., Ohkubo, T., Ohnuma, M., Deconihout, B. and Hono, K. 2004. Nanocrystallization of $Zr_{41.2}Ti_{13.8}Cu_{12.5}Ni_{10.0}Be_{22.5}$ metallic glass. *Acta Materialia* 52 (15), pp. 4427 – 4435

Maul, J., Strachnov, I., Karpuk, S., Bernhard, P., Oelsner, A., Schonhense, G. and Huber, G. 2006. Onset of crater formation during short pulse laser ablation. *Applied Physics A* 82 (1), pp. 43 – 47

Mazhukin, V.I., Nossov, V.V. and Smurov, I. 2007. Modeling of plasma-controlled surface evaporation and condensation of Al target under pulsed laser irradiation in the nanosecond regime. *Applied Surface Science* 253(19), pp. 7686-7691.

Mele, A., Giardini Guidoni, A., Kelly, R., Miotello, A., Orlando, S. and Teghil, R. 1996. Spatial distribution of laser-ablated material by probing a plasma plume in three dimensions. *Applied Surface Science* 96-98, pp. 102 – 111.

Miotello, A. and Kelly, R. 1995. Critical assessment of thermal models for laser sputtering at high fluencies. *Applied Physics Letters* 67 (24), pp. 3532 – 3537.

Moscicki, T., Hoffman, J. and Szymanski, Z. 2011. Modelling of plasma formation during nanosecond laser ablation. *Archives of Mechanics* 63 (2), pp. 99 – 116

O'Neill, W. and Li, K. 2009. High-Quality Micromachining of Silicon at 1064 nm Using a High-Brightness MOPA-Based 20-W Yb Fiber Laser. *Selected Topics in Quantum Electronics, IEEE Journal of Quantum Electronics* 15 (2), pp. 462 - 470

Orazi, L., Cuccolini, G., Fortunato, A. and Tani, G. 2010. An automated procedure for material removal rate prediction in laser surface micromanufacturing. *International Journal of Advanced Manufacturing Technology* 46, pp. 163 – 171

Otto, A., Koch, H., Leitz, K-H. and Schmidt, M. 2011. Numerical Simulations – A Versatile Approach for Better Understanding Dynamics in Laser Material Processing. *Physics Proceedia* 12, pp. 11 – 20.

Overton, G., Hausken, T., Belforte, D.A. and Holton, C. 2012. *ANNUAL REVIEW AND FORECAST: Economic aftershocks keep laser markets unsettled.* Laser Focus World. Available at: http://www.laserfocusworld.com/articles/print/volume-48/issue-01/features/economic-aftershocks-keep-laser-markets-unsettled.html

Peker, A. and .Johnson, W.L. 1993. A highly processable metallic glass: $Zr_{41.2}Ti_{13.8}Cu_{12.5}Ni_{10.0}Be_{22.5}$. *Applied Physics Letters* 63 (17), pp. 2342-2344

Petkov, P.V., Dimov, S.S., Minev, R. and Pham, D.T. 2008. Laser milling: pulse duration effects on surface integrity. *Proceedings of IMechE Part B: Journal of Engineering Manufacture* 222, pp. 35 – 45

Pierson, H.O. 1996. *Handbook of Refractory Carbides and Nitrides: Properties, Characteristics, Processing and Applications.* Noyes Publications, New Jersey.

Pham, D.T., Dimov, S.S. and Petkov, P. 2002. Laser milling. *Proc Instn Mech Engrs* 216 (Part B), pp. 657 – 667.

Plohl, G. 2010. Pulsed Laser Ablation. *Seminar Available at: http://mafija.fmf.uni-lj.si/seminar/files/2009_2010/Pulsed_Laser_Ablation.pdf*

Quintana, I., Dobrev, T., Aranzabr, A., Lalev, G. and Dimov, S. 2009. Investigation of Amorphous and Crystalline Ni Alloys Response to Machining with Micro-second and Pico-second Laser. *Applied Surface Science* 255 (13-14), pp. 6641-6646

Quintino, L., Costa, A., Miranda, R., Yapp, D., Kumar, V. and Kong, C.J. 2007. Welding with high power fiber lasers – A preliminary study. *Materials and Design* 28 (4), pp. 1231-1237

Raciukaitis, G., Brikas, M., Gecys, P. and Gedvilas, M. 2008. Accumulation effects in laser ablation of metals with high-repetition rate lasers. *Proceedings of SPIE* 7005

Ready, J.F. 1965. Effects due to absorption of laser radiation. *Journal of Applied Physics* 36 (2)

Roy, R.K. 2001. *Design of Experiments Using The Taguchi Approach: 16 Steps to Product Improvement.* John Wiley and Sons.

Russo, R.E., Mao, X. and Mao, S.S. 2002. The Physics of Laser Ablation in Microchemical Analysis/ *Analytical Chemistry* 74 (3), pp. 70A – 77A.

Saklakoglu, I.E. and Kasman, S. 2011. Investigation of micro-milling process parameters for surface roughness and milling depth. *International Journal of Advanced Manufacturing Technology* 54 (5-8), pp. 567 – 578

Salama, I.A., Quick, N.R. and Kar, A. 2005. Microstructural and electrical resistance analysis of laser-processed SiC substrates for wide bandgap semiconductor materials. *Journal of Materials Science* 40, pp. 3969-3980

Sami, M. and Yilbas, B.S. 1998. Three-dimensional electron-kinetic theory approach for laser heating: Moving heat source consideration. *Physica A* 256, pp. 439-462.

Sano T., Takahashi K., Hirose A. and Kobayashi K. 2007. Femtosecond Laser Ablation of $Zr_{55}Al_{10}Ni_5Cu_{30}$ Bulk Metallic Glass. *Materials Science Forum*, 539-543 pp. 1951-1954.

Schaaf, P. 2010. *Laser Processing of Materials: Applications and Developments.* Springer Science and Business Media

Schroers J., Pham Q. and Desai A. 2007. Thermoplastic Forming of Bulk Metallic Glass - A Technology for MEMS and Microstructure Fabrication. *Journal of Microelectromechanical Systems* 16 (2), pp 240-247.

Schroers, J., Kumar, G., Hodges, T.M., Chan, S. and Kyriakides, R. 2009. Bulk metallic glasses for biomedical applications. *JOM* 61 (9), pp. 21 – 29

Schroers, J., Masuhr, A., Johnson, W.L. and Busch, R. 1999. Pronounced asymmetry in the crystallization behaviour during constant heating and cooling of a bulk metallic glass-forming liquid. *Physical Review B* 60 (17), pp. 855-858

Schwarz-Selinger, T., Cahill, D.G., Chen, S-C., Moon, S-J. and Grigoropoulos, C.P. 2001. Micron-scale modifications of Si surface morphology by pulsed-laser texturing. *Physical Review B* 64, pp. 155323 1-7

Selada, A., Manaia, A., Vieira, M.T. and Pouzada, A.S. 2011. Effect of LBM and large-area EBM finishing on micro-injection moulding surfaces. *The International Journal of Advanced Manufacturing Technology* 52 (1-4), pp. 171 – 182

Semerok, A., Salle, B., Wagner, J-F. And Petite, G. 2002. Femtosecond, picoseconds and nanosecond laser microablation: Laser plasma and crater investigation. *Laser and Particle Beams* 20 (1), pp. 67 – 72

Shen, Z.H., Zhang, S.Y., Lu, J. and No, X.W. 2001. Mathematical modelling of laser induced heating and melting in solids. *Optics and Laser Technology* 33 (8), pp. 533 – 537.

Sokolowski-Tinten, K., Bialkowski, J., Cavalleri, A., von der Linder, D., Oparin, A., Meyer-ter-Vehn, J. and Anisimov, S.I. 1998. Transient Stated of Matter during Short Pulse Laser Ablation. *Physical Review Letters* 81 (1), pp. 224-227

SPI Lasers. 2008. Laser Scribing Thin Film Molybdenum for Photovoltaic cells. *Application Note* Available at: *http://www.worldlasers.com/articles/research/wl_AppsNotesFinal.pdf*

Spritzer, W.G., Kleinman, D. and Walsh, D. 1959 Infrared properties of hexagonal silicon carbide. *Physical Review* 133 (1), pp. 127-132

Stafe, M., Negutu, C. and Popescu, I.M. 2006. Combined experimental and theoretical investigation of multiple-nanosecond laser ablation of metals. *Journal of optoelectronics and advanced materials* 8 (3), pp. 1180 – 1186.

Suryanarayana, C. and Inoue, A. 2011. *Bulk Metallic Glasses.* CRC Press.

Tang, Y.F., Silva, S.R.P., and Rose, M.J. 2001. Super sequential lateral growth of Nd:YAG laser crystallized hydrogenated amorphous silicon. *Applied Physics Letters* 78 (2), pp. 186-188

Tani, G., Orazi, L., Fortunato, A. and Cuccolini, G. 2007. The Influence of Plasma Plume in Laser Milling for Mold Manufacturing. *Journal of Laser Micro/Nanoengineering* 2 (3), pp. 225 – 229

Tao, M., Chokshi, A.H., Conner, R.D., Ravichandran, G. and Johnson, W.L. 2010. Deformation and crystallization of Zr-based amorphous alloys in homogenous flow regime. *Journal of Materials Research* 25 (6), pp. 1137- 1148.

Thirumaleshwar, M. 2009. *Fundamentals of Heat and Mass Transfer.* Pearson Education India.

Thomson, W.L. 1871. XLVI. Hydrokinetic solutions and observations. *The London, Edinburgh and Dublin Philosophical Magazine and Journal of Science* 42 (281), pp. 362-377

Vladiou, I., Stafe, M., Negutu, C. and Popescu, I.M. 2008. The dependence of the ablation rate of metals on nanosecond laser fluence and wavelength. *Journal of Optoelectronics and Advanced Materials* 10(12), pp. 3177-3181.

Voevodin, A.A. and Zabinski, J.S. 2006. Laser surface texturing for adaptive solid lubrication.*Wear* 261(11–12), pp. 1285-1292

Voisey, K.T., Kudesia, S.S., Rodden, W.S.O., Hand, D.P., Jones, J.D.C. and Clyne, T.W. 2003. Melt ejection during laser drilling of metals. *Materials Science and Engineering A* 356, pp. 414-424

Von der Linde, D. and Sokolowski-Tinten, K. 2000. The physical mechanisms of short-pulse laser ablation. *Applied Surface Science* 154-155, pp. 1 – 10.

Wang, G., Huang, Y.J., Shagiev, M. and Shen, J. 2012. Laser welding of $Ti_{40}Zr_{25}Ni_3Cu_{12}Be_{20}$ bulk metallic glasses. *Materials Science and Engineering A* 541, pp. 33-37.

Wang, HP., Yang, SJ. and Wei, BB. 2012. Density and structure of undercooled liquid titanium. *Condensed matter physics* 57 (7), pp. 719-723

Wang, X.D., Michalowski, A., Walter, D., Sommer, S., Kraus, M., Liu, J.S. and Dausinger, F. 2009. Laser drilling of stainless steel with nanosecond double-pulse. *Optics and Laser Technology* 41, pp. 148 – 153.

Wang, X., Shen, Z.H., Lu, J. and Ni, X.W. 2010. Laser-induced damage thresholds of silicon in millisecond, nanosecond and picosecond regimes. *Journal of Applied Physics* 108, pp. 033103-1- 033103 – 7.

Waniuk, T.A., Schroers, J. and Johnson, W.L. 2001. Critical cooling rate and thermal stability of Zr-Ti-Cu-Ni-Be alloys *Applied Physics Letters* 78 (9), pp. 1213-1215

Welsch, G., Boyer, R. and Collings, E.W. 1993. *Materials properties handbook: Titanium alloys*. ASM International.

Wilkes, K.E., Dinwiddie, R.B. and Graves, R.S. 1996. *Thermal Conductivity 23.* CRC Press.

Wu, B. and Shin, Y.C. 2006. Modeling of nanosecond laser ablation with vapour formation. *Journal of Applied Physics* 99, pp. 084310 – 1 – 084310 – 8.

Xiao, C.J., Li, Z.X. and Deng, X.R. 2011. Grain-size effects on thermal properties of $BaTiO_3$ ceramics. *Bull. Mater. Sci.* 34 (4), pp. 963 – 966

Xie, J. and Kar, A. 1997. Mathematical modelling of melting during laser materials processing. *Journal of Applied Physics* 81 (7), pp. 3015 – 3022.

Yasa, E. and Kruth, J.P. 2010. Investigation of laser and process parameter for Selective Laser Erosion. *Precision Engineering* 34 (1), pp. 101-112

Yilbas, B.S. 1996. Analytical solution for time unsteady laser pulse heating of semi-infinite solid. *International Journal of Mechanical Science* 39 (6), pp. 671 – 682.

Yilbas, B.S. and Mansoor, S.B. 2009. Laser pulse heating and phase changes in the irradiatied region: Temperature-dependent thermal properties case. *International Journal of Thermal Sciences* 48, pp. 761 – 772

Yoo, J.H., Jeong, S.H., Greif, R. and Russo, R.E. 2000. Explosive change in crater properties during high power nanosecond laser ablation of silicon. *Journal of Applied Physics* 88(3), pp. 1638 – 1649

Zhang, L. and Wang, X.D. 2008. Hybrid atomistic-macroscale modeling of long-time phase change in nanosecond laser–material interaction*.* *Applied Surface Science* 255(5, Part 2), pp. 3097-3103.

Zhang, Y. and Faghri, A. 1999. Vaporization, melting and heat conduction in the laser drilling process. *International Journal of Heat and Mass Transfer* 42 (10), pp. 1175 – 1790.

Zhigilei, L.V., Lin, Z., Ivanov, D.S., Leveugle, E., Duff, W.H., Thomas, D., Sevilla, C. and Guy, S.J. 2010. Atomic/Molecular-Level Simulations of Laser-Materials Interactions. In: Miotello and Ossi. 2010. *Laser-Surface Interactions for New Materials Production; Tailoring Structure and Properties.* Springer Series in Materials Science Vol, 130. Ch.3. pp. 43 – 79.

Zhu, Z., Zhou, X., Liu, Q., Lin, J. and Zhao, S. 2012. Fabrication of Micro-Structured Surfaces on Bulk Metallic Glasses Based on Fast Tool Servo Assisted Diamond Turning. *Science of Advanced Materials* 4, pp. 906-911.

Zimmer, K., Braun, A. and Bigl, F. 2000. Combination of different processing methods for the fabrication of 3D polymer structures by excimer laser machining. *Applied Surface Science* 154-155. pp. 601-604.

Publications and Presentations

Williams, E., Brousseau, E.B. and Rees, A. 2014. Nanosecond Yb fibre laser milling of aluminium: effect of process parameters on the achievable surface finish and machining efficiency. *International Journal of Advanced Manufacturing Technology* 74(5-8), pp. 769 – 780.

Madge, M., Brousseau, E.B., Eaton, M., Featherston, C.A. and **Williams, E**. 2014. Adhesive Bonding of Laser Processed CFRP Panels. *Presentation at the 16th International Conference on Experimental Mechanics, ICEM16, Cambridge, Uk, July 7-11, 2014*

Williams, E. and Brousseau, E.B. 2013. Single pulse nanosecond laser processing of zirconium-based bulk metallic glass. *International Conference on Multi-Material Micro Manufacture, 4M2013, San Sebastian, Spain, October 8-10, 2013,* pp. 152 – 155

Williams, E., Brousseau, E.B., Harrison, P. and Gabzdyl, J. 2013. Nanosecond Yb fibre laser: effect of process parameters on the achievable surface finish and machining efficiency. *Presentation at the International Laser Applications Symposium 2013, ILAS2013, Nottingham, UK, March 12-13, 2013*